

OPTOELECTRONICS OF TWO  
DIMENSIONAL TRANSITION METAL  
DICHALCOGENIDES

A THESIS SUBMITTED TO THE UNIVERSITY OF MANCHESTER  
FOR THE DEGREE OF DOCTOR OF PHILOSOPHY  
IN THE FACULTY OF SCIENCE & ENGINEERING

2018

**Mark Danovich**

School of Physics and Astronomy

# Contents

<b>Abstract</b>	<b>6</b>
<b>Declaration</b>	<b>7</b>
<b>Copyright Statement</b>	<b>8</b>
<b>Acknowledgements</b>	<b>9</b>
<b>1 Introduction</b>	<b>11</b>
<b>2 Overview</b>	<b>16</b>
2.1 2D transition metal dichalcogenides . . . . .	16
2.2 Symmetry of 2D TMDCs . . . . .	18
2.3 Spin-orbit coupling . . . . .	20
2.4 $\mathbf{k} \cdot \mathbf{p}$ model for TMDCs . . . . .	22
2.5 Optical selection rules . . . . .	23
2.6 Phonons in TMDCs . . . . .	24
2.6.1 Electron-phonon coupling . . . . .	26
2.7 Excitons, trions and biexcitons in TMDCs . . . . .	27
2.7.1 Excitons . . . . .	28
2.7.2 Trions . . . . .	31
2.7.3 Biexcitons . . . . .	33
2.8 Heterobilayers of TMDCs . . . . .	34
<b>3 Kinetics of electrons and holes in TMDCs</b>	<b>39</b>
3.1 Introduction . . . . .	39
3.2 Fast relaxation of photo-excited carriers . . . . .	40

3.3	Auger recombination of dark excitons . . . . .	47
<b>4</b>	<b>Bound complexes in monolayer TMDCs</b>	<b>53</b>
4.1	Introduction . . . . .	53
4.2	Semidark trions and biexcitons in WS <sub>2</sub> and WSe <sub>2</sub> . . . . .	54
4.3	Excitonic complexes in TMDCs . . . . .	77
<b>5</b>	<b>Bound complexes in heterobilayer TMDCs</b>	<b>102</b>
5.1	Introduction . . . . .	102
5.2	Localized complexes in heterobilayer TMDCs . . . . .	103
<b>6</b>	<b>Multilayer films of TMDCs</b>	<b>121</b>
6.1	Introduction . . . . .	121
6.2	Intersubband optics in few-layer films of TMDCs . . . . .	122
<b>7</b>	<b>Conclusions</b>	<b>146</b>
<b>A</b>	<b>HP and LO phonons coupling in TMDCs</b>	<b>150</b>

# List of Tables

2.1	Character table for point group $C_{3h}$ . . . . .	18
2.2	Character table for point group $D_{3h}$ . . . . .	25

# List of Figures

2.1	TMDCs crystal structure . . . . .	17
2.2	DFT calculated band structure of TMDCs . . . . .	17
2.3	DFT bands orbital decomposition . . . . .	19
2.4	DFT bands out-of-plane spin projection for MoSe <sub>2</sub> and WSe <sub>2</sub> . . . . .	20
2.5	Schematic band structures for MX <sub>2</sub> and WX <sub>2</sub> near the K/K' points . .	21
2.6	DFT calculated phonon dispersions of MoS <sub>2</sub> and phonon modes vibrations.	25
2.7	Bright and dark excitons in MoX <sub>2</sub> and WX <sub>2</sub> . . . . .	31
2.8	Bright and dark trions in MoX <sub>2</sub> and WX <sub>2</sub> . . . . .	32
2.9	Bright and dark biexcitons in MoX <sub>2</sub> and WX <sub>2</sub> . . . . .	34
2.10	Hetrobilayer type-II band alignment . . . . .	35
2.11	Twisted hetrobilayer in real space, reciprocal space, and interlayer ex- citon dispersion . . . . .	36
A.1	HP and LO coupling strengths in 2D TMDCs . . . . .	152

# The University of Manchester

Mark Danovich

Doctor of Philosophy

Optoelectronics of two dimensional transition metal dichalcogenides

March 23, 2018

Two dimensional transition metal dichalcogenides provide a host of unique optoelectronic properties, attributed to their two dimensional nature and unique band structure, making them promising for future optoelectronics device applications. In the work presented in this thesis, we focus on the theoretical understanding and modelling of the optoelectronic properties of monolayer transition metal dichalcogenides, their heterostructures and multilayers.

We studied the relaxation rates of photo-excited carriers leading to the formation of electron-hole pairs and their subsequent radiative recombination, resulting in emission of light. We find sub-ps relaxation times, attributed to the strong coupling of carriers with optical phonons, allowing the efficient formation of strongly bound multi-particle complexes such as excitons, trions and biexcitons, which can recombine radiatively if allowed by selection rules. We classify the various complexes according to their optical activity, and predict using diffusion quantum Monte Carlo calculations the resulting photoluminescence spectra in these materials.

We proposed a novel, material specific, Auger process in  $\text{WS}_2$  and  $\text{WSe}_2$  involving dark excitons, which dominates over radiative processes for relatively low carrier densities, providing an explanation to the observed low quantum efficiencies in these materials. In the same pair of materials, we have shown how the ground state dark trions and biexcitons can become bright and recombine radiatively through an electron-electron intervalley scattering process, resulting in new observable lines in the photoluminescence spectra of these materials.

The ability to form van der Waals heterostructures of two or more layers of these materials, allows for new degrees of freedom to be explored and utilised. The heterobilayer system made of  $\text{MoSe}_2/\text{WSe}_2$  has a type-II band alignment, allowing for the formation of interlayer bound complexes with carriers localized on opposite layers. We studied the bound complexes formed in this bilayer system, localized on donor impurities. We used quantum Monte Carlo methods to obtain binding energies and wave functions, and calculated the radiative rates and doping dependent photoluminescence spectra of these complexes for closely aligned layers, and asymptotic behaviour for strongly misaligned layers.

Finally, we studied few-layers of 2H-stacked transition metal dichalcogenides. The van der Waals quantum well structure results in the splitting of the conduction and valence bands into multiple subbands with energy spacings covering densely the infrared to far-infrared spectral range. We developed a hybrid  $\mathbf{k} \cdot \mathbf{p}$ -tight binding model parameterised by DFT calculations of monolayer and bulk crystals of the studied materials. We used the model to describe the subband dispersions, transition energies, phonon induced broadening and resulting absorption lineshapes for both p-doped and n-doped few-layer films.

# **Declaration**

No portion of the work referred to in the thesis has been submitted in support of an application for another degree or qualification of this or any other university or other institute of learning.

# Copyright Statement

- i. The author of this thesis (including any appendices and/or schedules to this thesis) owns certain copyright or related rights in it (the “Copyright”) and s/he has given The University of Manchester certain rights to use such Copyright, including for administrative purposes.
- ii. Copies of this thesis, either in full or in extracts and whether in hard or electronic copy, may be made **only** in accordance with the Copyright, Designs and Patents Act 1988 (as amended) and regulations issued under it or, where appropriate, in accordance with licensing agreements which the University has from time to time. This page must form part of any such copies made.
- iii. The ownership of certain Copyright, patents, designs, trade marks and other intellectual property (the “Intellectual Property”) and any reproductions of copyright works in the thesis, for example graphs and tables (“Reproductions”), which may be described in this thesis, may not be owned by the author and may be owned by third parties. Such Intellectual Property and Reproductions cannot and must not be made available for use without the prior written permission of the owner(s) of the relevant Intellectual Property and/or Reproductions.
- iv. Further information on the conditions under which disclosure, publication and commercialisation of this thesis, the Copyright and any Intellectual Property and/or Reproductions described in it may take place is available in the University IP Policy (see <http://documents.manchester.ac.uk/DocuInfo.aspx?DocID=487>), in any relevant Thesis restriction declarations deposited in the University Library, The University Library’s regulations (see <http://www.manchester.ac.uk/library/aboutus/regulations>) and in The University’s Policy on Presentation of Theses.

# Acknowledgements

I would first like to thank my supervisor Prof. Vladimir I. Fal'ko for providing me with the opportunity to perform research in condensed matter Physics under his supervision, for participating in conferences and schools with leading researches, and for many insightful and inspiring discussions.

I would like to acknowledge Prof. Igor I. Aleiner whose support was essential for the research presented in this thesis through discussions during his visits to Lancaster University and the National Graphene Institute. I would also like to thank Dr. David A. Ruiz-Tijerina for the collaboration in the last year of my PhD, for his suggestions, ideas and general company.

I would like to thank my family for their constant support and belief in me, allowing me to pursue my dreams. My grandmother Prof. Elena S. Domnina and grandfather Prof. Konstantin N. Danovich for inspiring me as a child to be curious and inquisitive, and my mother Nataly Danovich and my father Dr. David Danovich for their support and help during my studies in all aspects. Lastly, I would like to thank my girlfriend Rebecca Thornton for her support throughout these three and a half years.

I would like to dedicate this thesis to my father Dr. David Danovich who has always been there for me, encouraged me to always be and do the best I can, and without him none of this would be possible.

Blank Page

# Chapter 1

## Introduction

Since the discovery of graphene in 2004, attempts have been made to apply similar methods to isolate single layers of other stacked three-dimensional materials and study their properties. This resulted in a wide variety of materials with a wide range of properties and potential applications, ranging from insulators (hBN), direct band gap semiconductors ( $\text{MoS}_2$ ), metals ( $\text{NbSe}_2$ ) and semi-metals ( $\text{WTe}_2$ ). From the technological point-of-view, the possibility of having atomically-thin devices, with superior characteristics and the ability to tune their desired properties by combining different layers of these materials in a Lego-like manner to form van der Waals heterostructures is very promising and revolutionary [1]. From the theoretical point-of-view, these two dimensional (2D) materials provide an exciting playground for condensed matter theory studies to explore new and exotic phenomena unique to these ideal 2D systems.

One particular shortcoming of graphene, motivating the further search for new 2D materials was the lack of a finite band gap. The isolation of a single layer of  $\text{MoS}_2$  and the demonstration of a direct band gap [2] with significant optical response as compared to the bulk material have made it promising for both electronic and optoelectronic applications, and started an expansive research on the family of the semiconducting direct band gap 2D transition metal dichalcogenides (TMDCs) comprising of  $\text{MoS}_2$ ,  $\text{MoSe}_2$ ,  $\text{WS}_2$ , and  $\text{WSe}_2$ . These studies revealed numerous exciting properties of these materials including: direct band gap in the visible range, valley circular dichroism [3, 4], Berry curvature and spin-valley effects [5, 6, 7], strong spin-orbit coupling and large spin-orbit splitting [8], strong light-matter coupling [9], and tightly bound excitons and trions [10, 11] up to room temperature.

The preferable optical properties of monolayer TMDCs and their heterostructures, have been utilised and demonstrated in optoelectronic devices such as: photodetectors, phototransistors, light emitting diodes, photodiodes, and solar cells [12, 13, 14, 15, 16, 17], as well as single photon emitters [18].

The utilisation of TMDCs in optoelectronic devices requires an understanding of the processes governing the optoelectronic properties of these materials. The reduced dimensionality of these materials has important implications on the density of states of the carriers, interaction between carriers, interaction between carriers and phonons, and interaction with the environment, all influencing the resulting optical properties of these materials.

Light emission from semiconductors involves the radiative recombination of electron-hole pairs. These are formed by light with a photon energy greater than the band gap, exciting electrons from the valence band into the conduction band. The radiative recombination is then governed by the kinetics of the carriers relaxing from the excited states, which involves interaction with phonons, interaction with other carriers, and with impurities, as well as the selection rules and conservation laws governing the light-matter coupling and recombination. Electron-electron scattering can also give rise to non-radiative Auger-type processes where the energy of the recombining electron-hole pair is transferred to another carrier. The relative importance of such processes determines the efficiency of these materials for light emission.

The modified Coulomb interaction between electrons and holes in these two dimensional materials due to the reduced screening as compared to the three dimensional case [19, 20], leads to the most prominent feature observed in the optical studies of TMDCs, these are the strongly bound multi-particle complexes, such as excitons and trions, with a wide range of possible configurations due to the spin and valley degrees of freedom in these materials. The photon energies resulting from the recombination of these complexes are determined by their binding energies as well as the recombination process. Therefore, an understanding of the resulting optical spectra requires the classification of the various complexes, calculation of their binding energies and understanding the processes resulting in their radiative recombination.

The two dimensional nature of these materials, allows to naturally stack them together in the form of van der Waals heterostructures, formed by different TMDCs, or

few-layers of the same TMDC. This allows to extend the applicability of these materials for device applications, introducing new degrees of freedom, such as the choice of materials, their stacking and alignment. The stacking of different TMDCs in a heterobilayer results in a staggered band structure with electrons and holes localized on opposite layers, allowing the formation of interlayer complexes with modified optical properties and recombination processes. The momentum mismatch between the electrons and holes in the misaligned and incommensurate layers, raises the question of how these complexes can recombine to emit light. A possible channel proposed in this thesis involves the localization of complexes on donor impurities, which result in distinct optical spectra with strong dependences on the alignment and doping in the system.

Alternatively, multilayers of the same van der Waals coupled TMDCs, form a quantum well like structure, with the states in the growth direction being quantized, forming subbands. This allows to extend the optical applicability of these materials from their main interband gap ( $\sim 2$  eV) in the visible range to the smaller intersubband gaps ( $\sim 10 - 100$  meV) in the highly useful and popular infrared spectral range, which has applications in various industries. Utilizing these subbands in optoelectronic applications requires the modelling and characterization of the resulting optical properties of these subbands, the coupling to light, symmetry properties and broadening sources. In this thesis we analyse the subband structures for both p-doped and n-doped few layer TMDCs and obtain the resulting intersubband absorption spectra.

This thesis focuses on the optoelectronics of monolayer TMDCs, their heterostructures and multilayer structures. The published (or submitted) papers included in this thesis study the introduced aspects related to the optoelectronics of TMDCs, which are of both theoretical and application interest, elucidating and extending the understanding of the potential, limitations, and directions of research for these materials, for the use in future device applications. The chapters form a sequential and coherent picture of specific processes and features, characterizing and governing the optical properties of these materials, starting from the monolayer, to heterobilayers and finally multilayers, each containing the relevant published works in a journal format. The thesis is organized as follows:

## Chapter 2

Chapter 2 provides a general background and literature review of transition metal dichalcogenides.

## Chapter 3

Chapter 3 deals with kinetic processes in monolayer TMDCs. It includes two publications on the relaxation of photo-excited carriers due to emission of optical phonons, leading to pico-second relaxation times due to strong coupling to optical phonons [21] and the Auger recombination of dark excitons in  $\text{WS}_2$  and  $\text{WSe}_2$ , providing a possible explanation for the observed low quantum efficiencies in these materials.

## Chapter 4

Chapter 4 deals with bound complexes in monolayer TMDCs. The work presented includes the radiative recombination of semidark trions and biexcitons in  $\text{WS}_2$ ,  $\text{WSe}_2$  [22], where we present a novel process for the optical activation of the dark ground state trions and biexcitons in  $\text{WS}_2$  and  $\text{WSe}_2$ , and the classification of excitonic complexes into dark and bright, and the resulting emission spectra obtained from the calculated binding energies of the various complexes using diffusion quantum Monte Carlo methods [23].

## Chapter 5

Chapter 5 deals with donor bound complexes in heterobilayer  $\text{MoSe}_2/\text{WSe}_2$ , and includes the publication [24]. We obtain the radiative recombination rates and doping dependent spectra of donor bound complexes for both closely aligned and asymptotics for strongly misaligned layers, using the localized nature of the donor to overcome the valley mismatch between electrons and holes, which suppresses the radiative recombination. We use quantum Monte Carlo calculations to obtain binding energies using the full screened bilayer interaction and overlap integrals between wave functions of the complexes.

## Chapter 6

Chapter 6 deals with 2H-stacked few-layers and bulk TMDCs. We present a  $\mathbf{k} \cdot \mathbf{p}$ -tight binding model describing the subband energies and dispersions in few-layer 2H-stacked TMDCs and obtain the intersubband optical absorption line shapes for lightly p-doped and n-doped films, and provide potential device configurations utilising these materials.

## Chapter 7

Chapter 7 provides the conclusions of the thesis and outlook on future research directions.

# Chapter 2

## Overview

### 2.1 2D transition metal dichalcogenides

Monolayer transition metal dichalcogenides (TMDCs) are atomically thin materials with a unit cell described by  $\text{MX}_2$ , where a transition metal M is covalently bonded to two chalcogen atoms X and arranged in a triangular lattice with two sublattices giving a hexagonal crystal as shown in Fig. 2.1a. The primitive lattice vectors are given by  $\mathbf{a}_1 = a(1, 0)$  and  $\mathbf{a}_2 = \frac{a}{2}(1, \sqrt{3})$ , where  $a$  is the lattice constant. The reciprocal lattice vectors are given by  $\mathbf{b}_1 = (\frac{2\pi}{a}, -\frac{2\pi}{\sqrt{3}a})$  and  $\mathbf{b}_2 = (0, \frac{4\pi}{\sqrt{3}a})$ , giving a hexagonal Brillouin zone (BZ) with two inequivalent points (valleys) at the corners  $\mathbf{K}$  and  $\mathbf{K}' = -\mathbf{K}$ , with  $|\mathbf{K}| = \frac{4\pi}{3a}$ . The metal-chalcogen distance in the unit cell is given by  $d_{MX} = a/\sqrt{3}$ , such that the two chalcogen positions in the unit cell with the metal at the origin  $M = (0, 0, 0)$ , are given by  $X_{1,2} = \frac{a}{2}(1, \frac{1}{\sqrt{3}}, \pm \frac{d_{xx}}{2})$ , where  $d_{XX}$  is the distance in the out of plane direction between the two chalcogen atoms.

The most common and widely studied TMDCs, which we will focus on in this thesis, consist of  $\text{M} = \text{Mo}, \text{W}$  (Molybdenum or Tungsten) and  $\text{X} = \text{S}, \text{Se}$  (Sulphur or Selenium), which are found to be direct band gap semiconductors with the conduction band (CB) minimum and valence band (VB) maximum located at the corners of the BZ,  $K/K'$  valleys, as shown in Fig. 2.2.

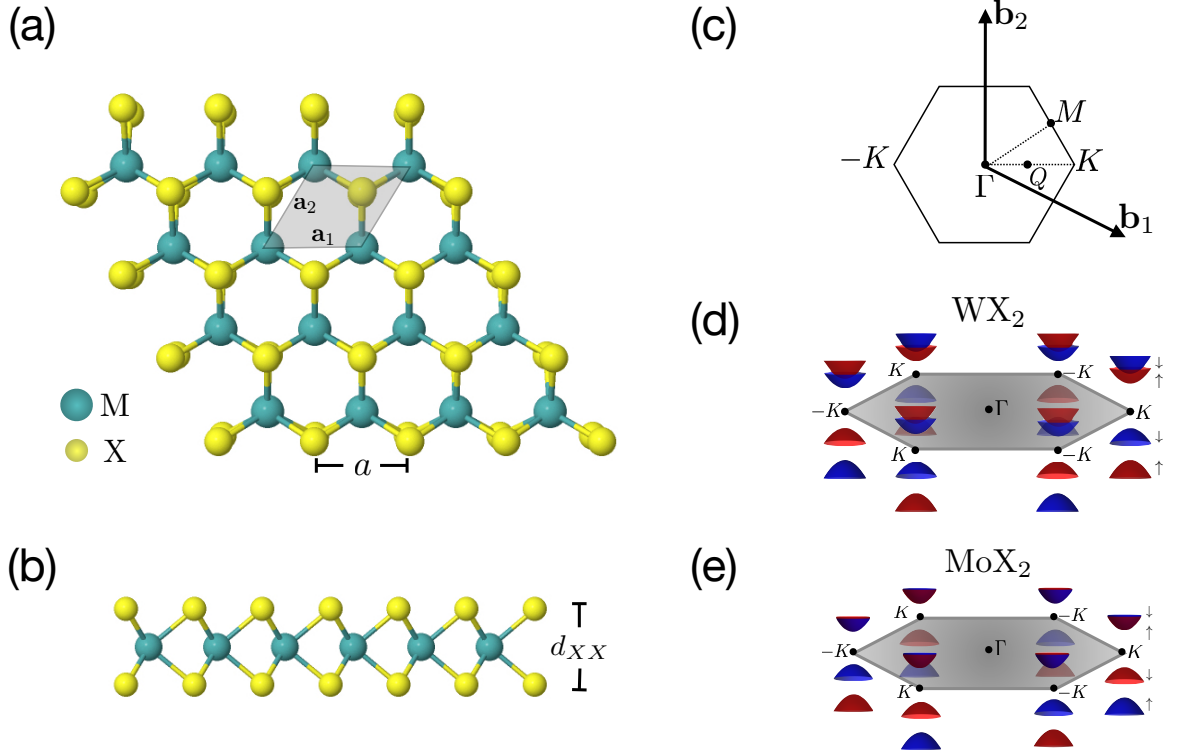


Figure 2.1: (a) Top view and (b) side view of a monolayer TMDC, showing the hexagonal lattice structure with two sublattices composed of the metal (green) and chalcogen (yellow) atoms. The grey shaded region is the primitive unit cell constructed using the two primitive lattice vectors  $\mathbf{a}_1, \mathbf{a}_2$  of magnitude  $a$  corresponding to the lattice constant. (c) Hexagonal Brillouin zone of 2D TMDC crystals including the symmetry points  $\Gamma, M, K$  and the reciprocal lattice vectors  $\mathbf{b}_1, \mathbf{b}_2$ . (d) Sketch of the spin-orbit split conduction and valence band edges at the corners of the Brillouin zone for  $\text{WX}_2$  and (e)  $\text{MoX}_2$  ( $X=\text{S}, \text{Se}$ ).

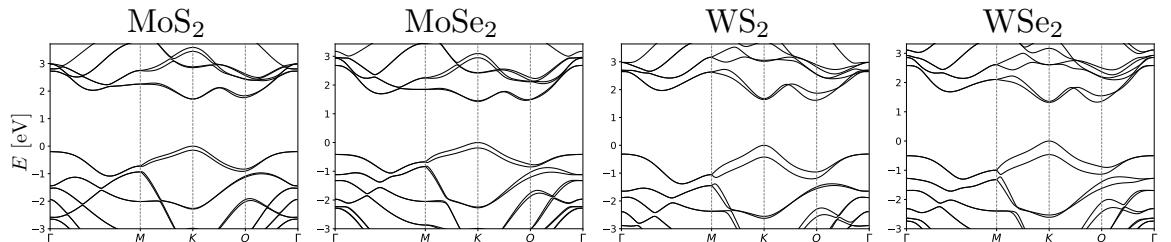


Figure 2.2: DFT calculated band dispersions of the four studied monolayer TMDCs  $\text{MoS}_2$ ,  $\text{MoSe}_2$ ,  $\text{WS}_2$  and  $\text{WSe}_2$ , along a path in the Brillouin zone going through the symmetry points ( $\Gamma \rightarrow M \rightarrow K \rightarrow \Gamma$ ), showing the direct band gap at the  $K$  point, and the spin-orbit splitting in the valence and conduction bands. DFT data was provided by Celal Yelgel, calculations were performed using Quantum ESPRESSO [25].

## 2.2 Symmetry of 2D TMDCs

The symmetry analysis and properties of a physical system have important implications on the description of the eigenstates and energies of the Hamiltonian describing the system. The point group symmetry of the TMDCs crystals, giving the symmetry operations leaving the crystal invariant is the  $D_{3h}$  point group. The symmetry operations consist of  $C_3, C_3^2$ : rotations by  $2\pi/3$  and  $4\pi/3$  about an axis perpendicular to the plane,  $\sigma_h$ : mirror reflection in the out of plane direction ( $z \rightarrow -z$ ),  $3\sigma_v$ : three mirror planes perpendicular to the plane and passing through the rotation axis (including  $x \rightarrow -x$ ),  $3C'_2$ : three rotations by  $\pi$  about an axis in the plane, and  $2S_3$ : two  $C_3$  about the axis perpendicular to the plane followed by out of plane mirror reflection. In particular, TMDCs monolayer crystals lack inversion symmetry ( $\mathbf{r} \rightarrow -\mathbf{r}$ ), which has important consequences for the electronic states as will be shown.

When considering the electronic states at the CB and VB edges at the  $K/K'$  valleys, the point group symmetry is reduced from the  $\Gamma$ -point full crystal point group, with the group of the  $K$  wave vector being the Abelian point group  $C_{3h}$  [26] with the character table given in Table 2.1, containing the two  $C_3$  rotations, the out of plane mirror symmetry  $\sigma_h$  and their combinations. From group theory we know that the electronic states can be classified into the irreducible representations (irreps) of the point group symmetry of the system according to their transformation under the symmetry operations of the point group. States belonging to the same irrep are related by symmetry operations and therefore have the same energy. As the irreps of the  $C_{3h}$  point group are one-dimensional, the states are non degenerate and can be chosen as the eigenstates of the  $C_3$  symmetry operation.

Table 2.1: Character table for the irreducible representations of the point group  $C_{3h}$ . The irreps corresponding to the VB and CB state at the  $K/K'$  are denoted,  $\omega = e^{i\frac{2\pi}{3}}$ .

$C_{3h}$	$E$	$C_3$	$C_3^2$	$\sigma_h$	$S_3$	$\sigma_h C_3^2$
$A' (\text{VB}-K/K')$	1	1	1	1	1	1
$A''$	1	1	1	-1	-1	-1
$E'_1 (\text{CB}-K)$	1	$\omega$	$\omega^*$	1	$\omega$	$\omega^*$
$E'_2 (\text{CB}-K')$	1	$\omega^*$	$\omega$	1	$\omega^*$	$\omega$
$E''_1$	1	$\omega$	$\omega^*$	-1	$-\omega$	$-\omega^*$
$E''_2$	1	$\omega^*$	$\omega$	-1	$-\omega^*$	$-\omega$

Density functional theory (DFT) calculations have shown [28, 27, 29] that the states

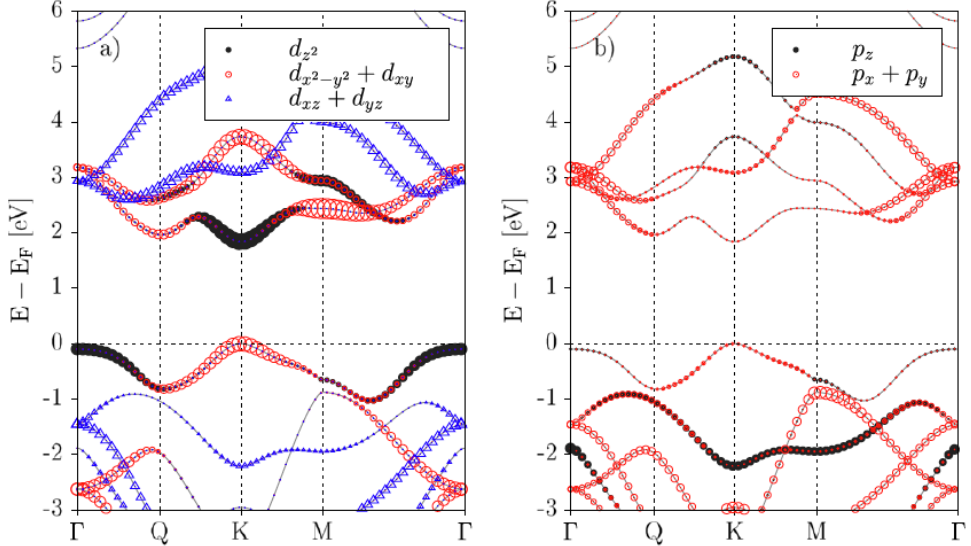


Figure 2.3: MoS<sub>2</sub> bands orbital composition, separated into (a) metal  $d$ -orbitals, (b) chalcogen  $p$ -orbitals. Figure taken from Ref. [27] under the terms of Creative Commons Attribution 3.0 licence.

of the CB and VB electrons at the  $K/K'$  points are composed predominantly from the even under  $z \rightarrow -z$  metal  $d$ -orbitals ( $d_{z^2}, d_{x^2-y^2}, d_{xy}$ ), with a small contribution from the chalcogen  $p$ -orbitals (see Fig. 2.3). Additionally, in order to be classified under the irreps of  $C_{3h}$  they must transform into themselves under the symmetry operation  $C_3$ , which means they are eigenstates of the angular momentum operator  $\hat{L}_z = -i\hbar \frac{\partial}{\partial \phi}$ . The appropriate combinations of orbitals satisfying this are  $d_{\pm 2} = \frac{1}{\sqrt{2}}(d_{xy} \pm id_{x^2-y^2})$  for the valence band with magnetic quantum number  $m_z = \pm 2$  for the  $K$  and  $-K$  valleys, respectively, and  $d_0 = d_{z^2}$  with  $m_z = 0$  for the conduction band. As such, the CB Bloch states at the two valleys belong to the  $E'_1$  and  $E'_2$  irreps, which are complex conjugates of each other, and the VB states belong to the  $A'$  irrep. This can be summarized as [26, 30]

$$\begin{aligned}\hat{C}_3|\phi_c^\tau\rangle &= e^{i\tau\frac{2\pi}{3}}|\phi_c^\tau\rangle, \\ \hat{C}_3|\phi_v^\tau\rangle &= |\phi_v^\tau\rangle,\end{aligned}\tag{2.1}$$

where the rotation centre is at the centre of the hexagon, and  $|\phi_c^\tau\rangle, |\phi_v^\tau\rangle$  are the Bloch states at the  $K/K'$  valleys, given in terms of the metal d-orbitals as [26]

$$\phi_\alpha^\tau(\mathbf{r}) = \frac{1}{\sqrt{N}} \sum_{\mathbf{R}} e^{i\tau\mathbf{K}\cdot(\mathbf{R}+\mathbf{r}_0)} d_{\tau m_\alpha}(\mathbf{r} - (\mathbf{R} + \mathbf{r}_0)),\tag{2.2}$$

where the summation is over the lattice vectors  $\mathbf{R}$ ,  $\mathbf{r}_0$  is the metal position relative to the hexagon centre, and  $\alpha = c, v$  with  $m_c = 0, m_v = 2$  is the magnetic quantum

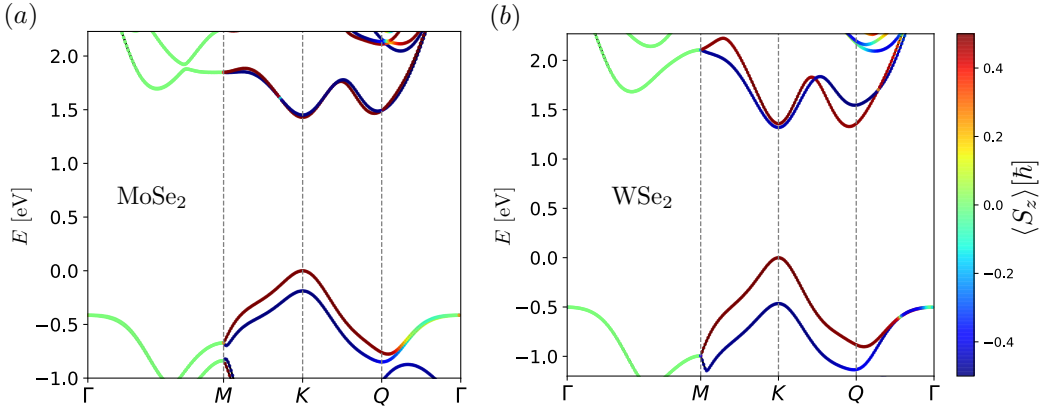


Figure 2.4: DFT calculated band structure including spin–orbit coupling for (a) MoSe<sub>2</sub> and (b) WSe<sub>2</sub> showing the expectation value of the  $\hat{S}_z$  spin operator at different  $\mathbf{k}$  points along the path in the Brillouin zone, with red (blue) indicating spin up (down). DFT data was provided by Celal Yelgel.

numbers for the  $d_0, d_2$  orbitals, composing the conduction and valence band states, respectively. Note, that the eigenvalue under  $C_3$  rotation is a combination of rotating the orbital and the plane wave parts of the Bloch wave function [30].

## 2.3 Spin-orbit coupling

The spin-orbit (SO) interaction is given by  $\hat{H}_{so} \propto \frac{1}{r} \frac{dV(r)}{dr} \hat{\mathbf{L}} \cdot \hat{\mathbf{S}}$ , where  $V(r)$  is the potential from the nucleus and  $\hat{\mathbf{L}}, \hat{\mathbf{S}}$  are the angular momentum and spin operators. The heavy metal atoms present in TMDCs crystals and their  $d$ -orbitals composing the Bloch states at the CB and VB edges, result in strong spin-orbit (SO) coupling effects having profound impact on the resulting optoelectronic properties of these materials.

The  $\hat{\sigma}_h$  ( $z \rightarrow -z$ ) symmetry implies that the out of plane spin projection  $s_z$  is a good quantum number,  $[\hat{H}, \hat{S}_z] = 0$  where  $\hat{S}_z = \frac{\hbar}{2}\sigma_z$  is the out of plane spin operator given in terms of Pauli matrices, such that the electronic bands can be associated with a given spin projection  $s_z = \uparrow, \downarrow$  [31], and SO splitting of these bands is possible through the Zeeman term  $\hat{H}_{so} \propto \hat{L}_z \hat{S}_z$ , as shown in Fig. 2.4.

The VB states at the  $K/K'$ –valleys being composed primarily from the  $d_{\pm 2}$  ( $m_z = \pm 2$ ) orbitals (Fig. 2.3), resulting in large SO splitting of order  $\sim 100$  meV. The CB  $K/K'$ –point states being composed primarily from the metal  $d_0$  orbitals, having magnetic quantum number  $m_z = 0$ , leading to zero SO splitting. A non-zero contribution

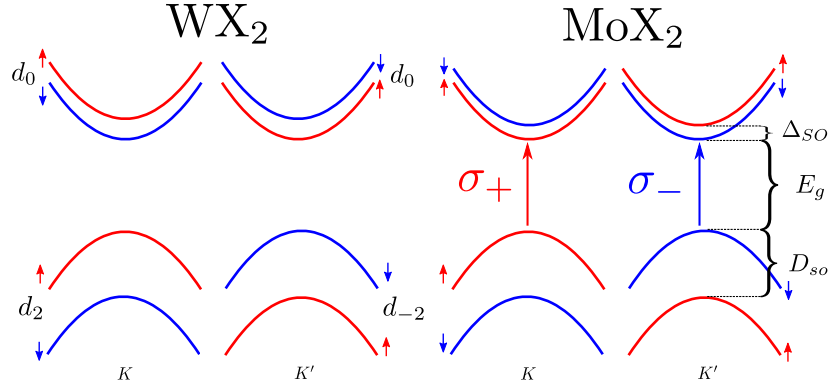


Figure 2.5: Schematics of the electronic band structure at the  $K/K'$  points for  $\text{WX}_2$  (left) and  $\text{MoX}_2$  (right) TMDCs, showing the spin-orbit splitting in the CB and VB, and the spin-valley locking. The colours indicate the out of plane spin projection  $s_z = \uparrow, \downarrow$ . The dominant orbitals making up the electronic states are indicated next to the CB and VB, and the optical selection rules for the two valleys are demonstrated with the circular light polarization  $\sigma_{\pm}$ .

however comes from first-order perturbation corrections due to the chalcogen  $p_{\pm 1}$  orbitals as well as second order perturbation correction from  $d_{\pm 1}$  bands from higher conduction bands [28, 30], leading to a weaker but still significant SO splitting of few to few tens of meV, in particular for the Tungsten based TMDCs.

The large SO splitting in the VB together with time reversal symmetry and lack of inversion symmetry imply that the spin projection of holes in the VB is locked with their valley index, with opposite spin states in a given valley being frozen out due to the large energy difference. This feature is known as spin-valley locking in which holes at the  $K$  valley band have spin projection  $\uparrow$  whereas holes at the  $K'$  valley band edge have spin projection  $\downarrow$ , with both states degenerate in energy due to time reversal symmetry,  $E_{s_z}(\mathbf{K}) = E_{-s_z}(-\mathbf{K})$  (see Fig. 2.5).

In the CB, first-principle calculations have shown that the SO splitting has opposite splitting order in  $\text{WS}_2, \text{WSe}_2$  as compared to  $\text{MoS}_2, \text{MoSe}_2$  [27, 28, 32]. The sign of the spin-orbit splitting between the two spin polarized bands comes from the competition of the chalcogen  $p_{\pm 1}$ -orbitals and the higher conduction bands  $d_{\pm 1}$ -orbitals [28]. The result is that the Tungsten based TMDCs have opposite out-of-plane spin projections for the top VB and lower CB, as opposed to Molybdenum based TMDCs, Fig. 2.5.

## 2.4 $\mathbf{k} \cdot \mathbf{p}$ model for TMDCs

The low energy CB and VB states reside at the  $K$  and  $K'$  points of the BZ as shown in Fig. 2.2. It is therefore, beneficial to have a description of the bands in the vicinity of this points. This is achieved using the  $\mathbf{k} \cdot \hat{\mathbf{p}}$  method, where  $\hat{\mathbf{p}}$  is the momentum operator and  $\mathbf{k}$  is a wave vector measured relative to the  $K/K'$  points. The Hamiltonian describing the states at the vicinity of the  $K$  point is given by [27]

$$H = E_0 + \frac{\hat{p}^2}{2m} + V(r) + \frac{\hbar}{m} \mathbf{k} \cdot \hat{\mathbf{p}}, \quad (2.3)$$

where  $E_0$  is the total energy offset, the second term is the kinetic energy and  $V(r)$  is the crystal potential. Given the solution to the Schrödinger equation at the  $K$  point ( $k = 0$ ), the  $\mathbf{k} \cdot \mathbf{p}$  term,  $H_{\mathbf{k}\mathbf{p}} = \frac{\hbar}{m} \mathbf{k} \cdot \hat{\mathbf{p}}$  is treated in perturbation theory in the basis of the Bloch eigenstates at the  $K$  point. The two-band model in the basis of the CB and VB states at the  $K/K'$  points, spanned by the metal  $d$ -orbitals,  $|\phi_c^\tau\rangle = |d_0\rangle$  for the conduction band and  $|\phi_v^\tau\rangle = |d_{\pm 2}\rangle$  for the valence band, is given for a specific spin component by [27, 33],

$$H_{\mathbf{k}\mathbf{p}}^\tau = \begin{pmatrix} \frac{E_g}{2} + \alpha k^2 & \gamma(\tau k_x - ik_y) \\ \gamma(\tau k_x + ik_y) & -\frac{E_g}{2} + \beta k^2 \end{pmatrix}, \quad (2.4)$$

where  $E_g$  is the band gap at the  $K/K'$  point,  $\tau = \pm$  is the valley index corresponding to  $K$  or  $-K$ , respectively,  $\alpha$  and  $\beta$  are related to interband coupling with higher bands, and  $\gamma$  is related to the momentum matrix element between CB and VB states and to the Fermi velocity in the crystals through  $\frac{v_F}{c} = \frac{\gamma}{hc} \approx 10^{-3}$ , with  $c$  the speed of light in vacuum. Additional terms can be added to this model to describe effects of trigonal warping due to the  $C_3$  symmetry [26]. The spin components and spin-orbit splitting in the conduction and valence bands can also be incorporated in Eq. 2.4 by the terms  $\Delta_{c/v}\sigma_z\tau$ , where  $\sigma_z$  is the third Pauli matrix, and  $2\Delta_{c/v}$  are the spin-orbit splittings in the conduction/valence bands.

The eigenstates and eigenvalues describing the electronic states in the vicinity of the  $K/K'$  valleys up to second order in  $\frac{\gamma k}{E_g}$  are given by [34],

$$\begin{aligned} |u_{c,k}^\tau\rangle &= \left(1 - \frac{\gamma^2 k^2}{2E_g^2}\right) |u_{c,0}^\tau\rangle + \frac{\tau\gamma k}{E_g} e^{i\tau\phi_k} |u_{v,0}^\tau\rangle, \quad E_c(k) = \frac{E_g}{2} + \left(\alpha + \frac{\gamma^2}{E_g}\right) k^2; \\ |u_{v,k}^\tau\rangle &= -\frac{\tau\gamma k}{E_g} e^{-i\tau\phi_k} |u_{c,0}^\tau\rangle + \left(1 - \frac{\gamma^2 k^2}{2E_g^2}\right) |u_{v,0}^\tau\rangle, \quad E_v(k) = -\frac{E_g}{2} - \left(\frac{\gamma^2}{E_g} - \beta\right) k^2, \end{aligned} \quad (2.5)$$

from which we define the effective mass of the carriers in the CB and VB bands according to  $\frac{\hbar^2}{2m_c} = \alpha + \frac{\gamma^2}{E_g}$ , and  $\frac{\hbar^2}{2m_v} = \beta - \frac{\gamma^2}{E_g}$ , giving a parabolic dispersion in the vicinity of the  $K/K'$  valleys, with electron-hole asymmetry. The values of the different parameters obtained from fitting to DFT calculations are given for the four TMDCs in [27].

## 2.5 Optical selection rules

One of the most characteristic properties of TMDCs is related to their coupling to light and the selection rules involved. The coupling to light is given by the minimal substitution in the Hamiltonian by the replacement  $\hat{\mathbf{p}} \rightarrow \hat{\mathbf{p}} + \frac{e}{c}\mathbf{A}$  (or  $\mathbf{k} \rightarrow -\frac{i}{\hbar}\nabla - \frac{e}{hc}\mathbf{A}$  in the  $\mathbf{k} \cdot \mathbf{p}$  Hamiltonian in Eq. 2.4, [35]), where  $e$  is the electron charge,  $c$  is the speed of light, and  $\mathbf{A}$  is the vector potential of the electromagnetic field, and we assume the vector potential to be uniform in space, due to the large typical wave length of light relative to the unit cell size. The term in the Hamiltonian giving the coupling to light is given by

$$\hat{H}_r = \frac{e}{mc}\hat{\mathbf{p}} \cdot \mathbf{A} = \frac{e}{2mc}(\hat{p}_+A_- + \hat{p}_-A_+), \quad (2.6)$$

where in the second equality we used  $\hat{p}_{\pm} = \hat{p}_x \pm i\hat{p}_y$  and similarly for the vector potential  $\mathbf{A}$ . The vector potential  $A_{\pm}$  describes a photon with a given circular polarization (right or left), such that the momentum matrix element  $p_{\pm}$  are tied with specific circular polarization. The momentum matrix element is given using the Feynman-Hellman theorem by [36],

$$\hat{\mathbf{p}}^{cv} = \frac{m}{\hbar}\langle u_{c,k}^{\tau} | \nabla_{\mathbf{k}} \hat{H}_{kp} | u_{v,k}^{\tau} \rangle, \quad (2.7)$$

giving at the valley  $\tau$ ,

$$\hat{p}_{\pm}^{cv} = \frac{m\gamma}{\hbar}(1 \pm \tau), \quad (2.8)$$

Therefore, we see that the two valleys are coupled exclusively to circularly polarized light with opposite orientation (as required by time reversal symmetry between the two valleys), a property known as valley circular dichroism. This allows to excite separately electron-hole pairs in the two valleys using left or right circularly polarized light, and similarly radiative recombination of electron-hole pairs at the  $K/K'$  valleys results in emission of left/right circularly polarized light, respectively [3, 4, 37].

Additionally, as the momentum operator does not couple different spin projections or different valley indexes, an important selection rule for the emission/absorption of in-plane polarized light is the conservation of out of plane spin projection  $s_z$  and valley index. With reference to Fig. 2.5, the spin-valley locking property, and significant SO splitting in the VB and CB discussed in section 2.3, restricts the bands, which can be coupled by an in-plane polarized light. In particular, the opposite SO splitting between CB and VB in WS<sub>2</sub>, WSe<sub>2</sub> prevents the light absorption or emission for carriers in the band edges, making them dark, whereas for MoS<sub>2</sub>, MoSe<sub>2</sub> they are bright having the same spin projections. Including the selection rules, the radiative matrix element can be given generally as,

$$\langle u_{c,\mathbf{k}}^{\tau,s_z} | \hat{H}_r | u_{v,\mathbf{k}}^{\tau',s'_z} \rangle = \frac{e\gamma}{2\hbar c} (1 \pm \tau) A_{\mp} \delta_{\tau,\tau'} \delta_{s,s_z}. \quad (2.9)$$

An additional way to interpret the optical selection rules has to do with angular momentum conservation in the light absorption (or emission) process [4, 30]. A right/left handed circular polarization carries angular momentum with projection  $m_z = \pm 1$ . An absorption of such light, therefore requires a corresponding change in the angular momentum of the electronic states, which due to the discrete 3-fold rotational symmetry is conserved modulus 3, as confirmed by the relations in Eq. 2.1.

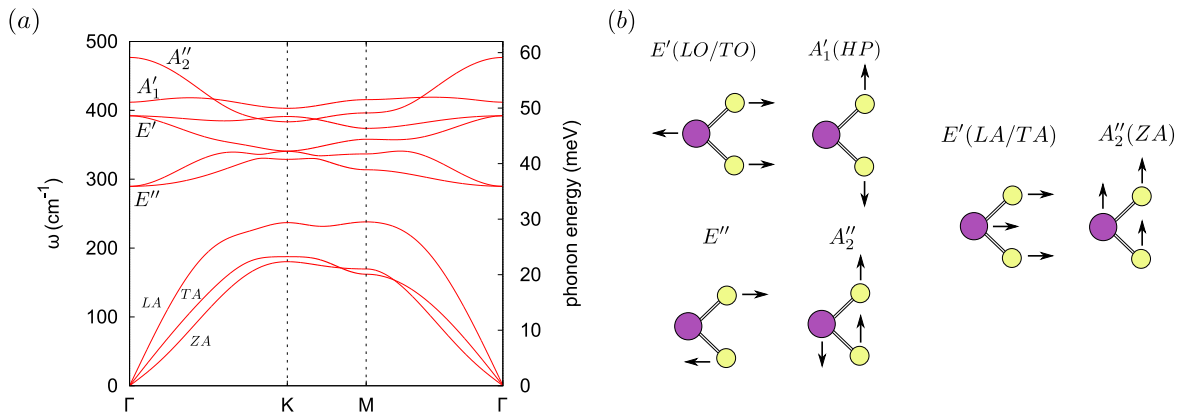
## 2.6 Phonons in TMDCs

Phonons or lattice vibrations play an important role in determining the properties of given crystals through their interaction with the electrons, influencing both optical [21, 38] as well as transport (mobility) [39, 39] related properties. Similarly to the electronic states, the description of phonons is connected to the symmetry properties of the crystal. The unit cell containing three atoms combined with three spatial degrees of freedom per atom imply nine vibrational modes of which three are acoustical and six are optical phonon modes. The nine phonon modes at the  $\Gamma$  point can be further classified according to the irreducible representations (irreps) of the crystal,  $D_{3h}$  (Table 2.2). The representation of the vibrational modes is given by the direct product of the equivalence and vector representations [40],

$$\Gamma_{vib} = \Gamma_{eq} \otimes \Gamma_{vec.} \quad (2.10)$$

Table 2.2: Character table for the irreducible representations of the point group  $D_{3h}$ .

$D_{3h}$	$E$	$2C_3$	$3C'_2$	$\sigma_h$	$2S_3$	$3\sigma_v$
$A'_1$	1	1	1	1	1	1
$A'_2$	1	1	-1	1	1	-1
$E'$	2	-1	0	2	-1	0
$A''_1$	1	1	1	-1	-1	-1
$A''_2$	1	1	-1	-1	-1	1
$E''$	2	-1	0	-2	1	0
$\Gamma_{vib}$	9	0	-1	1	-2	3

Figure 2.6: (a) DFT calculated phonon spectrum of monolayer MoS<sub>2</sub>. (b) The  $\Gamma$ -point phonon modes, and the atomic displacements of the chalcogens and metal in the given phonon modes, classified according to the irreps of  $D_{3h}$ .

The character of the equivalence representation is given by the number of atoms invariant (up to lattice vector translation) under the given symmetry operation, and the three dimensional vector ( $x, y, z$ ) representation for  $D_{3h}$  is given by  $\Gamma_{vec} = E' \oplus A''_2$ , where  $E'$  corresponds to the in-plane vector ( $x, y$ ), and  $A''_2$  corresponds to the out of plane coordinate  $z$ . The reduction of the vibrational modes representation into the irreps of  $D_{3h}$  is given by

$$\Gamma_{vib} = 2E' \oplus A'_1 \oplus 2A''_2 \oplus E'', \quad (2.11)$$

where each irrep corresponds to single or degenerate phonon modes, depending on the dimensionality of the irrep. Fig. 2.6 shows the DFT calculated phonon dispersions for monolayer MoS<sub>2</sub> and the classification of the  $\Gamma$ -point phonon modes into irreps of  $D_{3h}$ , as well as the atomic displacements within the unit cell, which transform according to the corresponding irreps.

### 2.6.1 Electron-phonon coupling

The electron-phonon interaction Hamiltonian is given in second quantization notation by

$$H_{e-ph} = \sum_{\mu} \sum_{\mathbf{q}, \mathbf{k}} g_{\mu, \mathbf{q}} c_{\mathbf{k}+\mathbf{q}}^\dagger c_{\mathbf{k}} (a_{\mu, -\mathbf{q}}^\dagger + a_{\mu, \mathbf{q}}), \quad (2.12)$$

where  $c_{\mathbf{k}}(c_{\mathbf{k}}^\dagger)$  denotes an annihilation (creation) operator of an electron with wave vector  $\mathbf{k}$ , and  $a_{\mu, \mathbf{q}}(a_{\mu, \mathbf{q}}^\dagger)$  denotes an annihilation(creation) operator of a phonon in mode  $\mu$  and wave vector  $\mathbf{q}$ . The two processes described by the Hamiltonian involve phonon absorption with wave vector  $\mathbf{q}$  or phonon emission with wave vector  $-\mathbf{q}$ , both resulting in an electron scattered from wave vector  $\mathbf{k}$  to wave vector  $\mathbf{k} + \mathbf{q}$ . The electron-phonon coupling constant  $g_{\mu, \mathbf{q}}$  is given by the matrix element[39, 41, 42]

$$g_{\mu, \mathbf{q}} = \langle \mathbf{k} + \mathbf{q} | \delta V_\mu(\mathbf{r}) | \mathbf{k} \rangle, \quad (2.13)$$

where  $\delta V_\mu(\mathbf{r})$  is the change in the potential acting on the electrons due to the lattice displacement induced by the phonon mode  $\mu$ . Using group theory we can determine whether a given phonon coupling is non zero. The selection rule is given by

$$\Gamma_\mu \in \Gamma_{c/v} \otimes \Gamma_{c/v}, \quad (2.14)$$

where  $\Gamma_{c/v}$  is the irrep of the Bloch states of the carriers at the CB or VB, and  $\Gamma_\mu$  is the irrep of the phonon normal mode. In particular, the conduction and valence band states, at the  $K$  and  $K'$  points of the BZ, are even under mirror plane reflection  $\hat{\sigma}_h$ , therefore only the phonon modes which are symmetric under  $\hat{\sigma}_h$ , are coupled to the carriers. Additionally, for the acoustic and transverse optical phonon modes, as they both transform according to the  $E'$  irrep or the vector representation, in order for the interaction to be a scalar, or transforming according to the identity irrep  $A'_1$ , the coupling must be of the form  $\delta V_\mu \propto \mathbf{q} \cdot \mathbf{u}_\mu$ , where the proportionality constant has units of energy independent of the wave vector  $\mathbf{q}$ . Therefore, for  $\Gamma$ -point ( $q \rightarrow 0$ ) phonons the coupling is vanishingly small.

## 2.7 Excitons, triions and biexcitons in TMDCs

The 2D confinement of carriers in monolayer TMDCs together with the relatively high effective masses of the carriers (electrons and holes) results in tightly bound multi-particle complexes such as: excitons (electron-hole pairs), triions (charged excitons) and biexcitons (two bound excitons), which are bound by the Coulomb interaction between the constituents, with binding energies in the range of tens to hundreds of meV, significantly higher than in conventional semiconductors, as obtained using *ab initio* calculations [43, 23, 44], and confirmed in photoluminescence experiments. Therefore, the optical response of these materials is dominated by the tightly bound complexes [45, 46]. The modified dielectric environment and the reduced dimensionality of two dimensional materials, result in a modification to the electron-electron interaction in 2D, which is given in momentum space by [43, 19, 47, 48],

$$V_{\mathbf{q}} = \frac{2\pi e^2}{\epsilon q(1 + r_* q)}, \quad (2.15)$$

where  $r_* = 2\pi\kappa$  is the screening length related to the polarizability of the material  $\kappa$ , and  $\epsilon$  is the dielectric constant of the environment of the monolayer ( $\epsilon = 1$  for vacuum). This form of the interaction is similar to the regular Coulomb interaction in 3D,  $V_q = 4\pi e^2/\epsilon q$ , with the additional momentum dependent static dielectric function  $\epsilon(q) = 1 + r_* q$ , originating from the reduced dimensionality, and the in-plane polarizability of the material. Following a Fourier transformation into real space, the interaction potential in real space is known as the Keldysh potential given by [43, 19],

$$V(r) = \frac{\pi e^2}{2\epsilon r_*} [H_0(r/r_*) - Y_0(r/r_*)], \quad (2.16)$$

where  $H_0(r)$  is the Struve function and  $Y_0(r)$  a Bessel function of the second kind. In real space, the screening length  $r_*$  can be seen as defining two limiting regimes. At distances greater than the screening length ( $r > r_*$ ), the potential reduces to an unscreened Coulomb potential  $\sim e^2/\epsilon r$ , while at shorter distances it reduces to a logarithmic potential  $\sim e^2/\epsilon r_* \log(r_*/r)$  [48, 49]. Most notably, the modified interaction results in a modification to the simple 2D Hydrogen-like spectrum in free space, approaching the 2D hydrogen limit for large principle quantum number  $n$  [20, 43, 44].

Additionally, the spin and valley degrees of freedom of the carriers result in a large variety of possible complexes [50]. In particular, the different ordering of the spin-orbit

splitting in the CB between the Tungsten and Molybdenum based TMDCs (Fig. 2.5) results in optically active (bright) and inactive (dark) complexes in accordance with the optical selection rules discussed in 2.5 and Eq. 2.9.

### 2.7.1 Excitons

Within the effective mass approximation the exciton state can be described as a superposition of electron and hole Bloch states connected by an envelope function with a spread much greater than the unit cell, also known as the Wannier-Mott exciton. The exciton state is given by [35],

$$|X\rangle = \int d^2\mathbf{r}_e d^2\mathbf{r}_h \frac{e^{i\mathbf{Q}\cdot\mathbf{R}_{cm}}}{\sqrt{S}} \Phi_X(\mathbf{r}_e - \mathbf{r}_h) \Psi_{c,\tau,s}^\dagger(\mathbf{r}_e) \Psi_{v,\tau',s'}(\mathbf{r}_h) |0\rangle, \quad (2.17)$$

where  $\Psi_{c/v,\tau,s}^{(\dagger)}(\mathbf{r}_\alpha)$  are the conduction (c) or valence (v) band field operators in valley  $\tau$  with spin projection  $s$ ,  $\mathbf{Q}$  is the exciton centre of mass wave vector,  $\mathbf{R}_{cm} = \frac{m_e \mathbf{r}_e + m_h \mathbf{r}_h}{m_X}$  is the centre of mass coordinate with  $m_X = m_e + m_h$  the total exciton mass given by the sum of the electron and hole masses,  $S$  is the sample area normalization factor, and  $\Phi_X(\mathbf{r})$  is the wave function describing the relative motion of the electron and hole. Alternatively, the exciton state can be described in momentum space using the creation and annihilation operators described by the relation

$$\Psi_{c/v,\tau,s}^\dagger(\mathbf{r}) = \sum_{\mathbf{k}} \frac{e^{-i(\tau\mathbf{K}+\mathbf{k})\cdot\mathbf{r}}}{\sqrt{S}} c_{c/v,\tau,s}^\dagger(\mathbf{k}). \quad (2.18)$$

Using this in Eq. (2.17) we get,

$$|X\rangle = \frac{1}{\sqrt{S}} \sum_{\mathbf{q}} \tilde{\Phi}_x(\mathbf{q}) c_{c,\tau,s}^\dagger\left(\frac{m_e}{m_X} \mathbf{Q} + \mathbf{q}\right) c_{v,\tau',s'}\left(\mathbf{q} - \frac{m_h}{m_X} \mathbf{Q}\right), \quad (2.19)$$

where  $\mathbf{q} = \frac{m_h \mathbf{k}_e + m_e \mathbf{k}_v}{m_X}$  is the relative momentum of the electron and hole,  $\mathbf{Q} = \mathbf{k}_e - \mathbf{k}_v$  is the centre of mass momentum of the exciton<sup>1</sup>, and  $\tilde{\Phi}_X(\mathbf{q})$  is the Fourier transform of the relative motion wave function

$$\tilde{\Phi}_X(\mathbf{q}) = \int d^2\mathbf{r} e^{-i\mathbf{q}\cdot\mathbf{r}} \Phi_X(\mathbf{r}). \quad (2.20)$$

In this picture, the exciton can be viewed as a superposition of electron and hole states with wave vectors modulated by the Fourier transform of the relative motion

---

<sup>1</sup>Note that the wave vector here is that of the valence band state, the corresponding hole (missing electron) wave vector is  $\mathbf{k}_h = -\mathbf{k}_v$ .

wave function. The real space relative motion wave function is peaked at zero separation with a width  $a_X \approx 10 \text{ \AA}$  being the exciton's effective Bohr radius, and the corresponding relative motion wave function in momentum space is centred around  $q = 0$  relative momentum with width  $\sim 1/a_X$ , indicating that the contribution to the exciton wave function mainly comes from the carriers with wave vectors of order  $k \leq 1/a_X$ .

The exciton relative motion wave function is obtained by solving the time-independent Schrödinger equation

$$\left[ -\frac{\hbar^2 \nabla_e^2}{2m_e} - \frac{\hbar^2 \nabla_h^2}{2m_h} + V(|\mathbf{r}_e - \mathbf{r}_h|) \right] \psi(R_{cm}) \Phi_X(\mathbf{r}_e - \mathbf{r}_h) = E \psi(R_{cm}) \Phi_X(|\mathbf{r}_e - \mathbf{r}_h|), \quad (2.21)$$

where the exciton's wave function was separated into a centre of mass part and relative motion part. Changing the coordinates from  $\mathbf{r}_e, \mathbf{r}_h$  to the relative motion  $\mathbf{r} = \mathbf{r}_e - \mathbf{r}_h$ , and centre of mass motion  $\mathbf{R}_{cm}$ , we separate the problem to the centre of mass motion and relative motion. The Schrödinger equation for the relative motion is given by

$$\left[ -\frac{\hbar^2 \nabla^2}{2\mu} + V(r) \right] \Phi_X(r) = -E_b \Phi_X(r), \quad (2.22)$$

where  $\mu = \frac{m_e m_h}{m_X}$  is the exciton's reduced mass and  $V(r)$  is the electron-hole interaction potential and  $E_b$  is the binding energy such that the total exciton energy (measured relative to the band gap) is  $E = -E_b + \frac{\hbar^2 Q^2}{2m_X}$ .

Eq. 2.22 can be solved numerically for the binding energy and wave function of the ground state or excited states using the finite element method, giving binding energies of order  $\sim 0.5 \text{ eV}$  [23].

The strong binding of the electron and hole in the exciton result in a strong coupling to light [51], giving fast radiative recombination times. To obtain the radiative rate of the bright excitons we consider the light-mater Hamiltonian given in second quantization by

$$\hat{H}_r = \frac{e\gamma}{\hbar c} \sqrt{\frac{4\pi\hbar c}{qV}} \sum_{q_z, \mathbf{q}_{||}, \tau, s} a_{\mathbf{q}, \tau}^\dagger \int d^2 \mathbf{r} e^{-i\mathbf{q}_{||} \cdot \mathbf{r}} \Psi_{v, \tau, s}^\dagger(\mathbf{r}) \Psi_{c, \tau, s}(\mathbf{r}) + H.c. \quad (2.23)$$

The light vector potential field is expanded in terms of right and left handed circularly polarized modes denoted by the valley index  $\tau = \pm$ , with  $a_{\mathbf{q}_{||}, \tau}^\dagger$  denoting a photon creation operator with in-plane wave vector  $\mathbf{q}_{||}$  and polarization  $\tau = \pm$ , determined by

the valley of the recombining electron and hole. The radiative rate is obtained using Fermi's Golden rule,

$$\tau^{-1} = \frac{2\pi}{\hbar} \sum_{\mathbf{q}} |M_r|^2 \delta(E_i - E_f), \quad (2.24)$$

where the summation is over the final state photon wave vector. The radiative matrix element is given by,

$$M_r = \langle \mathbf{q} | H_r | X \rangle = \frac{e\gamma}{\hbar c} \sqrt{\frac{4\pi\hbar c}{Lq}} \Phi_X(0) \delta_{\mathbf{q}_{||}, \mathbf{Q}}, \quad (2.25)$$

where  $\mathbf{Q}$  is the centre of mass wave vector of the exciton, and  $\delta_{\mathbf{q}_{||}, \mathbf{Q}}$  ensures in-plane momentum conservation in the process. Using this in the Fermi Golden rule gives,

$$\tau^{-1} = \frac{1}{\hbar} \frac{8\pi^2 e^2 \gamma^2}{\hbar c} |\Phi_X(0)|^2 \int \frac{dq_z}{2\pi} \frac{1}{\sqrt{Q^2 + q_z^2}} \delta(E_X + \frac{\hbar^2 Q^2}{2m_X} - \hbar c \sqrt{Q^2 + q_z^2}), \quad (2.26)$$

where we converted the summation over  $q_z$  to integration. Here  $E_X$  is the exciton's energy given by  $E_g - \epsilon_X^b$ . In order for the energy conservation delta function to be satisfied we see that the exciton's centre of mass wave vector has an upper bound given by,

$$Q < \frac{E_X}{\hbar c}. \quad (2.27)$$

This restriction known as the light cone (as it gives a cone shape in momentum space) comes from the momentum and energy conservation condition for the in-plane momentum carried by the emitted photon. Therefore, excitons with a wave vector outside the light-cone cannot recombine radiatively and are optically inactive [52]. Using a typical exciton energy of  $\sim 2$  eV, we get  $Q < 0.01 \text{ nm}^{-1}$ , which translates to a kinetic energy of  $\hbar^2 Q^2 / (2m_X) \sim 5 \mu\text{eV}$ . Due to the small exciton wave vector as compared to the BZ, or the kinetic energy as compared to the exciton energy, the radiative transition can be taken as vertical, i.e. the photon carries zero in-plane momentum. Eq. 2.26 then simplifies to

$$\tau^{-1} = \frac{8\pi}{\hbar} \frac{e^2}{\hbar c} \frac{\gamma^2 |\Phi_X(0)|^2}{E_X}. \quad (2.28)$$

This gives an intrinsic exciton radiative lifetime of  $\tau \sim 0.1 - 0.2$  ps for the four free standing monolayer TMDCs. Similar values are reported in [52, 53]. This is compared to measured radiative lifetimes of  $\sim 2$  ps at  $T = 7$  K for MoSe<sub>2</sub> and WS<sub>2</sub> [54].

Finally, in Fig. 2.7 we show the various excitons configurations formed from the electrons and holes at the  $K$  and  $K'$  valleys in MoX<sub>2</sub> and WX<sub>2</sub> TMDCs [55, 23]

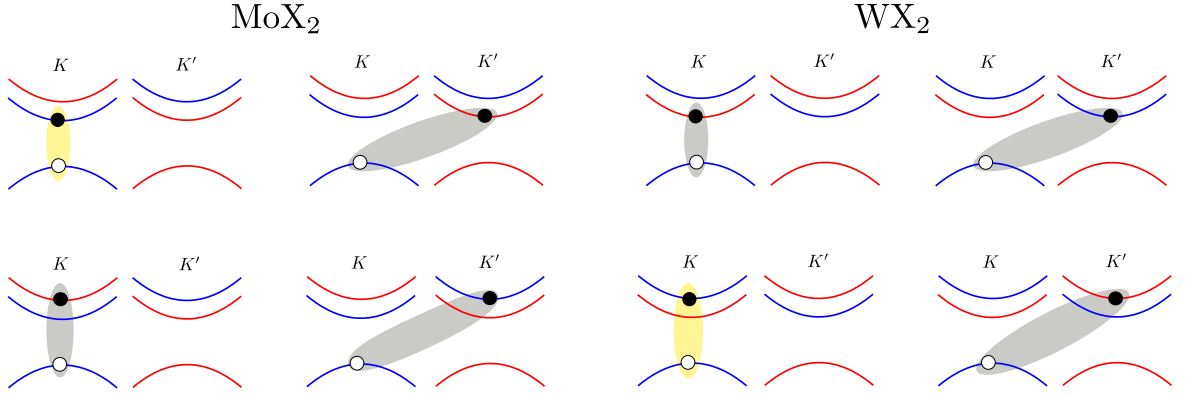


Figure 2.7: Excitons configurations in  $\text{MoX}_2$  (left) and  $\text{WX}_2$  (right) with indication of optical activity with grey (dark) and yellow (bright). Additional configuration with the same optical activity is obtained by time reversal of the configurations shown taking  $K \rightarrow -K$ .

with different choices of out-of-plane spin projections. In particular, the optically inactive excitonic states (grey) are dark due to either spin or valley mismatch, as dictated by the optical selection rules in Eq. 2.9. The dark excitons due to valley (momentum) mismatch can become bright with the assistance of additional carriers or through phonon scattering as proposed in [38]. The spin-mismatched dark excitons can become bright through spin-flip processes as proposed in [35].

As obtained in section 2.5, the opposite ordering of the spin-split CB in the Mo based and W based TMDCs results in the ground state exciton in  $\text{MoX}_2$  to be bright, whereas in  $\text{WX}_2$  to be dark. The excited state excitons involving the upper spin split band has the opposite dark/bright classification in the two types of TMDCs. In thermal equilibrium the excited exciton state population will be suppressed by the Boltzmann factor  $\propto e^{-\frac{\Delta_{so}}{k_B T}}$ , resulting in weaker intensity in the PL spectrum at low temperatures as compared to the spin orbit splitting, however the intensity increases at higher temperatures when the upper spin-splits bands are populated [56, 57, 23].

## 2.7.2 Trions

The trions (negatively or positively charged excitons) can be viewed as an electron bound to an exciton, described in second quantization (for the negatively charged exciton) by,

$$|T\rangle = \int d^2\mathbf{r}_1 d^2\mathbf{r}_2 d^2\mathbf{r}_h \frac{e^{i\mathbf{Q}\cdot\mathbf{R}_{cm}}}{\sqrt{S}} \Phi_T(\mathbf{r}_1, \mathbf{r}_2, \mathbf{r}_h) \Psi_{c,\tau_1,s_1}^\dagger(\mathbf{r}_1) \Psi_{c,\tau_2,s_2}^\dagger(\mathbf{r}_2) \Psi_{v,\tau_h,s_h}(\mathbf{r}_h) |0\rangle, \quad (2.29)$$

where the centre of mass coordinate is given by  $\mathbf{R}_{cm} = \frac{m_1\mathbf{r}_1 + m_2\mathbf{r}_2 + m_h\mathbf{r}_h}{m_T}$  with  $m_T = m_1 + m_2 + m_h$  the trion mass, and with the envelope function  $\Phi_T$  describing the relative motion of the carriers given by the solution to a similar equation to Eq. 2.21 with the Keldysh interaction between each pair of carriers, giving a binding energy of the order  $\sim 30$  meV [43, 44, 58], with good agreement between theory and experiments. Note that the trion wave function must be antisymmetric with respect to the exchange of two electrons, therefore either the spatial or valley/spin indices must be antisymmetric. The tightly bound ground state trions are found to be composed of the symmetric envelope function (zero angular momentum state) and having different valley or spin indices [43, 59].

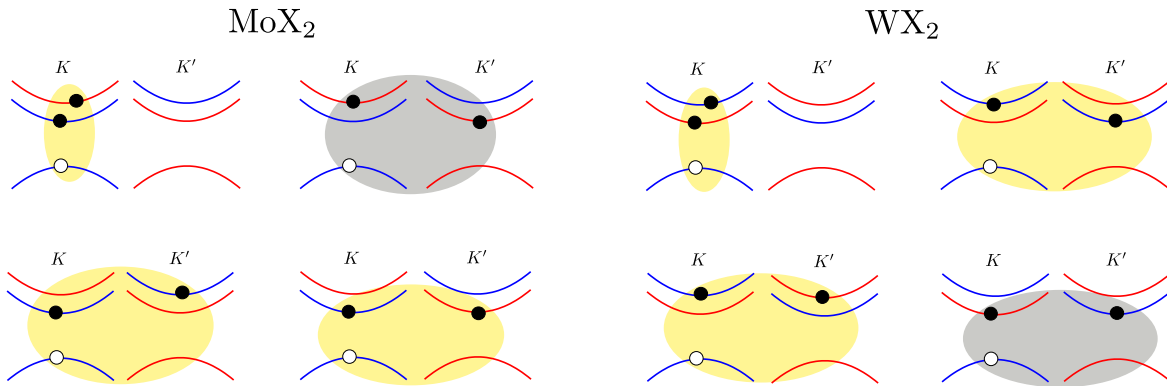


Figure 2.8: Tightly bound trions in  $\text{MoX}_2$  and  $\text{WX}_2$ . Yellow(grey) configurations indicate bright(dark) trions.

Similarly to the excitons, the trion states with electron and hole in the same valley with opposite spin projections in the CB and VB are optically inactive due to spin conservation, and configurations with the second electron residing in an opposite valley cannot recombine with the hole due to the large momentum transfer involved, as shown in Fig. 2.8, [23]. The radiative rate is evaluated in a similar manner, however an important difference compared to the exciton case is the final state consisting of a photon and an electron, as opposed to only a photon in the exciton case. The implication is that the trion is not limited by a light cone for the centre of mass motion, as the final state electron can take the centre of mass momentum of the initial state trion emitting a photon with negligible in-plane wave vector. The energy conservation for the trion radiative recombination is given by

$$E_T + \frac{\hbar^2 Q^2}{2m_T} = \hbar\omega + \frac{\hbar^2 Q^2}{2m_e}, \quad (2.30)$$

where  $E_T$  is the trion energy with zero centre of mass momentum. Assuming the trions to be in thermal equilibrium, the trion kinetic energy can be approximated by the thermal energy as  $\frac{\hbar^2 Q^2}{2m_T} \approx k_B T$ , such that the resulting photon energy is given by,

$$\hbar\omega = E_T - \frac{m_X}{m_e} k_B T. \quad (2.31)$$

The second term on the right is called the recoil energy, and results in the photon's energy to be red-shifted due to the remaining electron kinetic energy [60, 22]. A further implication of the recoil energy is in the resulting PL line shape. For a thermal distribution of trions we have for the line shape [61],

$$I(\hbar\omega) \propto \int d^2\mathbf{Q} e^{-\frac{\hbar^2 Q^2}{2m_T k_B T}} |M|^2 \delta(\hbar\omega - E_T + \frac{m_X \hbar^2 Q^2}{m_e 2m_T}) \propto |M|^2 e^{-\frac{\hbar\omega - E_T}{k_B T} \frac{m_e}{m_X}} \Theta(\hbar\omega - E_T), \quad (2.32)$$

where  $M$  is the radiative matrix element, and  $\Theta$  is the Heaviside function. Therefore, the resulting line shape is antisymmetric with a cut-off at the intrinsic trion energy and a tail towards lower energy determined by the temperature [60]. Finally, the temperature dependent PL intensity of the different lines in equilibrium is weighted by the Boltzmann factor with the energy of the relevant line, such that the ground state trion in  $\text{MoX}_2$  does not require an activation. However the bright trion in  $\text{WX}_2$  is weighted by the Boltzmann factor  $\propto e^{-\frac{\Delta_{SO}}{k_B T}}$ . The excited bright complexes in  $\text{WX}_2$  consisting of both electrons in the upper spin-orbit split bands are suppressed by the factor  $\propto e^{-\frac{2\Delta_{SO}}{k_B T}}$ , resulting in strong suppression of the line's intensity at low temperatures compared to the spin-orbit splitting in the CB [23].

### 2.7.3 Biexcitons

Biexcitons consist of two excitons bound to each other, and are described in second quantization in a similar way to the excitons and trions by,

$$|B\rangle = \int d^2\mathbf{r}_e d^2\mathbf{r}_{e'} d^2\mathbf{r}_h d^2\mathbf{r}_{h'} \frac{e^{i\mathbf{Q}\cdot\mathbf{R}_{cm}}}{\sqrt{S}} \Phi_B(\mathbf{r}_e, \mathbf{r}_{e'}, \mathbf{r}_h, \mathbf{r}_{h'}) \times \Psi_{c,\tau_e,s_e}^\dagger(\mathbf{r}_e) \Psi_{c,\tau_{e'},s_{e'}}^\dagger(\mathbf{r}_{e'}) \Psi_{v,\tau_h,s_h}(\mathbf{r}_h) \Psi_{v,\tau_{h'},s_{h'}}(\mathbf{r}_{h'}) |0\rangle, \quad (2.33)$$

with the centre of mass coordinate given by  $\mathbf{R}_{cm} = \frac{\mathbf{r}_e m_e + \mathbf{r}_{e'} m_{e'} + \mathbf{r}_h m_h + \mathbf{r}_{h'} m_{h'}}{m_B}$ , and  $m_B = m_e + m_{e'} + m_h + m_{h'}$  is the biexciton mass, and  $\Phi_B$  is the relative motion wave function for the four carriers. The theoretically calculated binding energies of biexcitons in

TMDCs are of the order of  $\sim 20$  meV [43, 58], making these complexes observable even close to room temperature.

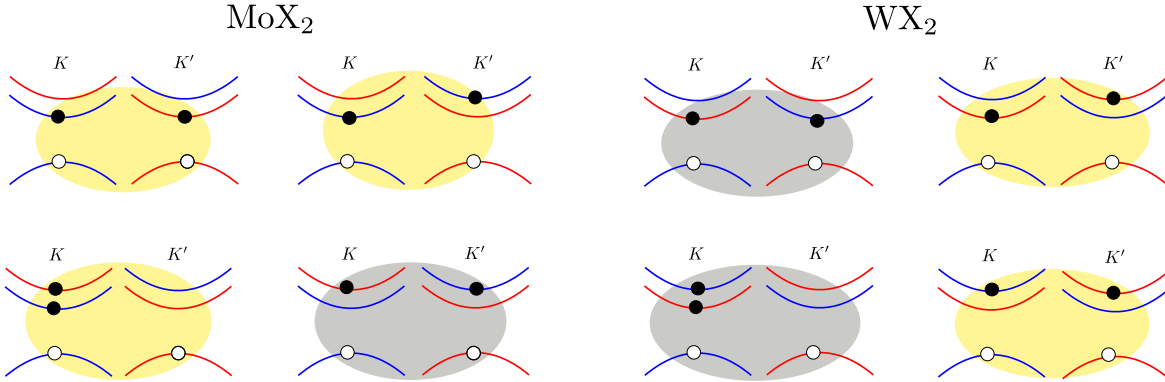


Figure 2.9: Tightly bound biexcitons in  $\text{MoX}_2$  and  $\text{WX}_2$ . Yellow(grey) configurations indicate bright(dark) biexcitons.

In Fig. 2.9 we show the biexcitons configurations for  $\text{MX}_2$  and  $\text{WX}_2$  classified as dark or bright according to the optical selection rules [23]. Two additional configurations can be obtained by time reversal, having the same optical properties. The presence of two excitons implies that in the configuration where the two excitons are in different valleys and satisfy the optical selection rules, both excitons can recombine, doubling the radiative rate.

The radiative decay of a biexciton leaves a free exciton in the final state. Therefore, similarly to the trion case, the emitted photon energy is reduced by the recoil energy of the remaining exciton,

$$\hbar\omega = E_B - k_B T, \quad (2.34)$$

where  $E_B$  is the intrinsic biexciton energy. The resulting PL line shape is therefore asymmetric with a tail towards lower energies.

## 2.8 Heterobilayers of TMDCs

Heterobilayers of 2D TMDCs are formed by stacking two different TMDCs on top of each other. The two monolayers are coupled by weak van der Waals interaction allowing the two monolayers to retain their favourable optoelectronic properties. It was found that the combination of particular pairs among the four common TMDCs discussed thus far,  $\text{MoS}_2$ ,  $\text{MoSe}_2$ ,  $\text{WS}_2$  and  $\text{WSe}_2$ , into heterobilayers result in a particular band alignment known as a type-II band alignment [62, 63, 64]. In such a band

alignment, the conduction band minimum belongs to one layer and the valence band maximum belongs to the other layer, such that the electrons are localized on one layer and the holes are localized on the other, Fig. 2.10.

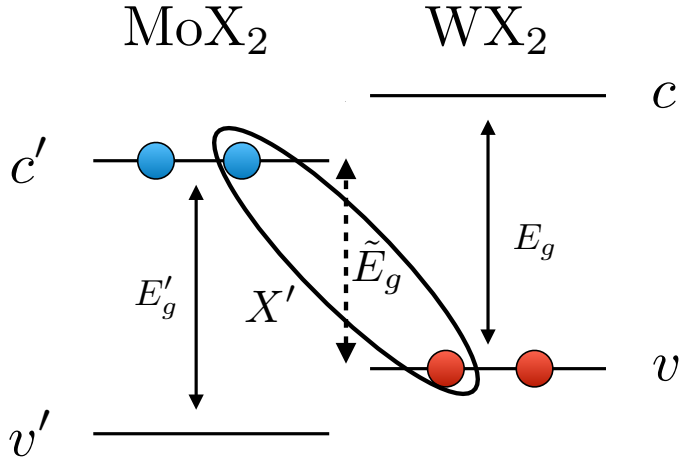


Figure 2.10: Schematic demonstration of type-II band alignment of Molybdenum and Tungsten based TMDCs heterobilayer, showing the conduction and valence band edges of the two monolayers, and the interlayer exciton  $X'$  composed of electron and hole localized on opposite layers. Figure adapted from [24].

The Coulomb interaction between the electrons and holes in the two layers results in the formation of interlayer bound complexes, the simplest being an interlayer exciton. The energy of these interlayer complexes as revealed in photoluminescence experiments [65], depends on the interlayer band gap, being smaller than the band gap in the individual monolayers, as well as the complex's binding energy, which is reduced as compared to the monolayer, due to the separation in real space between the carriers.

An additional consequence of the stacking of heterobilayers of TMDCs on the optical and electronic properties of these systems, has to do with the real space alignment and incommensurability of the two monolayers. In particular, the lattice constants of the four TMDCs are not exactly the same, and can differ by as much as 4% [27]. These real space differences translate directly into reciprocal space where the BZ of the two monolayers have different sizes and are rotated with respect to each other. The electrons and holes in each layer, found in the vicinity of the  $K$  valleys of the respective layers, are therefore separated from each other in reciprocal space by the wave vector  $\Delta K$  (Fig. 2.11b) given by [66, 24]

$$\Delta K = K_{\text{MoX}_2} \sqrt{\delta^2 + \theta^2}; \quad \delta = 1 - \frac{a_{\text{MoX}_2}}{a_{\text{WX}_2}}, \quad (2.35)$$

where  $\delta$  is the lattice mismatch and  $\theta$  is the twist angle. As direct radiative recombination requires the electron and hole to have the same crystal momentum, the direct recombination is suppressed in incommensurate and twisted heterobilayer TMDCs due to momentum and energy conservation.

The interlayer exciton composed of the electron and hole localized on the opposite layers has a dispersion of the form,

$$E_{X'} = \tilde{E}_g - \epsilon_{\tilde{X}}^b + \frac{\hbar^2(\mathbf{Q} - \Delta\mathbf{K})^2}{2M_{\tilde{X}}}, \quad (2.36)$$

where  $\epsilon_{\tilde{X}}^b$  is the exciton binding energy, and the exciton centre of mass momentum is given by  $\mathbf{Q} = \mathbf{k}_e + \mathbf{k}_h$ , measured relative to a common point ( $K$  point in  $\text{WX}_2$ ). In particular, the dispersion minima corresponding to both carriers in their respective valleys is found at a finite  $Q$ , preventing the direct radiative recombination (Fig. 2.11c). As the light cone position found at  $Q = 0$ , the interlayer exciton therefore has a finite kinetic energy given by  $E(Q = 0) = \frac{\hbar^2 \Delta K^2}{2M_{\tilde{X}}}$ , [67].

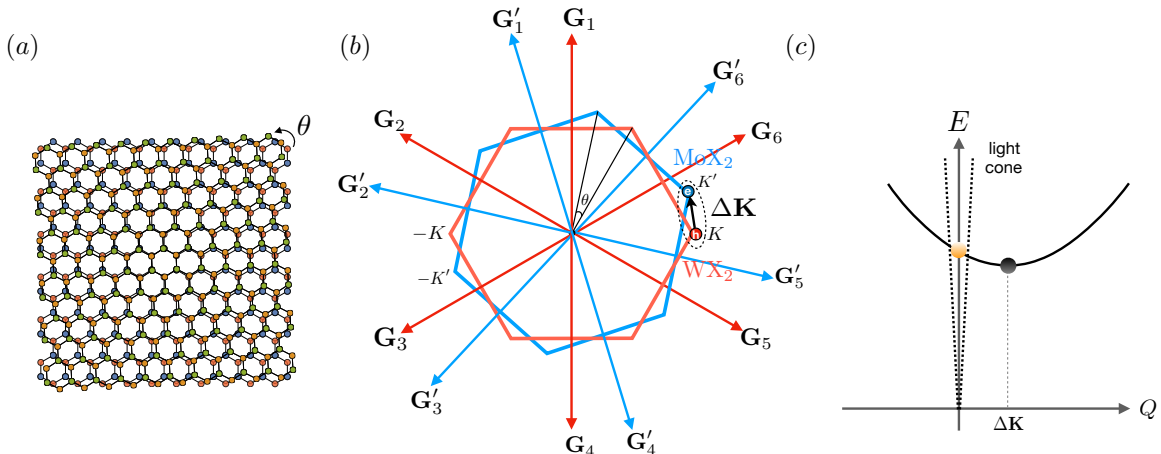


Figure 2.11: (a) Heterobilayer of twisted monolayers in real space with a twist angle  $\theta$ . (b) Rotated Brillouin zones of the two monolayers with the first circle of reciprocal lattice vectors of the two rotated monolayer,  $\mathbf{G}, \mathbf{G}'$ . The electron and hole are found at the  $\tau(\pm)K(\pm)$  valleys ( $\tau = \pm$ ) of the two layers separated by a wave vector  $\Delta K$ . (c) The interlayer exciton  $\tilde{X}$  dispersion, as a function of the centre of mass momentum  $Q$ .

The optical properties of the heterobilayer system and the interlayer complexes depend crucially on the coupling between the layers [68]. The Bloch state on a given layer in band  $n$ , with wave vector  $\mathbf{k}$  measured relative to valley  $\tau K$ , can be written as a linear combination of the atomic orbitals localized on the atomic positions with

appropriate phases, in accordance with Bloch's theorem

$$\Psi_{n,\mathbf{k}^{(\prime)}}(\mathbf{r}) = \frac{1}{\sqrt{N^{(\prime)}}} \sum_{\mathbf{R}^{(\prime)}} \phi_n(\mathbf{r} - \mathbf{R}) e^{i(\tau^{(\prime)}\mathbf{K}^{(\prime)} + \mathbf{k}^{(\prime)}) \cdot \mathbf{R}^{(\prime)}}, \quad (2.37)$$

where  $R^{(\prime)}$  are the lattice vectors,  $N^{(\prime)}$  is the number of unit cells, and  $\phi_{n^{(\prime)}}(\mathbf{r} - \mathbf{R}^{(\prime)})$  is the orbital corresponding to band  $n^{(\prime)}$  localized on the lattice site  $\mathbf{R}^{(\prime)}$ , in the top(bottom) layer. Given two incommensurate layers with reciprocal wave vectors  $\mathbf{G}, \mathbf{G}'$ , respectively, the hopping amplitude between two Bloch states is given by the matrix element of the interlayer coupling Hamiltonian  $\hat{H}_t$ , which is treated as a perturbation to the eigenstates of the two monolayers [66, 69],

$$T_{n,n'} = \langle n, \mathbf{k} | \hat{H}_t | n', \mathbf{k}' \rangle = \sum_{\mathbf{G}, \mathbf{G}'} \delta_{\tau\mathbf{K}+\mathbf{k}+\mathbf{G}, \tau'\mathbf{K}'+\mathbf{k}'+\mathbf{G}'} t_{nn'}(\tau\mathbf{K} + \mathbf{k} + \mathbf{G}), \quad (2.38)$$

$$t_{nn'}(\mathbf{q}) = \frac{1}{\sqrt{AA'}} \int \tilde{t}_{nn'}(\mathbf{r}) e^{i\mathbf{q} \cdot \mathbf{r}} d^2\mathbf{r}; \quad \tilde{t}_{nn'}(\mathbf{R}' - \mathbf{R}) = \langle \phi_{n,\mathbf{R}} | \hat{H}_t | \phi_{n',\mathbf{R}'} \rangle,$$

where  $A, A'$  are the unit cells of the two layers, respectively. The main quantity determining the coupling in Eq. 2.38 is  $t_{nn'}(\mathbf{k})$ , which is the Fourier component of the overlap between the orbitals making up the bands, localized on two lattice sites separated by the in-plane position vector  $\mathbf{r}$ . The Kronecker delta function appearing in the sum, ensures momentum conservation in the tunnelling process between the layers. As the crystal momentum is defined up to a reciprocal lattice vectors, we have a summation over the reciprocal lattice vectors of the two layers. The hopping integral  $\tilde{t}_{nn'}$  being a smooth function of the orbitals' distance implies that  $t(\mathbf{q})$  decays rapidly for increasing values of the reciprocal lattice vectors [66], and can therefore be restricted to the first set of reciprocal lattice vectors in the two layers.

For aligned and commensurate ( $\Delta K \sim 0$ ) layers there are three contributions from the three equivalent  $K$  points, which are related by a  $C_3$  symmetry operation, giving for the tunnelling amplitudes [66, 69],

$$T_{n,n'} = t_{nn'}(\mathbf{K}) + t_{nn'}(\hat{C}_3\mathbf{K}) + t_{nn'}(\hat{C}_3^2\mathbf{K}) = \left[ 1 + e^{i\frac{2\pi}{3}(m_{n'} - m_n)} + e^{i\frac{4\pi}{3}(m_{n'} - m_n)} \right] t_{nn'}, \quad (2.39)$$

where in the second equality we used the fact that the states in the CB and VB states are eigenstates of  $C_3$  symmetry operation 2.1. For an AA-stacking corresponding to the second layer simply displaced in the out of plane direction, this gives for the

tunnelling amplitudes between the different bands at the  $K$ -valley (with values for the  $-K$  valley obtained by time reversal) [66, 69],

$$\begin{aligned} T_{cc'} &= 3t_{cc'}, \\ T_{vv'} &= 3t_{vv'}, \\ T_{cv'} &= T_{vc'} = 0. \end{aligned} \tag{2.40}$$

The other common stacking is 2H (or AB), in which the second layer displaced in the out of plane direction, is further rotated by  $180^\circ$  relative to the centre of the hexagon. In such a stacking, the tunnelling takes place between states in the  $K$  valley in one layer to states in the  $-K$  valley in the other, giving using Eq. 2.39 [66, 69],

$$\begin{aligned} T_{cc'} &= 0, \\ T_{vv'} &= 3t_{vv'}, \\ T_{cv'} &= T_{vc'} = 0, \end{aligned} \tag{2.41}$$

such that for this stacking the K-point conduction bands are decoupled.

# Chapter 3

## Kinetics of electrons and holes in TMDCs

### 3.1 Introduction

The radiative recombination process following the excitation of electron-hole pairs to energy above the bottom of the conduction band, requires the relaxation of the hot-carriers into the minimum of the respective conduction and valence bands, at which point the electrons and holes bind into excitons, which can recombine radiatively and emit light. The relaxation time of the carriers and the understanding of the relaxation processes is therefore of importance for the optical response of these materials and their performance in potential optoelectronic device applications. The most common path of energy relaxation in semiconductors is through dissipation of the energy into lattice vibrations in the form of phonons, and particularly optical phonons with a finite energy at the  $\Gamma$ -point ( $q = 0$ ). TMDCs being polar materials results in an electron-phonon coupling due to the electrostatic potential induced by the longitudinal optical (LO) phonon. The modified dielectric function in 2D,  $\epsilon(\mathbf{q}) = 1 + r_* q$ , however, calls for a modification to the 3D Fröhlich coupling having the form  $\propto 1/q$ . In the work presented in 3.2 we obtain the modified coupling for 2D materials having a finite coupling at  $q = 0$ , with the coupling strength determined by the Born effective charge of the metal and chalcogen (See also Appendix A for a more detailed derivation). This results in relaxation times of order sub-picoseconds to picoseconds for the four TMDCs.

In parallel to the relaxation process, non-radiative processes can hinder the efficiency of the radiative recombination process, by transferring the energy from the recombination to an additional carrier as opposed to emission of a photon. Following the carrier relaxation and formation of bound electron-hole pairs (excitons), the excitonic complexes can either recombine radiatively and emit light or decay into free carriers through non-radiative processes. The efficiency of optoelectronic devices depends on the competition between the radiative and non-radiative processes. The observed efficiency of photoluminescence experiments in TMDCs was found to be  $\sim 1 - 10\%$ . This low efficiency is surprising considering the direct band gap nature, strong light-matter coupling, and in particular the reduced phase space for scattering in Auger type processes due to the two dimensional nature of the materials, which due to both momentum and energy conservation constrain the final allowed momentum state, requiring a near resonance condition for the process to take place. This therefore calls for a specific process that can quench the emission of light in these materials. In the work presented in 3.3 we propose a non-radiative (Auger) recombination process in  $\text{WS}_2$  and  $\text{WSe}_2$  where the opposite ordering of the spin-orbit splitting in the conduction and valence bands makes the ground state excitons dark, leading to a bottleneck in the low temperature radiative recombination. By comparing the non-radiative rate to a corresponding radiative process, we estimated the relative importance of the Auger process. We find that the non-radiative process can dominate over the corresponding radiative process for relatively low carrier densities  $< 10^{11} \text{ cm}^{-2}$ , therefore providing a possible quenching mechanism for light emission in these materials, explaining the observed low quantum efficiencies.

## 3.2 Fast relaxation of photo-excited carriers in 2D transition metal dichalcogenides

The results presented in this section are reported in the publication [21]: “Fast Relaxation of Photo-Excited Carriers in 2-D Transition Metal Dichalcogenides” in *IEEE Journal of Selected Topics in Quantum Electronics*, vol. **23**, no. 1, pp. 168-172, Jan.-Feb. 2017. © 2017 IEEE. Reprinted, with permission.

My contribution to this work: Performed all the relaxation rates calculations, prepared

figures, analysed the results and written the manuscript.

Full author list: M. Danovich, I. L. Aleiner, N. D. Drummond, V. I. Fal'ko.

Author contributions: N.D. performed the DFT calculations to obtain the Born effective charges. All authors contributed to the writing of the paper.

# Fast Relaxation of Photo-Excited Carriers in 2-D Transition Metal Dichalcogenides

Mark Danovich, Igor L. Aleiner, Neil D. Drummond, and Vladimir I. Fal'ko

**Abstract**—We predict a fast relaxation of photo-excited carriers in monolayer transition metal dichalcogenides, which is mediated by the emission of longitudinal optical (LO) and homopolar (HP) phonons. By evaluating Born effective charges for MoS<sub>2</sub>, MoSe<sub>2</sub>, WS<sub>2</sub>, and WSe<sub>2</sub>, we find that, due to the polar coupling of electrons with LO phonons, and the HP phonons lattice deformation potential, the cooling times for hot electrons and holes from excitation energies of several hundred meV are at ps-scale.

**Index Terms**—TMDCs, optoelectronics, ultrafast relaxation.

## I. INTRODUCTION

MONOLAYER transition metal dichalcogenides (TMDCs) offer a unique possibility to create nm-thin optoelectronic devices [1]–[9], in particular when used in van der Waals heterostructures with other two-dimensional (2D) crystals [10]. The optoelectronic functionality of TMDCs is determined by their high-efficiency optical absorption in the visible optical range [11] as well as the fact that their monolayers are direct-band-gap 2D materials. Because of their promise for optoelectronics, it is important to understand the process of cooling (energy relaxation) of photo-excited carriers in TMDCs. In this paper we show that photo-excited carriers can emit  $\Gamma$ -point optical phonons at a sub-ps time scale. Such a high speed of relaxation of electrons and holes excited to energies  $> 150$  meV above the band edge arises from polar coupling to the longitudinal optical (LO) phonons, and the deformation potential induced by the out of plane homopolar (HP) phonon mode. In the theory reported in this Letter, we analyze the phonon-mediated cooling of hot electrons/holes in TMDCs, taking into account two phonon modes coupled to the intra-band intra-valley relaxation processes: the in-plane LO phonon and the out of plane HP vibrational mode [12]. Density functional theory (DFT) modeling produces electron (hole) couplings to the corner of the Brillouin zone ( $K$ -point) phonons, which are weaker by at least an order of magnitude [13]–[17]. We also note that advance DFT methods have shown that the energy difference between the  $Q$  and  $K$  valleys in

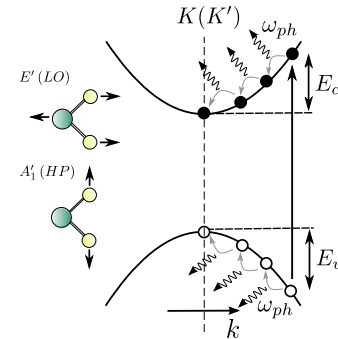


Fig. 1. Sketch of the energy relaxation of photo-excited carriers in the valence (v) and conduction (c) bands of TMDCs through phonon emission. The use of the parabolic approximation in the description of electron and hole dispersion in each valley ( $K$  or  $K'$ ) sets a constraint,  $E \leq 0.25$  eV on the excitation energies of the charge carriers. The insets show side view of the atomic displacements in the LO and HP modes.

the conduction band in MoS<sub>2</sub> and MoSe<sub>2</sub> are large enough to exclude  $K \rightarrow Q$  scattering from our considerations [15], [18].

## II. CARRIER-PHONON INTERACTION

The carrier-phonon interaction in TMDCs is given by the Hamiltonian

$$H_{e-\text{ph}} = \sum_{\substack{\vec{q}, \vec{k} \\ \mu = \text{LO, HP}}} g_{\mu, \vec{q}} c_{\vec{k} + \vec{q}}^\dagger c_{\vec{k}} (a_{\mu, -\vec{q}}^\dagger + a_{\mu, \vec{q}}), \quad (1)$$

where  $c_{\vec{k}}^\dagger$  ( $c_{\vec{k}}$ ) are the creation (annihilation) operators for a charge carrier (electron or hole) in the vicinity of one of the valleys, ( $K$  or  $K'$ ), near the corners of the hexagonal Brillouin zone of the 2D crystal [19], [20], with  $\vec{k}$  measured from the valley center (see Fig. 1). The operators  $a_{\mu, \vec{q}}^\dagger$  ( $a_{\mu, \vec{q}}$ ) are the phonon creation (annihilation) operators for mode  $\mu = \text{LO}$  or  $\text{HP}$  with wavevector  $\vec{q}$ , where  $|q| \ll |K|$ . The two phonon modes<sup>1</sup> accounted for in the relaxation process are shown in Fig. 1.

The LO mode, which corresponds to the irreducible representation  $E'$  of the symmetry group  $D_{3h}$  of the crystal, couples to the charge carriers through the polarization induced by the lattice deformation,  $\vec{P} = \frac{Ze}{A} \vec{u}$ , where  $Z$  is the Born charge,  $\vec{u}$  is the relative displacement of the two sublattices in the LO vibration,  $A$  is the unit cell area, and  $e$  is the electron charge.

To estimate the Born charge we used DFT [22] to calculate the Born effective charges of the atoms in the lattice of monolayer

Manuscript received March 29, 2016; revised May 12, 2016; accepted June 15, 2016. This work was supported by the Simons Foundation, the ERC Synergy Grant Hetero2D and the EC-FET European Graphene Flagship.

M. Danovich and V. I. Fal'ko are with the National Graphene Institute, University of Manchester, Manchester M13 9PL, U.K. (e-mail: mark.danovich@postgrad.manchester.ac.uk; vladimir.falko@manchester.ac.uk).

I. L. Aleiner is with the Department of Physics, Columbia University, New York, NY 10027 USA (e-mail: aleiner@phys.columbia.edu).

N. D. Drummond is with the Department of Physics, Lancaster University, Lancaster LA1 4YB, U.K. (e-mail: n.drummond@lancaster.ac.uk).

Color versions of one or more of the figures in this paper are available online at <http://ieeexplore.ieee.org>.

Digital Object Identifier 10.1109/JSTQE.2016.2583059

<sup>1</sup>TMDCs have six optical modes denoted by the irreducible representations of the point group  $D_{3h}$  ( $A'_1, A''_2, E', E''$ ), and three acoustical modes denoted by LA, TA, and ZA, where LA and TA are the in-plane longitudinal and transverse modes, and ZA is the out-of-plane mode. We neglect the transverse optical and acoustical modes due to their weak coupling at the  $\Gamma$  point,  $q \rightarrow 0$ .

TABLE I  
TMDC PARAMETERS USED IN THE MODELLING  
OF THE PHONON EMISSION RATES

	MoS <sub>2</sub>	MoSe <sub>2</sub>	WS <sub>2</sub>	WSe <sub>2</sub>
$\frac{m_c}{m_0}$ Ref. [11]	0.46	0.56	0.26	0.28
$\frac{m_v}{m_0}$ Ref. [11]	0.54	0.59	0.35	0.36
$A [\text{\AA}^2]$ Ref. [11]	8.65	9.37	8.65	9.37
$\frac{M_r}{M}$	38.4	59.7	47.5	85.0
$\frac{m_p}{m}$	160	254	248	342
$\hbar\omega_{\text{LO}}$ [meV] Ref. [13]	49	37	44	31
$\hbar\omega_{\text{HP}}$ [meV] Ref. [13]	51	30	52	31
$D_c$ [eV/\text{\AA}] Ref. [13]	5.8	5.2	3.1	2.3
$D_v$ [eV/\text{\AA}] Ref. [13]	4.6	4.9	2.3	3.1
$Z$	-1.08	-1.80	-0.47	-1.08
$r_*$ [\text{\AA}] Ref. [21]	41	52	38	45

TABLE II  
VALUES OF DERIVED AND FITTED PARAMETERS IN Eqs. (5) AND (6)

	MoS <sub>2</sub>	MoSe <sub>2</sub>	WS <sub>2</sub>	WSe <sub>2</sub>
$k_c [\text{\AA}^{-1}]$	0.077	0.074	0.055	0.048
$k_v [\text{\AA}^{-1}]$	0.083	0.076	0.064	0.054
$\tau_c^{-1} [\text{ps}^{-1}]$	112	296	11	45
$\tau_v^{-1} [\text{ps}^{-1}]$	130	312	14	58
$\tau_{\text{HP},c}^{-1} [\text{ps}^{-1}]$	6.8	7.7	0.69	0.54
$\tau_{\text{HP},v}^{-1} [\text{ps}^{-1}]$	5.0	7.2	0.5	1.3
$a_c [\frac{\text{ps}}{\text{meV}}]$	$2.3 \cdot 10^{-3}$	$3.9 \cdot 10^{-3}$	0.029	0.017
$b_c [\frac{\text{ps}}{\sqrt{\text{meV}}}]$	0.012	0.033	0.24	0.17
$c_c [\text{ps}]$	0.14	0.15	1.27	0.70
$a_v [\frac{\text{ps}}{\text{meV}}]$	$2.7 \cdot 10^{-3}$	$2.6 \cdot 10^{-3}$	0.023	0.012
$b_v [\frac{\text{ps}}{\sqrt{\text{meV}}}]$	0.017	0.018	0.18	0.10
$c_v [\text{ps}]$	0.15	0.10	1.03	0.45

TMDCs. The latter are defined by the response of the atomic displacements in a unit cell to a homogeneous electric field. Hence, we write

$$Z \equiv Z_{xx} = Z_{yy}; Z_{ij} = \frac{1}{e} \frac{\partial F_j(s)}{\partial E_i} \Big|_{E=0}, \quad (2)$$

where  $F(s)$  is the force acting on atom  $s$  at its zero-field equilibrium position. We used the CASTEP plane-wave basis code [23], [24] to calculate the Born effective charge tensors for MoS<sub>2</sub>, MoSe<sub>2</sub>, WS<sub>2</sub>, and WSe<sub>2</sub>,<sup>2</sup> see Table I. We used the Perdew–Burke–Ernzerhof [27] exchange–correlation functional, norm-conserving pseudopotentials, a plane-wave cutoff energy of  $\sim 816$  eV, a  $97 \times 97$  Monkhorst–Pack grid of  $\mathbf{k}$ -points, and (for the in-plane components of the Born effective charge tensors) an artificial (out-of-plane) periodicity of  $\sim 16$  Å. We verified that our results are converged with respect to these parameters. For the out-of-plane component we found a significant dependence on the artificial periodicity, which we removed by extrapolating to infinite layer separation.

The LO phonon coupling (the same for electrons and holes) is given by,<sup>3</sup>

$$g_{\text{LO}} = \frac{i}{A} \sqrt{\frac{\hbar}{2NM_r\omega_{\text{LO}}}} \frac{2\pi Ze^2}{1 + qr_*}, \quad (3)$$

where  $N$  is the number of unit cells,  $M_r$  is the reduced mass of the two sublattices, and  $\omega_{\text{LO}}$  is the LO phonon frequency. The

<sup>2</sup>Note that Eq. (2) is evaluated using Eqs. (40) and (42) of Ref. [25]. To evaluate Eq. (42) of Ref. [25], derivatives of the Kohn–Sham orbitals with respect to the atomic positions and with respect to the wavevector are required. The latter are evaluated within the parallel-transport gauge by minimizing the functional in Eq. (70) of Ref. [26].

<sup>3</sup>Starting from the electrostatic interaction energy in 2D,  $E = \frac{1}{2} \int \frac{d^2\vec{r} d^2\vec{r}'}{|\vec{r} - \vec{r}'|} \sigma(\vec{r})\sigma(\vec{r}') + \frac{1}{2\kappa} \int d^2\vec{r} (P_{\perp}^2 + P_{\text{op}}^2)$ , with  $\sigma(\vec{r}) = e\rho(\vec{r}) - \nabla \cdot \vec{P}_{\text{op}}(\vec{r}) - \nabla \cdot \vec{P}_{\perp}(\vec{r})$ , where  $\rho(r)$  is the 2D carrier density,  $\vec{P}_{\text{op}}$  is the optical phonon induced polarization,  $\vec{P}_{\perp}$  is the remaining in-plane polarization, and  $\kappa$  is the in-plane rigidity. Assuming the adiabatic approximation, we Fourier transform the integrand, and integrate out  $P_{\perp}$ , we obtain the dielectric screening  $1/(1 + 2\pi\kappa q)$ , from which we define the screening length as  $r_* = 2\pi\kappa$ , and the carrier-phonon coupling is obtained from the term containing  $\rho_q^* \vec{P}_{\text{op},q}$ , which are the Fourier components of the electron density and the optical phonon induced polarization vector.

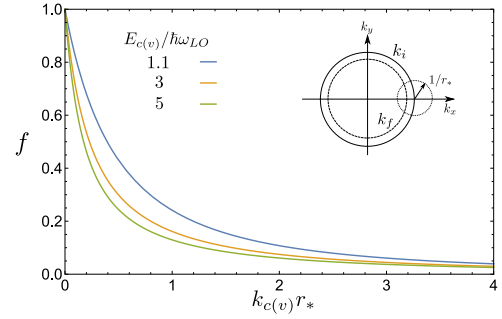


Fig. 2. Dimensionless function  $f(k_c(v)r_*)$  in Eq. (5a) for different carrier energies,  $E_c(v)/\hbar\omega_{\text{LO}} = 1.1, 3$  and  $5$ . The inset sketches the kinematics for the phonon emission process in momentum space for the carrier undergoing energy relaxation with initial state wavevector  $k_i$  and final-state wavevector  $k_f$ . The circle with radius  $1/r_*$  defines the region of phonon wavevectors  $q$  that give the dominant contribution to the scattering rate. As the number of available final states scales as the circumference of the iso-energy circle in momentum space, for a given  $r_*$  the asymptotic behavior of the scattering rate for high carrier energies is given by  $\tau \sim 1/k_i \propto 1/\sqrt{E}$ .

dielectric screening of the electric field of LO mode deformations is described [3], [28] by the factor  $1/(1 + qr_*)$ , where  $r_*$  is a length scale defined by  $r_* = a_z(\epsilon_{||} - 1)/2$ , where  $a_z$  and  $\epsilon_{||}$  are the  $z$ -axis lattice constant and in-plane dielectric constant of a bulk crystal of the corresponding TMDC [21], [28]. The values used for the screening lengths are taken from the DFT calculated 2D polarizabilities in Ref. [21].

The HP mode (which corresponds to the irreducible representation  $A'_1$  of the symmetry group  $D_{3h}$ ) couples with the carriers through the lattice deformation potential<sup>4</sup>

$$g_{\text{HP}}^{\alpha} = \sqrt{\frac{\hbar}{2NM\omega_{\text{HP}}}} D^{\alpha}, \quad \alpha = c \text{ or } v, \quad (4)$$

where  $M$  is the total atomic mass within the unit cell,  $\omega_{\text{HP}}$  is the HP phonon frequency, and we distinguish electrons in the conduction band ( $c$ ) and holes in the valence band ( $v$ ). Here

<sup>4</sup>For the LO/TO mode at the  $\Gamma$ -point, the pseudo-potential induced by the atomic displacements, which is a scalar function, will contain the factor  $\nabla \cdot \vec{u}$ . Hence, it would appear in the power-law expansion together with the wavevector  $\vec{q}$  of the phonon, and will vanish at the  $\Gamma$ -point. For the LO phonon mode, this factor  $q$  is canceled by the  $1/q$  factor coming from the 2D Fourier transform of the Coulomb potential, resulting in a finite contribution at the  $\Gamma$ -point in Eq. (3).

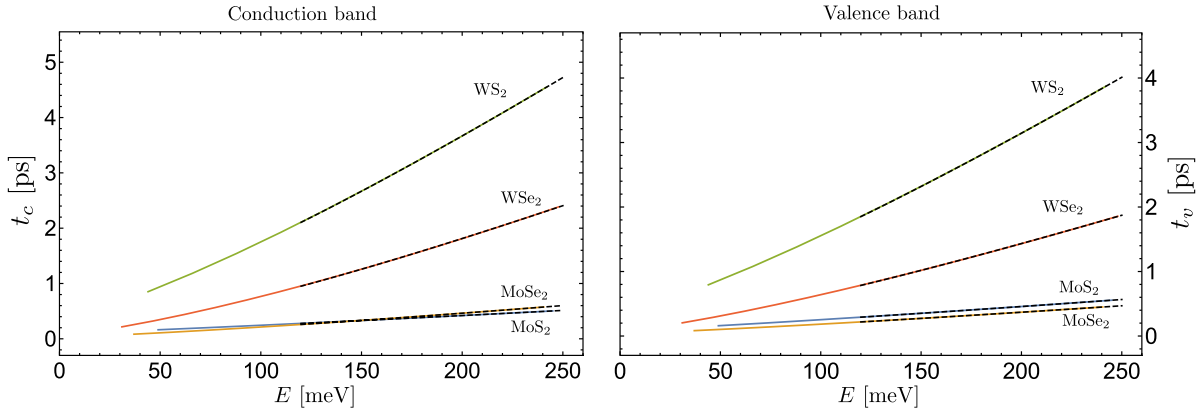


Fig. 3. Hot carrier cooling time as a function of initial conduction-band (Left) and valence-band (Right) carrier energy  $E$  for four TMDC materials. The dashed lines are asymptotic fits of the form in Eq. (6c).

we follow the definitions given in Refs. [13], [14], [18] for the coupling and, below, we use the deformation potentials for the HP phonon mode reported in Ref. [13].

### III. SCATTERING RATES

The emission of both LO and HP phonons by a photo-excited electron/hole with initial momentum  $k_i$  measured from the center of the corresponding ( $K$  or  $K'$ ) valley, is characterized by the rate calculated using the Fermi golden rule

$$\tau^{-1} = \frac{2\pi}{\hbar} \sum_{\vec{q},\mu} |\langle f | H_{e-ph} | i \rangle|^2 \delta(E_f - E_i).$$

This yields

$$\begin{aligned} \tau_{\text{LO},\alpha}^{-1} &= \tau_\alpha^{-1} f \left( \frac{E_\alpha}{\hbar \omega_{\text{LO}}}, k_\alpha r_* \right), \quad \alpha = c \text{ or } v \\ \tau_\alpha^{-1} &= \frac{2\pi^2 Z^2 E_B}{\hbar} \frac{m_\alpha}{M_r} \frac{a_B^2}{A} \frac{E_B}{\hbar \omega_{\text{LO}}}; \\ f &= \frac{1}{\pi} \frac{k_\alpha}{k_i} \int_{u_-}^{u_+} \frac{du}{(1 + u k_\alpha r_*)^2 \sqrt{1 - [\frac{k_\alpha}{2k_i}(u + \frac{1}{u})]^2}}; \end{aligned} \quad (5a)$$

$$u_\pm = \frac{k_i}{k_\alpha} \left( 1 \pm \sqrt{1 - \frac{k_\alpha^2}{k_i^2}} \right); \quad k_\alpha = \sqrt{\frac{2m_\alpha \omega_{\text{LO}}}{\hbar}};$$

$$\tau_{\text{HP},\alpha}^{-1} = \frac{m_\alpha A D_\alpha^2}{2M \hbar^2 \omega_{\text{HP}}}. \quad (5b)$$

Note that these scattering rates are valid only for carrier energies above the corresponding optical phonon energy. Furthermore, the rate of emission of the HP phonon is independent of the carrier energy, due to the constant coupling coefficient and the constant density of states for 2D carriers with parabolic dispersion. For the LO phonon mode we express the scattering rate in terms of a dimensionless integral by performing a change of variables, defining the dimensionless variable  $u = q/k_{c(v)}$ , where  $k_{c(v)}$  is the carrier wavevector corresponding to an energy of  $\hbar \omega_{\text{LO}}$ , and  $a_B$  and  $E_B$  are the Bohr radius and energy. In Table II we list the values of the parameter  $\tau_{c(v)}^{-1}$  for various

TMDCs, and in Fig. 2 we show the shape of the function  $f$  for different carrier energies  $E_{c(v)}$ . The decrease of this scattering rate upon increasing  $r_*$  or excitation energy can be understood from the diagram depicting the kinematic phase space for a carrier emitting an optical phonon.

Comparing the values of  $\tau_{c(v)}^{-1}$  and  $\tau_{\text{HP},c(v)}^{-1}$  in Eqs. (5a), (5b), and Table II, we see that emission of the LO phonon mode with  $r_* = 0$ , dominates in the relaxation over the HP phonon. The two rates become comparable for sufficiently large carrier energies or sufficiently large  $r_*$  values. Asymptotically, we have for the LO phonon,  $\tau_{\text{LO}}^{-1} \sim 1/(r_* \sqrt{E})$ ; therefore, the boundary between the two modes is given by<sup>5</sup>  $\frac{r_* \sqrt{m E}}{\hbar} \sim 4\pi Z^2 \frac{a_B^2 E_B^2}{A^2 D_\alpha^2} \frac{M}{M_r} \frac{\omega_{\text{HP}}}{\omega_{\text{LO}}}$ , where  $E$  is the energy of the photo-excited carrier and  $m$  is its band mass.

### IV. RELAXATION TIMES

For hot carriers excited to the energy  $E \gg \hbar \omega_{\text{LO/HP}}$ , we write the cooling rate as

$$\frac{dE}{dt} = -\frac{\hbar \omega_{\text{LO}}}{\tau_{\text{LO}}(E)} - \frac{\hbar \omega_{\text{HP}}}{\tau_{\text{HP}}}, \quad (6a)$$

so that we can determine the relaxation time as a function of the initial carrier energy  $E$  as

$$t(E) = \int_0^E \frac{d\epsilon}{\frac{\hbar \omega_{\text{LO}}}{\tau_{\text{LO}}(\epsilon)} + \frac{\hbar \omega_{\text{HP}}}{\tau_{\text{HP}}}}. \quad (6b)$$

For hot carriers excited to the energy  $E \gg \hbar \omega_{\text{LO/HP}}$ , Eqs. (5a), (5b) yield  $\tau_{\text{LO}}^{-1} \propto 1/\sqrt{E}$  (also see Fig. 2) and  $\tau_{\text{HP}}^{-1}$  is a constant, so that we find an analytical asymptotic form for the cooling time of charge carriers from the initial energy  $E$  to the bottom of the band,

$$t(E) \approx aE - b\sqrt{E} + c. \quad (6c)$$

The fitted values of the parameters  $a$ ,  $b$  and  $c$  for the conduction and valence bands relaxation times are listed in Table II

<sup>5</sup>This parameter was derived by equating  $\tau_{\text{LO}}^{-1} \sim \tau_{\text{HP}}^{-1}$ , and using the asymptotic form of  $\tau_{\text{LO}}^{-1}$  for large carrier energies. The corresponding values are, 13, 18, 15 and 57 for electrons and 20, 21, 27, and 31 for holes in MoS<sub>2</sub>, MoSe<sub>2</sub>, WS<sub>2</sub>, and WSe<sub>2</sub>, respectively.

and correspond to the numerically obtained [29] relaxation time curves shown in Fig. 3 for the conduction (c) and valence (v) bands.

## V. CONCLUSION

We calculated the scattering rates and relaxation times of photo-excited carriers in TMDCs due to optical phonon emission. We obtained relaxation times of a few ps for all the materials studied, with  $\text{MoSe}_2$  and  $\text{MoS}_2$  having the shortest sub-ps relaxation times for all carrier energies up to 0.25 eV, which is determined by their respective unit cell Born charges,  $Z_{\text{MoSe}_2} = -1.80$  and  $Z_{\text{MoS}_2} = -1.08$ , and respective optical deformation potentials (Table I). For  $\text{WS}_2$  and  $\text{WSe}_2$ , we find smaller unit cell Born charges,  $Z_{\text{WS}_2} = -0.47$  and  $Z_{\text{WSe}_2} = -1.08$ , and smaller HP deformation potentials, resulting in longer relaxation times. However, for these two 2D materials, an additional channel of  $K \rightarrow Q$  intervalley relaxation is possible, due to a smaller  $E_{\text{KQ}}^c$  splitting than in Mo-based dichalcogenides, so that the rates shown in Eq. (5) give only the lower bound for the speed of relaxation in  $\text{WS}_2$  and  $\text{WSe}_2$ . The introduction of a dielectric environment through a substrate or full encapsulation, will have two main effects on the calculated relaxation times. First, the electric potential induced by the LO phonon will be reduced in the long wavelength limit by the dielectric constant of the environment  $\epsilon_e$ , therefore reducing the LO phonon coupling by a factor of  $\epsilon_e^{-6}$ . The HP phonon mode on the other hand will not be affected in such a way, as its coupling mechanism does not involve an electric field. Second, carriers in the TMDC monolayer can emit phonons in the substrate, thus increasing the total scattering rate. The obtained fast carrier cooling rates and the subsequent formation of excitons which can radiatively recombine and emit light, can lead to high quantum efficiencies, crucial for the range of optoelectronics device applications utilizing TMDCs, including light emitters, photodetectors, and novel valleytronic devices.

## ACKNOWLEDGMENT

The author would like to thank M. Calandra, T. Heinz, K. Novoselov, M. Potemski, A. Tartakovskii, and V. Zólyomi for useful discussions.

## REFERENCES

- [1] D. Jariwala, V. K. Sangwan, L. J. Lauhon, T. J. Marks, and M. C. Hersam, "Emerging device applications for semiconducting two-dimensional transition metal dichalcogenides," *ACS Nano*, vol. 8, no. 2, pp. 1102–1120, 2014. [Online]. Available: <http://dx.doi.org/10.1021/nn500064s>
- [2] Q. H. Wang, K. Kalantar-Zadeh, A. Kis, J. N. Coleman, and M. S. Strano, "Electronics and optoelectronics of two-dimensional transition metal dichalcogenides," *Nature Nanotechnol.*, vol. 7, no. 11, pp. 699–712, 2012. [Online]. Available: <http://dx.doi.org/10.1038/nnano.2012.193>
- [3] A. Chernikov *et al.*, "Exciton binding energy and nonhydrogenic rydberg series in monolayer  $\text{ws}_2$ ," *Phys. Rev. Lett.*, vol. 113, Aug. 2014, Art. no. 076802. [Online]. Available: <http://link.aps.org/doi/10.1103/PhysRevLett.113.076802>
- [4] X. Xu, W. Yao, D. Xiao, and T. F. Heinz, "Spin and pseudospins in layered transition metal dichalcogenides," *Nature Nanotechnol.*, vol. 10, no. 5, pp. 343–350, 2014. [Online]. Available: <http://dx.doi.org/10.1038/nphys2942>
- [5] K. F. Mak, K. He, J. Shan, and T. F. Heinz, "Control of valley polarization in monolayer  $\text{mos}_2$  by optical helicity," *Nature Nanotechnol.*, vol. 7, no. 8, pp. 494–498, 2012. [Online]. Available: <http://dx.doi.org/10.1038/nnano.2012.96>
- [6] D. Xiao, G.-B. Liu, W. Feng, X. Xu, and W. Yao, "Coupled spin and valley physics in monolayers of  $\text{mos}_2$  and other group-vi dichalcogenides," *Phys. Rev. Lett.*, vol. 108, p. 196802, May. 2012. [Online]. Available: <http://link.aps.org/doi/10.1103/PhysRevLett.108.196802>
- [7] G. Sallen *et al.*, "Robust optical emission polarization in  $\text{mos}_2$  monolayers through selective valley excitation," *Phys. Rev. B*, vol. 86, Aug. 2012, Art. no. 081301. [Online]. Available: <http://link.aps.org/doi/10.1103/PhysRevB.86.081301>
- [8] T. Cao *et al.*, "Valley-selective circular dichroism of monolayer molybdenum disulphide," *Nature Commun.*, vol. 3, 2012, Art. no. 887. [Online]. Available: <http://dx.doi.org/10.1038/ncomms1882>
- [9] H. Zeng, J. Dai, W. Yao, D. Xiao, and X. Cui, "Valley polarization in  $\text{mos}_2$  monolayers by optical pumping," *Nature Nanotechnol.*, vol. 7, no. 8, pp. 490–493, 2012. [Online]. Available: <http://dx.doi.org/10.1038/nnano.2012.95>
- [10] A. K. Geim and I. V. Grigorieva, "Van der waals heterostructures," *Nature*, vol. 499, no. 7459, pp. 419–425, Jul. 2013. [Online]. Available: <http://dx.doi.org/10.1038/nature12385>
- [11] A. Kormányos *et al.*, "k dot p theory for two-dimensional transition metal dichalcogenide semiconductors," *2D Mater.*, vol. 2, no. 2, 2015, Art. no. 022001.
- [12] H. Dery and Y. Song, "Polarization analysis of excitons in monolayer and bilayer transition-metal dichalcogenides," *Phys. Rev. B*, vol. 92, Sep. 2015, Art. no. 125431. [Online]. Available: <http://link.aps.org/doi/10.1103/PhysRevB.92.125431>
- [13] Z. Jin, X. Li, J. T. Mullen, and K. W. Kim, "Intrinsic transport properties of electrons and holes in monolayer transition-metal dichalcogenides," *Phys. Rev. B*, vol. 90, Jul. 2014, Art. no. 045422. [Online]. Available: <http://link.aps.org/doi/10.1103/PhysRevB.90.045422>
- [14] X. Li *et al.*, "Intrinsic electrical transport properties of monolayer silicene and  $\text{mos}_2$  from first principles," *Phys. Rev. B*, vol. 87, Mar. 2013, Art. no. 115418. [Online]. Available: <http://link.aps.org/doi/10.1103/PhysRevB.87.115418>
- [15] L. Zeng *et al.*, "Phonon-limited electron mobility in single-layer  $\text{mos}_2$ ," *Chinese Physics Letters*, vol. 31, 2012, Art. no. 027391.
- [16] M. Calandra, private communication.
- [17] V. Zólyomi, unpublished.
- [18] K. Kaasbjerg, K. S. Thygesen, and K. W. Jacobsen, "Phonon-limited mobility in n-type single-layer  $\text{mos}_2$  from first principles," *Phys. Rev. B*, vol. 85, Mar. 2012. [Online], Art. no. 115317. Available: <http://link.aps.org/doi/10.1103/PhysRevB.85.115317>
- [19] G.-B. Liu, D. Xiao, X. Xu, and W. Yao, "Electronic structures and theoretical modelling of two-dimensional group-vib transition metal dichalcogenides," *Chem. Soc. Rev.*, vol. 44, pp. 2643–2663, 2015. [Online]. Available: <http://dx.doi.org/10.1039/C4CS00301B>
- [20] H. Zeng and X. Cui, "An optical spectroscopic study on two-dimensional group-vi transition metal dichalcogenides," *Chem. Soc. Rev.*, vol. 44, pp. 2629–2642, 2015.
- [21] T. C. Berkelbach, M. S. Hybertsen, and D. R. Reichman, "Theory of neutral and charged excitons in monolayer transition metal dichalcogenides," *Phys. Rev. B*, vol. 88, Jul. 2013, Art. no. 045318. [Online]. Available: <http://link.aps.org/doi/10.1103/PhysRevB.88.045318>
- [22] S. Baroni, S. de Gironcoli, A. Dal Corso, and P. Giannozzi, "Phonons and related crystal properties from density-functional perturbation theory," *Rev. Mod. Phys.*, vol. 73, pp. 515–562, Jul. 2001. [Online]. Available: <http://link.aps.org/doi/10.1103/RevModPhys.73.515>
- [23] S. J. Clark *et al.*, "First principles methods using castep," *Z. Kristallogr.*, vol. 220, 2005, Art. no. 567. [Online]. Available: <http://www.degruyter.com/view/j/zkri.2005.220.issue-5-6-2005/zkri.220.5.567.65075/zkri.220.5.567.65075.xml>
- [24] K. Refson, P. R. Tulip, and S. J. Clark, "Variational density-functional perturbation theory for dielectrics and lattice dynamics," *Phys. Rev. B*, vol. 73, Apr. 2006, Art. no. 155114. [Online]. Available: <http://link.aps.org/doi/10.1103/PhysRevB.73.155114>
- [25] X. Gonze and C. Lee, "Dynamical matrices, born effective charges, dielectric permittivity tensors, and interatomic force constants from density-functional perturbation theory," *Phys. Rev. B*, vol. 55, pp. 10 355–10 368, Apr. 1997. [Online]. Available: <http://link.aps.org/doi/10.1103/PhysRevB.55.10355>

<sup>6</sup>For example, full encapsulation by hexagonal Boron Nitride results in [30]  $\epsilon_e = \sqrt{\epsilon_{\perp}\epsilon_{||}} \approx 4.4$ .

- [26] X. Gonze, "First-principles responses of solids to atomic displacements and homogeneous electric fields: Implementation of a conjugate-gradient algorithm," *Phys. Rev. B*, vol. 55, pp. 10 337–10 354, Apr. 1997. [Online]. Available: <http://link.aps.org/doi/10.1103/PhysRevB.55.10337>
- [27] J. P. Perdew, K. Burke, and M. Ernzerhof, "Generalized gradient approximation made simple," *Phys. Rev. Lett.*, vol. 77, pp. 3865–3868, Oct. 1996. [Online]. Available: <http://link.aps.org/doi/10.1103/PhysRevLett.77.3865>
- [28] B. Ganchev, N. Drummond, I. Aleiner, and V. Fal'ko, "Three-particle complexes in two-dimensional semiconductors," *Phys. Rev. Lett.*, vol. 114, Mar. 2015, Art. no. 107401. [Online]. Available: <http://link.aps.org/doi/10.1103/PhysRevLett.114.107401>
- [29] J.-Z. Zhang, A. Dyson, and B. K. Ridley, "Momentum relaxation due to polar optical phonons in algan/gan heterostructures," *Phys. Rev. B*, vol. 84, Oct. 2011, Art. no. 155310. [Online]. Available: <http://link.aps.org/doi/10.1103/PhysRevB.84.155310>
- [30] A. Principi *et al.*, "Plasmon losses due to electron-phonon scattering: The case of graphene encapsulated in hexagonal boron nitride," *Phys. Rev. B*, vol. 90, Oct. 2014, Art. no. 165408. [Online]. Available: <http://link.aps.org/doi/10.1103/PhysRevB.90.165408>

**Mark Danovich** received the B.Sc. degree and the M.Sc. degree in 2014 from the Hebrew University of Jerusalem, Jerusalem, Israel. He is currently working toward the Ph.D. degree in physics at the National Graphene Institute, University of Manchester, Manchester, U.K.

**Igor L. Aleiner** received the Ph.D. degree from the University of Minnesota, Minneapolis, MN, USA, in 1996. He was a Research Scientist at Nippon Electric Corporation Research Institute, Princeton, NJ, USA, and at the State University of New York, New York, NY, USA. He is currently with the Department of Physics, Columbia University, New York.

**Neil D. Drummond** received the Ph.D. degree from Cambridge University, Cambridge, U.K. He is currently with the Department of Physics, Lancaster University, Lancaster, U.K.

**Vladimir I. Fal'ko** received the Ph.D. degree from the Institute for Solid State Physics, Russian Academy of Sciences, Chernogolovka, Russia. He was at the Max-Planck-Institut, Stuttgart, Germany, Oxford University, Oxford, U.K., and Lancaster University, Lancaster, U.K. He is currently the Research Director at the National Graphene Institute, University of Manchester, Manchester, U.K.

### 3.3 Auger recombination of dark excitons in WS<sub>2</sub> and WSe<sub>2</sub> monolayers

The results presented in this section are reported in the publication [38]: “Auger recombination of dark excitons in WS<sub>2</sub> and WSe<sub>2</sub>”, 2016, *2D Materials*, **3**, 035011.

My contribution to this work: Performed all rates calculations, performed the DFT calculations of band structures, obtained the character table for the extended group  $C_{3v}''$ , prepared figures, analysed the results, and wrote the manuscript.

Full author list: M. Danovich, V. Zólyomi, V. I. Fal'ko, I. L. Aleiner. Author contributions: V.Z. performed the DFT calculation for the Auger matrix element, I.A. contributed to the symmetry analysis of the phonons, V.F. and I.A. contributed to writing of the paper and discussions.

## 2D Materials



### PAPER

#### OPEN ACCESS

RECEIVED  
1 July 2016

REVISED  
26 July 2016

ACCEPTED FOR PUBLICATION  
2 August 2016

PUBLISHED  
17 August 2016

# Auger recombination of dark excitons in WS<sub>2</sub> and WSe<sub>2</sub> monolayers

Mark Danovich<sup>1</sup>, Viktor Zólyomi<sup>1</sup>, Vladimir I Fal'ko<sup>1</sup> and Igor L Aleiner<sup>2</sup>

<sup>1</sup> National Graphene Institute, University of Manchester, Booth St E, Manchester M13 9PL, UK

<sup>2</sup> Physics Department, Columbia University, New York, NY 10027, USA

E-mail: [mark.danovich@postgrad.manchester.ac.uk](mailto:mark.danovich@postgrad.manchester.ac.uk)

**Keywords:** Auger recombination, excitons, TMDCs

Original content from this work may be used under the terms of the Creative Commons Attribution 3.0 licence.

Any further distribution of this work must maintain attribution to the author(s) and the title of the work, journal citation and DOI.



### Abstract

We propose a novel phonon assisted Auger process unique to the electronic band structure of monolayer transition metal dichalcogenides (TMDCs), which dominates the radiative recombination of ground state excitons in tungsten based TMDCs. Using experimental and density functional theory computed values for the exciton energies, spin-orbit splittings, optical matrix element, and the Auger matrix elements, we find that the Auger process begins to dominate at carrier densities as low as  $10^{9-10} \text{ cm}^{-2}$ , thus providing a plausible explanation for the low quantum efficiencies reported for these materials.

Recently, there was an expansive interest in monolayer transition metal dichalcogenides (TMDCs) due to their potential in optoelectronic applications [1–3]. In contrast to bulk TMDC crystals, the monolayers of MoS<sub>2</sub>, MoSe<sub>2</sub>, WS<sub>2</sub>, and WSe<sub>2</sub> are direct band semiconductors. Contrary to III–V semiconductors, in these hexagonal 2D crystals the conduction (*c*) and valence (*v*) bands edges are at the *K*/*K'* points of the Brillouin zone (BZ) rather than at the  $\Gamma$ -point. Several experiments have already demonstrated a strong light-matter interaction in these 2D crystals [4].

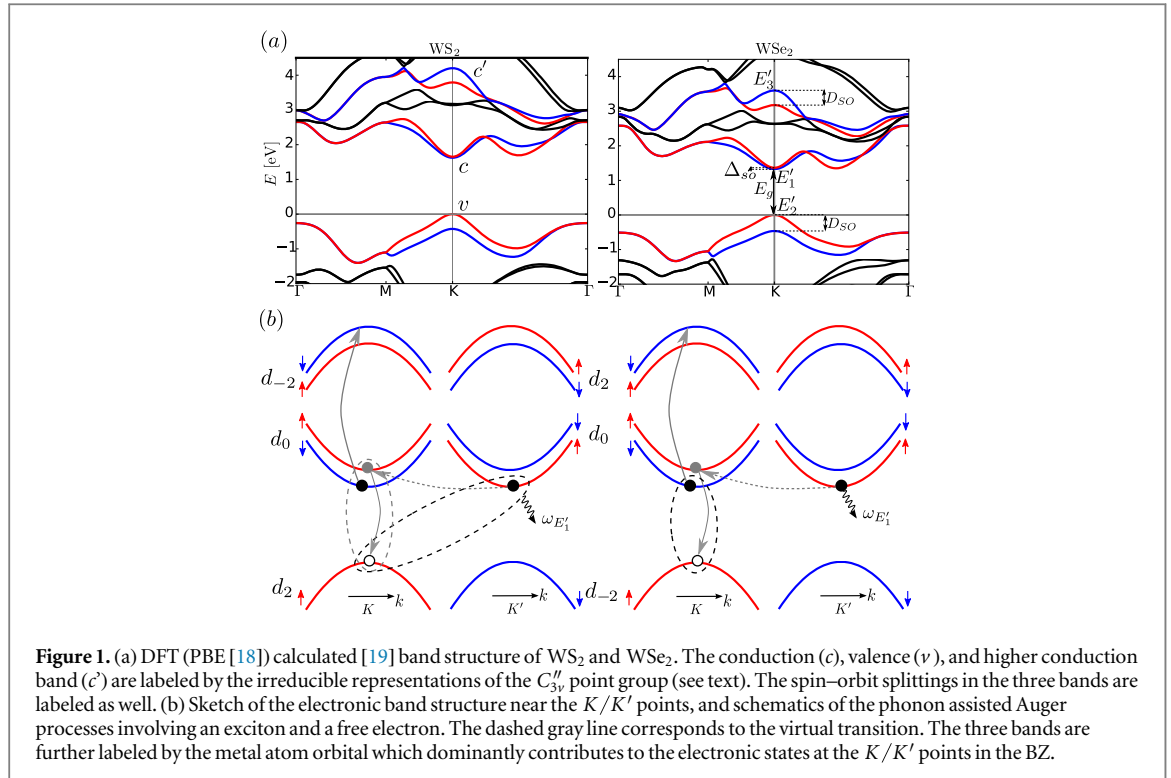
Potentially practical implementations of these TMDC atomic crystals in optoelectronic devices require high quantum efficiency (defined as the ratio of emitted to absorbed photons) of the optical process. The quantum efficiency depends on various external parameters such as the temperature, sample quality, excitation power, doping, and the specific material. However, despite the recent progress in improving the quality of 2D TMDCs, the quantum efficiencies observed in photoluminescence experiments [5–9] for the different materials were: for MoS<sub>2</sub>,  $\sim 10^{-3}$  [5, 9],  $\sim 10^{-4}$  [8] at room temperature, and for WS<sub>2</sub> and WSe<sub>2</sub>,  $\sim 10^{-2}$  at 10 K [8]. Such systematically low quantum efficiencies call for finding the mechanism responsible for the non-radiative recombination of electron-hole pairs, excitons, or trions. Previous theoretical and experimental works have suggested exciton-exciton annihilation [10–15] for exciton densities above  $\sim 10^{10} \text{ cm}^{-2}$ , exciton capture by defects [9, 16], and phonon scattering [17] as possible non-

radiative mechanisms for excitons in these materials. Here, we show that there exists a phonon assisted Auger recombination process illustrated in figure 1, which is specific for 2D TMDC semiconductors. By explicit comparison of the phonon assisted radiative recombination rate of ground state excitons in monolayers of WS<sub>2</sub> and WSe<sub>2</sub> with the rate due to the suggested Auger mechanism, we find that the latter starts dominating at electron densities as low as  $10^{9-10} \text{ cm}^{-2}$ . The specific band structure of 2D TMDCs defies the common wisdom (based on III–V semiconductors studies) that the 2D confinement quenches Auger recombination processes. Namely, electrons from the vicinity of the conduction band (*c*) edge, can undergo a transition into one of the higher bands (*c'* in figure 1) which is almost in resonance with the exciton annihilation. Both *c* and *c'* bands are comprised of d-orbitals of the same metal atom, facilitating the Auger transition.

The electron band structure near the corners of the BZ is described by

$$\hat{H}_0 = \sum_{\nu\sigma\tau} \int d^2\vec{r} \Psi_{\nu\sigma\tau}^\dagger \epsilon_{\nu\sigma\tau} (-i\hbar \nabla) \Psi_{\nu\sigma\tau}, \quad (1)$$

where  $\nu = v, c, c'$ ,  $\sigma = \pm(\uparrow, \downarrow)$ , and  $\tau = \pm(K, K')$ . With reference to the band structure shown in figure 1, the relevant spectrum of electrons in the vicinity of the BZ corners can be described using the effective mass approximation as  $\epsilon_\nu = E_{\nu\sigma\tau} + \frac{\hbar^2 k^2}{2m_\nu}$ . Here we count energies from the *v* band edge and  $E_v = -\frac{D_{SO}}{2}(1 - \tau\sigma)$ , with  $m_v < 0$ . For the



conduction bands we use  $E_c = E_g + \frac{\Delta_{\text{SO}}}{2}(1 + \tau\sigma)$ , and  $E_{c'} = 2E_g + \Upsilon - \frac{D_{\text{SO}}}{2}(1 + \tau\sigma)$ , with  $m_{c'} < 0$ . Due to mirror plane symmetry ( $\sigma_h$ ) of 2D TMDCs, the electron spin projection on to the  $z$ -axis normal to the plane  $\sigma$ , is a good quantum number. The signs of spin-orbit splittings in  $E_c$  reflect the inverted order of spin-split states in  $c$  and  $v$  bands specific to tungsten based TMDCs [20–22] (in contrast to their molybdenum counterparts). This results in a ground state exciton/trion which is dark due to spin and momentum conservation constraints [23–25], requiring emission of  $K$ -point phonons for recombination. At low temperatures the bright excitons population will be small compared to the dark excitons, requiring an activation of the  $c$  band spin-orbit splitting energy  $\Delta_{\text{SO}}$ , which results in increased photoluminescence at higher temperatures as observed in some experiments [23].

To classify suitable options for the radiative and non-radiative transitions in 2D  $\text{WS}_2$  and  $\text{WSe}_2$ , we analyze its symmetry group and write down the corresponding terms in the Hamiltonian. The point group of 2D TMDCs is  $D_{3h}$ , which is a direct product group,  $C_{3v} \otimes \sigma_h$ , where  $\sigma_h$  is the horizontal mirror reflection. The states belonging to the  $v$ ,  $c$ , and  $c'$  bands near the  $K/K'$ -points are composed of the  $d_0$ ,  $d_2$  and  $d_{-2}$  metal orbitals which posses  $z \rightarrow -z$  symmetry [21], and therefore belong to the identity irreducible representation (IrRep) of  $\sigma_h$ . As a result, we can focus on the point group  $C_{3v}$  for the classification of the electronic states into IrReps, as well as the classification of phonon modes coupling to the electrons states. Since

**Table 1.** Character table for the irreducible representations (IrRep) of the extended point group  $C_{3v}''$ , and their correspondence to the relevant fermionic and bosonic fields, and dark excitons.

$C_{3v}''$	$E$	$t, t^2$	$2C_3$	$9\sigma_v$	$2tC_3$	$2t^2C_3$	
$A_1$	1	1	1	1	1	1	
$A_2$	1	1	1	-1	1	1	
$E$	2	2	-1	0	-1	-1	$(\mathcal{E}_x, \mathcal{E}_y)$ , intravalley $X_E$
$E'_1$	2	-1	-1	0	2	-1	$\Psi_c$
$E'_2$	2	-1	2	0	-1	-1	$\Psi_v$
$E'_3$	2	-1	-1	0	-1	2	$\Psi_{c'}, \text{inter-valley } X_{E'_3}$
$D_{xy}$	12	0	0	0	-3	-3	Phonons
$D_z$	3	0	0	1	3	0	$b$

the states at the  $K$  and  $K'$ -points are degenerate, it is advantageous to treat them simultaneously. This is achieved by tripling the unit cell, resulting in a three times smaller BZ in which the  $K$  and  $K'$  points are folded into the  $\Gamma$ -point [26]. Tripling of the unit cell is achieved by factoring out two translations from the space group of the crystal resulting in the new point group  $C_{3v}'' = C_{3v} + tC_{3v} + t^2C_{3v}$ , where  $t$  denotes translation by a lattice vector, and  $t^3 = 1$ . The character table of the new point group containing 18 elements and 6 IrReps is given in table 1. In the same table we list the electron and photon fields corresponding to the IrReps. The decomposition of the direct products of IrReps is shown in table 2.

Using table 1 one can write down the Hamiltonian for the interaction of the electrons with light [27, 28],

**Table 2.** Product table for the irreducible representations of the extended point group  $C_{3v}''$ .

$C_{3v}''$	$A_1$	$A_2$	$E$	$E'_1$	$E'_2$	$E'_3$
$A_1$	$A_1$	$A_2$	$E$	$E'_1$	$E'_2$	$E'_3$
$A_2$	$A_2$	$A_1$	$E$	$E'_1$	$E'_2$	$E'_3$
$E$	$E$	$E$	$A_1 \oplus A_2 \oplus E$	$E'_1 \oplus E'_3$	$E'_1 \oplus E'_3$	$E'_1 \oplus E'_2$
$E'_1$	$E'_1$	$E'_1$	$E'_2 \oplus E'_3$	$A_1 \oplus A_2 \oplus E'_1$	$E \oplus E'_3$	$E \oplus E'_2$
$E'_2$	$E'_2$	$E'_2$	$E'_1 \oplus E'_3$	$E \oplus E'_3$	$A_1 \oplus A_2 \oplus E'_2$	$E \oplus E'_1$
$E'_3$	$E'_3$	$E'_3$	$E'_1 \oplus E'_2$	$E \oplus E'_2$	$E \oplus E'_1$	$A_1 \oplus A_2 \oplus E'_3$

$$H_r = \frac{e\hbar\nu}{E_g} \sum_{\sigma,\tau} \int d^2\vec{r} \Psi_{c\sigma\tau}^\dagger \Psi_{v\sigma\tau} (\mathcal{E}_x + i\tau\mathcal{E}_y) + \text{h.c.}, \quad (2)$$

where  $e$  is the electron charge,  $\nu$  is the velocity originating from the off-diagonal momentum matrix element, and  $\vec{\mathcal{E}}$  is the electric field of light. We note that for the excitons,  $\Psi_c^\dagger(\vec{r}_1)\Psi_v(\vec{r}_2) \rightarrow X^\dagger(\vec{R})\phi(\vec{r}_1 - \vec{r}_2)$ , where  $\vec{R}$  is the center-of-mass position of the exciton, and  $\phi(\vec{r}_1 - \vec{r}_2)$  is the electron and hole relative motion wavefunction. All possible states of the exciton boson operator  $X$ , can be further classified according to the IrReps. The dark and bright excitonic states transform according to the direct product representation of the  $c$  and  $v$  band states  $E'_1 \otimes E'_2 = E \oplus E'_3$ . The excitons can further be classified according to the spin projection  $S_z$ . Due to conservation of spin, the bright state must have  $S_z = 0$ , which corresponds to the excited state transforming according to the  $E$  IrRep, and only such a combination enters into equation (2). The  $(E'_3, S_z = 0)$  states are the intervalley excitons that are dark due to the momentum mismatch. However, these states can radiatively recombine with the help of phonon emission. According to table 2, this can be provided by phonons from  $E'_1$  and  $E'_2$  IrReps. The other exciton doublets,  $(E, |S_z| = 1)$  and  $(E'_3, |S_z| = 1)$ , are absolutely dark due to spin conservation ( $\sigma_h$  reflection changes the sign of the spin projection  $S_z$ ). According to the sign of the spin-orbit splitting in the  $c$  band (see text after equation (1)),  $(E'_3, S_z = 0)$  and  $(E, |S_z| = 1)$  are the exciton ground states. Therefore, the decay of these states is the bottleneck for the PL. In this case the PL quantum efficiency is determined by the ratio of the radiative and non-radiative Auger rates.

The Auger process is caused by the electron-electron scattering with momentum transfer of the order of inverse lattice constant, therefore in the effective mass approximation it is described by a contact interaction. Table 2 shows that the only combination allowed by symmetry is

$$H_c = \frac{\alpha\hbar^2}{m_{c'}} \sum_{\sigma,\tau} \int d^2\vec{r} (\Psi_{v\sigma}^\dagger \Psi_{c'-\sigma}^\dagger \Psi_{c-\sigma} \Psi_{c\sigma}) \vec{r}_\tau + \text{h.c..} \quad (3)$$

Here,  $\alpha$  is a dimensionless parameter computed from the matrix element of the Coulomb interaction in the basis of the density functional theory (DFT) wavefunctions (see table 3). Also, the only allowed Auger process

involves all carriers in the same valley<sup>3</sup>. This implies that at low temperatures due to the exclusion principle, the additional electron must come through phonon emission from the opposite valley.

According to table 2, the initial dark state exciton ( $E'_3, S_z = 0$ ) and the electron ( $E'_1$ ) direct product does not include the final state  $c'$  state  $E'_3$ , making the direct process impossible, hence requiring an extra phonon in the final state. Using table 2, one finds that this additional phonon in the final state should be the same  $\sigma_h$  symmetric ( $E'_1$  or  $E'_2$ ) as involved in the radiative process, allowing the direct comparison of the radiative and Auger rates without relying on the knowledge of the strength of the electron-phonon interaction constants<sup>4</sup>. To consider the electron-phonon interaction only on symmetry grounds, we list in table 1 the representations corresponding to the in-plane  $D_{xy}$ , and out of plane  $D_z$  modes in the tripled unit cell, which is needed to describe all  $\sigma_h$  symmetric phonon modes in the  $\Gamma$  and  $K$  points. From the decomposition  $D_{xy} = 2E \oplus E'_1 \oplus 2E'_2 \oplus E'_3$  and  $D_z = A_1 \oplus E'_1$ , we conclude that the existence and number of modes needed to facilitate the processes described are protected by symmetry. To mention, in our earlier studies[29] we noticed that the coupling of  $c$  band electrons with the homopolar phonon mode  $A_1$  is very strong, which hints that the  $E'_1$  mode of  $D_z$  would be the most relevant for the process.

The Hamiltonian describing the  $E'_1$  phonon and its interaction with the  $c$  band electrons

$$H_{ph} = \hbar\omega \sum_\tau \int d^2\vec{r} b_\tau^\dagger(\vec{r}) b_\tau(\vec{r}) + g \sum_{\sigma,\tau} \int d^2\vec{r} (\Psi_{c\sigma\tau}^\dagger \Psi_{c\sigma-\tau} b_\tau^\dagger + \text{h.c.}), \quad (4)$$

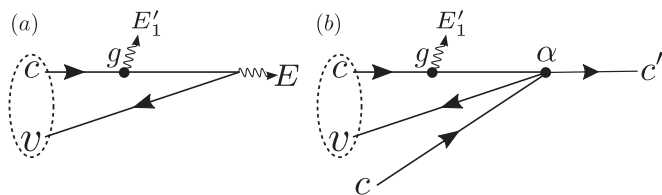
where  $b(r)$  is the phonon operator in mode  $E'_1$  with energy  $\hbar\omega$ , and  $g$  is the coupling coefficient. The rates were calculated using the Fermi Golden rule applied to the Feynman amplitudes shown in figure 2. The

<sup>3</sup> The initial state consisting of two electrons in the  $c$  band has the decomposition  $E'_1 \otimes E'_1 = A_1 \oplus A_2 \oplus E'_1$ , and the final state with one electron in the  $v$  band and the other electron in the  $c'$  band transform according to  $E'_2 \otimes E'_3 = E \oplus E'_1$ . The common IrRep is  $E'_1$  which corresponds to the states with both initial and final state carriers residing in the same valley.

<sup>4</sup> The process involving the emission of an  $E'_2$  phonon mode, which couples to the hole, involves the hole scattering into the lower spin-split  $v$  band which results in the appearance of the large  $D_{SO}$  spin-orbit splitting in the denominator of the rates. Therefore, we neglect the contribution of the  $E'_2$  phonon assisted process to the total rates.

**Table 3.** Material parameters used for the rates calculation.

	$\frac{m_c}{m}$	$\frac{m_v}{m}$	$\frac{m_{c'}}{m}$	$\Delta_{SO}$ (meV)	$D_{SO}$ (eV)	$E_g$ (eV)	$\Upsilon$ (eV)	$\frac{v}{c}$	$\alpha$
WS <sub>2</sub>	0.26	-0.35	-0.39	30	0.42	2.0	0.6	$1.7 \times 10^{-3}$	0.5
WSe <sub>2</sub>	0.28	-0.36	-0.35	38	0.46	1.7	0.6	$1.6 \times 10^{-3}$	0.6

<sup>a</sup> [20]<sup>b</sup> [28]**Figure 2.** Diagrams for the calculation of quantum mechanical amplitudes for the (a) phonon assisted radiative process, and (b) phonon assisted Auger process.

radiative rate (with photon line shifted down by  $\hbar\omega$  from the dark exciton energy) is given by

$$\frac{1}{\tau_{r, X_{E'_1}}} = \frac{8E_g e^2}{3\hbar} \left(\frac{v}{c}\right)^2 \frac{|\phi(0)|^2 g^2}{(\Delta_{SO} + \hbar\omega)^2} \quad (5)$$

and the non-radiative rates by

$$\frac{1}{\tau_{A, X}} = \frac{E_g}{\hbar} \frac{\hbar^2 n_e}{|m_{c'}| E_g} \frac{\alpha^2 |\phi(0)|^2 g^2}{[\Delta_{SO} + \hbar\omega + \xi_X]^2}, \quad (6)$$

where  $n_e$  is the electron density, and  $\xi_X = \frac{|m_{c'}|}{|m_v| + m_c} Y$  for  $X = X_{E'_1}$ , and  $\xi_X = \frac{|m_{c'}|}{m_c} \Upsilon$  for  $X = X_{E_1}$ .<sup>5</sup>

Taking the ratio of the Auger and radiative rates we obtain

$$\frac{\tau_{r, X_{E'_1}}}{\tau_{A, X_{E'_1}}} = \frac{n_e}{n_e^*}, \quad (7)$$

where the characteristic density is given by

$$n_e^* = \frac{8|m_{c'}| E_g}{3\hbar^2} \left(\frac{v}{\alpha c}\right)^2 \left(\frac{e^2}{\hbar c}\right) \left(1 + \frac{|m_v| + m_c}{\Delta_{SO} + \hbar\omega}\right)^2. \quad (8)$$

We emphasize that the latter equation does not involve the unknown electron–phonon coupling constant. Therefore, we can estimate the values of  $n_e^*$  for WS<sub>2</sub> and WSe<sub>2</sub> based on the parameters of these 2D crystals found in DFT and the experimentally known  $E_g$  listed in table 3

$$n_e^*(WS_2) \sim 10^{10} \text{ cm}^{-2}, n_e^*(WSe_2) \sim 4 \times 10^9 \text{ cm}^{-2}. \quad (9)$$

These electron concentrations which determine the threshold for efficient photoluminescence are remarkably low. This suggests that the proposed mechanism of Auger recombination dominates over the radiative recombination for all realistic structures.

## Acknowledgments

The authors thank T Heinz, M Potemski and A Tartakovski for discussions. This work was supported by Simons Foundation (IA), ERC Synergy Grant Hetero2D (VF,MD), EC-FET European Graphene Flagship (VF,VZ), EPSRC grant EP/N010345/1 (VF).

## References

- [1] Jariwala D, Sangwan V K, Lauhon L J, Marks T J and Hersam M C 2014 *ACS Nano* **8** 1102–20
- [2] Wang Q H, Kalantar-Zadeh K, Kis A, Coleman J N and Strano M S 2012 *Nat. Nanotechnol.* **7** 699–712
- [3] Cao T *et al* 2012 *Nat. Commun.* **3** 887
- [4] Liu X, Galfsky T, Sun Z, Xia F, Lin E c, Lee Y H, Kéna-Cohen S and Menon V M 2015 *Nat. Photon.* **9** 30–4

- [5] Mak K F, Lee C, Hone J, Shan J and Heinz T F 2010 *Phys. Rev. Lett.* **105** 136805
- [6] Splendiani A, Sun L, Zhang Y, Li T, Kim J, Chim C Y, Galli G and Wang F 2010 *Nano Lett.* **10** 1271–5
- [7] Wang H, Zhang C and Rana F 2015 *Nano Lett.* **15** 339–45
- [8] Ye Y, Wong Z J, Lu X, Ni X, Zhu H, Chen X, Wang Y and Zhang X 2015 *Nat. Photon.* **9** 733–7
- [9] Wang H, Zhang C and Rana F 2015 *Nano Lett.* **15** 339–45
- [10] Mouri S, Miyauchi Y, Toh M, Zhao W, Eda G and Matsuda K 2014 *Phys. Rev. B* **90** 155449
- [11] Yu Y, Yu Y, Xu C, Barrette A, Gundogdu K and Cao L 2016 *Phys. Rev. B* **93** 201111
- [12] Yuan L and Huang L 2015 *Nanoscale* **7** 7402–8
- [13] Sun D, Rao Y, Reider G A, Chen G, You Y, Brézin L, Harutyunyan A R and Heinz T F 2014 *Nano Lett.* **14** 5625–9
- [14] Kumar N, Cui Q, Ceballos F, He D, Wang Y and Zhao H 2014 *Phys. Rev. B* **89** 125427
- [15] Konabe S and Okada S 2014 *Phys. Rev. B* **90** 155304
- [16] Wang H, Strait J H, Zhang C, Chan W, Manolatou C, Tiwari S and Rana F 2015 *Phys. Rev. B* **91** 165411
- [17] Selig M, Berghäuser G, Raja A, Nagler P, Schüller C, Heinz T F, Korn T, Chernikov A, Malic E and Knorr A 2016 Excitonic linewidth and coherence lifetime in monolayer transition metal dichalcogenides arXiv:1605.03359
- [18] Perdew J P, Burke K and Ernzerhof M 1996 *Phys. Rev. Lett.* **77** 3865–8
- [19] Giannozzi P *et al* 2009 *J. Phys.: Condens. Matter* **21** (19pp) 395502
- [20] Kormnyos A, Burkard G, Gmitra M, Fabian J, Zolyomi V, Drummond N D and Fal'ko V 2015 *2D Mater.* **2** 022001
- [21] Liu G B, Xiao D, Yao Y, Xu X and Yao W 2015 *Chem. Soc. Rev.* **44** 2643–63
- [22] Echeverry J P, Urbaszek B, Amand T, Marie X and Gerber I C 2016 *Phys. Rev. B* **93** 121107
- [23] Zhang X X, You Y, Zhao S Y F and Heinz T F 2015 *Phys. Rev. Lett.* **115** 257403
- [24] Dery H and Song Y 2015 *Phys. Rev. B* **92** 125431
- [25] Yu H, Cui X, Xu X and Yao W 2015 *Natl. Sci. Rev.* **2** 57–70
- [26] Basko D M 2008 *Phys. Rev. B* **78** 125418
- [27] Esser A, Runge E, Zimmermann R and Langbein W 2000 *Phys. Rev. B* **62** 8232–9
- [28] Palummo M, Bernardi M and Grossman J C 2015 *Nano Lett.* **15** 2794–800
- [29] Danovich M, Aleiner I L, Drummond N D and Falko V I 2016 *IEEE J. Sel. Top. Quantum Electron.* **1–1** ISSN 1077-260X
- [30] Chernikov A, Berkelbach T C, Hill H M, Rigosi A, Li Y, Aslan O B, Reichman D R, Hybertsen M S and Heinz T F 2014 *Phys. Rev. Lett.* **113** 076802
- [31] Sohier T, Calandra M and Mauri F 2016 Two-dimensional fröhlich interaction in transition-metal-dichalcogenides monolayers: theoretical modeling and first-principles calculations arXiv:1605.08207
- [32] Jin Z, Li X, Mullen J T and Kim K W 2014 *Phys. Rev. B* **90** 045422

# Chapter 4

## Bound complexes in monolayer TMDCs

### 4.1 Introduction

Understanding the optical spectra of monolayer TMDCs, as interpreted in terms of excitons, trions and biexcitons has recently become an issue due to the demonstration that ground-state excitons in  $\text{WS}_2$  and  $\text{WSe}_2$  are dark, as well as a disagreement between theory and experiment on the classification of the optical spectra in particular for the biexciton lines. The two types of spin-orbit splitting in Molybdenum and Tungsten based monolayer TMDCs, together with the time reversal related  $K$  and  $K'$  valleys at the corners of the Brillouin zone, result in a variety of possible complexes with different optical activity, giving a rich temperature and doping dependent spectra. In order to gain a proper understanding of the observed spectra in the two kinds of monolayer TMDCs, a classification of the various complexes into their optical activity, calculation of their binding energies, and prediction on the resulting photon energies are required.

The dark ground state negatively charged excitons (trions) and neutral biexcitons in  $\text{WS}_2$ ,  $\text{WSe}_2$  consist of electrons in the two opposite  $K, K'$  valleys with opposite out-of-plane spin projections, and holes in the top valence band residing in one (for trions) or both valleys (for excitons), making them dark due to both spin and momentum conservation preventing the emission of light. In the work presented in 4.2, we analyse a novel mechanism for the radiative recombination of these complexes and answer

questions regarding the recombination rates, position of the lines, and line shapes. This mechanism involves an intervalley electron-electron scattering, which mixes the dark ground states with the bright states of complexes composed of the electrons in the upper spin-orbit split bands, thus transferring optical oscillator strength to the dark states. In the proposed theory, we produce a microscopic *ab-initio* model for this process and use it to estimate radiative lifetimes of these "semidark" excitonic species, and their signatures in the temperature dependent photoluminescence as compared to the bright complexes. In particular, the difference between the initial and final state carriers result in a red-shift of the emission line as compared to the corresponding excited bright complexes. Finally, these complexes being in the ground state, are expected to be particularly dominant at low temperatures.

In the work presented in 4.3 we provide a detailed classification of the excitons, trions and biexcitons in  $\text{MoX}_2$  and  $\text{WX}_2$  type TMDCs according to the optical activity, and activation behaviour as determined by the spin-orbit splitting. Using group theory arguments we demonstrate the coupling of the dark exciton ground state in  $\text{WS}_2/\text{WSe}_2$  due to spin mismatch, to an out-of-plane polarized light, resulting in a photon emission at an energy lower than the bright exciton by the spin-orbit splitting. Finally, the full photoluminescence spectra including also donor and acceptor bound complexes for the two types of materials is presented, with binding energies calculated using diffusion quantum Monte Carlo. The photon energies resulting from recombination of donor bound biexciton, are in good agreement with experimentally classified biexcitons, suggesting a modification to the experimental interpretation of the observed spectra.

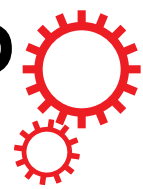
## 4.2 Semidark trions and biexcitons in $\text{WS}_2$ and $\text{WSe}_2$

The results presented in this section are reported in [22]: "Dark trions and biexcitons in  $\text{WS}_2$  and  $\text{WSe}_2$  made bright by e-e scattering", *Scientific Reports* **7**, 45998, (2017). My contribution to this work: Performed the calculations, prepared the figures, analysed the results and written the manuscript and supplementary material.

Full author list: M. Danovich, V. Zólyomi, V. I. Fal'ko

Author contributions: V.Z. performed the DFT calculations for the intervalley scattering matrix element and the band structures in the supplementary material. V.F. contributed to writing the manuscript.

# SCIENTIFIC REPORTS



OPEN

## Dark trions and biexcitons in WS<sub>2</sub> and WSe<sub>2</sub> made bright by e-e scattering

Received: 10 January 2017

Accepted: 07 March 2017

Published: 06 April 2017

Mark Danovich, Viktor Zólyomi &amp; Vladimir I. Fal'ko

The direct band gap character and large spin-orbit splitting of the valence band edges (at the K and K' valleys) in monolayer transition metal dichalcogenides have put these two-dimensional materials under the spot-light of intense experimental and theoretical studies. In particular, for Tungsten dichalcogenides it has been found that the sign of spin splitting of conduction band edges makes ground state excitons radiatively inactive (dark) due to spin and momentum mismatch between the constituent electron and hole. One might similarly assume that the ground states of charged excitons and biexcitons in these monolayers are also dark. Here, we show that the intervalley ( $K \leftrightarrows K'$ ) electron-electron scattering mixes bright and dark states of these complexes, and estimate the radiative lifetimes in the ground states of these “semi-dark” trions and biexcitons to be  $\sim 10$  ps, and analyse how these complexes appear in the temperature-dependent photoluminescence spectra of WS<sub>2</sub> and WSe<sub>2</sub> monolayers.

The truly 2D nature of TMDCs<sup>1–7</sup> enhances the effects of Coulomb interaction<sup>8,9</sup>, resulting in charge complexes such as excitons<sup>10–13</sup>, trions<sup>13</sup> and biexcitons<sup>14</sup> with binding energies that are orders of magnitude larger compared to conventional semiconductors such as GaAs. These complexes, which dominate the optical response of these materials, are comprised of spin/valley polarised electrons and holes residing at the corners K and K' of the hexagonal Brillouin zone (BZ), where the selection rules of optical transitions require the same spin and valley states of the involved electrons at the conduction and valence band edges. As a result, the opposite spin projections of the conduction (*c*) and valence (*v*) band edges, found in monolayers of WS<sub>2</sub> and WSe<sub>2</sub>, makes ground state excitons in these 2D crystals dark<sup>15,16</sup>, so that their radiative transition would require help from defects, phonons<sup>17</sup> or magnetic field<sup>18,19</sup>.

Applying the spin and valley selection rules to ground state trions and biexcitons might imply that these charge complexes are dark, too. In the ‘dark’ (*d*) state both electrons are in the bottom spin-orbit split states of *c*-band, whereas in the state to be ‘bright’ (*b*), one of the electrons has to be in the excited spin-split state. Here, we show that an intervalley scattering<sup>20,21</sup> of the *c*-band electrons mixes dark and bright states of complexes (Fig. 1), hence transferring some optical strength from *b*- to *d*-states and making dark state ‘semi-dark’. For the resulting recombination line of such semi-dark complexes, we find that it is shifted downwards in energy (relative to the bright trion line) by  $2\Delta_{SO}$ , twice the *c*-band spin-orbit splitting.

With the reference to Fig. 1, the basis of trion, T (biexciton, B) states,  $T_{\sigma_c \tau_c \sigma_v \tau_v}^{\sigma_v \tau_v}$  ( $B_{\sigma_c \tau_c \sigma_v \tau_v}^{\sigma_v \tau_v}$ ), can be described by spin,  $\sigma = \uparrow, \downarrow$  and valley,  $\tau = K, K'$  quantum numbers of their constituent *c*- and *v*-band states. In these notations, dark ground state exciton complexes  $T_d$  ( $B_d$ ) are  $T_{\downarrow K, \uparrow K'}^{\uparrow K}$  and  $T_{\downarrow K, \uparrow K'}^{\downarrow K'}$  ( $B_{\downarrow K, \uparrow K'}^{\uparrow K, \downarrow K'}$ ), and the excited states  $T_{\uparrow K, \downarrow K'}^{\uparrow K'}$  and  $T_{\uparrow K, \downarrow K'}^{\downarrow K'} (B_{\uparrow K, \downarrow K'}^{\uparrow K, \downarrow K'})$  are bright,  $T_b$  ( $B_b$ ) (Supplementary material S1). These states are mixed by the intervalley interaction illustrated by a sketch in Fig. 1

$$H_{iv} = \frac{\hbar^2 \chi}{2m_c} \sum_{\sigma, \tau} \int d^2 \vec{r} \Psi_{c, \sigma, -\tau}^\dagger(\vec{r}) \Psi_{c, -\sigma, \tau}^\dagger(\vec{r}) \Psi_{c, -\sigma, -\tau}(r) \Psi_{c, \sigma, \tau}(\vec{r}). \quad (1)$$

Here,  $\Psi_{c, \sigma, \tau}(\vec{r})$  are the conduction band electron field operators. The large momentum transfer between two electrons changing their valley states is determined by their Coulomb interaction at the unit cell scale, parametrised by a dimensionless factor  $\chi$ . We estimate the size of this factor using both a tight-binding model and density functional theory (DFT). For the tight-binding model, we use the DFT calculated orbital decomposition

National Graphene Institute, University of Manchester, Booth St E, Manchester M13 9PL, UK. Correspondence and requests for materials should be addressed to M.D. (email: mark.danovich@postgrad.manchester.ac.uk)

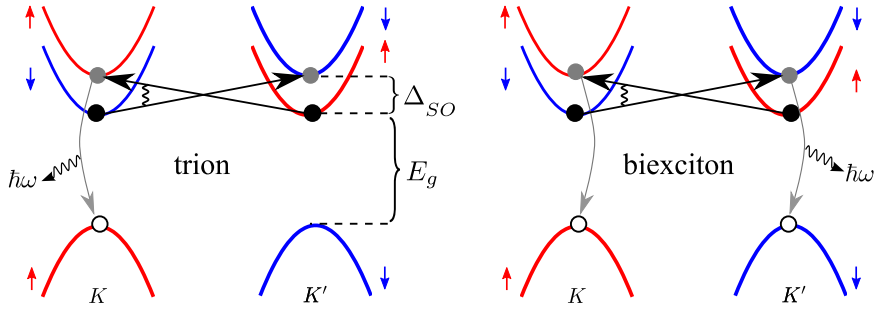


**Figure 1. Intervalley electron-electron scattering process.** Schematics of the band structures of  $WX_2$  near the  $K, K'$  points of the BZ, and the intervalley scattering process that mixes dark and bright states of trions (T) and biexcitons (B).  $E_g$  is the band gap and  $\Delta_{SO}$  stands for the conduction band spin splitting. Due to the large spin-orbit splitting in the valence band, the valence band is shown only for the higher-energy spin-polarised states.

	$\chi_{DFT}$	$\chi_{TB}$	$\mu_T$ [meV]	$\mu_B$ [meV]	$\tau_X$ [ps]	$\tau_{sd}(T)$ [ps]	$\tau_{sd}(B)$ [ps]
WS <sub>2</sub>	1.0	1.6	18[29]	8.6[13]	0.25	7.8[3.9]	15[7.0]
WSe <sub>2</sub>	1.3	2.0	19[30]	9.2[14]	0.26	9.4[4.7]	18[8.0]

**Table 1. Scattering matrix elements and radiative lifetimes.** Listed are the Intervalley scattering parameter  $\chi$  calculated using DFT and tight binding (TB) model and the corresponding trion and biexciton mixing parameters  $\mu T/B$  obtained using the electron-electron contact pair densities calculated in ref. 24 using diffusion quantum Monte Carlo, shown as DFT [TB], and the radiative lifetimes of the bright exciton, semi-dark trion and biexciton.

to construct the Bloch states at the Brillouin zone corners, and we use a 3D Coulomb potential for the interaction between electrons. As the  $c$ -band states at the  $K/K'$  points are primarily composed<sup>6,7</sup> of the metal  $5d_{z^2}$  orbitals centred at the lattice sites  $\vec{R}$  of metallic atoms in TMDC lattice,  $\phi(\vec{r} - \vec{R})$ , which we use to construct the tight-binding model Bloch states, to find

$$\chi = \frac{m_c}{m} \frac{A}{a_B} |C|^4 \sum_{\vec{R}} e^{i\vec{K} \cdot \vec{R}} \int d^3 \vec{r}_1 d^3 \vec{r}_2 \frac{|\phi(\vec{r}_1)|^2 |\phi(\vec{r}_2)|^2}{|\vec{r}_2 - \vec{r}_1 + \vec{R}|}. \quad (2)$$

Here,  $\vec{K} = \left( \frac{4\pi}{3a_0}, 0 \right)$  with  $a_0$  the lattice constant of  $WX_2$ ,  $A = \frac{\sqrt{3}}{2} a_0^2$  is the unit cell area,  $m_c$  is the  $c$ -band electron effective mass,  $m$  is the free electron mass,  $a_B$  is the Bohr radius, and  $C$  is the transition metal  $5d_{z^2}$  orbital amplitude in the  $c$ -band edge at the  $K$  point (supplementary material S2.2). Similarly, we evaluated  $\chi$  from wave functions obtained using DFT implemented in the local density approximation and VASP<sup>22</sup> code (neglecting spin-orbit coupling). We used a plane-wave basis corresponding to 600 eV cutoff energy and a  $12 \times 12$  grid of k-points in the 2D Brillouin zone. We also had to employ periodic boundary conditions in the  $z$ -direction; for this reason we used a large inter-layer distance of 20 Å to mimic the limit of an isolated monolayer. The form factor was calculated by post-processing the DFT wave functions, by taking the matrix element of the bare Coulomb interaction between the initial and final states of the scattering process (see supplementary material S2.1). These two calculations have returned values of the intervalley scattering factor  $\chi$ , as listed in Table 1. In the basis of  $[|d\rangle; |b\rangle]$  of dark and bright states of trions,  $[T_{\downarrow K, \uparrow K'}^{\uparrow K}; T_{\uparrow K, \downarrow K'}^{\uparrow K}]$  and  $[T_{\downarrow K, \uparrow K'}^{\downarrow K'}; T_{\uparrow K, \downarrow K'}^{\downarrow K'}]$ , or biexcitons  $[B_{\downarrow K, \uparrow K'}^{\uparrow K, \downarrow K'}; B_{\uparrow K, \downarrow K'}^{\uparrow K, \downarrow K'}]$ , the coupling in equation (1) leads to the mixing described by a  $2 \times 2$  matrix

$$H = \begin{pmatrix} E_b^{T/B} & \mu_{T/B} \\ \mu_{T/B}^* & E_d^{T/B} \end{pmatrix}, \quad \mu_T = \frac{\hbar^2 \chi}{m_c} g_T, \quad \mu_B = \frac{\hbar^2 \chi}{m_c} g_B,$$

$$E_b^T = 2E_g + 2\Delta_{SO} - \varepsilon_X - \varepsilon_T + \delta',$$

$$E_d^T = 2E_g - \varepsilon_X - \varepsilon_T + \delta,$$

$$E_b^B = 2E_g + 2\Delta_{SO} - \varepsilon_X - \varepsilon_B + 2\delta',$$

$$E_d^B = 2E_g - \varepsilon_X - \varepsilon_B + 2\delta. \quad (3)$$

Where  $E_g$  is the band gap,  $\varepsilon_X$ ,  $\varepsilon_T$ , and  $\varepsilon_B$  are the exciton, trion, and biexciton binding energies, respectively, and  $\delta$ ,  $\delta'$  stand for the intravalley and intervalley electron-hole exchange<sup>23</sup>,  $\delta \approx 6$  meV, which we will neglect in the following calculations. Note that the effective masses of the  $c$ -band spin split bands differ by<sup>7</sup> ~30–40% with the lower bands having the higher effective electron mass. This results in slightly higher binding energies for the dark

	$\frac{m_c}{m}$	$\frac{m_v}{m}$	$\Delta_{SO}$	$A$	$r_*$	$E_{X_b}$	$\varepsilon_T$	$\varepsilon_B$	$\frac{v}{c}$
	[meV]		[Å <sup>2</sup> ]	[nm]		[eV]	[meV]	[meV]	
WS <sub>2</sub>	0.26	-0.35	32	8.65	3.8	2	34	24	$1.7 \times 10^{-3}$
WSe <sub>2</sub>	0.28	-0.36	37	9.38	4.5	1.7	31	20	$1.6 \times 10^{-3}$

**Table 2. Material parameters.** Listed are the effective  $c$ - and  $v$ -band electron masses  $m_c$  and  $m_v$ ,  $c$ -band spin-orbit splitting  $\Delta_{SO}$ , unit cell area  $A$ , 2D screening length  $r_*$ , bright exciton energy  $E_{X_b}$ , trion binding energy  $\varepsilon_T$ , biexciton binding energy  $\varepsilon_B$ , and the velocity related to the off diagonal momentum matrix element relative to the speed of light  $v/c$ .

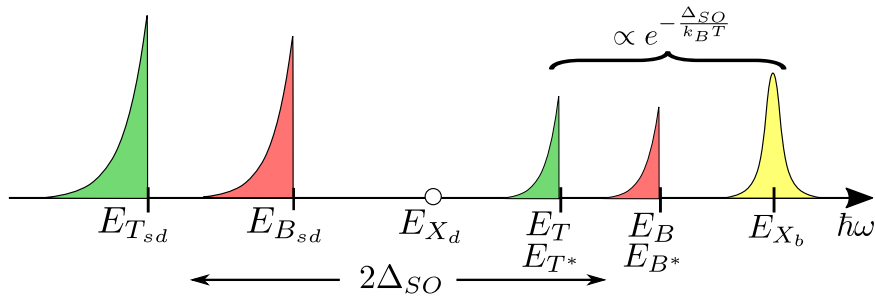


**Figure 2. Low temperature photoluminescence spectrum of WX<sub>2</sub>.** Sketch of the low temperature ( $k_B T < \Delta_{SO}$ ) photoluminescence spectrum of WX<sub>2</sub> including the bright exciton, dark and bright trions (green) and dark and bright biexcitons (red). The excited bright trions and excitons are denoted by  $T^*$  and  $B^*$ . The dark exciton ( $X_d$ ) energy is marked as a reference point  $E_{X_d} = E_{X_b} - \Delta_{SO}$ .

ground state charge complexes compared to the excited states, resulting in a larger value for their energy difference  $E_b - E_d$ . The mixing parameter  $\mu \equiv \langle b | H_{iv} | d \rangle = \frac{\hbar^2 \chi}{m_c} \int \prod_i d^2 \vec{r}_i |\Phi_{T/B}|^2 \delta(\vec{r}_e - \vec{r}_{e'})$ , (where  $\Phi_{T/B}$  stands for the wave function of the trion or biexciton and  $i = e, e', h, (h')$ , is determined by the electron-electron contact pair densities<sup>24</sup> in the trion,  $g_T$  and biexciton,  $g_B$ . The mixing of the dark and bright states results in a slight shift of their energies and, most importantly, in a finite radiative decay rate,  $\tau_{sd}^{-1}$  of the semi-dark (sd) trions ( $T$ ) and biexcitons ( $B$ ),

$$\begin{aligned} \frac{1}{\tau_{sd}} &\approx \left( 1 - \frac{1}{\sqrt{1 + \left( \frac{\mu_{T/B}}{\Delta_{SO}} \right)^2}} \right) \frac{\alpha_{T/B}}{2} \tau_X^{-1}, \\ \frac{1}{\tau_X} &= \frac{8\pi}{\hbar} \frac{e^2}{\hbar c} \frac{\hbar^2 v^2}{E_{X_b}} |\Phi_X(0)|^2, \end{aligned} \quad (4)$$

where  $\tau_X^{-1}$  is the radiative decay rate of the bright exciton<sup>25–27</sup>, determined by the electron-hole overlap factor  $|\Phi_X(0)|^2$  ( $\Phi_X(r_{ch})$  is the envelope wave function describing relative motion of the electron and hole in the exciton),  $v$  is the velocity related to the off diagonal momentum matrix element. The values of the factors  $\alpha_T = \frac{1}{2}$  and  $\alpha_B = 1$  have been estimated based on the following consideration (see supplementary material S3). As the exciton's binding energy is significantly larger than that of the trion or biexciton, these bound complexes can be viewed as strongly-bound, with an additional weakly bound electron in the case of a trion, or an exciton in the case of a biexciton. For a trion, this results in a reduction of the recombining electron-hole contact pair density by a factor of two as compared to the exciton, as the hole is shared between the two electrons such that the recombining electron (which has the right spin projection), will be near it only half of the time. In the case of the biexciton, each electron spends half of the time near its hole with which it can recombine, and half of the time near the other hole. As there are two excitons able to recombine we get  $\alpha_B = 1$ . The resulting values for the lifetimes (using the material parameters in Table 2) are summarized in Table 1.

The mixing of the dark and bright states produces photoluminescence lines shown schematically in Fig. 2. The emitted photon energies of these lines are determined by both the binding energies and the shake-up into the higher-energy spin-split  $c$ -band in the final state,

$$\begin{aligned}
 E_{X_b} &= E_g + \Delta_{SO} - \varepsilon_X, \\
 E_{T_{sd}/B_{sd}} &\approx E_{X_b} - \varepsilon_{T/B} - 2\Delta_{SO}, \\
 E_{T/B} &\approx E_{X_b} - \varepsilon_{T/B},
 \end{aligned} \tag{5}$$

Being the ground states, the semi-dark trion and biexcitons ( $T_{sd}$ ,  $B_{sd}$ ) do not require an activation and therefore should appear in the spectrum even at low temperatures. In contrast, the bright states do require thermal activation, resulting in a  $e^{-\Delta E/k_B T}$  temperature dependence of their lines intensities. For the bright exciton, trion [ $T_{\uparrow K, \uparrow K'}^{\uparrow K}$ ;  $T_{\downarrow K, \downarrow K'}^{\downarrow K'}$ ] and biexciton [ $B_{\uparrow K, \uparrow K'}^{\uparrow K, \downarrow K'}$ ;  $B_{\downarrow K, \downarrow K'}^{\downarrow K, \uparrow K'}$ ] we have  $\Delta E \approx \Delta_{SO}$ , while for the excited mixed dark and bright trion ( $T^*$ ) [ $T_{\uparrow K, \downarrow K'}^{\uparrow K}$ ;  $T_{\downarrow K, \uparrow K'}^{\downarrow K'}$ ] and biexciton ( $B^*$ ) [ $B_{\uparrow K, \downarrow K'}^{\uparrow K, \downarrow K'}$ ,  $\Delta E \approx 2\Delta_{SO}$ . Also, the presence of a final state electron or exciton results in an antisymmetric line shape with a cutoff due to the recoil kinetic energy of the remaining electron or exciton that shifts the emission line to a lower energy. A typical recoil kinetic energy is  $\frac{m_x}{m_c} k_B T$  for the triions and  $k_B T$  for biexcitons, with  $k_B$  the Boltzmann constant,  $m_x$  the exciton mass, and  $m_c$  the  $c$ -band electron effective mass.

In conclusion, we have shown that intervalley electron-electron scattering makes “dark” ground state triions and biexcitons in Tungsten dichalcogenides WS<sub>2</sub> and WSe<sub>2</sub> optically active, with a lifetime  $\tau_{T/B} \sim 10$  ps, to compare with a sub-ps lifetime of bright excitons in 2D TMDCs.

## References

- Wang, H. Q., Kalantar-Zadeh, K., Kis, A., Coleman, J. N. & Strano, M. S. Electronics and optoelectronics of two-dimensional transition metal dichalcogenides. *Nat. Nanotechnol.* **7**(11), 699–712 11 (2012).
- Cao, T. *et al.* Valley-selective circular dichroism of monolayer molybdenum disulphide. *Nat. Commun.* **3**, 887 06 (2012).
- Xiao, D., Liu, G. B., Feng, W., Xu, X. & Yao, W. Coupled spin and valley physics in monolayers of MoS<sub>2</sub> and other group-vi dichalcogenides. *Phys. Rev. Lett.* **108**, 196802 (May 2012).
- Jones, A. M. *et al.* Optical generation of excitonic valley coherence in monolayer wse<sub>2</sub>. *Nat Nano* **8**(9), 634–638 09 (2013).
- Zeng, H., Dai, J., Yao, W., Xiao, D. & Cui, X. Valley polarization in MoS<sub>2</sub> monolayers by optical pumping. *Nat Nano* **7**(8), 490–493 08 (2012).
- Liu, G. B., Xiao, D., Yao, Y., Xu, X. & Yao, W. Electronic structures and theoretical modelling of two-dimensional group-vib transition metal dichalcogenides. *Chem. Soc. Rev.* **44**, 2643–2663 (2015).
- Kormanyos, A. *et al.* k·p theory for two-dimensional transition metal dichalcogenide semiconductors. *2D Materials* **2**(2), 022001 (2015).
- Chernikov, A. *et al.* Exciton binding energy and nonhydrogenic rydberg series in monolayer WS<sub>2</sub>. *Phys. Rev. Lett.* **113**, 076802 (Aug 2014).
- Cudazzo, P., Tokatly, I. V. & Rubio, A. Dielectric screening in two-dimensional insulators: Implications for excitonic and impurity states in graphane. *Phys. Rev. B* **84**, 085406 (Aug 2011).
- Mak, K. F. *et al.* Tightly bound triions in monolayer MoS<sub>2</sub>. *Nat Mater* **12**(3), 207–211 03 (2013).
- Qiu, D. Y., da Jornada, F. H. & Louie, S. G. Optical spectrum of MoS<sub>2</sub>: Many-body effects and diversity of exciton states. *Phys. Rev. Lett.* **111**, 216805 (Nov 2013).
- Ramasubramanian, A. Large excitonic effects in monolayers of molybdenum and tungsten dichalcogenides. *Phys. Rev. B* **86**, 115409 (Sep 2012).
- Berkelbach, T. C., Hybertsen, M. S. & Reichman, D. R. Theory of neutral and charged excitons in monolayer transition metal dichalcogenides. *Phys. Rev. B* **88**, 045318 (Jul 2013).
- You, Y. *et al.* Observation of biexcitons in monolayer WSe<sub>2</sub>. *Nat Phys* **11**(6), 477–481 06 (2015).
- Echeverry, J. P., Urbaszek, B., Amand, T., Marie, X. & Gerber, I. C. Splitting between bright and dark excitons in transition metal dichalcogenide monolayers. *Phys. Rev. B* **93**, 121107 (Mar 2016).
- Zhang, X. X., You, Y., Yang, S., Zhao, F. & Heinz, T. F. Experimental evidence for dark excitons in monolayer WSe<sub>2</sub>. *Phys. Rev. Lett.* **115**, 257403 (Dec 2015).
- Danovich, M., Zólyomi, V., Fal’ko, V. I. & Aleiner, I. L. Auger recombination of dark excitons in ws<sub>2</sub> and wse<sub>2</sub> monolayers. *2D Materials* **3**(3), 035011 (2016).
- Zhang, X. X. *et al.* Magnetic brightening and control of dark excitons in monolayer WSe<sub>2</sub>. cond-mat/1612.03558v1 (2016).
- Molas, M. R. *et al.* Brightening of dark excitons in monolayers of semiconducting transition metal dichalcogenides. cond-mat/1612.02867v1 2D materials, **4**(2), 021003 (2017).
- Yu, H., Cui, X., Xu, X. & Yao, W. Valley excitons in two-dimensional semiconductors. *National Science Review* **2**(1), 57–70 (2015).
- Dery, H. Theory of intervalley coulomb interactions in monolayer transition-metal dichalcogenides. *Phys. Rev. B* **94**, 075421 (Aug 2016).
- Kresse, G. & Furthmüller, J. Efficient iterative schemes for *ab initio* total-energy calculations using a plane-wave basis set. *Phys. Rev. B* **54**, 11169–11186 (Oct 1996).
- Plechinger, G. *et al.* Trion fine structure and coupled spin-valley dynamics in monolayer tungsten disulfide. *Nat Commun* **7**, 09 (2016).
- Syniszewski, M., Mostaani, E., Drummond, N. D., Aleiner, I. & Fal’ko, V. I. Binding energies of triions and biexcitons in two-dimensional semiconductors from diffusion quantum Monte Carlo calculations. *Phys. Rev. B* **95**, 081301 (Feb 2017).
- Palummo, M., Bernardi, M. & Grossman, J. C. Exciton radiative lifetimes in two-dimensional transition metal dichalcogenides. *Nano Letters* **15**(5), 2794–2800 (2015).
- Slobodeniuk, A. O. & Basko, D. M. Spin-flip processes and radiative decay of dark intravalley excitons in transition metal dichalcogenide monolayers. *2D Materials* **3**(3), 035009 (2016).
- Wang, H. *et al.* Radiative lifetimes of excitons and triions in monolayers of the metal dichalcogenide mos<sub>2</sub>. *Phys. Rev. B* **93**, 045407 (Jan 2016).
- Hanbicki, A. T., Currie, M., Kiouseoglou, G., Friedman, A. L. & Jonker, B. T. Measurement of high exciton binding energy in the monolayer transition-metal dichalcogenides ws<sub>2</sub> and wse<sub>2</sub>. *Solid State Communications* **203**, 16–20 2 (2015).
- Kylänpää, I. & Komsa, H. P. Binding energies of exciton complexes in transition metal dichalcogenide monolayers and effect of dielectric environment. *Phys. Rev. B* **92**, 205418 (Nov 2015).

## Acknowledgements

This work was supported by the EU Graphene Flagship Project, the Engineering and Physical Sciences Research Council (EPSRC, EP/N010345/1), and the European Research Council (ERC Synergy Grant Hetero2D). The authors would like to thank I. Aleiner, T. Heinz, M. Potemski, M. Syniszewski, A. Tartakovski and X. Xu for useful discussions.

# **Supplementary material: “Dark trions and biexcitons in WS<sub>2</sub> and WSe<sub>2</sub> made bright by e-e scattering”**

Mark Danovich<sup>1</sup>, Viktor Zólyomi<sup>1</sup> & Vladimir I. Fal’ko<sup>1</sup>

<sup>1</sup>*National Graphene Institute, University of Manchester, Booth St E, Manchester M13 9PL, UK*

## **S1 Group theory analysis of excitons, trions and biexcitons in Tungsten dichalcogenides**

### **S1.1 Introduction**

Group theory allows to utilize the symmetry properties of the Hamiltonian in order to gain insight into selection rules for microscopic processes in quantum systems. As a starting point, the eigenstates of the Hamiltonian are classified according to the irreducible representations (IrReps) of the symmetry group, in our case the point group  $C_{3h}$ . In monolayer TMDCs, DFT calculations<sup>1,2</sup> (see also S2.1) have found that band edges of monolayer WS<sub>2</sub> and WSe<sub>2</sub> are found at the two inequivalent corners,  $K$  and  $K'$  of the Brillouin zone. Hence, for the sake of their classification we consider the extended point group<sup>3,4</sup>,  $C''_{3v} = C_{3v} + tC_{3v} + t^2C_{3v}$ , where  $t$  are translations by a lattice vector. This enables us to treat states of excitons and complexes at  $K$ ,  $K'$  and zero momentum in the same fashion. The character table and product table for the IrReps of the extended point group  $C''_{3v}$  are

**Table S1:**  $C_{3v}''$  character table.

Character table for the irreducible representations (IrRep) of the extended point group  $C_{3v}''$ , and their correspondence to the conduction ( $c$ ) and valence ( $v$ ) band electrons states.

$C_{3v}''$	$E$	$t, t^2$	$2C_3$	$9\sigma_v$	$2tC_3$	$2t^2C_3$
$A_1$	1	1	1	1	1	1
$A_2$	1	1	1	-1	1	1
$E$	2	2	-1	0	-1	-1
$E'_1 (c)$	2	-1	-1	0	2	-1
$E'_2 (v)$	2	-1	2	0	-1	-1
$E'_3$	2	-1	-1	0	-1	2

given in Tables S1, S2, respectively. DFT calculations<sup>1,2</sup> (see also S2.1) have also found that at the  $K$  and  $K'$  valleys, the orbital composition of the Bloch states is dominated by the  $z \rightarrow -z$  symmetric  $d$ -orbitals ( $d_0$  for the  $c$ -band and  $d_{\pm 2}$  for the  $v$ -band in the two valleys) of transition metal, allowing to classify the  $c$  and  $v$ -band Bloch states at the  $K$  and  $K'$  valleys as transforming according to the two dimensional IrReps of the extended point group,  $E'_1$  and  $E'_2$ , respectively.

Using classification of the single electron states, we consider excitons, trions, and biexcitons. For this, we take direct products of the corresponding IrReps, and, then, apply the product rules for the IrReps of  $C_{3v}''$ , shown in Table S2. This group theory analysis enables us to identify excitonic basis states that can be mixed by the intervalley e-e scattering, leading to the class of semi-dark trions and biexcitons discussed in the main text.

**Table S2:**  $C_{3v}''$  product table.

Product table for the irreducible representations of the extended point group  $C_{3v}''$ .

$C_{3v}''$	$A_1$	$A_2$	$E$	$E'_1$	$E'_2$	$E'_3$
$A_1$	$A_1$	$A_2$	$E$	$E'_1$	$E'_2$	$E'_3$
$A_2$	$A_2$	$A_1$	$E$	$E'_1$	$E'_2$	$E'_3$
$E$	$E$	$E$	$A_1 \oplus A_2 \oplus E$	$E'_2 \oplus E'_3$	$E'_1 \oplus E'_3$	$E'_1 \oplus E'_2$
$E'_1 (c)$	$E'_1$	$E'_1$	$E'_2 \oplus E'_3$	$A_1 \oplus A_2 \oplus E'_1$	$E \oplus E'_3$	$E \oplus E'_2$
$E'_2 (v)$	$E'_2$	$E'_2$	$E'_1 \oplus E'_3$	$E \oplus E'_3$	$A_1 \oplus A_2 \oplus E'_2$	$E \oplus E'_1$
$E'_3$	$E'_3$	$E'_3$	$E'_1 \oplus E'_2$	$E \oplus E'_2$	$E \oplus E'_1$	$A_1 \oplus A_2 \oplus E'_3$

## S1.2 Excitons

The exciton states transform according to the direct product representation of the  $c$ - and  $v$ -band states given by

$$E'_1 \otimes E'_2 = E \oplus E'_3. \quad (\text{S1})$$

The 2D IrRep  $E$  corresponds to the intravalley excitons with both electron and hole residing in either the  $K$  or  $K'$  valleys, and the 2D IrRep  $E'_3$  corresponds to the intervalley excitons with the electron and hole residing in opposite valleys making the exciton dark due to momentum mismatch. By further introducing the spin projections of the electron and hole, we have for each representation two possible total spin projections,  $|S_z| = 1$  corresponding to dark excitons due to spin conservation, and  $S_z = 0$  corresponding to bright exciton states. Using the notation intro-

duced in the text for trions and biexcitons, the  $E$  IrRep dark intravalley exciton states are given by  $[X_{\downarrow K}^{\uparrow K}; X_{\uparrow K'}^{\downarrow K'}]$  with  $|S_z| = 1$ , and the bright intravalley excitonic states by  $[X_{\uparrow K}^{\uparrow K}; X_{\downarrow K'}^{\downarrow K'}]$  with  $|S_z| = 0$ . Similarly, for the intervalley excitons transforming according to  $E'_3$ , which are dark due to momentum conservation, we have  $[X_{\uparrow K'}^{\uparrow K}; X_{\downarrow K}^{\downarrow K'}]$  with  $S_z = 0$ , and  $[X_{\downarrow K'}^{\uparrow K}; X_{\uparrow K}^{\downarrow K'}]$  with  $S_z = 1$ , being dark due to both spin and momentum conservation.

### S1.3 Trions

Next we classify the trion states composed of two electrons and a hole. The strongly bound trion states require the two-electron wave function to be symmetric with respect to exchanging the electrons coordinates and the two electrons to have different spin/valley indices corresponding to a singlet state, as obtained in ref. 5 using Monte Carlo calculations. The two-electron state transforms according to the direct product of the  $c$ -band electrons representations given by

$$E'_1 \otimes E'_1 = A_1 \oplus A_2 \oplus E'_1. \quad (\text{S2})$$

According to Table S1, the symmetric combination of the two electrons transforms according to  $A_1$  or  $E'_1$ . The identity representation corresponds to both electrons residing in opposite valleys, while the 2D IrRep  $E'_1$  corresponds to both electrons residing in the same valley  $K$  or  $K'$ . Next, to obtain the representation of the trion we include the hole state  $E'_2$  and take the direct product of the two electrons and the hole. This gives in the first case

$$A_1 \otimes E'_2 = E'_2, \quad (\text{S3})$$

corresponding to the hole residing in either the  $K$  or  $K'$  valleys and the electrons residing in opposite valleys. Including the spin projection this corresponds to the following trion states,  $[T_{\downarrow K, \uparrow K'}^{\uparrow K}; T_{\downarrow K, \uparrow K'}^{\downarrow K}]$  which are the semi-dark singlet ground state trions, and  $[T_{\uparrow K, \downarrow K'}^{\uparrow K}; T_{\uparrow K, \downarrow K'}^{\downarrow K'}]$  which are the excited bright trion singlet states. As the excited bright and semi-dark trion states both transform according to the same  $E'_2$  IrRep, the two states can be mixed through the electron-electron intervalley scattering introduced in the main text, which transforms as the identity representation. The bright trion triplet states with both electrons in opposite valleys also transform according to the  $E'_2$  IrRep and are given by  $[T_{\uparrow K, \uparrow K'}^{\uparrow K}; T_{\downarrow K, \downarrow K'}^{\downarrow K'}]$ , and the dark trion triplet states (due to spin conservation) are given by  $[T_{\downarrow K, \downarrow K'}^{\uparrow K}; T_{\uparrow K, \uparrow K'}^{\downarrow K'}]$ . In the second case, choosing for the two-electron representation the  $E'_1$  IrRep,

$$E'_1 \otimes E'_2 = E \oplus E'_3. \quad (\text{S4})$$

Here,  $E$  corresponds to states with the two electrons and hole residing in the same valley  $K$  or  $K'$ . Requiring the electrons to have opposite spin projections gives the following bright trion states  $[T_{\uparrow K, \downarrow K}^{\uparrow K}; T_{\uparrow K', \downarrow K'}^{\downarrow K'}]$ .  $E'_3$  corresponds to the two electrons residing in the same valley while the hole is in the opposite valley, giving the dark trion states (due to momentum conservation)  $[T_{\uparrow K, \downarrow K}^{\downarrow K'}; T_{\uparrow K', \downarrow K}^{\uparrow K}]$ .

## S1.4 Biexcitons

The bound biexciton states are composed of a spatially symmetric wave function for the two electrons and for the two holes. This corresponds to the IrReps  $A_1 \oplus E'_1$  for the two electrons, and

$A_1 \oplus E'_2$  for the two holes. Taking the direct product of the two-electron and two-hole states gives the possible representations of the biexciton states

$$(A_1 \oplus E'_1) \otimes (A_1 \oplus E'_2) = A_1 \oplus E'_1 \oplus E \oplus E'_3 \oplus E'_2. \quad (\text{S5})$$

The states transforming according to the IrRep  $E$  correspond to both electrons and both holes residing in the same valley, similarly the  $E'_3$  IrRep corresponds to both electrons residing in the same valley and both holes residing in the opposite valley to the electrons, and finally  $E'_2$  corresponds to both electrons residing in opposite valleys, and both holes residing in the same valley. As these three cases require one of the holes to reside in the lower spin-orbit split band in order for the biexciton to be bound, we do not consider these states. Of particular interest is the  $A_1$  representation corresponding to both electrons and both holes residing in opposite valleys. Including the spin projections this corresponds to the following biexciton state,  $B_{\downarrow K, \uparrow K'}^{\uparrow K, \downarrow K'}$  which is the semi-dark (due to momentum conservation) ground state singlet biexciton, and  $B_{\uparrow K, \downarrow K'}^{\uparrow K, \downarrow K'}$  which is the excited bright state singlet biexciton. As the two states transform according to the same IrRep  $A_1$ , they can also be mixed by the electron-electron intervalley scattering process as in the trions case. The biexciton triplet states are given by  $B_{\uparrow K, \uparrow K'}^{\uparrow K, \downarrow K'}$  and  $B_{\downarrow K, \downarrow K'}^{\uparrow K, \downarrow K'}$  both being optically bright. The biexciton states transforming according to the  $E_1$  IrRep are bright having both electrons in the same valley and both holes in opposite valleys,  $[B_{\uparrow K, \downarrow K}^{\uparrow K, \downarrow K'}; B_{\uparrow K', \downarrow K'}^{\uparrow K, \downarrow K'}]$ .

**Table S3: Group theory classification.**

Summary of the group theory classification of excitonic complexes,  $X$ -excitons,  $T$ -trions, and  $B$ - Biexcitons, in Tungsten dichalcogenides according to the irreducible representations of the extended point group  $C_{3v}''$ .

	IrRep	States	Bright	Dark	Exciton or complex (see Fig. 2)
$X$	$E$	$[X_{\downarrow K}^{\uparrow K}; X_{\uparrow K'}^{\downarrow K'}]$	✓	✓	$X_d$
		$[X_{\uparrow K}^{\uparrow K}; X_{\downarrow K'}^{\downarrow K'}]$			$X_b$
	$E'_3$	$[X_{\uparrow K'}^{\uparrow K}; X_{\downarrow K}^{\downarrow K'}]$	✓	✓	$X_d$
		$[X_{\downarrow K'}^{\uparrow K}; X_{\uparrow K}^{\downarrow K'}]$		✓	
$T$	$E'_2$	$[T_{\downarrow K, \uparrow K'}^{\uparrow K}; T_{\downarrow K, \uparrow K'}^{\downarrow K'}]$	✓	✓	$T_{sd}$
		$[T_{\uparrow K, \downarrow K'}^{\uparrow K}; T_{\uparrow K, \downarrow K'}^{\downarrow K'}]$			$T^*$
		$[T_{\uparrow K, \uparrow K'}^{\uparrow K}; T_{\downarrow K, \downarrow K'}^{\downarrow K'}]$	✓	✓	$T$
	$E$	$[T_{\uparrow K, \downarrow K}^{\uparrow K}; T_{\uparrow K', \downarrow K'}^{\downarrow K'}]$	✓		$T$
	$E'_3$	$[T_{\uparrow K, \downarrow K}^{\downarrow K'}; T_{\uparrow K', \downarrow K}^{\uparrow K}]$		✓	—
$B$	$A_1$	$B_{\downarrow K, \uparrow K'}^{\uparrow K, \downarrow K'}$	✓	✓	$B_{sd}$
		$B_{\uparrow K, \downarrow K'}^{\uparrow K, \downarrow K'}$			$B^*$
		$B_{\uparrow K, \uparrow K'}^{\uparrow K, \downarrow K'}$	✓		$B$
		$B_{\downarrow K, \downarrow K'}^{\uparrow K, \downarrow K'}$	✓		$B$
	$E'_1$	$[B_{\uparrow K, \downarrow K}^{\uparrow K, \downarrow K'}; B_{\uparrow K', \downarrow K}^{\uparrow K, \downarrow K'}]$	✓		$B$

## S2 Model calculations of the intervalley scattering matrix element

### S2.1 Ab initio density functional theory

In the DFT calculations the wave functions were obtained in the local density approximation, using a plane-wave basis of 600 eV cutoff energy and a k-point grid of  $12 \times 12$  in the 2D Brillouin zone. We used the VASP<sup>10</sup> code for these calculations, which employs periodic boundary conditions in three dimensions even for 2D materials; for this reason we used a large inter-layer distance of 20 Å to mimic the limit of an isolated monolayer. The form factor was calculated by post-processing the DFT wave functions, simply taking the matrix element of the bare Coulomb interaction between the initial and final states of the scattering process. In the calculation of this matrix element we neglected spin-orbit coupling.

The form factor was calculated in reciprocal space by Fourier transforming Eq. (2) in the main text, leading to a summation on the grid of reciprocal lattice vectors. This technique is sensitive to the plane-wave cutoff energy. We have therefore tested the sensitivity of the form factor to the cutoff energy by calculating it for WS<sub>2</sub> with an extremely reduced cutoff of 100 eV and an increased cutoff of 900 eV. We found that reducing the cutoff reduces the form factor by 10 %, while increasing the cutoff increases the form factor by 3 %.

Convergence of the calculation was also tested for the inter-layer separation. We found that

decreasing the separation to 15 Å only changes the form factors by less than 1 %.

In Fig. S1 we show the DFT calculated band structure for  $\text{WS}_2$  and  $\text{WSe}_2$ , showing the band edges at the  $K$  point and the spin-orbit splitting. In Tables S4 and S5 we list the DFT obtained orbital decomposition of the electron states at the  $K/K'$  points in the conduction and valence bands demonstrating the dominance of the transition metal  $d$  orbitals.

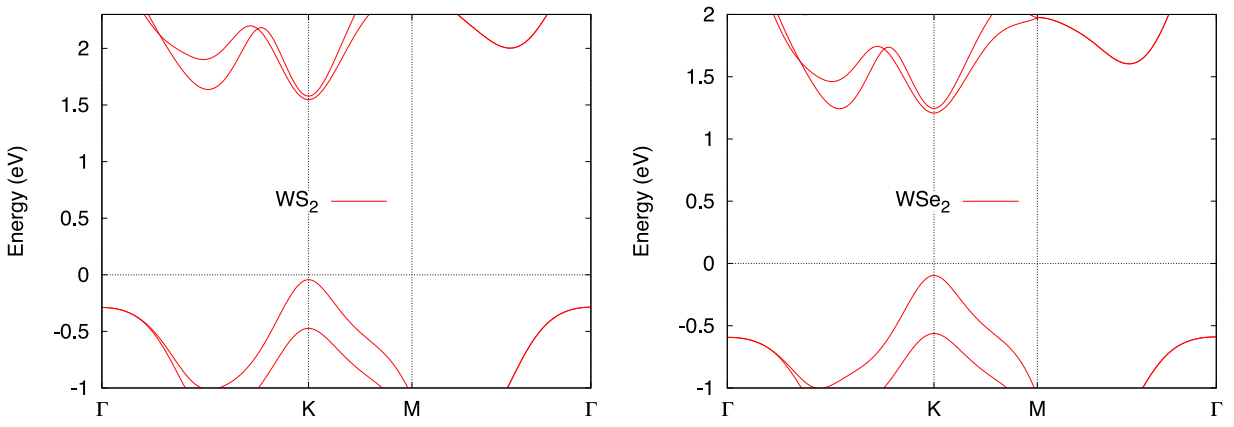


**Figure S1 | DFT calculated band structure of  $\text{WX}_2$ .**

**Table S4 | DFT calculated orbital decomposition at the  $K/K'$  point in  $\text{WS}_2$ .**

band	$\text{W} - 5d_{z^2}$	$\text{W} - 5d_{x^2-y^2}$	$\text{W} - 5d_{xy}$	$\text{W} - 6s$	$\text{S} - p_x$	$\text{S} - p_y$
$c$	86.9%	0	0	7.8%	2.6%	2.6%
$v$	0	39.5%	39.5%	0	10.2%	10.2%

**Table S5 | DFT calculated orbital decomposition at the  $K/K'$  point in WSe<sub>2</sub>.**

band	W - 5d <sub>z<sup>2</sup></sub>	W - 5d <sub>x<sup>2</sup>-y<sup>2</sup></sub>	W - 5d <sub>xy</sub>	W - 6s	Se - p <sub>x</sub>	Se - p <sub>y</sub>
<i>c</i>	85.9%	0	0	8.1%	2.2%	2.2%
<i>v</i>	0	40.1%	40.1%	0	9.2%	9.2%

## S2.2 Tight-binding model

In the tight binding model, the Bloch wave function of the conduction band electrons at the  $K$  point, using only the transition metal *d*-orbital is given by

$$\Psi(\vec{r}) = \frac{C}{\sqrt{N}} \sum_i e^{i\vec{K} \cdot \vec{R}_i} \phi(\vec{r} - \vec{R}_i), \quad (\text{S6})$$

where  $N$  is the number of unit cells,  $\vec{R}_i$  is the lattice vector coinciding with the transition metal atoms positions, and  $C$  is the weight of the  $5d_{z^2}$  orbital  $\phi$  centred on  $\vec{R}_i$ . The value of  $C$  is obtained from the orbital decomposition given in Tables S4, S5 for WS<sub>2</sub> and WSe<sub>2</sub>, respectively. The 3D coulomb matrix element is given by

$$M = e^2 \int \frac{d^3 \vec{r}_1 d^3 \vec{r}_2}{|\vec{r}_2 - \vec{r}_1|} \Psi^*(\vec{r}_1) \Psi^*(\vec{r}_2) \Psi(\vec{r}_1) \Psi(\vec{r}_2). \quad (\text{S7})$$

Plugging in the Bloch wave function and using the two-centre approximation for the electron-electron Coulomb interaction we get

$$M = e^2 |C|^4 \sum_{\vec{R}} e^{i\vec{K} \cdot \vec{R}} \int d^3 \vec{r}_1 d^3 \vec{r}_2 \frac{|\phi(\vec{r}_1)|^2 |\phi(\vec{r}_2)|^2}{|\vec{r}_2 - \vec{r}_1 + \vec{R}|}, \quad (\text{S8})$$

where the summation is over the lattice sites  $\vec{R} = l\vec{a}_1 + n\vec{a}_2$ , where  $\vec{a}_1 = a_0(1, 0)$ , and  $\vec{a}_2 = \frac{a_0}{2}(1, \sqrt{3})$  are the lattice primitive vectors,  $a_0$  is the lattice constant, and  $l, n$  are integers. Finally,

the matrix element is related to the dimensionless parameter  $\chi$  through the intervalley interaction Hamiltonian giving,

$$\chi = \frac{m_c}{m} \frac{A}{a_B} |C|^4 \sum_{\vec{R}} e^{i\vec{K}\cdot\vec{R}} \int d^3\vec{r}_1 d^3\vec{r}_2 \frac{|\phi(\vec{r}_1)|^2 |\phi(\vec{r}_2)|^2}{|\vec{r}_2 - \vec{r}_1 + \vec{R}|}, \quad (\text{S9})$$

where  $m_c$  is the  $c$ -band electron mass,  $m$  is the free electron mass,  $A$  is the unit cell area, and  $a_B$  is the Bohr radius.

For the atomic orbital entering into the Coulomb matrix element we use the Roothaan-Hartree-Fock (RHF) atomic orbitals<sup>6,7</sup> which consist of a linear combination of Slater-type orbitals,

$$\phi_{nlm}(\vec{r}) = Y_m^l(\theta, \phi) \sum_j C_j S_j(r) = Y_m^l(\theta, \phi) R_{nl}(r), \quad (\text{S10})$$

where  $n$ ,  $l$ , and  $m$  are the principle, azimuthal and magnetic quantum numbers, and  $Y_m^l(\theta, \phi)$  are the spherical harmonics. The Slater-type radial orbital  $S(r)$  has the general form

$$S(r) = N_s r^{n-1} e^{-Zr}, \quad (\text{S11})$$

here  $N_s = \frac{(2Z)^{n+1/2}}{\sqrt{(2n)!}}$  is a normalization constant, and  $Z$  is the orbital exponent. Using the tables in ref. [7] we construct the Tungsten  $5d_{z^2}$  orbital, with the radial part given by (in atomic units)

$$\begin{aligned} R_{5d}(r) = & -1070.29e^{-29.4731r} r^2 - 1297.24e^{-18.363r} r^2 \\ & + 1192.26e^{-12.073r} r^3 + 239.385e^{-7.9781r} r^3 \\ & - 56.2785e^{-5.19312r} r^4 - 7.74766e^{-3.14551r} r^4 \\ & - 0.18956e^{-1.79159r} r^4, \end{aligned} \quad (\text{S12})$$

and the angular part is  $Y_0^2(\theta, \phi) = \frac{1}{4}\sqrt{\frac{5}{\pi}}(3\cos^2\theta - 1)$ .

We separate the calculation of the matrix element into two parts, first taking  $\vec{R} = 0$  giving the on-site contribution, and then allowing for  $\vec{R} \neq 0$ . For the on-site contribution with  $\vec{R} = 0$ , we expand the Coulomb potential in spherical harmonics

$$\frac{1}{|\vec{r}_2 - \vec{r}_1|} = \sum_{l=0}^{\infty} \frac{r_<^l}{r_>^{l+1}} \sum_{m=-l}^{m=l} \frac{4\pi}{2l+1} Y_m^l(\theta', \phi') Y_m^l(\theta, \phi), \quad (\text{S13})$$

which allows to separate the radial and angular integrations. The angular integration consists of products of three spherical harmonics which can be written in terms of Wigner 3j-symbols,

$$\begin{aligned} & \int Y_{m_1}^{l_1}(\theta, \phi) Y_{m_2}^{l_2}(\theta, \phi) Y_{m_3}^{l_3}(\theta, \phi) \sin \theta d\theta d\phi \\ &= \sqrt{\frac{(2l_1 + 1)(2l_2 + 1)(2l_3 + 1)}{4\pi}} \begin{pmatrix} l_1 & l_2 & l_3 \\ 0 & 0 & 0 \end{pmatrix} \begin{pmatrix} l_1 & l_2 & l_3 \\ m_1 & m_2 & m_3 \end{pmatrix}. \end{aligned} \quad (\text{S14})$$

The Wigner 3j-symbols impose selection rules on the possible values of the different angular momentum quantum numbers, thus reducing the number of terms in the sum and the number of integrations needed. In particular we must have,  $m_1 + m_2 + m_3 = 0$ ,  $|m_i| < l_i$ , and  $|l_1 - l_2| \leq l_3 \leq l_1 + l_2$ .

For the case of non-zero  $\vec{R}$ , since the wave functions have a typical spread smaller than the lattice constant, we use the following expansion<sup>8,9</sup> valid for  $|\vec{r}_1 + \vec{r}_2| < R$ ,

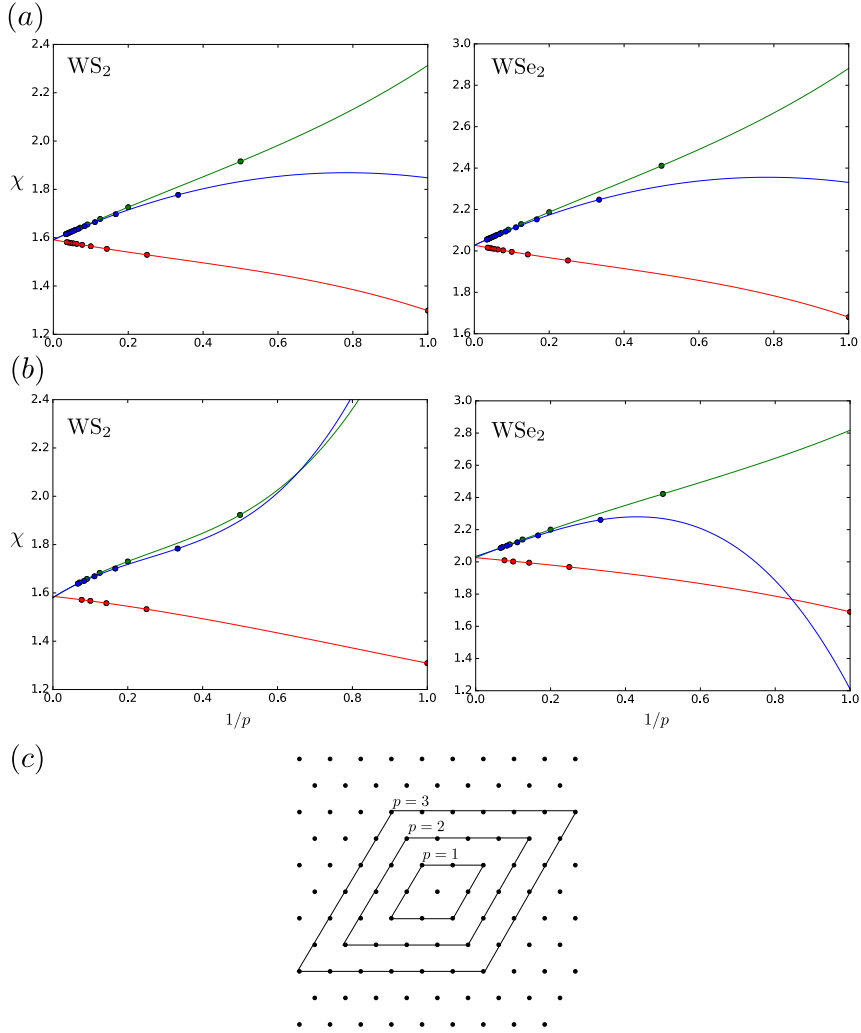


**Figure S2 | Convergence of the intervalley scattering matrix element calculation.**

(a) Analytical calculation of the matrix element as a function of the inverse number of lattice points in the summation. (b) Monte Carlo calculation results. We fit the points to third order polynomials and extract the value for  $1/p \rightarrow 0$  corresponding to summation over an infinite lattice. The data points are separated into three sequences with a period of 3, all converging to the same point. This behaviour of the sum is attributed to the phase factor in the summation involving the  $\vec{K}$  vector, and to the rhombic unit cell used in the summation. (c) Sketch of the rhombic unit cell used for the summation over the triangular lattice points for increasing values of  $p$ .

$$\begin{aligned}
\frac{1}{|\vec{r}_2 - \vec{r}_1 + \vec{R}|} &= \sum_{l_a, l_b=0}^{\infty} R^{-(l_a+l_b+1)} r_1^{l_a} r_2^{l_b} V_{l_a, l_b}; \\
V_{l_a, l_b} &= (4\pi)^{3/2} (-1)^{l_b} \binom{2(l_a + l_b)}{2l_a}^{1/2} \\
&\times [(2l_a + 1)(2l_b + 1)(2(l_a + l_b) + 1)]^{-1/2} \\
&\times \sum_{M=-(l_a+l_b)}^{l_a+l_b} (-1)^M Y_{-M}^L(\hat{R}) [Y^{l_a}(\hat{r}_1) \otimes Y^{l_b}(\hat{r}_2)]_M^{l_a+l_b}; \\
[Y^{l_a}(\hat{r}_1) \otimes Y^{l_b}(\hat{r}_2)]_M^{l_a+l_b} &= \sum_{m_a=-l_a}^{l_a} \sum_{m_b=-l_b}^{l_b} Y_{m_a}^{l_a}(\hat{r}_1) Y_{m_b}^{l_b}(\hat{r}_2) \\
&\times \langle l_a m_a; l_b m_b | (l_a + l_b) M \rangle.
\end{aligned} \tag{S15}$$

In Fig. S1 we show the convergence of the summation using both the detailed analytical method and a Monte Carlo calculation of the integral in Eq. (S9), showing that both methods converge to the same value for the dimensionless matrix element  $\chi$ .

### S3 Trion and biexciton oscillator strength estimation

The oscillator strength of the semi-dark trion and biexciton originates from the component of the excited bright state  $(T^*, B^*)$  in the mixed semi-dark and bright states. We express it using the oscillator strength of the exciton utilizing the fact that both the trion and biexciton can be regarded as a strongly bound exciton which is weakly bound to an electron in the trion case and another exciton in the biexciton case.

The oscillator strength is parametrized using  $\alpha_{T/B}$  in Eq. (4) of the main text, giving the radiative rate of the semi-dark states in terms of the exciton radiative rate. To obtain the value of this parameter we write the excited trion and biexciton wavefunciton as a symmetrized product of an exciton and an electron in the trion case, and a symmetrized product of two excitons in the biexciton case.

For the excited trion we have,

$$\Psi_T(\mathbf{r}_{e1}^{K\uparrow}, \mathbf{r}_{e2}^{K'\downarrow}, \mathbf{r}_{h1}^{K\uparrow}) = \frac{\Psi_X(\mathbf{r}_{e1}^{K\uparrow}, \mathbf{r}_{h1}^{K\uparrow})\Psi_e(\mathbf{r}_{e2}^{K'\downarrow}) + \Psi_X(\mathbf{r}_{e2}^{K'\downarrow}, \mathbf{r}_{h1}^{K\uparrow})\Psi_e(\mathbf{r}_{e1}^{K\uparrow})}{\sqrt{2}}. \quad (\text{S16})$$

The oscillator strength is determined to the electron-hole contact pair density, given by

$$\begin{aligned} g_{eh}^T &= \langle \Psi_T(\mathbf{r}_{e1}^{K\uparrow}, \mathbf{r}_{e2}^{K'\downarrow}, \mathbf{r}_{h1}^{K\uparrow}) | \delta(r_e - r_h) \delta_{\sigma_e, \sigma_h} \delta_{\tau_e, \tau_h} | \Psi_T(\mathbf{r}_{e1}^{K\uparrow}, \mathbf{r}_{e2}^{K'\downarrow}, \mathbf{r}_{h1}^{K\uparrow}) \rangle \\ &= \frac{1}{2} \int d^2 \mathbf{r}_{e1} |\Psi_X(\mathbf{r}_{e1}, \mathbf{r}_{e1})|^2 = \frac{g_{eh}^X}{2}. \end{aligned} \quad (\text{S17})$$

where  $\sigma_e, \sigma_h$  are the spins of the electron and hole,  $\tau_e, \tau_h$  are the valley indexes, and  $g_{eh}^X$  is the electorn-hole contact pair density of the exciton. Therefore we get  $\alpha_T = 1/2$ .

Similarly, for the biexciton

$$\Psi_B(\mathbf{r}_{e1}^{K\uparrow}, \mathbf{r}_{e2}^{K'\downarrow}, \mathbf{r}_{h1}^{K\uparrow}, \mathbf{r}_{h2}^{K'\downarrow}) = \frac{\Psi_X(\mathbf{r}_{e1}^{K\uparrow}, \mathbf{r}_{h1}^{K\uparrow})\Psi_X(\mathbf{r}_{e2}^{K'\downarrow}, \mathbf{r}_{h2}^{K'\downarrow}) + \Psi_X(\mathbf{r}_{e2}^{K'\downarrow}, \mathbf{r}_{h1}^{K\uparrow})\Psi_X(\mathbf{r}_{e1}^{K\uparrow}, \mathbf{r}_{h2}^{K'\downarrow})}{\sqrt{2}}. \quad (\text{S18})$$

The corresponding electron-hole contact pair density

$$g_{eh}^B = \frac{1}{2} \left( \int d^2 \mathbf{r}_{e1} |\Psi_X(\mathbf{r}_{e1}, \mathbf{r}_{e1})|^2 + \int d^2 \mathbf{r}_{e2} |\Psi_X(\mathbf{r}_{e2}, \mathbf{r}_{e2})|^2 \right) = g_{eh}^X. \quad (\text{S19})$$

The two terms in the parenthesis come from the two excitons in the two vallyes both being able to recombine, giving  $\alpha_B = 1$ .

1. Liu, G. B., Xiao, D., Yao, Y., Xu, X. and Yao, W. Electronic structures and theoretical modelling of two-dimensional group-vib transition metal dichalcogenides. *Chem. Soc. Rev.*, 44:2643–2663, 2015.
2. Kormanyos, A. et al. k.p theory for two-dimensional transition metal dichalcogenide semiconductors. *2D Materials*, 2(2):022001, 2015.
3. Danovich, M., Zólyomi, V., Fal'ko, V. I., and Aleiner, I. L. Auger recombination of dark excitons in ws 2 and wse 2 monolayers. *2D Materials*, 3(3):035011, 2016.
4. Basko, D. M. Theory of resonant multiphonon Raman scattering in graphene. *Phys. Rev. B*, 78:125418, Sep 2008.
5. Syniszewski, M., Mostaani, E., Drummond, N. D., Aleiner, I., and Fal'ko, V. I. Binding energies of trions and biexcitons in two-dimensional semiconductors from diffusion quantum Monte Carlo calculations. *Phys. Rev. B*, 95:081301, Feb 2017.
6. Wu, Y., Tong, Q., Liu, G. B., Yu, H., and Yao, W. Spin-valley qubit in nanostructures of monolayer semiconductors: Optical control and hyperfine interaction. *Phys. Rev. B*, 93:045313, Jan 2016.
7. McLean, A. D. and R. S. McLean, R. S. Roothaan–hartree–fock atomic wave functions slater basis-set expansions for z=55–92. *Atomic Data and Nuclear Data Tables*, 26(3–4):197–381, 1981.

8. Solov'yov, I. A., Yakubovich A. V., Solov'yov, A. V. and Greiner, W. Two-center-multipole expansion method: Application to macromolecular systems. *Phys. Rev. E*, 75:051912, May 2007.
9. Paolo, A. *Intermolecular Forces and Their Evaluation by Perturbation Theory*, volume 25 of *Lecture Notes in Chemistry*. Springer, Berlin, 1981.
10. Kresse, G. and Furthmüller, J. Efficient iterative schemes for *ab initio* total-energy calculations using a plane-wave basis set. *Phys. Rev. B*, 54:11169–11186, Oct 1996.

### 4.3 Diffusion quantum Monte Carlo study of excitonic complexes in TMDCs

The results presented in this section are reported in [23]: “Diffusion quantum Monte Carlo study of excitonic complexes in two-dimensional transition-metal dichalcogenides”, Physical Review B **96** (7), 075431 (2017).

My contribution to this work: Performed the group theory classification of the excitonic complexes and written Section II.B . Contributed to preparation of Figures 1, 2 and 4.

Full author list: E. Mostaani, M. Szyniszewski, C. H. Price, R. Maezono, M. Danovich, R. J. Hunt, N. D. Drummond, V. I. Fal’ko

Author contributions: E.M., M.S., C.P., R.H. and N.D. performed the diffusion quantum Monte Carlo calculations and wrote the manuscript with V.F.

# Diffusion quantum Monte Carlo study of excitonic complexes in two-dimensional transition-metal dichalcogenides

E. Mostaani

*Department of Physics, Lancaster University, Lancaster LA1 4YB, United Kingdom  
and Cambridge Graphene Centre, Engineering Department, University of Cambridge, 9 J. J. Thomson Avenue, Cambridge CB3 0FA, United Kingdom*

M. Szymiszewski

*National Graphene Institute, University of Manchester, Booth Street East, Manchester M13 9PL, United Kingdom  
and Department of Physics, Lancaster University, Lancaster LA1 4YB, United Kingdom*

C. H. Price

*Department of Physics, Lancaster University, Lancaster LA1 4YB, United Kingdom*

R. Maezono

*Japan Advanced Institute of Science and Technology, School of Information Science, Asahidai 1-1, Nomi, Ishikawa 923-1292, Japan*

M. Danovich

*National Graphene Institute, University of Manchester, Booth Street East, Manchester M13 9PL, United Kingdom*

R. J. Hunt

*Department of Physics, Lancaster University, Lancaster LA1 4YB, United Kingdom*

N. D. Drummond

*Department of Physics, Lancaster University, Lancaster LA1 4YB, United Kingdom*

V. I. Fal'ko

*National Graphene Institute, University of Manchester, Booth Street East, Manchester M13 9PL, United Kingdom*

(Received 14 June 2017; revised manuscript received 28 July 2017; published 22 August 2017)

Excitonic effects play a particularly important role in the optoelectronic behavior of two-dimensional semiconductors. To facilitate the interpretation of experimental photoabsorption and photoluminescence spectra we provide (i) statistically exact diffusion quantum Monte Carlo binding-energy data for a Mott-Wannier model of (donor/acceptor-bound) excitons, trions, and biexcitons in two-dimensional semiconductors in which charges interact via the Keldysh potential, (ii) contact pair-distribution functions to allow a perturbative description of contact interactions between charge carriers, and (iii) an analysis and classification of the different types of bright trions and biexcitons that can be seen in single-layer molybdenum and tungsten dichalcogenides. We investigate the stability of biexcitons in which two charge carriers are indistinguishable, finding that they are only bound when the indistinguishable particles are several times heavier than the distinguishable ones. Donor/acceptor-bound biexcitons have similar binding energies to the experimentally measured biexciton binding energies. We predict the relative positions of all stable free and bound excitonic complexes of distinguishable charge carriers in the photoluminescence spectra of WSe<sub>2</sub> and MoSe<sub>2</sub>.

DOI: [10.1103/PhysRevB.96.075431](https://doi.org/10.1103/PhysRevB.96.075431)

## I. INTRODUCTION

The last decade has witnessed a remarkable surge of interest in the properties of truly two-dimensional (2D), atomically thin semiconductors. These include monolayer transition-metal dichalcogenides (TMDCs) such as MoS<sub>2</sub>, MoSe<sub>2</sub>, WS<sub>2</sub>, and WSe<sub>2</sub>, which acquire a direct-gap character in hexagonal

monolayer form [1–4]. The direct gap and strong optical absorption of TMDCs suggest a range of potential optoelectronic applications, e.g., in photodetectors, photovoltaics, and light-emitting diodes. A particularly interesting aspect of monolayer TMDCs is the strong excitonic effects present in their photoabsorption and photoluminescence spectra [5–7], including nonhydrogenic Rydberg spectra [8,9] and lines ascribed to trions (charged excitons) [10–12] and biexcitons (bound pairs of excitons) [13–16]. The nonhydrogenic nature of the excitonic energy spectrum is due to lateral polarization effects in 2D crystals, which modify the form of the Coulomb interaction between charge carriers. Mott-Wannier models of 2D trions and biexcitons have been studied using quantum Monte Carlo (QMC) methods [17–25], variational methods [26–28], and

Published by the American Physical Society under the terms of the Creative Commons Attribution 4.0 International license. Further distribution of this work must maintain attribution to the author(s) and the published article's title, journal citation, and DOI.

hyperspherical harmonics approaches [29], and interpolation formulas linking the 2D-screened and  $1/r$  Coulomb interaction regimes have been proposed. Here we extend these studies to provide numerically exact binding-energy data for all nonlocal screening strengths, including an analysis of limiting behavior, and we classify the types of trions and biexcitons that can be observed in different TMDCs. We also investigate donor- and acceptor-bound charge-carrier complexes in TMDCs, such as donor-bound biexcitons and quintons, which have not to our knowledge been studied before.

The rest of the article is structured as follows. In Sec. II we describe the band structures of molybdenum and tungsten dichalcogenides and analyze the nature of the trions and biexcitons in these materials; furthermore, we perform a group theoretical analysis of exciton properties. In Sec. III we explain the Keldysh form of the screened Coulomb interaction between charges in 2D semiconductors, describe the ways in which charge-carrier complexes are expected to dissociate and recombine, and explain the importance of the contact pair distribution function (PDF). In Sec. IV we describe our computational methodology for solving the Mott-Wannier model of charge-carrier complexes. We present our numerical results for the binding energies and PDFs of the different complexes in Sec. V. Finally, we draw our conclusions in Sec. VI.

## II. BRIGHT AND DARK BIEXCITONS AND TRIONS IN MOYBDENUM AND TUNGSTEN DICHALCOGENIDES

### A. Classification of trions and biexcitons

In monolayer molybdenum and tungsten dichalcogenides the conduction-band minimum and valence-band maximum

occur at the  $K$  and  $K'$  points of the hexagonal Brillouin zone. Spin-orbit coupling induces a significant splitting of both the valence band and the conduction band at  $K$  and  $K'$ . In molybdenum diselenides, the valence-band maximum has the same spin as the conduction-band minimum within each valley, while in tungsten dichalcogenides such states have opposite spins [3]. Figure 1(a) presents examples of the ways in which biexcitons can be formed in molybdenum and tungsten dichalcogenides. The spin-splitting of the valence band (0.15–0.5 eV) is sufficiently large that no holes in the lower spin-split valence band are expected at room temperature; however, the spin splitting of the conduction band ( $\Delta' = 3\text{--}50 \text{ meV}$ ) is small enough that electrons can be found in the upper spin-split conduction band at room temperature [3].

An exciton, biexciton, or trion is said to be either *dark* or *semidark* when the recombination of an electron and hole is forbidden by spin and momentum conservation; otherwise the complex is said to be *bright*. Semidark complexes are those in which recombination can in fact take place due to intervalley scattering with an accompanying energy shift. The precise photon energies depend on whether the electrons occupy the higher- or lower-energy spin-split bands in the initial and final states. Furthermore, the intensity of a spectral line depends on the thermal occupancy of the initial state. Figures 1(b) and 1(c) present a classification of biexcitons in molybdenum and tungsten dichalcogenides with respect to the recombination energy and the intensity of the emitted photons. This intensity has the following temperature dependence:

$$I(T) \sim \begin{cases} \text{const.} & \text{for no electrons in the upper spin-split conduction band,} \\ e^{-\Delta'/k_B T} & \text{for one electron in the upper spin-split conduction band,} \\ e^{-2\Delta'/k_B T} & \text{for two electrons in the upper spin-split conduction band,} \end{cases} \quad (1)$$

where  $\Delta'$  is the spin-orbit-induced splitting of the conduction band,  $k_B$  is Boltzmann's constant, and  $T$  is the temperature. A similar classification can be made for trions; see Fig. 2. In a photoluminescence experiment, we expect to see energies attributed to different kinds of biexcitons and trions and emission lines of varying intensity, as explained in Sec. III C.

The opposite spin splittings of the conduction and valence bands in tungsten dichalcogenides result in the ground-state trions and biexcitons being dark, with the two electrons residing in opposite valleys. These dark complexes are coupled through an intervalley electron-electron scattering to their excited bright counterparts with both electrons residing in the upper spin-split conduction band. This coupling gives a finite oscillator strength to the dark ground states that is proportional to  $[\mu_{bd}/(2\Delta')]^2$ , where  $\mu_{bd}$  is the coupling matrix element between dark and bright states. As a result, the expected photoluminescence spectrum contains two additional lines resulting from the recombination of these “semidark” trions and biexcitons, at an energy shifted downwards by  $2\Delta'$  relative to the bright complexes, and having a temperature-independent intensity.

### B. Group theoretical analysis of excitons

Exciton wave functions can be classified according to the irreducible representation (irrep) of the point-group symmetry of the TMDC crystal,  $D_{3h}$ . As the states in the two valleys are degenerate, one can treat the two valleys simultaneously by using the extended group  $D''_{3h} = D_{3h} + tD_{3h} + t^2D_{3h}$ , where  $t$  denotes translation by a lattice vector. The character table of the extended group is given in Table IX.

TABLE I. Classification of exciton states into irreps of  $D''_{3h}$  and the polarization ( $\parallel$  and  $z$  for in-plane and out-of-plane, respectively) of the electric field to which the excitons are coupled.

Irrep	Excitons	Field
$E^+$	$X_{K\uparrow}^{K\uparrow}, X_{K'\downarrow}^{K'\downarrow}$	$E_{\parallel}$
$E^+$	$X_{K\downarrow}^{K\uparrow}, X_{K'\uparrow}^{K'\downarrow}$	
$A_2^-$	$X(\text{dark}): \{X_{K\uparrow}^{K\downarrow} - X_{K'\uparrow}^{K'\downarrow}\}$	$E_z$
$E^-$	$X_{K\uparrow}^{K\downarrow}, X_{K'\uparrow}^{K'\downarrow}$	
$A_1^-$	$\{X_{K\downarrow}^{K\uparrow} + X_{K'\uparrow}^{K'\downarrow}\}$	

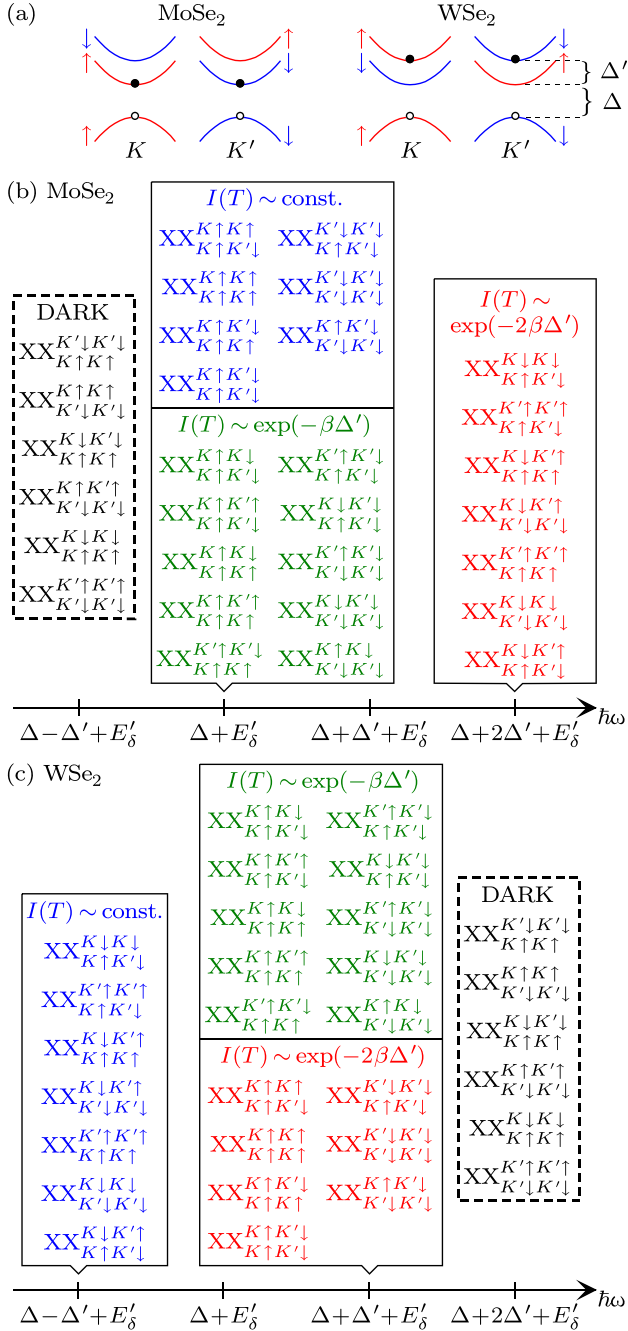
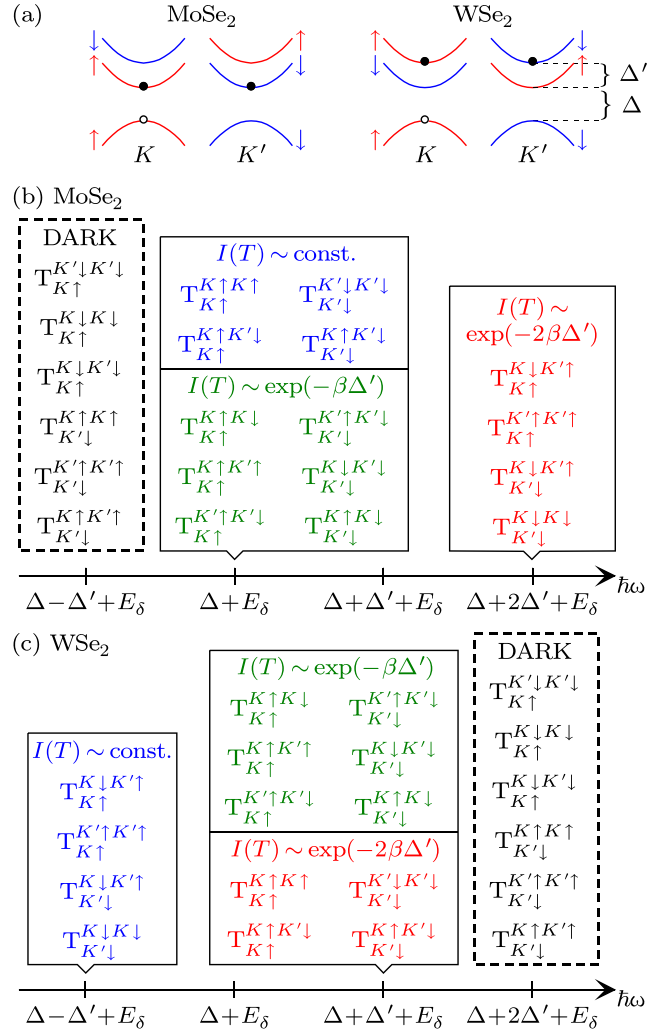


FIG. 1. (a) Spin-split valence and conduction bands for MoSe<sub>2</sub> (left) and WSe<sub>2</sub> and WS<sub>2</sub> (right). We only show the spin splitting of the conduction band; the spin splitting of the valence band is much larger, so that no holes in the lower spin-split valence band are expected at room temperature [3]. (b) and (c) Classification of biexciton recombination processes in molybdenum and tungsten dichalcogenides, respectively.  $\Delta$  is the band gap, while  $\Delta'$  is the spin splitting of the conduction band.  $E'_\delta \equiv E_{XX} - E_X$  is the difference between the total energies  $E_{XX}$  and  $E_X$  of a biexciton and an exciton.  $\hbar\omega$  indicates the photon energies at which peaks in photoluminescence spectra are expected to appear.  $XX_{k_1\sigma_1 k_2\sigma_2}^{k_3\sigma_3 k_4\sigma_4}$  denotes a biexciton consisting of conduction-band electrons in valleys  $k_1$  and  $k_2$  with spins  $\sigma_1$  and  $\sigma_2$  and valence-band holes in valleys  $k_3$  and  $k_4$  with spins  $\sigma_3$  and  $\sigma_4$ . For example, the biexcitons shown in (a) are both denoted by  $XX_{K\downarrow K'\uparrow}^{K\uparrow K'\downarrow}$ .



The total exciton wave function  $X$  is given in general by the product of three components: the spatial envelope function  $\Phi$ , the Bloch or lattice wave functions of the electron and hole  $U_k$ , and the spin part  $\chi$ :

$$X = \Phi(\mathbf{r}_e, \mathbf{r}_h) \otimes U_k(\mathbf{r}_e, \mathbf{r}_h) \otimes \chi(s_e, s_h). \quad (2)$$

The representations of the wave functions by irreps consist of the direct product of the individual irreps corresponding to the three components:  $\Gamma_X = \Gamma_\Phi \otimes \Gamma_U \otimes \Gamma_\chi$ . The tightly bound ground-state excitons are characterized by a maximally symmetrized envelope function corresponding to the identity irrep  $\Gamma_\Phi = A_1^+$ . Therefore the representations of the exciton states are determined by the irreps of the lattice and spin parts.

The conduction- and valence-band Bloch states transform according to the 2D irreps  $E'_1$  and  $E'_2$ , respectively. Using the product table, Table X, the lattice part of the exciton wave

function transforms as

$$E_1'^+ \otimes E_2'^+ = E^+ \oplus E_3'^+, \quad (3)$$

where the 2D irrep  $E^+$  corresponds to intravalley excitons in the  $K$  and  $K'$  valleys, and  $E_3'^+$  corresponds to intervalley excitons, which are dark due to momentum conservation. In the following, we will consider the  $E^+$  intravalley excitons only.

The exciton spin part consists of two spin-1/2 particles corresponding to the spinor 2D irrep  $D_{1/2}$ . The direct product of the two spinors can be decomposed into the crystal point group irreps as

$$D_{1/2} \otimes D_{1/2} = A_1^+ \oplus A_2^+ \oplus E^-. \quad (4)$$

Hence the total exciton representation is given by

$$E_{\text{lattice}}^+ \otimes (A_1^+ \oplus A_2^+ \oplus E^-)_{\text{spin}} = 2E^+ \oplus A_1^- \oplus A_2^- \oplus E^-. \quad (5)$$

The  $E^+$  irrep corresponds to the vector representation, and therefore the two  $E^+$  irreps correspond to excitons coupled to in-plane polarized light. The  $z$  coordinate transforms as the  $A_2^-$  irrep, and therefore the  $A_2^-$  exciton is coupled to out-of-plane polarized light, which involves a spin-flip process in recombination [30]. In the case of tungsten dichalcogenides, the  $A_2^-$  exciton is the ground-state exciton, and results in photon emission at an energy that is lower than the excited bright exciton by the spin-orbit splitting of the conduction band  $\Delta'$ . The  $A_1^-$  and  $E^-$  excitons are not coupled to light. A summary of the classification of exciton states is given in Table I using a notation similar to that used in Figs. 1 and 2. Finally, we note that the spin-flip transition resulting in the emission of out-of-plane polarized light corresponding to the  $A_2^-$  exciton is also relevant for ground-state trions and biexcitons in tungsten dichalcogenides, resulting in trion or biexciton emission at a photon energy shifted downwards relative to the excited bright states by  $\Delta'$ .

### III. CHARGE-CARRIER COMPLEXES IN 2D SEMICONDUCTORS

#### A. Screened Coulomb interaction between charge carriers

We model the charge carriers in a 2D semiconductor using a Mott-Wannier model, in which small numbers of quasielectrons and quasiholes are treated within the band effective mass approximation and interact via an appropriately screened Coulomb interaction. The band effective masses for different 2D semiconductors are assumed to be 2D-isotropic, and are discussed in Sec. V B 2. However, unlike quasi-2D electron(-hole) systems in GaAs/InAs heterostructures, the form of the Coulomb interaction is profoundly affected by the 2D nature of single-layer TMDCs, as we will now discuss.

Consider a charge density  $\rho(x, y)\delta(z)$  in the  $z = 0$  plane of the 2D material, embedded in an isotropic medium of permittivity  $\epsilon$ . The resulting electric displacement field is  $\mathbf{D} = -\epsilon\nabla\phi + \mathbf{P}_\perp(x, y)\delta(z) = -\epsilon\nabla\phi - \kappa[\nabla\phi(x, y, 0)]\delta(z)$ , where  $\phi$  is the electrostatic potential,  $\mathbf{P}_\perp(x, y)$  is the in-plane polarization, and  $\kappa$  is the in-plane susceptibility of the material. By using Gauss's law,  $\nabla \cdot \mathbf{D} = \rho\delta(z)$ , we obtain

$$\epsilon\nabla^2\phi = -\rho\delta(z) - \kappa[\nabla^2\phi(x, y, 0)]\delta(z). \quad (6)$$

After taking the Fourier transform, denoting the wave vector in the  $(x, y)$  plane by  $\mathbf{q}$ , and the wave number in the  $z$  direction by  $k$ , we find

$$\phi(\mathbf{q}, k) = \frac{\rho(\mathbf{q}) - \kappa q^2 \phi(\mathbf{q}, z=0)}{\epsilon(q^2 + k^2)}. \quad (7)$$

However

$$\begin{aligned} \phi(\mathbf{q}, z=0) &= \frac{1}{2\pi} \int \phi(\mathbf{q}, k) dk \\ &= \frac{1}{2\epsilon q} [\rho(\mathbf{q}) - \kappa q^2 \phi(\mathbf{q}, z=0)]. \end{aligned} \quad (8)$$

Rearranging, we find the in-plane electric potential to be

$$\phi(\mathbf{q}, z=0) = \frac{\rho(\mathbf{q})}{q(2\epsilon + q\kappa)}. \quad (9)$$

Therefore the electrostatic potential energy between charges  $q_i$  and  $q_j$  in a 2D semiconductor is

$$v(q) = \frac{q_i q_j}{2\epsilon q(1 + r_* q)}, \quad (10)$$

where  $r_* \equiv \kappa/(2\epsilon)$ . After taking the Fourier transform, the potential energy can be written as

$$v(r) = \frac{q_i q_j}{4\pi \epsilon r_*} V\left(\frac{r}{r_*}\right), \quad (11)$$

where  $r$  is the separation of the particles and

$$V(r/r_*) = \frac{\pi}{2} \left[ H_0\left(\frac{r}{r_*}\right) - Y_0\left(\frac{r}{r_*}\right) \right], \quad (12)$$

where  $H_n(x)$  is a Struve function and  $Y_n(x)$  is a Bessel function of the second kind. This result was first derived by Keldysh [31], and we refer to the interaction of Eq. (12) as the *Keldysh interaction*. At long range ( $r \gg r_*$ ) this potential becomes a Coulomb interaction:

$$V(r/r_*) \approx r_*/r, \quad (13)$$

while at short range ( $r \ll r_*$ ) it is approximately logarithmic:

$$V(r/r_*) \approx [\ln(2r_*/r) - \gamma] = \ln\left(\frac{2r_*}{\exp(\gamma)r}\right), \quad (14)$$

where  $\gamma$  is Euler's constant. We refer to the interaction potential of Eq. (14) as the *logarithmic interaction*. The Keldysh interaction is plotted in Fig. 3, along with the Coulomb ( $r_* = 0$ ) and logarithmic ( $r_* \rightarrow \infty$ ) approximations.

The following approximation to Eq. (12) was introduced in Ref. [32]:

$$V(r/r_*) \approx -\ln\left(\frac{r/r_*}{1+r/r_*}\right) - [\gamma - \ln(2)]e^{-r/r_*}. \quad (15)$$

This form of potential was used in the diffusion quantum Monte Carlo (DMC) study of Ref. [21]. It is also plotted in Fig. 3, where it can be seen that the error in Eq. (15) is as large as several percent in the region  $r \approx r_*$ . We compare DMC results obtained using Eqs. (12) and (15) in Sec. IV F.

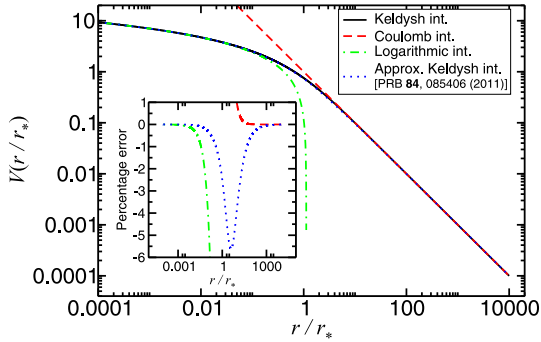


FIG. 3. Dimensionless interaction potential between charge carriers in a 2D semiconductor, as defined in Eq. (11). The inset shows the percentage error in different approximations [Eqs. (13), (14), and (15)] to the Keldysh interaction of Eq. (12).

Finally, the Mott-Wannier-Keldysh Schrödinger equation for a set of charged quasiparticles in a 2D semiconductor is

$$\left[ -\sum_i \frac{\hbar^2}{2m_i} \nabla_i^2 + \sum_{i>j} \frac{q_i q_j}{4\pi\epsilon r_*} V\left(\frac{r_{ij}}{r_*}\right) \right] \psi = E\psi, \quad (16)$$

where  $m_i$  and  $q_i$  are the band effective mass and charge of particle  $i$ ,  $r_{ij}$  is the separation of particles  $i$  and  $j$ , and  $E$  is the energy eigenvalue.

Now consider the situation in which the 2D semiconductor has a dielectric medium of permittivity  $\epsilon_a$  above it and a dielectric medium of permittivity  $\epsilon_b$  below it, as would be the case for a 2D semiconductor deposited on a substrate. In general this is a more complicated problem than the situation described above. However, if we take  $\epsilon \equiv (\epsilon_a + \epsilon_b)/2$  in the expressions above, the correction to the electrostatic energy of Eq. (11) is second order in  $\epsilon_a - \epsilon_b$ . Hence the Keldysh interaction remains valid when the permittivity  $\epsilon$  is chosen to be the average of the permittivities of the media on either side of the 2D semiconductor, provided these permittivities are similar.

## B. Units and scaling

### 1. Excitonic units

The energies of complexes interacting via the Keldysh or Coulomb interactions are given in terms of the exciton Rydberg,  $R_y^* = \mu e^4 / [2(4\pi\epsilon)^2 \hbar^2]$ , and lengths are given in terms of the exciton Bohr radius,  $a_0^* = 4\pi\epsilon\hbar^2 / (\mu e^2)$ , where  $\mu = m_e m_h / (m_e + m_h)$  is the reduced mass of electron-hole pairs, with  $m_e$  and  $m_h$  being the electron and hole masses, respectively.

Let  $\tilde{\mathbf{r}}_i = \mathbf{r}_i/a_0^*$ . Then Eq. (16) can be written as

$$\left[ -\sum_i \frac{\mu}{m_i} \tilde{\nabla}_i^2 + \sum_{i>j} \frac{2q_i q_j a_0^*}{e^2 r_*} V\left(\frac{\tilde{r}_{ij} a_0^*}{r_*}\right) \right] \psi = \mathcal{E}\psi, \quad (17)$$

where  $\mathcal{E} = E/R_y^*$ . Note that  $\mu/m_i$  only depends on the electron-hole mass ratio  $\sigma \equiv m_e/m_h$ . Hence for a fixed value of  $r_*/a_0^*$ , the dimensionless energy eigenvalues  $\mathcal{E}$  only depend on the mass ratio, not on the absolute masses. Furthermore, for an exciton we may write the Schrödinger equation in terms of the difference coordinate  $\mathbf{r}_{ch}$  as

$$\left[ -\tilde{\nabla}_{ch}^2 - \frac{2a_0^*}{r_*} V\left(\frac{\tilde{r}_{ch} a_0^*}{r_*}\right) \right] \psi = \mathcal{E}_X \psi, \quad (18)$$

so that for a given value of  $r_*/a_0^*$ , the dimensionless exciton energy eigenvalues  $\mathcal{E}_X$  are also independent of the mass ratio. For the case of the Coulomb interaction ( $r_* = 0$ ), the dimensionless ground-state energy of an isolated exciton is  $\mathcal{E}_X = -4$ , irrespective of the mass of the electron or the hole. The binding energies in excitonic Rydbergs of donor-bound trions, biexcitons, and donor-bound biexcitons only depend on  $r_*/a_0^*$  and the electron-hole mass ratio  $\sigma$ . Unfortunately, the energies of the different complexes go to zero in these units in the limit that  $r_* \rightarrow \infty$ , and so a separate set of units is required for the case of the logarithmic interaction, as discussed in Sec. III B 2.

### 2. Logarithmic interaction

For the limit  $r_* \rightarrow \infty$ , where the interaction is of logarithmic form, we use the dimensionless units introduced in Ref. [19]. The Schrödinger equation for a charge carrier complex with the logarithmic approximation to the interaction [Eq. (14)] is

$$\left[ -\sum_i \frac{\hbar^2}{2m_i} \nabla_i^2 + \sum_{i>j} \frac{q_i q_j}{4\pi\epsilon r_*} \ln\left(\frac{2r_*}{\exp(\gamma)r}\right) \right] \psi = E\psi. \quad (19)$$

Let

$$r_0 = \sqrt{\frac{4\pi\epsilon r_* \hbar^2}{2e^2 \mu}} \quad (20)$$

and

$$E_0 = \frac{e^2}{4\pi\epsilon r_*}. \quad (21)$$

Defining dimensionless coordinates  $\tilde{\mathbf{r}}_i = \mathbf{r}_i/r_0$  and a dimensionless energy  $\mathcal{E} = E/E_0$ , the Schrödinger equation can be written as

$$\left\{ -\sum_i \frac{\mu}{m_i} \tilde{\nabla}_i^2 - \sum_{i>j} \frac{q_i q_j}{e^2} [\ln(\tilde{r}_{ij}) + \ln(r_0/r_*) + \gamma - \ln(2)] \right\} \psi = \mathcal{E}\psi. \quad (22)$$

The only dependence of the dimensionless energy  $\mathcal{E}$  of the complex on  $r_*$  is through the pairwise additive constant

$$\mathcal{C} = - \sum_{i>j} \frac{q_i q_j}{e^2} \ln(r_0/r_*). \quad (23)$$

Note that

$$\sum_{i>j} \frac{q_i q_j}{e^2} = \begin{cases} -1 & \text{for an exciton or donor atom,} \\ -1 & \text{for a trion or donor-bound exciton,} \\ -2 & \text{for a biexciton or donor-bound trion,} \\ -2 & \text{for a donor-bound biexciton,} \\ \frac{(n_+ - n_-)^2 - n_+ - n_-}{2} & \text{for a complex of } n_+ \text{ charges } +e \text{ and } n_- \text{ charges } -e. \end{cases} \quad (24)$$

Hence the additive constant  $C$  cancels out of the binding energies of the different charge-carrier complexes defined in Sec. III C.

For an isolated exciton, we may write the Schrödinger equation in terms of the difference coordinate  $r_{\text{eh}}$  and reduced mass, giving

$$[-\tilde{\nabla}_{\text{eh}}^2 + \ln(\tilde{r}_{\text{eh}}) + \ln(r_0/r_*) + \gamma - \ln(2)]\psi = \mathcal{E}_X \psi. \quad (25)$$

The only dependence of the dimensionless energy eigenvalue  $\mathcal{E}_X$  on the mass ratio and  $r_*$  comes from the constant term  $\ln(r_0/r_*)$  in the Hamiltonian. Hence we may write the ground-state dimensionless energy as

$$\mathcal{E}_X = \mathcal{E}_{X0} - \ln(r_*/r_0), \quad (26)$$

where  $\mathcal{E}_{X0} = 0.41057747491(7)$  was evaluated by a finite-element method (see Sec. V A).

### C. Binding energies and spectra of charge-carrier complexes

We define the binding energies  $E_{X^-}^b$ ,  $E_{XX}^b$ ,  $E_{D^+X}^b$ ,  $E_{D^0X}^b$ , and  $E_{D^+XX}^b$  of a trion, biexciton, donor-bound exciton, donor-bound trion, and donor-bound biexciton, respectively, as follows:

$$E_{X^-}^b = E_X - E_{X^-}, \quad (27)$$

$$E_{XX}^b = 2E_X - E_{XX}, \quad (28)$$

$$E_{D^+X}^b = E_{D^0} - E_{D^+X}, \quad (29)$$

$$E_{D^0X}^b = E_{D^0} + E_X - E_{D^0X}, \quad (30)$$

$$E_{D^+XX}^b = E_{D^0X} - E_{D^+XX}, \quad (31)$$

where  $E_X$ ,  $E_{X^-}$ ,  $E_{XX}$ ,  $E_{D^0}$ ,  $E_{D^+X}$ ,  $E_{D^0X}$ , and  $E_{D^+XX}$  are the ground-state total energies of an exciton, trion, biexciton, donor atom, donor-bound exciton, donor-bound trion, and donor-bound biexciton, respectively. These are the binding energies with respect to dissociation into the most energetically competitive species. With the exceptions of the donor-bound exciton ( $D^+X$ ) and donor-bound biexciton ( $D^+XX$ ), each of the complexes dissociates into an exciton ( $X$ ) plus one other complex. Binding energies of charge-conjugated complexes (such as positive trions, acceptor-bound trions, and acceptor-bound biexcitons) are defined in an analogous fashion. Note that, under the definitions of Eqs. (27)–(31), a binding energy is *positive* for a bound complex.

The energy difference between the exciton peak in a photoluminescence experiment and the peak corresponding to a particular complex is equal to the energy required to separate a single exciton from that complex. Thus the energy difference between the exciton peak and the trion

peak is  $E_X - E_{X^-} = E_{X^-}^b$ , the energy difference between the exciton peak and the biexciton peak is  $2E_X - E_{XX} = E_{XX}^b$ , and the energy difference between the exciton peak and the donor-bound trion peak is  $E_X + E_{D^0} - E_{D^0X} = E_{D^0X}^b$ . On the other hand, the energy difference between the exciton peak and the donor-bound exciton peak is  $E_X - E_{D^+X} = E_{D^+X}^b + E_X - E_{D^0}$ , and the energy difference between the exciton peak and the donor-bound biexciton peak is  $E_X + E_{D^+X} - E_{D^+XX} = E_{D^+XX}^b + E_{D^0X}^b - E_{D^+X}^b$ . Some of these peaks are shown in Fig. 4. In addition there are expected to be offsets to the peak positions due to the spin splitting of the conduction bands of TMDCs, as described in Sec. III.

In Sec. V F we report DMC binding energies for quintons and other large charge-carrier complexes in tungsten and molybdenum dichalcogenides. In each of these cases the binding energy is defined to be the energy required to remove an exciton from the complex; this is the binding energy with respect to dissociation into the most energetically competitive products.

### D. Contact and exchange interactions between charge carriers

The Mott-Wannier model of a charge-carrier complex is valid provided the complex extends over many unit cells of the underlying crystal. However, when charge carriers are present at the same point in space there is an energy contribution due to local exchange and correlation effects [25]. Although the excitons in TMDCs are Mott-Wannier-like, their wave functions only extend over a small number of primitive unit cells, so that local exchange and correlation effects are expected to be significant. We may represent this effect within a Mott-Wannier model by introducing additional pairwise contact interaction potentials. For example, for a biexciton the Hamiltonian should include an additional term of the form

$$A^{ee}\delta(\mathbf{r}_{ee}) + A^{hh}\delta(\mathbf{r}_{hh}) + A^{eh}\sum_{i=1}^2 \sum_{j=1}^2 \delta(\mathbf{r}_{e_i h_j}), \quad (32)$$

where  $A^{ee}$ ,  $A^{hh}$ , and  $A^{eh}$  are constants and  $\mathbf{r}_{ee}$ ,  $\mathbf{r}_{hh}$ , and  $\mathbf{r}_{e_i h_j}$  are the electron-electron separation, the hole-hole separation, and the separation of electron  $i$  and hole  $j$ , respectively. Evaluating  $A^{ee}$ ,  $A^{hh}$ , and  $A^{eh}$  by *ab initio* calculations is challenging, and so we leave them as free parameters to be determined in experiments or subsequent *ab initio* calculations. If we evaluate the expectation value of this contact interaction then we find that the first-order perturbative correction to the total energy can be written as  $A^{eh}g_{XX}^{eh}(\mathbf{0}) + A^{ee}g_{XX}^{ee}(\mathbf{0}) + A^{hh}g_{XX}^{hh}(\mathbf{0})$ , where the electron-electron, hole-hole, and electron-hole

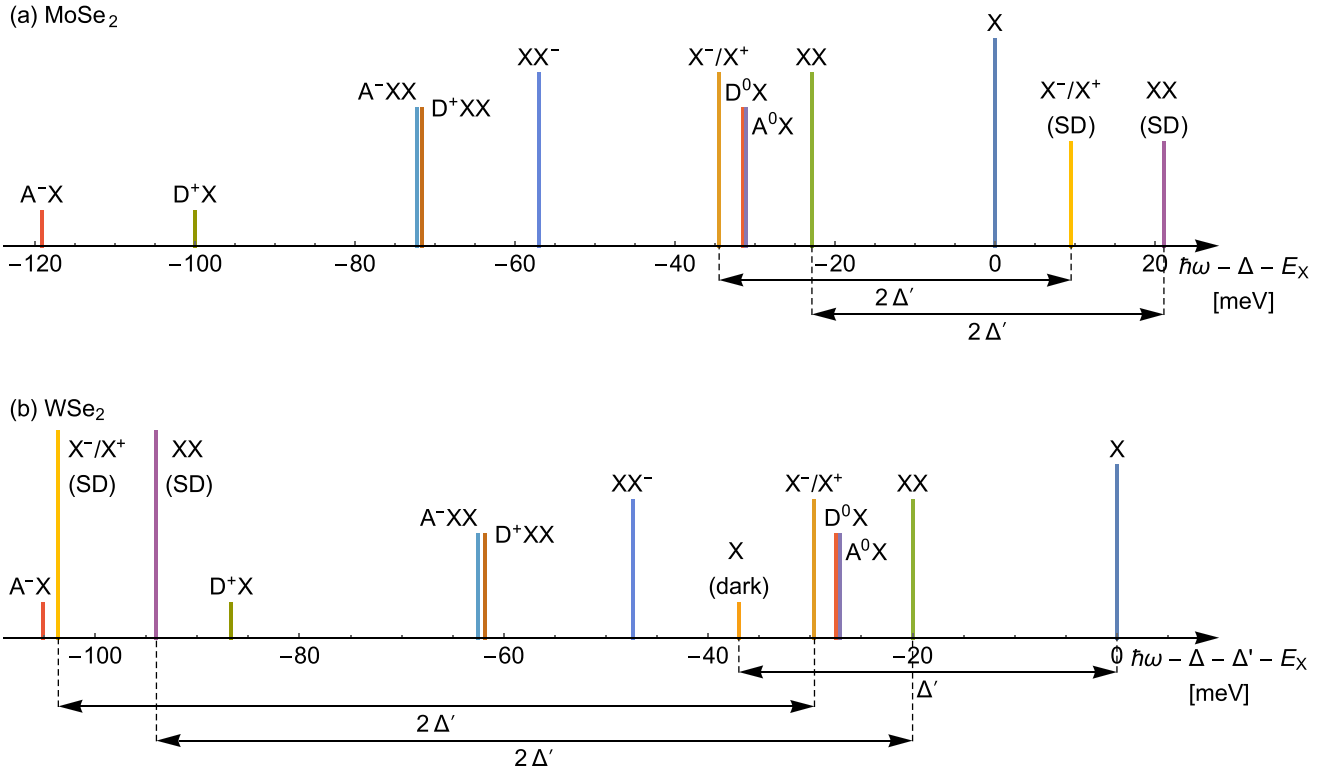


FIG. 4. Expected photoemission spectra for (a) MoSe<sub>2</sub> and (b) WSe<sub>2</sub>, showing lines for the different complexes studied in this work.  $\Delta$  and  $\Delta'$  are the quasiparticle band gap and the spin splitting of the conduction band, respectively. The numerical values of  $\Delta'$  are taken from density-functional-theory calculations with the Heyd-Scuseria-Ernzerhof (HSE06) hybrid functional [3].  $E_X$  is the total energy of an exciton. The lines show the frequency relative to the bright exciton peak arising due to the recombination of a single electron-hole pair in each complex; see Sec. III C. For example, the D<sup>0</sup>X line shows the frequency relative to the exciton peak of the process D<sup>0</sup>X → D<sup>0</sup> +  $\gamma$ . The trion and biexciton peaks labeled “SD” arise from semidark complexes, and are offset by  $2\Delta'$ , as explained in Sec. II A; the exciton peak labeled “dark” arises from the process described in Sec. II B; the other peaks arise from bright complexes. Donor- and acceptor-bound exciton peaks are shown with very low intensity due to the marginal stability of these complexes.

PDFs are

$$g_{XX}^{ee}(\mathbf{r}) = \langle \delta(\mathbf{r} - \mathbf{r}_{ee}) \rangle, \quad (33)$$

$$g_{XX}^{hh}(\mathbf{r}) = \langle \delta(\mathbf{r} - \mathbf{r}_{hh}) \rangle, \quad (34)$$

$$g_{XX}^{eh}(\mathbf{r}) = \left\langle \sum_{i=1}^2 \sum_{j=1}^2 \delta(\mathbf{r} - \mathbf{r}_{e_i h_j}) \right\rangle, \quad (35)$$

respectively. We report contact PDF data within the Mott-Wannier model.

In addition to the role of the contact PDF in evaluating perturbative corrections due to contact interactions, the PDF and contact PDF contain a wealth of physical information. The exciton recombination rate of a charge-carrier complex is proportional to the electron-hole contact PDF. Furthermore, the PDF gives a very direct indication of the spatial size and shape of a charge-carrier complex.

The contact PDF also plays a role in the intervalley scattering of carriers. As the intervalley scattering involves a large momentum transfer of the order of the inverse lattice constant, the interaction is short range and can be modeled by a contact interaction with both carriers in the same position. In particular, the electron-electron contact PDF for the semidark

trion and biexciton in tungsten-based TMDCs determines the coupling strength of the dark and bright states as  $\mu_{bd} \propto g^{ee}(0)$  and hence determines the recombination rates of the semidark states [33].

#### IV. COMPUTATIONAL METHODOLOGY

##### A. Quantum Monte Carlo modeling of excitonic complexes

Our total-energy and PDF calculations were carried out using the variational quantum Monte Carlo (VMC) and DMC approaches [34,35]. The ground-state wave function for a set of interacting, distinguishable particles is nodeless; hence the fixed-node DMC algorithm is exact for all the systems studied in this work with the exception of biexcitons with indistinguishable holes. We used a numerical representation of the potential of Eq. (12) that is accurate to at least eight significant figures. Trial wave functions were optimized using VMC with variance minimization [36,37] and energy minimization [38]. The DMC calculations were performed using time steps in the ratio 1 : 4 with the corresponding target configuration populations being in the ratio 4 : 1. Afterwards, the energies were extrapolated linearly to zero time step and hence, simultaneously, to infinite population. To perform all our calculations, the CASINO code was used [39].

QMC methods have previously been used to study 2D trions with nonlocal screening [19,21] and the Coulomb interaction [22] and 2D biexcitons with the Coulomb interaction (including indirect biexcitons in coupled-quantum-well heterostructures) [17,18,40,41] and in TMDCs with nonlocal screening [21,23]. In a recent work some of the present authors have investigated the binding energies of trions and biexcitons using DMC for a range of susceptibility parameters  $r_*$  and effective masses, and have represented the DMC data using simple interpolation formulas [25]. It was shown that for the applicable range of  $r_*$  values, 2D semiconductors are expected to show larger trion binding energies than biexciton binding energies, in contrast to the situation in quasi-2D systems such as GaAs/InAs quantum wells. Here we extend this work to include extreme cases and donor/acceptor-bound carrier complexes.

## B. Wave functions for complexes of distinguishable charge carriers

Our trial wave functions for complexes of distinguishable charge carriers were of the Jastrow form  $\Psi = \exp[J(\mathbf{R})]$ , where  $\mathbf{R}$  is the vector of all the particle coordinates. The Jastrow exponent  $J(\mathbf{R})$  included a pairwise sum of terms of the form [42].

$$u_{\text{ex2D}}(r) = \frac{[c_1 + \Gamma' \ln(r) + c_2 r]r^2}{1 + c_3 r^2} \quad (36)$$

for the Keldysh and logarithmic interactions, where  $r$  is interparticle distance,  $c_1, c_2 \leq 0$ , and  $c_3 \geq 0$  are optimizable parameters, and

$$\Gamma' = -\frac{q_i q_j m_i m_j}{2a_0^* \mu e^2 r_* (m_i + m_j)} \quad (37)$$

for distinguishable pairs of particles of charge  $q_i$  and  $q_j$  and mass  $m_i$  and  $m_j$ . Different constants  $c_i$  are used for each type of particle pair. This form satisfies the analog of the Kato cusp conditions [43,44]; i.e., it ensures that the local energy  $\Psi^{-1} \hat{H} \Psi$  is nondivergent at coalescence points, where  $\hat{H}$  is the Hamiltonian operator.

Where the interaction between the charge carriers was of Coulomb form, we used pairwise terms of the form

$$u_{\text{ex2D}}(r) = \frac{\Gamma r + c_1 r^2}{1 + c_2 r} \quad (38)$$

in the Jastrow exponent, where  $c_1 \leq 0$  and  $c_2 \geq 0$  are optimizable parameters, and

$$\Gamma = \frac{2q_i q_j m_i m_j}{a_0^* \mu e^2 (m_i + m_j)} \quad (39)$$

for distinguishable pairs of particles of mass  $m_i$  and  $m_j$  and charge  $q_i$  and  $q_j$ . This form satisfies the Kato cusp conditions [43,44].

Donor ions and other infinitely heavy particles were fixed point charges in our calculations. In this case  $u_{\text{ex2D}}$  provided a one-body Jastrow term between the free particles and the fixed particles that satisfies the Kato cusp conditions. In addition, cuspless one-body, two-body, and three-body polynomial terms truncated at finite range were used in our Jastrow factor [45,46].

## C. Wave functions for biexcitons with indistinguishable holes

For biexcitons with indistinguishable holes we used the trial wave function

$$\Psi = \exp[J(\mathbf{R})]x'_{\text{hh}}(\mathbf{R}), \quad (40)$$

where  $J$  is of the form described in Sec. IV B. For indistinguishable particles of mass  $m$  and charge  $q$  interacting via the logarithmic or Keldysh interactions, Eq. (37) must be replaced by  $\Gamma' = -q^2 m / (8a_0^* \mu e^2 r_*)$ , while for indistinguishable pairs of particles interacting via the Coulomb interaction, Eq. (39) must be replaced by  $\Gamma = q^2 m / (2a_0^* \mu e^2)$ .  $x'_{\text{hh}}$  is the  $x$  component of

$$\begin{aligned} \mathbf{r}'_{\text{hh}} = & \mathbf{r}_{\text{hh}} + \eta_{\text{hh}}(r_{\text{hh}}) \mathbf{r}_{\text{hh}} + \eta_{\text{eh}}(r_{e_1 h_1}) \mathbf{r}_{e_1 h_1} + \eta_{\text{eh}}(r_{e_1 h_2}) \mathbf{r}_{e_1 h_2} \\ & - \eta_{\text{eh}}(r_{e_2 h_1}) \mathbf{r}_{e_2 h_1} - \eta_{\text{eh}}(r_{e_2 h_2}) \mathbf{r}_{e_2 h_2}, \end{aligned} \quad (41)$$

where  $\eta_{\text{hh}}$  and  $\eta_{\text{eh}}$  are smoothly truncated polynomials, with optimizable expansion coefficients, and  $\mathbf{r}_{\text{hh}}$  and  $\mathbf{r}_{e_i h_j}$  are the hole-hole and electron-hole relative positions, respectively. Equation (41) is effectively a backflow [47,48] transformation;  $\Psi = \exp(J)x_{\text{hh}}$  introduces the correct nodal topology for the state that we want to consider and Eq. (41) maps the particle coordinates  $\{\mathbf{r}\}$  to quasiparticle coordinates  $\{\mathbf{r}'\}$  without changing the nodal topology. In Eq. (41),

$$\eta_{\text{hh}}(r) = \sum_{n=2}^{N_{\eta}^{\text{hh}}} a_n r^n (r - L)^C \Theta(L - r) \quad (42)$$

and

$$\eta_{\text{eh}}(r) = \sum_{m=0}^{N_{\eta}^{\text{eh}}} b_m r^m (r - L)^C \Theta(L - r) \quad (43)$$

are smoothly truncated polynomials with optimizable parameters  $\{a_n\}$  and  $\{b_m\}$ .  $L$  is a cutoff length,  $N_{\eta}^{\text{hh}}$  and  $N_{\eta}^{\text{eh}}$  determine the amount of variational freedom,  $C = 3$  to ensure smooth behavior at the cutoffs, and  $\Theta$  denotes the Heaviside function. We require  $b_1 = C b_0 / L$  to ensure that  $\eta$  does not affect the Kato cusp conditions, which are enforced by the Jastrow factor. We optimized the free parameters in our antisymmetric wave function using energy minimization [38].

For different values of  $N_{\eta}^{\text{hh}}$  and  $N_{\eta}^{\text{eh}}$  in Eqs. (42) and (43), we compare the VMC ground-state energy, variance, and DMC energy of biexcitons with indistinguishable electrons interacting via the logarithmic interaction in Table II. Analogous results for biexcitons interacting via the Keldysh interaction at finite  $r_*$  are shown in Table III. Our results show that increasing  $N_{\eta}^{\text{hh}}$  and  $N_{\eta}^{\text{eh}}$  slightly decreases the variances; nevertheless, the VMC and DMC energies are independent of the number of free parameters when  $N_{\eta}^{\text{hh}}, N_{\eta}^{\text{eh}} \geq 2$  to within our statistical error bars. We have used  $N_{\eta}^{\text{hh}} = N_{\eta}^{\text{eh}} = 3$  in our production calculations.

Biexcitons with distinguishable electrons and indistinguishable holes can trivially be mapped onto biexcitons with indistinguishable electrons and distinguishable holes by charge conjugation.

TABLE II. Effect of changing the number of free parameters in  $\eta$  [i.e., the values of  $N_\eta^{\text{hh}}$  and  $N_\eta^{\text{eh}}$  in Eqs. (42) and (43)] on the VMC ground-state energy ( $E_{\text{VMC}}$ ), VMC energy variance, and DMC energy ( $E_{\text{DMC}}$ ) for biexcitons with indistinguishable holes interacting via the logarithmic interaction. The mass ratio is  $\sigma = 0.1$  and the reduced mass is  $\mu = 0.5m_0$ , where  $m_0$  is the bare electron mass. In each case  $r_* = r_0$ .

$N_\eta^{\text{hh}} = N_\eta^{\text{eh}}$	$E_{\text{VMC}} (E_0)$	Variance ( $E_0^2$ )	$E_{\text{DMC}} (E_0)$
2	0.7604(3)	0.00920	0.7585(2)
3	0.7602(3)	0.00908	0.7584(2)
4	0.7605(3)	0.00914	0.7579(2)
6	0.7606(3)	0.00927	0.7580(2)

#### D. Time-step and population-control errors

We chose our DMC time steps such that the root-mean-square distance diffused by each particle in a single time step was much less than  $r_0$  for the logarithmic interaction, much less than  $a_0^*$  for the Coulomb interaction, and much less than  $\min\{r_0, a_0^*\}$  for the Keldysh interaction at finite  $r_*$ . In Fig. 5 we plot the DMC total energy of a biexciton with distinguishable particles against time step. The figure confirms that the linear extrapolation scheme described in Sec. IV A largely eliminates the effects of time-step bias, provided the time steps used are sufficiently small. For the logarithmic interaction with  $\sigma = 1$  and  $r_* = r_0$ , the time step should evidently be rather less than  $0.04\hbar/E_0$ .

Figures 6 and 7 show similar time-step tests performed for a negative trion and a donor-bound biexciton with the Keldysh interaction. For  $r_* \geq 0.25a_0^*$ , one should use time steps of less than  $0.01\hbar/R_y^*$  to be in the linear time-step bias regime, while for  $r_* < 0.25a_0^*$ , time steps of less than  $0.0025\hbar/R_y^*$  are required.

#### E. PDF calculations

The PDFs defined in Sec. III D were evaluated by binning the interparticle distances sampled in VMC and DMC calculations. The errors in the VMC and DMC PDFs are linear in the error in the trial wave function; however, the

TABLE III. Effect of changing the number of free parameters in  $\eta$  [i.e., the values of  $N_\eta^{\text{hh}}$  and  $N_\eta^{\text{eh}}$  in Eqs. (42) and (43)] on the VMC ground-state energy ( $E_{\text{VMC}}$ ), VMC energy variance, and DMC energy ( $E_{\text{DMC}}$ ) of biexcitons with indistinguishable holes interacting via the Keldysh interaction, with an electron-hole mass ratio of  $\sigma = 0.1$ .  $r_* = 0$  corresponds to the Coulomb interaction.

$r_*/a_0^*$	$N_\eta^{\text{hh}} = N_\eta^{\text{eh}}$	$E_{\text{VMC}} (R_y^*)$	Variance ( $R_y^{*2}$ )	$E_{\text{DMC}} (R_y^*)$
0	2	-8.608(1)	0.1709	-8.6100(4)
0	3	-8.608(1)	0.1658	-8.6112(4)
0	4	-8.606(1)	0.1718	-8.6108(4)
0	6	-8.608(1)	0.1719	-8.6108(4)
8	2	-0.6304(1)	0.0008	-0.6308(1)
8	3	-0.63020(8)	0.0007	-0.6306(2)
8	4	-0.6301(1)	0.0007	-0.6308(1)
8	6	-0.63024(8)	0.0007	-0.6309(1)

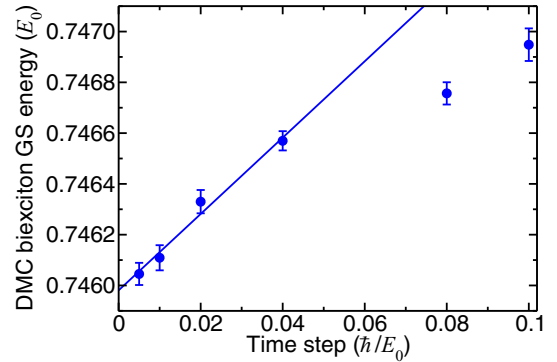


FIG. 5. DMC ground-state (GS) energy of a biexciton with distinguishable particles at mass ratio  $\sigma = 1$  against time step, with the logarithmic interaction between charges. The configuration population was varied in inverse proportion to the time step. The reduced mass is  $\mu = 0.5m_0$  and  $r_* = r_0$ .

error in the extrapolated estimate (twice the DMC estimate minus the VMC estimate) is quadratic in the error in the trial wave function [49]. Our reported PDFs were obtained by extrapolated estimation.

Contact PDF data have been calculated by extrapolating electron-hole and electron-electron PDFs to zero separation for each  $r_*$  value and mass ratio considered. To perform the extrapolation we fitted  $\exp[\tilde{g}(r)]$  to our PDF data at short range [50], where

$$\tilde{g}(r) = a'_0 + 2\Gamma' r^2 \ln(r) + a'_2 r^2 + a'_3 r^3 + \dots + a'_6 r^6 \quad (44)$$

for the Keldysh and logarithmic interactions and

$$\tilde{g}(r) = a_0 + 2\Gamma r + a_2 r^2 + \dots + a_6 r^6 \quad (45)$$

for the Coulomb interaction ( $r_* = 0$ ), where  $\Gamma'$  and  $\Gamma$  are defined in Eqs. (37) and (39) and  $a'_0, a'_2, \dots, a'_6$  and  $a_0, a_2, \dots, a_6$  are fitting parameters. These forms satisfy (the analog of) the Kimball cusp conditions [51]. The model functions were fitted to our PDF data at small  $r$ , with the data being weighted by  $2\pi r$ .

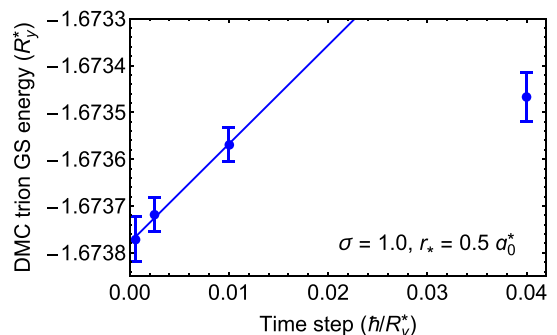


FIG. 6. DMC ground-state (GS) energy of a negative trion at mass ratio  $\sigma = 1$  and  $r_* = 0.5a_0^*$  against time step, with the Keldysh interaction between charges. The configuration population was varied in inverse proportion to the time step.

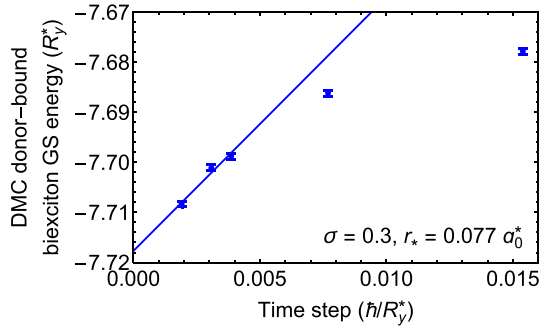


FIG. 7. DMC ground-state (GS) energy of a donor-bound biexciton at  $\sigma = 0.3$  and  $r_* = 0.077a_0^*$  against time step, with the Keldysh interaction between charges. The configuration population was varied in inverse proportion to the time step.

### F. Sensitivity of binding energy to the form of screened interaction

We have investigated whether the approximation to the Keldysh interaction given in Eq. (15), which has been used in previous QMC studies of excitonic complexes [21], leads to significant errors. For an exciton with  $r_* = a_0^*/2$ , the DMC total energies are  $E_X = -1.5358899(2)R_y^*$  and  $-1.4668074(3)R_y^*$  with the Keldysh interaction [Eq. (12)] and the approximate Keldysh interaction [Eq. (15)], respectively. This is a difference of about 4.5%, which is small but non-negligible. The DMC binding energies of trions with  $r_* = a_0^*/2$  and mass ratio  $\sigma = 1$  using the exact and approximate Keldysh interactions are  $0.1377(4)R_y^*$  and  $0.1335(3)R_y^*$ , respectively, so the error in the binding energy due to the approximate Keldysh interaction is about 3%. Since these errors are easily avoidable, we have used the exact Keldysh interaction in our production calculations.

## V. NUMERICAL RESULTS

### A. Excitons

The exciton ground-state energy is presented in Fig. 8. Our DMC data are in agreement with the results of finite-element

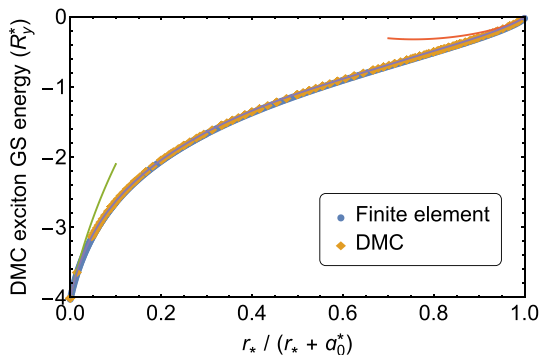


FIG. 8. Exciton ground-state (GS) energy evaluated using DMC and a finite-element method. The plot also shows the approximations to the ground-state energy obtained by first-order perturbation theory about the Coulomb limit (green) and by using the logarithmic approximation to the Keldysh potential (red).

calculations as implemented in the Mathematica software [52]. In excitonic units, the energy of an exciton is independent of the effective masses; see Sec. III B. In the Coulomb limit, one recovers the well-known excitonic energy of  $-4R_y^*$ . We can determine the behavior of the energy near the Coulomb limit by evaluating the first-order perturbative correction

$$\begin{aligned} \frac{\langle \Delta v \rangle}{R_y^*} &= \frac{32r_*(a_0^* + 4r_*)}{(a_0^*)^2 + 16r_*^2} \\ &\quad - \frac{128a_0^*r_*^2[\operatorname{csch}^{-1}(4r_*/a_0^*) + \sinh^{-1}(4r_*/a_0^*)]}{[(a_0^*)^2 + 16r_*^2]^{3/2}} \\ &\approx 32r_*/a_0^* + O((r_*/a_0^*)^2), \end{aligned} \quad (46)$$

where  $\Delta v = v_{\text{Keldysh}} - v_{\text{Coulomb}}$  is the difference between the Keldysh potential of Eq. (12) and the Coulomb potential of Eq. (13), and the expectation value is taken with respect to the exact ground-state wave function for the Coulomb interaction  $\Psi = \exp(-2r/a_0^*)$ . The correction is shown in Fig. 8 as a green line.

We have numerically evaluated the dimensionless constant  $\mathcal{E}_{X0}$  in Eq. (26) to be  $\mathcal{E}_{X0} = 0.41057739(7)$  using DMC and  $\mathcal{E}_{X0} = 0.41057747491(7)$  using the finite-element method. These results confirm the expected accuracy of the DMC method. The logarithmic-limit behavior from Eq. (26) is also shown in Fig. 8 (red line) and matches the DMC data near  $r_* \rightarrow \infty$ . The difference  $\Delta E_X/E_0$  between the exciton energies in units of  $E_0$  with the Keldysh and logarithmic interactions at large  $r_*$  was calculated numerically. Using the optimized ground-state wave function for the logarithmic interaction, we used VMC to evaluate the first-order perturbative approximation  $\Delta E_X/E_0 \approx \langle v_{\text{Keldysh}} - v_{\text{logarithmic}} \rangle$ . The results are presented in Fig. 9 and show that the leading-order error in the exciton energy due to the logarithmic interaction goes as  $\sqrt{a_0^*/r_*}$ .

We fitted the function

$$\frac{E_X}{R_y^*} = \frac{(1-y)\left[-4 + 33y + a_1y^{3/2} + \sum_{k=2}^5 a_k y^k + \ln(1-y)\right]}{1 + (1-y)y^3(b_1 + b_2y)}, \quad (47)$$

with  $a_5 = -29 + 2\mathcal{E}_{X0} - a_1 - a_2 - a_3 - a_4 - \ln 2$ , to our DMC exciton energy data, where  $y = r_*/(a_0^* + r_*)$  and the

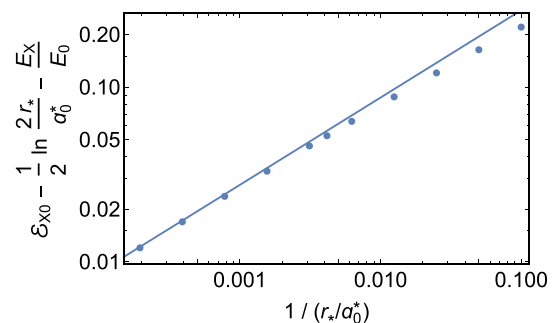


FIG. 9. Difference of dimensionless exciton energies with the Keldysh interaction and the logarithmic approximation to the Keldysh interaction, calculated using first-order perturbation theory within VMC. The solid line is a fit of  $a\sqrt{a_0^*/r_*}$  to the VMC data, with  $a = 0.871(2)$ .

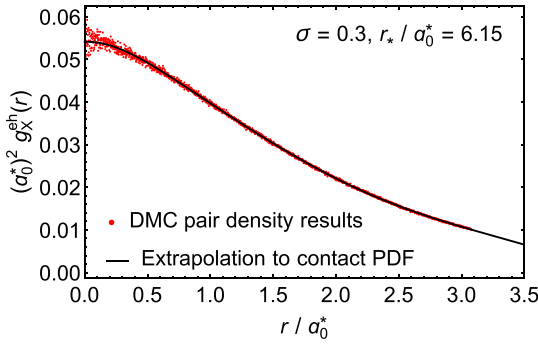


FIG. 10. PDF of an exciton with  $\sigma = 0.3$  and  $r_* = 6.15a_0^*$ . The contact PDF is extracted by fitting the numerical results to Eq. (44).

remaining  $\{a_i\}$  and  $\{b_i\}$  are six free fitting parameters. The fractional error in the fit of Eq. (47) to our DMC data is everywhere less than 0.5%.

Contact PDFs were extracted as described in Sec. IV E. An example of a fit to Monte Carlo-sampled PDF data is shown in Fig. 10, and our contact PDF results are shown in Fig. 11(a). In all our plots of contact PDFs the statistical error bars from the Monte Carlo calculation are smaller than the symbols. Unlike the DMC mixed estimate of the energy, the extrapolated estimate of the PDF depends on the stochastically optimized trial wave function and hence in some cases slight noise in the  $g(0)$  data is visible.

In the Supplemental Material [53] we provide a program for evaluating our fit to the total energy of an exciton [Eq. (47)], as well as fits to the binding energies of biexcitons, trions,

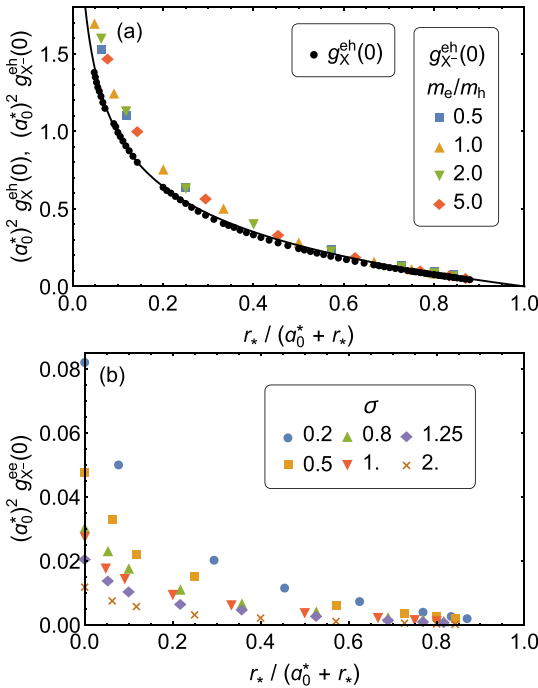


FIG. 11. (a) Electron-hole contact PDFs of an exciton (in black) and a negative trion (in color). (b) Electron-electron contact PDFs of a negative trion. These data were presented in Ref. [25], and are shown here for completeness.

donor-bound excitons, donor-bound trions, and donor-bound biexcitons. In addition, the program reports fits to contact PDFs for the different clusters.

## B. Biexcitons

### 1. Binding energies

We compare the stability of biexcitons with distinguishable and indistinguishable holes in the limit of the Coulomb interaction ( $r_* = 0$ ) in Fig. 12(a) and at  $r_* = 8a_0^*$  in Fig. 12(b). We find that biexcitons with indistinguishable holes are unbound for  $\sigma \gtrsim 0.3$ , while biexcitons consisting of distinguishable particles are bound at all mass ratios. The binding energies at  $\sigma = 0$  are obtained using the Born-Oppenheimer potentials as a function of heavy-hole separation  $r$  plotted in Fig. 13. We fitted  $U(r) = \alpha + \beta\sqrt{r} + \gamma r + \delta r^2$ , where  $\alpha, \beta, \gamma$ , and  $\delta$  are

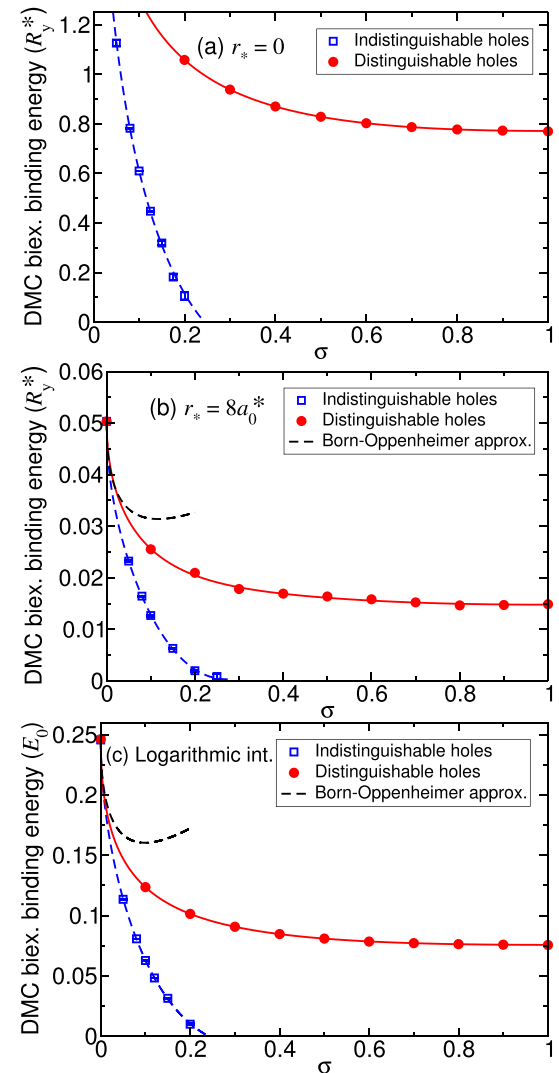


FIG. 12. DMC binding energies of biexcitons with distinguishable electrons and indistinguishable holes and biexcitons with distinguishable electrons and indistinguishable holes against mass ratio  $\sigma$  with (a) the Coulomb interaction ( $r_* = 0$ ), (b) the Keldysh interaction with  $r_* = 8a_0^*$ , and (c) the logarithmic interaction [Eq. (14)] between charge carriers.

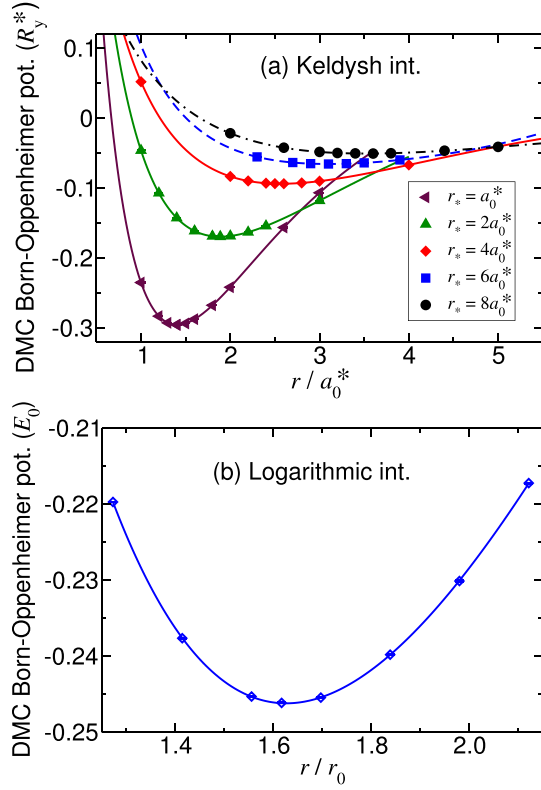


FIG. 13. DMC Born-Oppenheimer potential energy of a heavy-hole biexciton with distinguishable electrons against the hole separation for (a) the Keldysh interaction with  $r_* = a_0^*, 2a_0^*, 4a_0^*, 6a_0^*$ , and  $8a_0^*$ ; and (b) the logarithmic interaction between charge carriers. The zero of the Born-Oppenheimer potential energy in the plot is twice the isolated exciton energy.

fitting parameters, to our DMC data to find the minimum and the curvature about the minimum of the Born-Oppenheimer potential. For the logarithmic interaction we fitted  $U(r) = \zeta + \eta \exp(-r/d) + \kappa \ln(r)$  to our data, where  $\zeta$ ,  $\eta$ ,  $d$ , and  $\kappa$  are fitting parameters. The Born-Oppenheimer approximation in Fig. 12(b) for heavy holes is in agreement with our DMC calculations at small  $\sigma$ . Analogous results obtained with the logarithmic interaction are shown in Fig. 12(c). For  $\sigma \gtrsim 0.2$ , only biexcitons with distinguishable holes are stable. Hence it is only at extreme mass ratios, where exchange effects between the heavy particles are negligible, that biexcitons with indistinguishable particles are stable.

Figure 14 shows DMC binding energies for biexcitons with distinguishable particles interacting via the Keldysh interaction as a function of  $x = \sigma/(1 + \sigma)$  and rescaled in-plane susceptibility  $y = r_*/(a_0^* + r_*)$ . Our results are in agreement with path-integral Monte Carlo (PIMC) data at finite  $r_*$ , as shown in Fig. 15 [20]. However, the PIMC data obtained by Velizhanin and Saxena have much larger statistical errors and they quoted a previous DMC result [54] at  $r_* = 0$  due to the infeasibility of PIMC in this case. The function

$$\frac{E_{XX}^b}{R_y^*} = \frac{(1 - y) \sum_{i,j} a_{ij} [x^{i/2} + (1 - x)^{i/2}] y^j}{1 + \sum_{i,j} b_{ij} [x^{i/2} + (1 - x)^{i/2}] y^j} \quad (48)$$

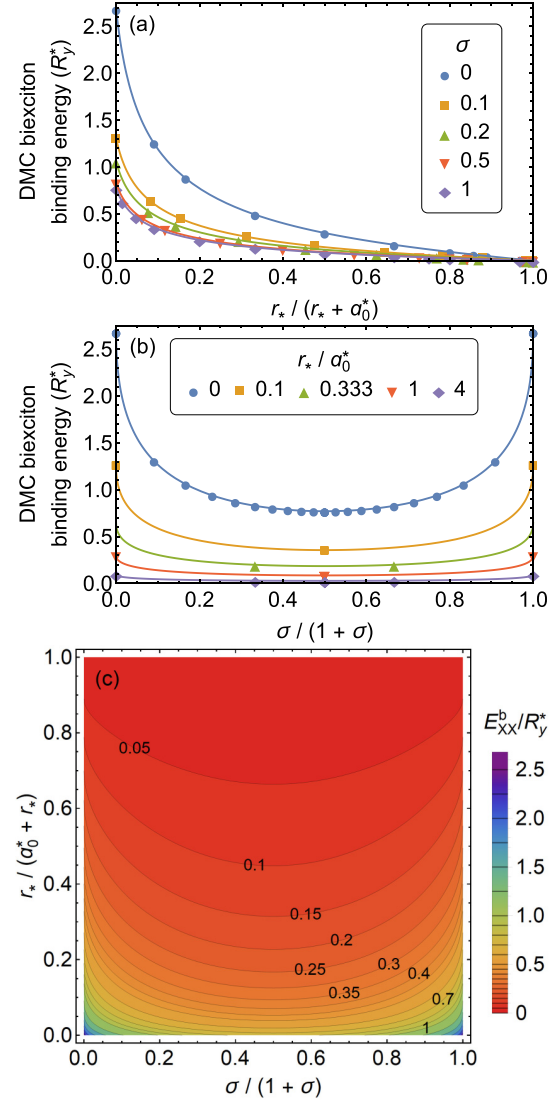


FIG. 14. (a) DMC binding energies of biexcitons with distinguishable particles against rescaled susceptibility  $r_*/(a_0^* + r_*)$ . (b) DMC binding energies of biexcitons with distinguishable particles against rescaled mass ratio  $\sigma/(1 + \sigma)$ . (c) DMC binding energies of biexcitons with distinguishable particles against rescaled susceptibility and rescaled mass ratio. The DMC results for distinguishable particles were reported in Ref. [25].

containing 17 fitting parameters  $\{a_{ij}\}$  and  $\{b_{ij}\}$  was fitted to our DMC binding-energy data, giving a fractional error of less than 1.5% everywhere. This choice of fitting function exhibits the correct behavior as  $\sigma \rightarrow 0$ , as derived in Appendix B 1, and is also invariant under charge conjugation ( $m_e \leftrightarrow m_h$ ). Equation (48) accurately reproduces the DMC biexciton binding energies over the whole space of possible susceptibility and mass-ratio parameters, unlike the simple fitting functions reported in Ref. [25]. The latter are by construction only valid in the currently experimentally relevant region and, because of the relative simplicity of the fitting function, give significantly larger fractional errors (up to 5%) than Eq. (48). The fitted binding energy can be evaluated using the program supplied in the Supplemental Material [53]. Binding-energy results in

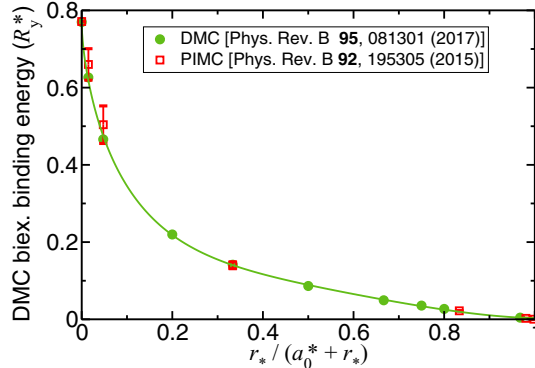


FIG. 15. Binding energies of biexcitons with distinguishable particles of equal mass ( $\sigma = 1$ ) against rescaled susceptibility  $r_*/(a_0^* + r_*)$ , as calculated using DMC [25] and PIMC [20].

the limit of large  $r_*$ , where the interaction is of logarithmic form, are given in Sec. V G.

In Table IV, we compare the DMC binding energies of biexcitons in monolayer TMDCs with experiment and with previous theoretical works. Our DMC binding energies are in good agreement with previous DMC binding energies where available [21] and also with PIMC calculations [23]. The small differences between DMC results in the literature must be due to the use of different effective masses, etc. Unfortunately, the theoretical biexciton binding energies are up to three times smaller than those reported in experimental works [13,15,16,55]. There is also a striking, qualitative disagreement with the experimental works regarding the trion and biexciton binding energies: the Mott-Wannier model with the Keldysh interaction predicts that the trion has a larger binding energy than the biexciton [21,25], while the experimental studies report that the biexciton peak occurs at lower energies than the trion peak in photoluminescence spectra (i.e., that the biexciton has a larger binding energy). The theoretical results are reported for a freestanding monolayer; any screening by the substrate and environment would further exacerbate the disagreement with experiment.

The ground-state wave function of a system of distinguishable particles is nodeless, and so DMC provides exact solutions to Mott-Wannier models of excitonic complexes. Hence the disagreement with experiment regarding the binding energies of biexcitons in 2D semiconductors could only arise for one or more of the following four reasons: (i) the 2D Mott-Wannier model with the Keldysh interaction between charge carriers is incorrect or incomplete; (ii) the parameters (band effective masses and  $r_*$  values) used in the model are incorrect; (iii) the exciton that remains after exciton recombination in a biexciton is not in its ground state [27]; or (iv) the experimental spectra have been misinterpreted or the peaks have been misclassified.

As explained in Sec. III D, there should be an additional contact interaction between charge carriers; however, the Mott-Wannier model with the Keldysh interaction apparently provides a good description [21,25] of the energies of excitons and trions, and there is no obvious reason to believe that contact interactions should be more important in a biexciton than in a trion or exciton. Moreover, it is unlikely that the contact interactions could be responsible for the threefold difference

between the theoretical and experimental biexciton binding energies.

The second possibility is that the Mott-Wannier model is in principle correct, but the band effective masses and in-plane susceptibilities used in the model are incorrect. These are taken from *ab initio* calculations, which might not provide a sufficiently accurate description of the electronic band structure. However, as shown in Sec. V B 2, the different mass ratios and in-plane susceptibilities reported in the literature do not significantly affect the binding energy; in fact the mass ratios and in-plane susceptibilities would need to be in error by more than an order of magnitude to explain the difference with experiment. Finally, if inappropriate model parameters are responsible for the disagreement with experiment regarding the biexciton binding energy, it is not clear why the Mott-Wannier model with the same parameters apparently provides a good description of excitons and trions.

We believe that the exciton that remains after exciton recombination in a biexciton is unlikely to be in an excited state, because the parent biexciton is in its nodeless ground state, which strongly overlaps with the product of the ground states of the two daughter excitons.

The misclassification of the experimental results may offer at least a partial explanation of the disagreement. By considering the behavior of the photoluminescence emission intensity, it has been argued that the observed peaks do indeed correspond to trions and biexcitons [15,16]. However, another possibility is that they could correspond to charge-carrier complexes involving donor or acceptor ions. In particular, the energies required to remove excitons from donor-bound biexcitons (see Sec. V F) are similar to the experimentally observed “biexciton” binding energies. If donor-bound biexcitons are responsible for the experimentally observed “biexciton peak” then we might expect the intensity of the peak to depend strongly on the doping of the sample. It is possible that other large charge-carrier complexes could also contribute to the spectra.

None of these options offers an entirely satisfactory explanation of the discrepancy. Further experimental and theoretical modeling work is required in order to understand the excitonic properties of 2D semiconductors.

## 2. Sensitivity of binding energies to effective masses and in-plane dielectric susceptibility

In Table V we compare the DMC binding energies of biexcitons with distinguishable particles for a variety of effective masses and in-plane screening lengths obtained by different first-principles methods. Since a range of masses is reported in the literature, we have taken the average of the reported masses that were supposedly obtained using the same method. The different model parameters in the literature lead to a spread of about 1 meV in the theoretical binding energies.

The sensitivities of the exciton total energy and the trion and biexciton binding energies to the model parameters are reported in Table VI. The energies depend relatively weakly on the in-plane permittivity  $r_*$ ; the errors arising from the uncertainty in the effective mass almost certainly dominate errors arising from the uncertainty in  $r_*$ . The sensitivity of the exciton energy to the effective masses is an order of

TABLE IV. Total energies of excitons ( $X$ ) and binding energies of biexcitons ( $XX$ ) and trions ( $X^-$  and  $X^+$ ) with distinguishable particles for different monolayer TMDCs suspended in vacuum ( $\epsilon = \epsilon_0$ ). We compare our results with values reported in the literature obtained by DMC, PIMC, hyperspherical harmonics (HH), stochastic variational (SV), and variational (V) methods. For each complex we use the values of  $m_e$ ,  $m_h$ , and  $r_*$  shown in bold in Table V to evaluate the fits of Eqs. (48) and (49). Note that the ditellurides adopt a 2H stacking arrangement in bulk and few-layer samples, which may complicate comparison with experiment.

TMDC	Ex. tot. en. $E_X$ (meV)			Biexciton binding energy $E_{XX}^b$ (meV)			Positive trion bind. en. $E_{X^+}^b$ (meV)	
	Eq. (47)	V [26]	Eq. (48)	DMC [21]	PIMC [23]	Exp.		
MoS <sub>2</sub>	-546.5	-540	23.5	22.7(3)	22.7(5)	70 [13], 40–60 [55]	22.5	22.1
MoSe <sub>2</sub>	-543.3	-470	22.9	17.7(3)	19.3(5)	$\simeq 20$ [56]	18.4	17.9
MoTe <sub>2</sub>	-385.7		13.4		14.4(4)			
WS <sub>2</sub>	-511.9	-500	23.4	23.3(3)	23.9(5)	65 [16], 65–70 [57], 45 [14]	23.6	23.1
WSe <sub>2</sub>	-461.1	-450	20.0	20.2(3)	20.7(5)	52 [15]	20.2	19.8
WTe <sub>2</sub>	-454.3		18.9					
Negative trion binding energy $E_{X^-}^b$ (meV)								
TMDC	Eq. (49)	DMC [21]	PIMC [23]	SV [27,28]	HH [29]	V [26]	Exp.	Eq. (49)
MoS <sub>2</sub>	35.0	33.8(3)	32.0(3)	33.7	32.8	26	40 [12,58], 18.0(15) [11], 43 [59]	34.9
MoSe <sub>2</sub>	34.5	28.4(3)	27.7(3)	28.2	27.6	21	30 [10,60]	34.4
MoTe <sub>2</sub>	22.5	21.0(2)					25 [61]	22.6
WS <sub>2</sub>	33.5	34.0(3)	33.1(3)	33.8	33.1	26	34 [62], 36 [8], 10–15 [14], 30 [16], 45 [63]	33.6
WSe <sub>2</sub>	29.6	29.5(3)	28.5(3)	29.5	28.3	22	30 [64,65]	29.6
WTe <sub>2</sub>	28.7							28.6

TABLE V. Comparison of electron and hole effective masses and  $r_*$  values obtained by different *ab initio* methods in the literature [many-body  $GW$  calculations, and density functional theory either in the local density approximation (LDA) or using the Perdew-Burke-Ernzerhof (PBE) or Heyd-Scuseria-Ernzerhof (HSE06) exchange-correlation functionals]. Where multiple results are available using a given method, we have taken the average of the published results. The reported  $r_*$  values and effective masses are not necessarily obtained using the same method. We assume that the materials are suspended in vacuum, i.e., that  $\epsilon = \epsilon_0$ . The effective masses are reported in units of the bare electron mass  $m_0$ . The binding energies  $E_{XX}^b$  are calculated using Eq. (48). The effective masses and  $r_*$  values shown in bold are used to evaluate the binding energies reported in Tables IV and VII.

		Effective masses			
TMDC	Method	$m_e/m_0$	$m_h/m_0$	$r_*/\text{\AA}$	$E_{XX}^b$ (meV)
MoS <sub>2</sub>	$GW$ [6]	<b>0.35</b>	<b>0.428</b>	<b>38.62</b> [6]	23.5
	$G_0W_0$ [5]	0.60	0.54	38.62 [6]	24.2
	LDA [3,66–70]	0.495	0.576	36.28 [71]	25.5
	PBE [3,23,72–74]	0.470	0.575	44.69 [23]	21.1
	HSE06 [75]	0.37	0.44	38.62 [6]	23.6
MoSe <sub>2</sub>	$GW$ [76]	<b>0.38</b>	<b>0.44</b>	51.71 [26]	18.0
	$G_0W_0$ [5]	0.70	0.55	51.71 [26]	18.7
	LDA [3,67,68]	0.59	0.686	<b>39.79</b> [71]	23.7
	PBE [3,23,72,77]	0.546	0.643	53.16 [23]	18.1
	$G_0W_0$ [5]	<b>0.69</b>	<b>0.66</b>	<b>73.61</b> [23]	13.4
MoTe <sub>2</sub>	LDA [68]	0.64	0.78	73.61 [23]	15.5
	PBE [77]	0.575	0.702	73.61 [23]	13.4
	$GW$ [76]	<b>0.27</b>	<b>0.32</b>	<b>37.89</b> [26]	23.4
WS <sub>2</sub>	$G_0W_0$ [5]	0.44	0.45	37.89 [26]	24.1
	LDA [3,67,68]	0.312	0.422	32.42 [71]	27.7
	PBE [3,23,72,77]	0.328	0.402	40.17 [23]	22.6
WSe <sub>2</sub>	$GW$ [76]	<b>0.29</b>	<b>0.34</b>	<b>45.11</b> [26]	20.0
	$G_0W_0$ [5]	0.53	0.52	45.11 [26]	20.8
	LDA [3,67,68]	0.36	0.476	34.72 [71]	26.2
WTe <sub>2</sub>	PBE [3,23,72]	0.342	0.428	47.57 [23]	19.4
	LDA [3]	<b>0.325</b>	<b>0.460</b>	<b>49.56</b> [71,78]	18.9
	PBE [79]	0.307	0.51	49.56 [71,78]	19.3

magnitude larger than the sensitivity of the trion binding energy, which is in turn an order of magnitude larger than the sensitivity of the biexciton binding energy. To account for the 30–40 meV disagreement with experiment over the biexciton binding energy the effective masses would have to be more than an order of magnitude larger than the *ab initio* values

TABLE VI. Sensitivity of binding energies to the three parameters that characterize the Mott-Wannier-Keldysh model of excitonic complexes in 2D semiconductors suspended in vacuum. The derivatives are evaluated using the effective mass and in-plane permittivity parameters reported in bold for different TMDCs in Table V.  $m_0$  is the bare electron mass.

TMDC	$\frac{\partial E_X}{\partial m_e}$ (meV/ $m_0$ )	$\frac{\partial E_X}{\partial m_h}$ (meV/ $m_0$ )	$\frac{\partial E_X}{\partial r_*}$ (meV/Å)	$\frac{\partial E_{XX}^b}{\partial m_e}$ (meV/ $m_0$ )	$\frac{\partial E_{XX}^b}{\partial m_h}$ (meV/ $m_0$ )	$\frac{\partial E_{X^-}^b}{\partial r_*}$ (meV/ $m_0$ )	$\frac{\partial E_{X^-}^b}{\partial m_e}$ (meV/ $m_0$ )	$\frac{\partial E_{X^-}^b}{\partial m_h}$ (meV/ $m_0$ )
MoS <sub>2</sub>	-240	-160	10	1.2	5.4	-0.56	10	9.2
MoSe <sub>2</sub>	-210	-160	9.9	1.4	4.3	-0.53	8.8	8.7
WS <sub>2</sub>	-310	-220	9.5	2.1	6.7	-0.56	13	12
WSe <sub>2</sub>	-240	-180	7.3	1.6	5.1	-0.41	10	9.6

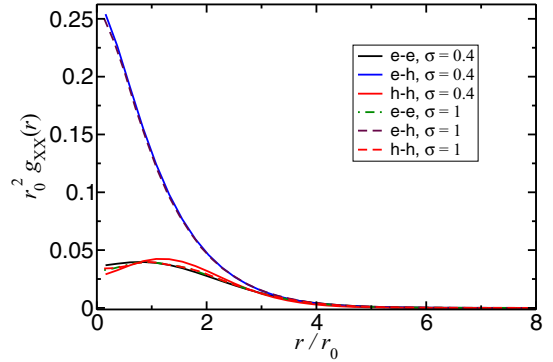


FIG. 16. PDF  $g_{XX}(r)$  of a biexciton with distinguishable particles interacting via the logarithmic interaction plotted against interparticle separation at two different electron-hole mass ratios  $\sigma$ .

reported in Table V and/or the  $r_*$  value would have to be an order of magnitude smaller. While there is still appreciable uncertainty in the *ab initio* effective mass and  $r_*$  values, it seems very unlikely that both density functional theory and many-body  $GW$  calculations would be in error by more than an order of magnitude.

### 3. PDFs

In Fig. 16, we show the PDFs of biexcitons with distinguishable particles interacting via the logarithmic interaction for two different mass ratios,  $\sigma = 0.4$  and  $\sigma = 1$ . The long-range biexciton wave function is relatively independent of the mass ratio. However, at short range the electron-hole PDF shows a peak near the separation that corresponds to the minimum of the Born-Oppenheimer potential-energy surface, which gets more pronounced at extreme mass ratios. As expected, the physical size of the biexciton is a low multiple of  $r_0$ .

Figure 17 presents the electron-hole and electron-electron contact ( $r = 0$ ) PDFs for a biexciton. Notice that  $g_{XX}^{eh} \approx 2g_X^{eh}$ . Fits to the contact PDFs can be evaluated using the program supplied as Supplemental Material [53].

### C. Trions

The binding energies of negative trions are presented in Fig. 18. We have fitted the function

$$\frac{E_{X^-}^b}{R_y^*} = \frac{(1-y) \sum_{i,j} a_{ij} (1-x)^{i/2} y^j}{1 + \sum_{i,j} b_{ij} (1-x)^{i/2} y^j}, \quad (49)$$

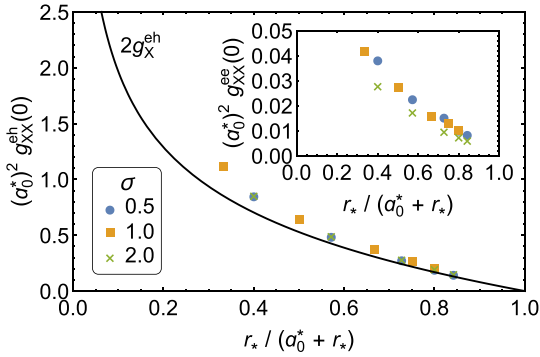


FIG. 17. Electron-hole contact PDF of a biexciton with distinguishable particles against rescaled susceptibility. The black line indicates twice the exciton electron-hole contact PDF. The inset shows the electron-electron contact PDF. These data were presented in Ref. [25], and are shown here for completeness.

where  $x = \sigma/(1 + \sigma)$ ,  $y = r_*/(r_* + a_0^*)$ , and the  $\{a_{ij}\}$  and  $\{b_{ij}\}$  are fitting parameters, to the DMC trion binding energies. Equation (49) satisfies the limiting behavior described in Appendix B 2, has 31 free fitting parameters, and the fractional error in the fit to our DMC data is everywhere less than 1%. Positive trion binding energies can be obtained by charge conjugating the corresponding negative trion. The program included in the Supplemental Material [53] can be used to evaluate Eq. (49). The resulting trion binding energies for various TMDCs are shown in Table IV. It can be seen that, in contrast to the biexciton binding energies, the trion binding energies are in excellent agreement with the available experimental results. As shown in Table VI, trion binding energies are significantly more sensitive to the effective mass values than biexciton binding energies; nevertheless, the *ab initio* effective masses would need to be in error by an implausibly large amount to change the trion binding energies by more than a few meV. Binding-energy results in the limit of large  $r_*$ , where the interaction is of logarithmic form, are given in Sec. V G.

Figures 11(a) and 11(b) present the electron-hole and electron-electron contact PDFs of trions. The fitting functions can be found in the program supplied as Supplemental Material [53].

#### D. Donor/acceptor-bound excitons

We present the binding energies of donor-bound excitons in Fig. 19. For  $\sigma \gtrsim 1$ , the binding energy is close to zero. In this region, the calculations were especially difficult, since the complex tends to unbind very easily. Therefore, during the wave function optimization, the cutoff lengths for the Jastrow factor were fixed at small values, to force the complex to be bound. In the limit  $\sigma \rightarrow \infty$ , the complex is expected to be unbound (see Appendix B 3), which is consistent with our results. Indeed, over a broad range of large electron-hole mass ratios and large  $r_*$  values, the DMC binding energy of the donor-bound exciton is either zero or extremely small, such that the binding energy cannot easily be resolved in DMC calculations. The following 50-parameter fitting formula has a fractional error that is mostly less than 2% in fits to our DMC

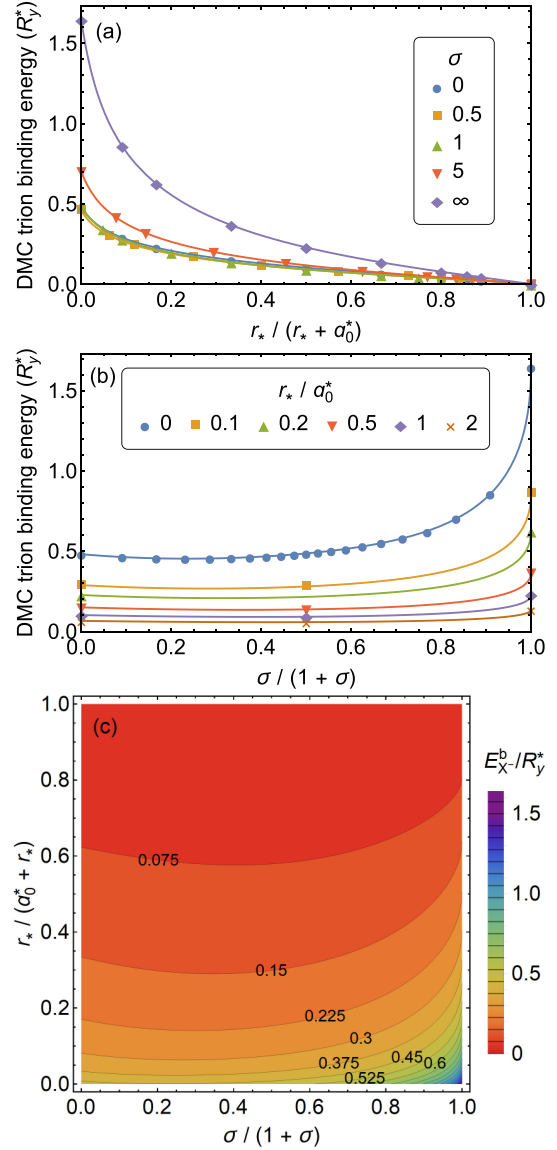


FIG. 18. (a) DMC binding energies of trions with distinguishable particles against rescaled susceptibility  $r_*/(a_0^* + r_*)$ . (b) DMC binding energies of trions with distinguishable particles against rescaled mass ratio  $\sigma/(1 + \sigma)$ . (c) DMC binding energies of trions with distinguishable particles against rescaled susceptibility and rescaled mass ratio. These data were presented in Ref. [25], and are shown here for completeness.

data:

$$E_{D+X}^b = (1 - x)^2 (1 - y) \left[ \sum_{i,j} a_{ij} x^i y^j - \left( \sum_{k=0}^4 b_k y^k \right)^2 \sqrt{x} \right]. \quad (50)$$

In this expression  $x = \sigma/(1 + \sigma)$  and  $y = r_*/(a_0^* + r_*)$ , while the  $\{a_{ij}\}$  are fitting parameters. Our fitting function can be evaluated using the program in the Supplemental Material [53]. We summarize our theoretical predictions for the binding energies of donor/acceptor-bound excitons in various TMDCs

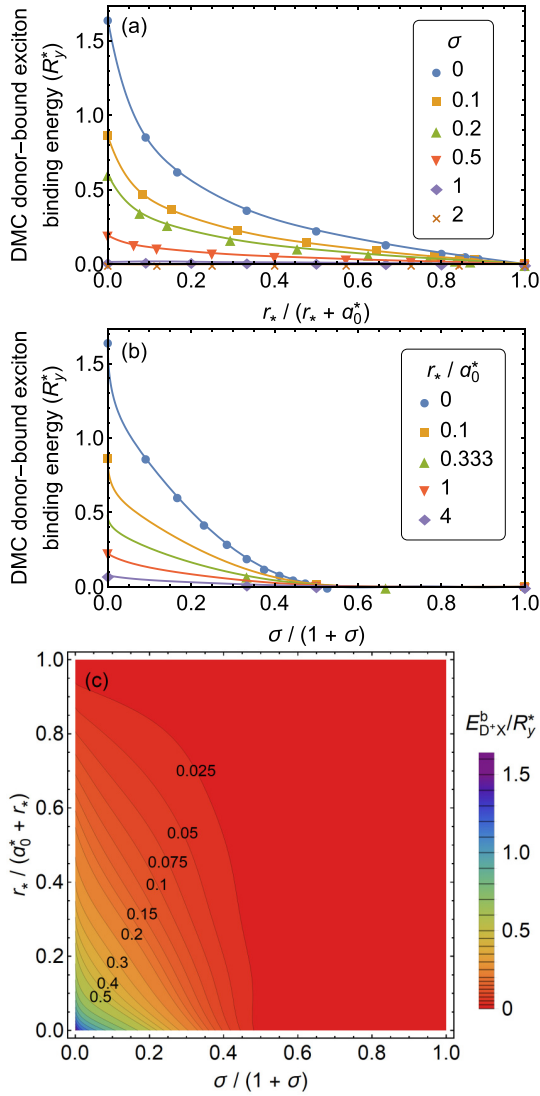


FIG. 19. (a) DMC binding energies of donor-bound excitons with against rescaled susceptibility  $r_*/(a_0^* + r_*)$ . (b) DMC binding energies of donor-bound excitons against rescaled mass ratio  $\sigma/(1 + \sigma)$ . (c) DMC binding energies of donor-bound excitons against rescaled susceptibility and rescaled mass ratio.

TABLE VII. As Table IV (using the  $r_*$  values and effective masses shown in bold in Table V), but for donor atoms ( $D^0$ ), acceptor atoms ( $A^0$ ), donor-bound excitons ( $D^+X$ ), acceptor-bound excitons ( $A^-X$ ), donor-bound trions ( $D^0X$ ), acceptor-bound trions ( $A^0X$ ), donor-bound biexcitons ( $D^{+XX}$ ), and acceptor-bound biexcitons ( $A^{-XX}$ ). The binding-energy results are our theoretical predictions using Eqs. (50), (51), and (52), while the energies of donor and acceptor atoms are calculated using Eq. (47) with infinite hole and electron masses, respectively. Note that the binding energy is defined with respect to dissociation into the most energetically favorable products, which do not always include an exciton; see the definitions in Sec. III C.

TMDC	Energy (meV)				Binding energy (meV)			
	$E_{D^0}$	$E_{A^0}$	$E_{D^+X}^b$	$E_{A^-X}^b$	$E_{D^0X}^b$	$E_{A^0X}^b$	$E_{D^{+XX}}^b$	$E_{A^{-XX}}^b$
MoS <sub>2</sub>	-638.5	-670.1	7.2	2.7	32.4	31.7	51.8	48.0
MoSe <sub>2</sub>	-636.8	-659.3	6.5	3.2	31.5	31.1	50.8	48.1
MoTe <sub>2</sub>	-447.8	-443.9	3.9	4.6	17.9	18.0	32.4	32.9
WS <sub>2</sub>	-606.8	-633.6	6.2	2.7	32.0	31.5	48.6	45.3
WSe <sub>2</sub>	-542.3	-563.6	5.5	2.6	27.5	27.1	43.4	40.8
WTe <sub>2</sub>	-519.0	-562.1	7.9	1.6	26.1	25.3	44.0	38.8

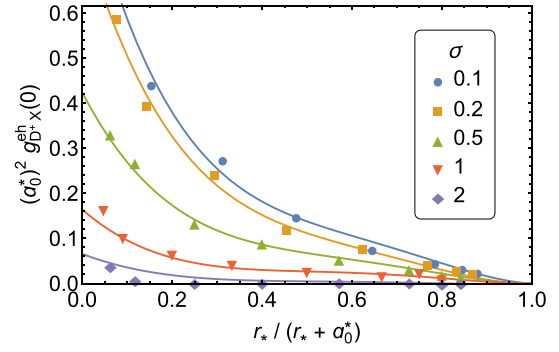


FIG. 20. Electron-hole contact PDF of a donor-bound exciton. The solid lines were obtained using the fitting function reported in the Supplemental Material [53].

in Table VII. Binding-energies in the limit of large  $r_*$ , where the interaction is of logarithmic form, are given in Sec. V G.

We have also calculated the electron-hole contact PDFs of donor-bound excitons, which are presented in Fig. 20. Our results confirm that the contact PDFs decrease to zero as  $\sigma \rightarrow \infty$ , as expected, because the light hole becomes unbound in this limit. Contact PDFs can be evaluated using the program supplied as Supplemental Material [53].

### E. Donor/acceptor-bound trions

Figure 21 presents the binding energies of donor-bound trions. We have devised the following 30-parameter fitting formula:

$$\frac{E_{D^0X}^b}{R_y^*} = \frac{(1-y)[\sum_{i,j} a_{ij} x^i y^j + b_0(1-y)\frac{x}{1-x} - b_1\sqrt{x}]}{1 + \sum_{i,j} c_{ij} x^i y^j}, \quad (51)$$

which includes the correct divergence as  $\sigma \rightarrow \infty$  and appropriate square-root behavior for the heavy-hole limit  $\sigma \rightarrow 0$  (see Appendix B 4). The  $\{a_{ij}\}$ ,  $\{b_i\}$ , and  $\{c_{ij}\}$  are fitting parameters. The fractional error in the fit to our DMC data is less than 3%. The program in our Supplemental Material [53] can be used to evaluate Eq. (51). Binding-energy results

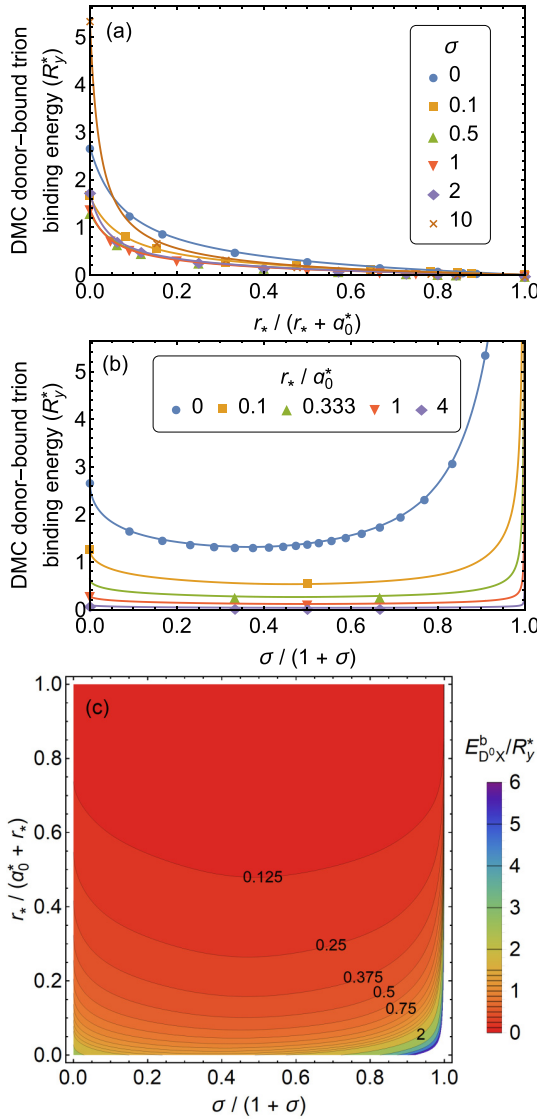


FIG. 21. (a) DMC binding energies of donor-bound trions with distinguishable particles against rescaled susceptibility  $r_*/(a_0^* + r_*)$ . (b) DMC binding energies of donor-bound trions with distinguishable particles against rescaled mass ratio  $\sigma/(1 + \sigma)$ . (c) DMC binding energies of donor-bound trions with distinguishable particles against rescaled susceptibility and rescaled mass ratio.

in the limit of large  $r_*$ , where the interaction is of logarithmic form, are given in Sec. V G.

Table VII reports theoretical binding energies for donor-bound trions with biexciton energies for several real materials. The binding energy of a donor-bound trion is slightly larger than the binding energy of a free biexciton. This leads us to expect two lines close together in the absorption/emission spectra of TMDCs, one corresponding to biexcitons, and another at slightly larger energy corresponding to donor-bound trions.

Contact PDFs for donor-bound trions have been extracted from our QMC data and are presented in Fig. 22 and in the Supplemental Material [53].

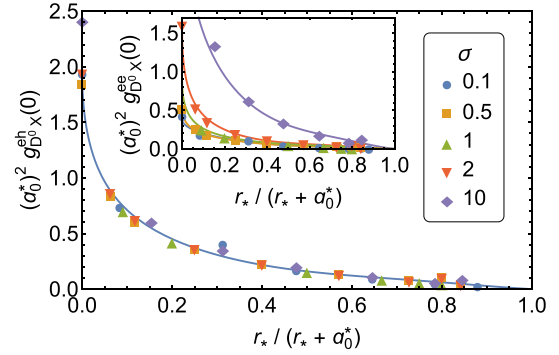


FIG. 22. Electron-hole contact PDFs of a donor-bound trion complex. The inset shows electron-electron contact PDFs. The solid lines were obtained using the fitting function reported in the Supplemental Material [53].

#### F. Donor/acceptor-bound biexcitons

Donor-bound biexciton binding energies have also been calculated and are presented in Fig. 23. A 38-parameter fitting formula similar to that of a donor-bound trion [Eq. (51)] was used:

$$\frac{E_{D^0XX}^b}{R_y^*} = \frac{(1 - y)[\sum_{i,j} a_{ij} x^i y^j - b_0 \sqrt{x} + b_1 x^{3/2}]}{1 + \sum_{i,j} c_{ij} x^i y^j}, \quad (52)$$

where  $x = \sigma/(1 + \sigma)$  and  $y = r_*/(a_0^* + r_*)$ , while the  $\{a_{ij}\}$ ,  $\{b_i\}$ , and  $\{c_{ij}\}$  are fitting parameters. This gives a fractional error of less than 3% everywhere when fitted to our DMC data. Equation (52) can be evaluated using the program supplied as Supplemental Material [53]. We summarize our theoretical predictions for the binding energies of donor/acceptor-bound biexcitons in various TMDCs in Table VII. Binding-energy results in the limit of large  $r_*$ , where the interaction is of logarithmic form, are given in Sec. V G.

The behavior of a donor-bound biexciton in the limit of heavy electrons is discussed in Appendix B 5. In the limit of heavy holes ( $\sigma \rightarrow 0$ ), this complex consists of three fixed positive particles and two light electrons and thus the question arises of how the three fixed, positive charges are positioned with respect to each other. The most natural position that three positive particles would assume is an equilateral triangle. To check whether this assumption is correct we first determined how the Born-Oppenheimer potential energy changes if we distribute the three positive charges in the corners of equilateral triangle and then vary the triangle side. Figure 24 shows the case of  $r_*/a_0^* = 1$  as an example. After finding the side length that minimizes the Born-Oppenheimer potential energy, we changed the position of one of the positive particles (fixing the remaining two) and again observed the effect on the Born-Oppenheimer potential energy. Figure 25 presents the results, which clearly show that the equilateral triangle is a local minimum of the Born-Oppenheimer potential-energy surface.

Closely related to donor-bound biexcitons are five-carrier complexes known as charged biexcitons or *quintons* ( $XX^-$ , i.e.,  $e^-e^-e^-h^+h^+$ ). In molybdenum and tungsten dichalcogenides these consist of two distinguishable holes with opposite spin and valley indices, and three distinguishable electrons that

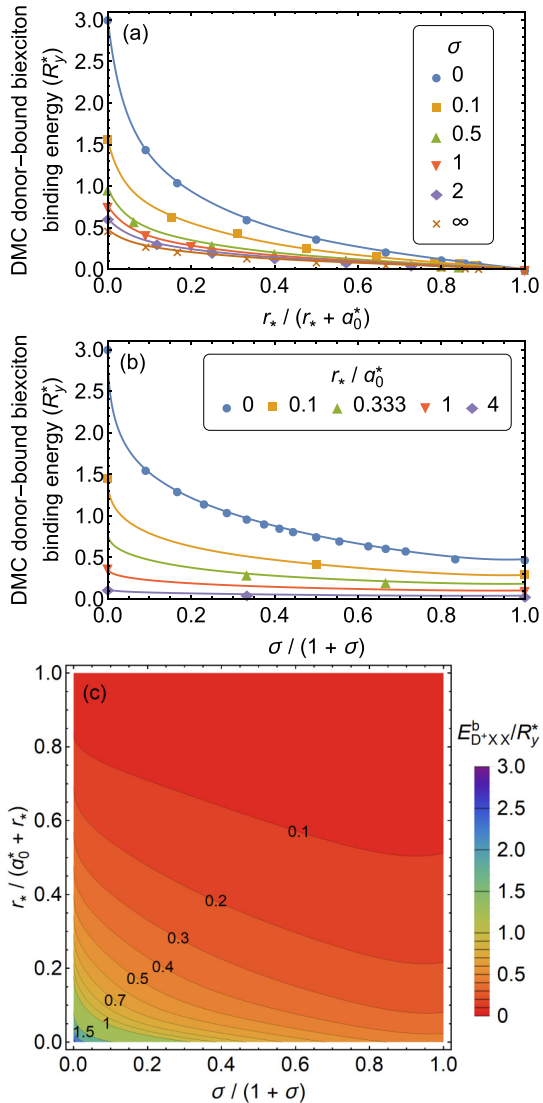


FIG. 23. (a) DMC binding energies of donor-bound biexcitons with distinguishable particles against rescaled susceptibility  $r_*/(r_0^* + r_*)$ . (b) DMC binding energies of donor-bound biexcitons with distinguishable particles against rescaled mass ratio  $\sigma/(1 + \sigma)$ . (c) DMC binding energies of donor-bound biexcitons with distinguishable particles against rescaled susceptibility and rescaled mass ratio.

differ in either their spin or their valley indices; see Fig. 1(a). The binding energy of a quinton is defined as the energy required to split it into a free exciton and a free trion [80]. Other possible large complexes are donor-bound double-negative excitons ( $D^-X$ , i.e.,  $D^+e^-e^-h^+$ ), donor-bound quintons ( $D^0XX$ , i.e.,  $D^+e^-e^-h^+h^+$ ), and even donor-bound double-negative biexcitons ( $D^-XX$ , i.e.,  $D^+e^-e^-e^-h^+h^+$ ). For molybdenum and tungsten dichalcogenides there are no further possibilities; we have exhausted the possible neutral or singly charged complexes that can be constructed from up to four distinguishable electrons, up to two distinguishable holes, and zero or one donor ion. Any larger charge-carrier complexes in molybdenum or tungsten dichalcogenides inevitably either include indistinguishable particles or involve the much larger energies required to excite holes in the lower spin-split

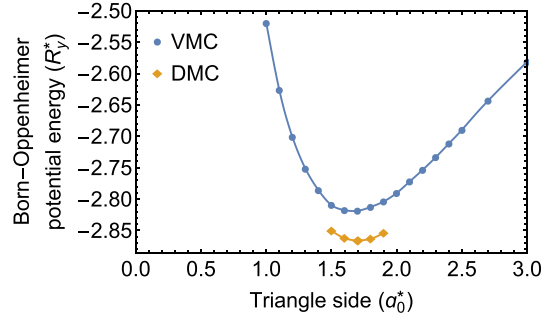


FIG. 24. Born-Oppenheimer potential energy of a complex of three positive, fixed ions and two electrons, with the positive ions placed at the corners of an equilateral triangle. Example for  $r_*/a_0^* = 1$ .

valence bands. In Table VIII we present our DMC binding-energy results for quintons and the other large complexes.

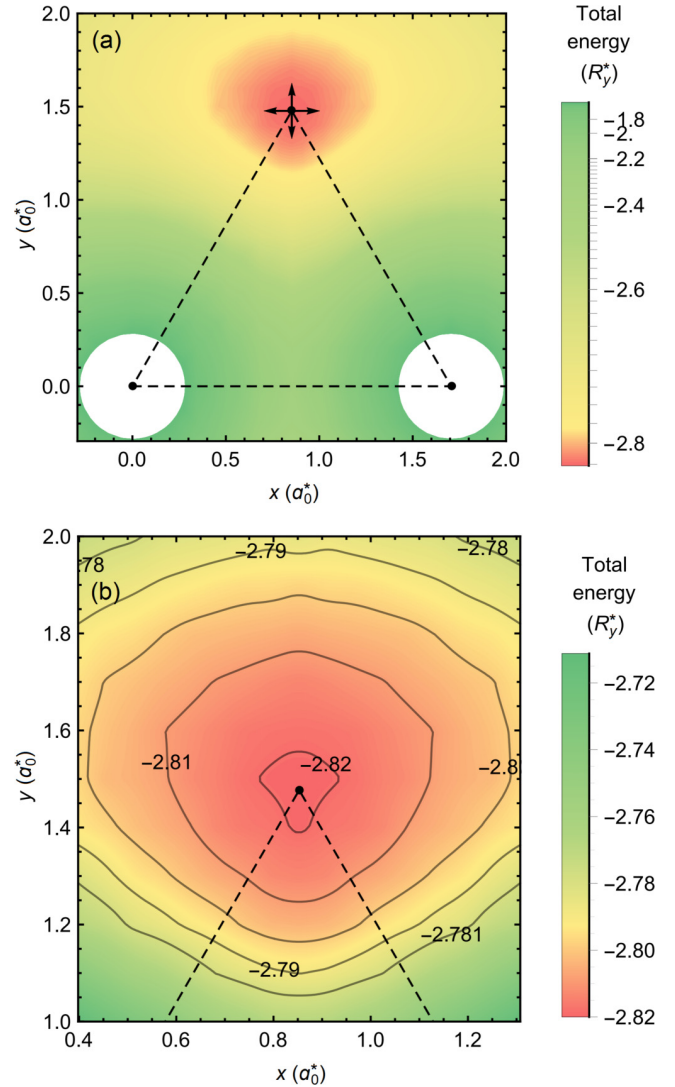


FIG. 25. (a) Born-Oppenheimer potential energy of a complex of three positive, fixed ions and two electrons. We fix two of the ions and change the position of the third one. Example for  $r_*/a_0^* = 1$ . (b) Vertex of the triangle of fixed, positive charges in greater detail.

Donor-bound double-negative biexcitons appear to be unstable to dissociation into free excitons plus donor-bound double-negative excitons, and hence are not included in Table VIII. As with donor-bound biexcitons, the energies required to remove excitons from the larger complexes such as quintons are relatively close to the experimentally observed biexciton binding energies.

Figure 26 presents the contact PDFs of a donor-bound biexciton, which are also reported in the Supplemental Material [53].

### G. Complexes with the logarithmic interaction

We have also studied complexes of distinguishable particles interacting with the purely logarithmic form of Eq. (14). The binding energies are presented in Fig. 27. The lines shown in Fig. 27 were obtained using Eqs. (47), (48), (49), (50), (51), and (52). To convert from excitonic units to logarithmic units we multiply the fitting function by  $R_y^*/E_0 = r_*/(2a_0^*) =$

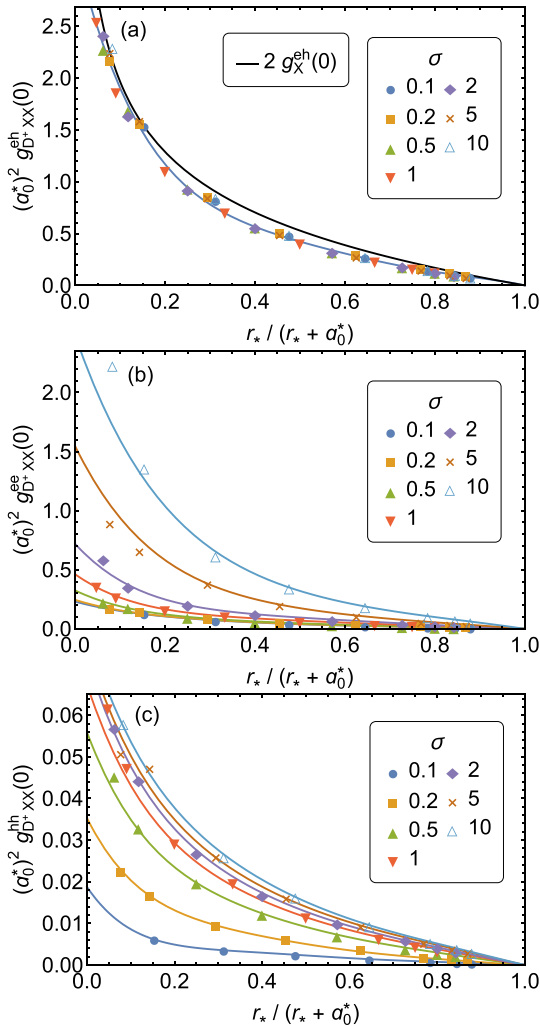


FIG. 26. (a) Electron-hole contact PDFs of a donor-bound biexciton. For comparison, the black line indicates twice the exciton contact PDF. (b) Electron-electron and (c) hole-hole contact PDFs of a donor-bound biexciton. The solid lines were obtained using the fitting function reported in the Supplemental Material [53].

TABLE VIII. Binding energies of larger charge-carrier complexes in different TMDCs. Binding energies are presented for quintons ( $XX^-$ ), which dissociate into excitons ( $X$ ) and negative trions ( $X^-$ ); donor-bound double-negative excitons ( $D^-X$ ), which dissociate into excitons ( $X$ ) and negative donor ions ( $D^-$ ); and donor-bound quintons ( $D^0XX$ ), which dissociate into excitons ( $X$ ) and donor-bound trions ( $D^0X$ ). The binding energies were evaluated using the effective mass and in-plane permittivity parameters reported in bold in Table V. The fitting functions of Eqs. (49) and (51) were used to evaluate the energies of negative donor ions and donor-bound trions.

TMDC	Binding energy (meV)		
	$XX^-$	$D^-X$	$D^0XX$
MoS <sub>2</sub>	58.6(6)	84.4(4)	61.6(6)
MoSe <sub>2</sub>	57.0(4)	57.9(2)	56.9(9)
MoTe <sub>2</sub>	33.8(3)		
WS <sub>2</sub>	57.4(3)	59.2(4)	58.2(6)
WSe <sub>2</sub>	52.5(7)	51.3(4)	51(1)
WTe <sub>2</sub>	47.5(3)		

$y/(2 - 2y)$  and take the limit that  $r_* \rightarrow \infty$ , i.e., that  $y \rightarrow 1$ . For complexes that have been studied previously, our results are in good agreement with earlier exact calculations [19].

## VI. CONCLUSIONS

In summary, we have discussed the different types of biexcitons and trions that can be observed in molybdenum and tungsten dichalcogenides. Furthermore, we have presented statistically exact DMC binding-energy data for biexcitons, trions, donor/acceptor-bound trions, and donor/acceptor-bound biexcitons in 2D semiconductors, including an analysis of extreme mass ratios. We have shown that biexcitons with indistinguishable charge carriers are unstable at experimentally relevant electron-hole mass ratios. Our calculations have used the effective interaction between charge carriers

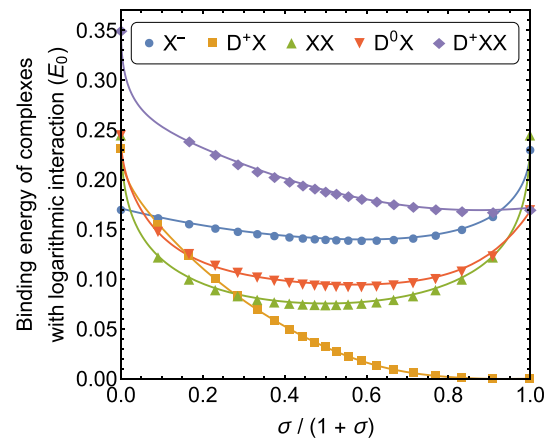


FIG. 27. DMC binding energies of negative trions ( $X^-$ ), biexcitons ( $XX$ ), donor-bound excitons ( $D^+X$ ), donor-bound trions ( $D^0X$ ), and donor-bound biexcitons ( $D^+XX$ ). Particles in the complexes interact via the logarithmic interaction. The  $X^-$  data were presented in Ref. [19], and are shown here for completeness.

TABLE IX. Character table for the irreps of the extended point group  $D_{3h}''$ . The superscript ( $\pm$ ) denotes the transformation under the  $\sigma_h$  operation and ' denotes representations with nontrivial transformation under translation.

$D_{3h}''$	$E$	$2t$	$2C_3$	$2tC_3$	$2t^2C_3$	$9t\sigma_v$	$\sigma_h$	$2t\sigma_h$	$2S_3$	$2tS_3$	$2t^2S_3$	$9tC'_2$
$A_1^+$	1	1	1	1	1	1	1	1	1	1	1	1
$A_2^+$	1	1	1	1	1	-1	1	1	1	1	1	-1
$A_1^-$	1	1	1	1	1	-1	-1	-1	-1	-1	-1	1
$A_2^-$	1	1	1	1	1	1	-1	-1	-1	-1	-1	-1
$E^+$	2	2	-1	-1	-1	0	2	2	-1	-1	-1	0
$E^-$	2	2	-1	-1	-1	0	-2	-2	1	1	1	0
$E_1'^+$	2	-1	-1	2	-1	0	2	-1	-1	2	-1	0
$E_1'^-$	2	-1	-1	2	-1	0	-2	1	1	-2	1	0
$E_2'^+$	2	-1	2	-1	-1	0	2	-1	2	-1	-1	0
$E_2'^-$	2	-1	2	-1	-1	0	-2	1	-2	1	1	0
$E_3'^+$	2	-1	-1	-1	2	0	2	-1	-1	-1	2	0
$E_3'^-$	2	-1	-1	-1	2	0	-2	1	1	1	-2	0

arising from screening effects in such materials. We have also presented contact PDF data that allow the investigation of additional contact interaction energies between charge carriers in 2D semiconductors within first-order perturbation theory. Our work provides a complete reference for the interpretation of spectral lines in photoabsorption and photoluminescence experiments on monolayer TMDCs in terms of a model of charge carriers moving within the effective mass approximation.

A broad range of theoretical works on 2D biexciton binding energies show excellent quantitative agreement with each other, but an enormous, threefold disagreement with experiment. By contrast, for trions there is good agreement between theory and experiment. We have considered and discounted various possible deficiencies in the theoretical models of charge-carrier complexes. We believe that the most likely explanation for the disagreement with experiment is a misinterpretation or misclassification of experimental optical spectra. In particular, we note that the energies required to remove excitons from donor-bound biexcitons are similar to the binding energies of experimentally observed biexcitons, suggesting that larger charge-carrier complexes could be responsible for the observed peak ascribed to biexcitons.

#### ACKNOWLEDGMENTS

We acknowledge support from the European Research Council synergy grant *Hetero2D*, the United Kingdom's Engineering and Physical Sciences Research Council (EPSRC), and the European Graphene Flagship project. M.S. was funded by the EPSRC doctoral training centre "NoWNANO" (Grant No. EP/G03737X/1) and the EPSRC standard grant "Non-perturbative and stochastic approaches to many-body localization" (Grant No. EP/P010180/1), and R.J.H. was funded by the EPSRC doctoral training centre "Graphene NOWNANO" (Grant No. EP/L01548X/1). Computer resources were provided by Lancaster University's High-End Computing Cluster. This work made use of the facilities of N8 HPC provided and funded by the N8 consortium and EPSRC (Grant No. EP/K000225/1). R.M. is grateful for financial support from MEXT-KAKENHI Grant No.

17H05478, support by FLAGSHIP2020, MEXT for computational resources, and Projects No. hp170269 and No. hp170220 at the K-computer. We acknowledge useful discussions with I. Aleiner, A. Tartakovski, M. Potemski, and T. Heinz. All relevant data present in this publication can be accessed at <http://dx.doi.org/10.17635/lancaster/researchdata/164>.

#### APPENDIX A: CHARACTER AND PRODUCT TABLES FOR THE $D_{3h}''$ SYMMETRY GROUP

Character and product tables for the  $D_{3h}''$  symmetry group of TMDCs are given in Tables IX and X.

#### APPENDIX B: MOLECULAR ANALOGIES AND BEHAVIOR OF BINDING ENERGIES AT EXTREME MASS RATIOS

##### 1. Biexcitons

In the limit that the hole mass is large, a biexciton resembles a 2D  $H_2$  molecule, and we may use the Born-Oppenheimer approximation [22]. The leading-order biexciton total energy is given by the minimum of the Born-Oppenheimer potential energy  $U(r)$ , where  $r$  is the exciton-exciton separation, plus the harmonic zero-point energy of the exciton-exciton vibrations.

TABLE X. Product table of the extended point group  $D_{3h}''$ . The relevant classification of the irreps according to  $C_s = \{I, \sigma_h\}$ , denoted by the superscript  $\pm$  in Table IX, is included for a given product by using  $+ \otimes + = +$ ,  $+ \otimes - = -$ , and  $- \otimes - = +$  and noting that all irreps in a given direct sum have the same  $C_s$  classification.

$\otimes A_1 A_2$	$E$	$E'_1$	$E'_2$	$E'_3$
$A_1 A_1 A_2$	$E$	$E'_1$	$E'_2$	$E'_3$
$A_2 A_2 A_1$	$E$	$E'_1$	$E'_2$	$E'_3$
$E E E A_1 \oplus A_2 \oplus E$	$E'_2 \oplus E'_3$	$E'_1 \oplus E'_3$	$E'_1 \oplus E'_2$	
$E'_1 E'_1 E'_1$	$E'_2 \oplus E'_3$	$A_1 \oplus A_2 \oplus E'_1$	$E \oplus E'_3$	$E \oplus E'_2$
$E'_2 E'_2 E'_2$	$E'_1 \oplus E'_3$	$E \oplus E'_3$	$A_1 \oplus A_2 \oplus E'_2$	$E \oplus E'_1$
$E'_3 E'_3 E'_3$	$E'_1 \oplus E'_2$	$E \oplus E'_2$	$E \oplus E'_1$	$A_1 \oplus A_2 \oplus E'_3$

Higher-order corrections to the energy arise from vibrational anharmonicity.

Consider a biexciton in which the charge carriers interact via the Keldysh interaction. Let  $\mathcal{U}(r/a_0)$  be the Born-Oppenheimer potential energy in Rydberg units for the case that the electron mass  $m_e$  is finite but the hole mass  $m_h$  is infinite. Then, at finite electron and hole masses, the Born-Oppenheimer potential is  $U(r) = \mathcal{U}(r/a_0)R_y$  where  $R_y = m_e e^4 / [2(4\pi\epsilon)^2 \hbar^2] = (m_e/\mu)R_y^*$  is the Rydberg and  $a_0 = 4\pi\epsilon\hbar^2/(m_e e^2) = (\mu/m_e)a_0^*$  is the Bohr radius. Note that  $\mathcal{U}(r/a_0)$  does not depend on the electron or hole mass.

Near the minimum of the potential  $r_{\min}$  we may write

$$\begin{aligned} U(r) &\approx U_{\min} + \frac{1}{2}U''_{\min}(r - r_{\min})^2 \\ &\equiv U_{\min} + \frac{1}{2}\frac{m_h + m_e}{2}\omega^2(r - r_{\min})^2, \end{aligned} \quad (\text{B1})$$

where  $(m_e + m_h)/2$  is the reduced mass of the two excitons,  $U_{\min} = \mathcal{U}_{\min}R_y$  is the minimum of potential,  $U''_{\min} = \mathcal{U}''_{\min}R_y/a_0^2$  is the second derivative of the potential at the minimum, and

$$\omega = \sqrt{\frac{2U''_{\min}}{m_h + m_e}} = \sqrt{\frac{2R_y\mathcal{U}''_{\min}}{a_0^2(m_h + m_e)}}. \quad (\text{B2})$$

The resulting ground-state energy in the harmonic approximation is

$$\begin{aligned} E &\approx U_{\min} + \hbar\omega/2 \\ &\approx \left[ \mathcal{U}_{\min} + \sqrt{\frac{\mathcal{U}''_{\min}m_e}{m_h}} \right] R_y^*, \end{aligned} \quad (\text{B3})$$

where we have used  $m_h \gg m_e$  in the last step. This suggests that a suitable fitting function for the binding energy of a biexciton with small  $\sigma \equiv m_e/m_h$  is a polynomial in powers of  $\sqrt{\sigma}$ . Similar conclusions hold for the case where the interaction between the charge carriers is logarithmic.

In the limit of heavy holes, the total energies of biexcitons with distinguishable and indistinguishable holes are identical, because exchange effects become negligible as the heavy holes localize. Hence a biexciton with indistinguishable holes must be bound when the hole mass is sufficiently large. Likewise, a biexciton with indistinguishable electrons has the same total energy as a biexciton with distinguishable electrons in the limit that the electron mass is large.

## 2. Negative trions

In the limit of heavy holes ( $\sigma \rightarrow 0$ ), a negative trion resembles a 2D  $H^-$  ion. The leading-order correction to the energy of an infinite-hole-mass negative trion is therefore due to the reduced-mass and mass-polarization perturbative corrections encountered in atomic physics, each of which gives a contribution to the energy that is linear in the electron-hole mass ratio  $\sigma$ .

In the limit of heavy electrons ( $\sigma \rightarrow \infty$ ), a negative trion resembles a charge-conjugated 2D  $H_2^+$  ion, and hence one can use the Born-Oppenheimer and harmonic approximations, as was done in Appendix B 1. The binding energy near the extreme mass limit varies as the square root of the mass ratio  $\sigma$ .

## 3. Donor-bound excitons

A donor-bound exciton in the limit of heavy holes is a charge conjugate of a negative trion with heavy electrons, and therefore will have a binding energy that varies as the square root of the mass ratio  $\sigma$ .

In a donor-bound exciton with heavy electrons, the positive donor ion and the heavy electron overlap, so the light hole is unbound. Therefore the binding energy in this limit is zero.

## 4. Donor-bound trions

The Born-Oppenheimer potential energy curve of a donor-bound trion with a heavy hole is the same as that of a biexciton, but this time the reduced mass is simply equal to the exciton mass. The binding energy varies as the square root of the mass ratio  $\sigma$ .

Now consider a donor-bound trion with two heavy electrons and a light hole. If the hole is very much lighter than the electrons then the hole will be extremely delocalized and will see the positive donor ion and two electrons ( $D^-$ ) as a fixed, negative point charge; the system therefore resembles an acceptor atom in which the hole is bound to a fixed, negative point charge. Hence  $E_{D^0X} \approx E_{D^-} + E_{A^0}$  in this limit, where  $E_{A^0}$  is the energy of an acceptor atom. In addition, if the electron mass is very much larger than the hole mass, the exciton ground-state energy is  $E_X \approx E_{A^0}$ . The binding energy of a donor-bound trion in the limit that the hole is much lighter than the electron mass is therefore  $E_{D^0X}^b = E_{D^0} + E_X - E_{D^0X} \approx E_{D^0} - E_{D^-}$ , which is the electron affinity of a donor atom. Note that the electron affinity of a donor atom is equal to the binding energy of a negative trion in the limit of large hole mass.

The exciton Rydberg goes to zero in the limit that the hole mass goes to zero; hence the binding energy of a donor-bound trion in excitonic units goes to infinity as the hole-to-electron mass ratio goes to zero ( $\sigma \rightarrow \infty$ ).

## 5. Donor-bound biexcitons

A donor-bound biexciton with two heavy holes resembles a trihydrogen cation ( $H_3^+$ ). This molecular ion is an important component of the interstellar medium [81], and it is known that the protons in  $H_3^+$  form an equilateral triangle. In Sec. V F we verify that 2D donor-bound biexcitons with heavy holes also adopt an equilateral triangular structure, and we calculate the bond length by minimizing the Born-Oppenheimer potential energy.

Consider a donor-bound biexciton with two heavy electrons and two light holes. The binding energy of a donor-bound biexciton in the limit that the holes ( $h_{\text{light}}^+$ ) are much lighter than the electrons ( $e_{\text{heavy}}^-$ ) is

$$\begin{aligned} E_{D^+XX}^b &= E_{D^+e_{\text{heavy}}^-e_{\text{heavy}}^+h_{\text{light}}^+} - E_{D^+e_{\text{heavy}}^-e_{\text{heavy}}^+h_{\text{light}}^+h_{\text{light}}^+} \\ &\approx E_{A^0} - E_{A^+}, \end{aligned} \quad (\text{B4})$$

which is the hole affinity of an acceptor atom (in the limit of large electron mass,  $D^+e^-e^-$  acts like a fixed negative point charge). Note that the hole affinity of an acceptor atom is equal to the binding energy of a positive trion in the limit of large electron mass.

- [1] K. F. Mak, C. Lee, J. Hone, J. Shan, and T. F. Heinz, *Phys. Rev. Lett.* **105**, 136805 (2010).
- [2] A. Splendiani, L. Sun, Y. Zhang, T. Li, J. Kim, C.-Y. Chim, G. Galli, and F. Wang, *Nano Lett.* **10**, 1271 (2010).
- [3] A. Kormányos, G. Burkard, M. Gmitra, J. Fabian, V. Zólyomi, N. D. Drummond, and V. Fal'ko, *2D Mater.* **2**, 022001 (2015).
- [4] J. S. Ross, P. Klement, A. M. Jones, N. J. Ghimire, J. Yan, D. G. Mandrus, T. Taniguchi, K. Watanabe, K. Kitamura, W. Yao, D. H. Cobden, and X. Xu, *Nat. Nano.* **9**, 268 (2014).
- [5] A. Ramasubramaniam, *Phys. Rev. B* **86**, 115409 (2012).
- [6] T. Cheiwchanchamnangij and W. R. L. Lambrecht, *Phys. Rev. B* **85**, 205302 (2012).
- [7] D. Y. Qiu, F. H. da Jornada, and S. G. Louie, *Phys. Rev. Lett.* **111**, 216805 (2013).
- [8] A. Chernikov, T. C. Berkelbach, H. M. Hill, A. Rigos, Y. Li, O. B. Aslan, D. R. Reichman, M. S. Hybertsen, and T. F. Heinz, *Phys. Rev. Lett.* **113**, 076802 (2014).
- [9] Z. Ye, T. Cao, K. O'Brien, H. Zhu, X. Yin, Y. Wang, S. G. Louie, and X. Zhang, *Nature (London)* **513**, 214 (2014).
- [10] J. S. Ross, S. Wu, H. Yu, N. J. Ghimire, A. M. Jones, G. Aivazian, J. Yan, D. G. Mandrus, D. Xiao, W. Yao, and X. Xu, *Nat. Commun.* **4**, 1474 (2013).
- [11] K. F. Mak, K. He, C. Lee, G. H. Lee, J. Hone, T. F. Heinz, and J. Shan, *Nat. Mater.* **12**, 207 (2013).
- [12] Y. Lin, X. Ling, L. Yu, S. Huang, A. L. Hsu, Y.-H. Lee, J. Kong, M. S. Dresselhaus, and T. Palacios, *Nano Lett.* **14**, 5569 (2014).
- [13] C. Mai, A. Barrette, Y. Yu, Y. G. Semenov, K. W. Kim, L. Cao, and K. Gundogdu, *Nano Lett.* **14**, 202 (2014).
- [14] J. Shang, X. Shen, C. Cong, N. Peimyoo, B. Cao, M. Eginligil, and T. Yu, *ACS Nano* **9**, 647 (2015).
- [15] Y. You, X.-X. Zhang, T. C. Berkelbach, M. S. Hybertsen, D. R. Reichman, and T. F. Heinz, *Nat. Phys.* **11**, 477 (2015).
- [16] G. Plechinger, P. Nagler, J. Kraus, N. Paradiso, C. Strunk, C. Schüller, and T. Korn, *Phys. Status Solidi RRL* **9**, 457 (2015).
- [17] D. Bressanini, M. Mella, and G. Morosi, *Phys. Rev. A* **57**, 4956 (1998).
- [18] M. Y. J. Tan, N. D. Drummond, and R. J. Needs, *Phys. Rev. B* **71**, 033303 (2005).
- [19] B. Ganchev, N. Drummond, I. Aleiner, and V. Fal'ko, *Phys. Rev. Lett.* **114**, 107401 (2015).
- [20] K. A. Velizhanin and A. Saxena, *Phys. Rev. B* **92**, 195305 (2015).
- [21] M. Z. Mayers, T. C. Berkelbach, M. S. Hybertsen, and D. R. Reichman, *Phys. Rev. B* **92**, 161404 (2015).
- [22] G. G. Spink, P. López Ríos, N. D. Drummond, and R. J. Needs, *Phys. Rev. B* **94**, 041410 (2016).
- [23] I. Kylianpää and H.-P. Komsa, *Phys. Rev. B* **92**, 205418 (2015).
- [24] A. Chaves, M. Z. Mayers, F. M. Peeters, and D. R. Reichman, *Phys. Rev. B* **93**, 115314 (2016).
- [25] M. Szyniszewski, E. Mostaani, N. D. Drummond, and V. I. Fal'ko, *Phys. Rev. B* **95**, 081301 (2017).
- [26] T. C. Berkelbach, M. S. Hybertsen, and D. R. Reichman, *Phys. Rev. B* **88**, 045318 (2013).
- [27] D. K. Zhang, D. W. Kidd, and K. Varga, *Nano Lett.* **15**, 7002 (2015).
- [28] D. W. Kidd, D. K. Zhang, and K. Varga, *Phys. Rev. B* **93**, 125423 (2016).
- [29] R. Y. Kezerashvili and S. M. Tsiklauri, *Few-Body Syst.* **58**, 18 (2016).
- [30] G. Wang, C. Robert, M. M. Glazov, F. Cadiz, E. Courtade, T. Amand, D. Lagarde, T. Taniguchi, K. Watanabe, B. Urbaszek, and X. Marie, *Phys. Rev. Lett.* **119**, 047401 (2017).
- [31] L. V. Keldysh, *J. Exp. Theor. Phys.* **29**, 658 (1979).
- [32] P. Cudazzo, I. V. Tokatly, and A. Rubio, *Phys. Rev. B* **84**, 085406 (2011).
- [33] M. Danovich, V. Zólyomi, and V. I. Fal'ko, *Sci. Rep.* **7**, 45998 (2017).
- [34] D. M. Ceperley and B. J. Alder, *Phys. Rev. Lett.* **45**, 566 (1980).
- [35] W. M. C. Foulkes, L. Mitas, R. J. Needs, and G. Rajagopal, *Rev. Mod. Phys.* **73**, 33 (2001).
- [36] C. J. Umrigar, K. G. Wilson, and J. W. Wilkins, *Phys. Rev. Lett.* **60**, 1719 (1988).
- [37] N. D. Drummond and R. J. Needs, *Phys. Rev. B* **72**, 085124 (2005).
- [38] C. J. Umrigar, J. Toulouse, C. Filippi, S. Sorella, and R. G. Hennig, *Phys. Rev. Lett.* **98**, 110201 (2007).
- [39] R. J. Needs, M. D. Towler, N. D. Drummond, and P. López Ríos, *J. Phys.: Condens. Matter* **22**, 023201 (2010).
- [40] R. M. Lee, N. D. Drummond, and R. J. Needs, *Phys. Rev. B* **79**, 125308 (2009).
- [41] R. Maezono, P. López Ríos, T. Ogawa, and R. J. Needs, *Phys. Rev. Lett.* **110**, 216407 (2013).
- [42] For biexcitons with distinguishable particles, we used the Jastrow form introduced in the Supplemental Material to Ref. [19].
- [43] T. Kato, *Commun. Pure Appl. Math.* **10**, 151 (1957).
- [44] R. T. Pack and W. Byers Brown, *J. Chem. Phys.* **45**, 556 (1966).
- [45] N. D. Drummond, M. D. Towler, and R. J. Needs, *Phys. Rev. B* **70**, 235119 (2004).
- [46] P. López Ríos, P. Seth, N. D. Drummond, and R. J. Needs, *Phys. Rev. E* **86**, 036703 (2012).
- [47] R. P. Feynman, *Phys. Rev.* **94**, 262 (1954).
- [48] R. P. Feynman and M. Cohen, *Phys. Rev.* **102**, 1189 (1956).
- [49] D. M. Ceperley and M. H. Kalos, in *Monte Carlo Methods in Statistical Physics*, edited by K. Binder (Springer-Verlag, Heidelberg, 1979), 2nd ed., p. 145.
- [50] N. D. Drummond, P. López Ríos, R. J. Needs, and C. J. Pickard, *Phys. Rev. Lett.* **107**, 207402 (2011).
- [51] J. C. Kimball, *Phys. Rev. A* **7**, 1648 (1973).
- [52] Mathematica, Version 11.0.1, Wolfram Research, Inc., Champaign, Illinois, USA, 2016.
- [53] See Supplemental Material at <http://link.aps.org/supplemental/10.1103/PhysRevB.96.075431> for a PYTHON program that reports fits to the binding energies of charge-carrier complexes in 2D semiconductors, together with contact pair-distribution functions.
- [54] B. Stébé and A. Ainane, *Superlattices Microstruct.* **5**, 545 (1989).
- [55] E. J. Sie, A. J. Frenzel, Y.-H. Lee, J. Kong, and N. Gedik, *Phys. Rev. B* **92**, 125417 (2015).
- [56] K. Hao, J. F. Specht, P. Nagler, L. Xu, K. Tran, A. Singh, C. K. Dass, C. Schüller, T. Koren, M. Richter, A. Knorr, X. Li, and G. Moody, *Nat. Commun.* **8**, 15552 (2017).
- [57] I. Paradisanos, S. Germanis, N. T. Pelekanos, C. Fotakis, E. Kymakis, G. Kiouseoglou, and E. Stratakis, *Appl. Phys. Lett.* **110**, 193102 (2017).
- [58] C. H. Lui, A. J. Frenzel, D. V. Pilon, Y.-H. Lee, X. Ling, G. M. Akselrod, J. Kong, and N. Gedik, *Phys. Rev. Lett.* **113**, 166801 (2014).

- [59] Y. Zhang, H. Li, H. Wang, R. Liu, S.-L. Zhang, and Z. Qiu, *ACS Nano* **9**, 8514 (2015).
- [60] A. Singh, G. Moody, S. Wu, Y. Wu, N. J. Ghimire, J. Yan, D. G. Mandrus, X. Xu, and X. Li, *Phys. Rev. Lett.* **112**, 216804 (2014).
- [61] I. Gutiérrez Lezama, A. Arora, A. Ubaldini, C. Barreteau, E. Giannini, M. Potemski, and A. F. Morpurgo, *Nano Lett.* **15**, 2336 (2015).
- [62] B. Zhu, X. Chen, and X. Cui, *Sci. Rep.* **5**, 9218 (2015).
- [63] B. Zhu, H. Zeng, J. Dai, Z. Gong, and X. Cui, *Proc. Natl. Acad. Sci. USA* **111**, 11606 (2014).
- [64] A. Srivastava, M. Sidler, A. V. Allain, D. S. Lembke, A. Kis, and A. Imamoglu, *Nat. Phys.* **11**, 141 (2015).
- [65] A. M. Jones, H. Yu, N. J. Ghimire, S. Wu, G. Aivazian, J. S. Ross, B. Zhao, J. Yan, D. G. Mandrus, D. Xiao, W. Yao, and X. Xu, *Nat. Nanotechnol.* **8**, 634 (2013).
- [66] E. S. Kadantsev and P. Hawrylak, *Solid State Commun.* **152**, 909 (2012).
- [67] Z. Jin, X. Li, J. T. Mullen, and K. W. Kim, *Phys. Rev. B* **90**, 045422 (2014).
- [68] J. Chang, L. F. Register, and S. K. Banerjee, *J. Appl. Phys.* **115**, 084506 (2014).
- [69] E. Scalise, M. Houssa, G. Pourtois, V. Afanas'ev, and A. Stesmans, *Phys. E (Amsterdam, Neth.)* **56**, 416 (2014).
- [70] S. Yu, H. D. Xiong, K. Eshun, H. Yuan, and Q. Li, *Appl. Surf. Sci.* **325**, 27 (2015).
- [71] A. Kumar and P. Ahluwalia, *Phys. B (Amsterdam, Neth.)* **407**, 4627 (2012).
- [72] D. Wickramaratne, F. Zahid, and R. K. Lake, *J. Chem. Phys.* **140**, 124710 (2014).
- [73] L. Dong, R. R. Namburu, T. P. O'Regan, M. Dubey, and A. M. Dongare, *J. Mater. Sci.* **49**, 6762 (2014).
- [74] W. S. Yun, S. W. Han, S. C. Hong, I. G. Kim, and J. D. Lee, *Phys. Rev. B* **85**, 033305 (2012).
- [75] H. Peelaers and C. G. Van de Walle, *Phys. Rev. B* **86**, 241401 (2012).
- [76] H. Shi, H. Pan, Y.-W. Zhang, and B. I. Yakobson, *Phys. Rev. B* **87**, 155304 (2013).
- [77] L. Liu, S. B. Kumar, Y. Ouyang, and J. Guo, *IEEE Trans. Electron Devices* **58**, 3042 (2011).
- [78] N. Lu, C. Zhang, C.-H. Lee, J. P. Oviedo, M. A. T. Nguyen, X. Peng, R. M. Wallace, T. E. Mallouk, J. A. Robinson, J. Wang, K. Cho, and M. J. Kim, *J. Phys. Chem. C* **120**, 8364 (2016).
- [79] H. Y. Lv, W. J. Lu, D. F. Shao, Y. Liu, S. G. Tan, and Y. P. Sun, *Europhys. Lett.* **110**, 37004 (2015).
- [80] The most energetically competitive products of the dissociation of a quinton are either a trion plus an exciton or a biexciton plus a free charge carrier; the energy difference between the two possible sets of products is given by the difference of the trion and biexciton binding energies. For all the 2D semiconductors considered here, the trion binding energy is larger than the biexciton binding energy [25], so that an exciton and a trion are the most energetically competitive species into which a quinton may dissociate.
- [81] D. W. Martin, E. W. McDaniel, and M. L. Meeks, *Astrophys. J.* **134**, 1012 (1961).

# Chapter 5

## Bound complexes in heterobilayer TMDCs

### 5.1 Introduction

Monolayers of different TMDCs stacked on top of each other result in weakly van der Waals coupled heterobilayers, with the individual layers retaining their electronic and optical properties, however having new interlayer properties resulting from the energetic alignment of the conduction and valence band edges, the incommensurability of the lattice structure and the alignment of the layers. These result in the electrons and holes to be separated in both real space and momentum space, with the former reducing the overlap of the electron and hole wave functions, and the latter in particular suppressing the radiative recombination due to energy and momentum conservation.

Typically, the single layers have an intrinsic n- or p-doping due to impurities in the samples. These impurities provide deep potential wells, which can capture the free, long-lived interlayer complexes, resulting in localized complexes. In the work presented in this chapter we study the heterobilayer system composed of MoSe<sub>2</sub> and WSe<sub>2</sub> monolayers. We aim to answer questions regarding the binding energies of these complexes, the possibility of their radiative recombination and the radiative rates for direct recombination and with the aid of phonon emission, both for closely aligned and misaligned layers.

To study these complexes, a proper description of the interaction between the carriers, and between carriers and impurities residing in the same or opposite layers is

required. In particular the monolayer Keldysh interaction used to describe Coulomb bound complexes in monolayers needs to be modified to describe the combined screening effects from both layers. We obtain the full interaction for the bilayer system and use variational and diffusion quantum Monte Carlo calculations to obtain the binding energies and wave functions of interlayer complexes involving electrons and holes on opposite layers and donor atoms on one layer. The localized nature of these complexes implies a spread in momentum space that can overcome the momentum mismatch between the valleys of the two layers, providing a finite optical matrix element. Using the appropriate limits for the bilayer interaction for the long range (as compared to the screening length in the two layers) and short range interaction, we obtain the radiative rates of the simplest complexes at both close alignment, finding  $\sim \mu s^{-1}$  rates, and the asymptotics behaviour for large misalignment using perturbation theory in the short range interaction between carriers and impurities, finding a strong angular dependence  $\propto \theta^{-8}$ . Finally, the multi-carrier nature of the complexes implies a doping dependent spectra, which we model and demonstrate.

## 5.2 Localized interlayer complexes in heterobilayer transition metal dichalcogenides

The results presented in this chapter are reported in [24]: “Localized interlayer complexes in heterobilayer transition metal dichalcogenides”, arXiv:1802.06005, (2018). (Submitted to *Phys. Rev. B*).

My contribution to this work: Prepared the results figures, carried the calculations of the matrix elements, contributed to the writing and editing of the manuscript and wrote Appendix E.

Full author list: M. Danovich, D. Ruiz-Tijerina, R. J. Hunt, M. Szymiszewski, N. D. Drummond, V. I. Fal’ko

Author contributions: All authors contributed to writing and editing the manuscript. D.T. contributed to the calculation of the matrix elements, prepared the figures of the diagrams giving the recombination amplitudes and wrote Appendices C, D. R.H., M.S. and N.D. performed the diffusion and variational quantum Monte Carlo calculations of the binding energies and overlap integrals, and wrote Appendix B.

# Localized interlayer complexes in heterobilayer transition metal dichalcogenides

M. Danovich, D. A. Ruiz-Tijerina and V. I. Fal'ko  
*National Graphene Institute, University of Manchester,  
Booth St E, Manchester M13 9PL, United Kingdom*

R. J. Hunt, M. Szyniszewski, and N. D. Drummond  
*Department of Physics, Lancaster University, Lancaster LA1 4YB, United Kingdom*  
(Dated: February 19, 2018)

We present theoretical results for the radiative rates and doping-dependent photoluminescence spectrum of interlayer excitonic complexes localized by donor impurities in MoSe<sub>2</sub>/WSe<sub>2</sub> twisted heterobilayers, supported by quantum Monte Carlo calculations of binding energies and wave-function overlap integrals. For closely aligned layers, radiative decay is made possible by the momentum spread of the localized complexes' wave functions, resulting in few  $\mu\text{s}^{-1}$  radiative rates. For strongly misaligned layers, the short-range interaction between the carriers and impurity provides a finite radiative rate with a strong asymptotic twist angle dependence  $\propto \theta^{-8}$ . Finally, phonon-assisted recombination is considered, with emission of optical phonons in both layers resulting in additional weaker emission lines, red-shifted by the phonon energy.

## I. INTRODUCTION

Recent advances in the study of two-dimensional (2D) materials have allowed the realization of van der Waals (vdW) heterostructures consisting of vertically stacked 2D layers, resulting in unique properties and potential novel device applications [1–5]. The layers forming these heterostructures are only weakly bound by vdW forces, and largely retain their individual characteristic properties. Yet, the weak interlayer coupling allows the different properties of various 2D materials to be combined.

One such family of vdW heterostructures are heterobilayers of 2D transition metal dichalcogenides (TMDs), which have attracted much interest due to their unique optical properties, dominated by strongly bound excitonic complexes [6, 7] and spin- and valley-dependent optical selection rules [8, 9]. The most commonly studied heterobilayers are of the form MoX<sub>2</sub>/WX<sub>2</sub>, with X = S or Se, due to their type-II (staggered) band alignment, in which the lowest conduction band (CB) edge and the highest valence band (VB) edge are spatially confined to different layers [10, 11]. In this configuration, electrostatic interactions between electrons and holes across the heterostructure result in the formation of interlayer excitonic complexes, whose constituent carriers are spatially separated in the out-of-plane direction. Optical signatures of these interlayer complexes have been reported in photoluminescence (PL) experiments [12–14], where new PL peaks are observed in the spectra of bilayer regions. These signatures appear at energies below the monolayer photoemission lines, due to the smaller interlayer band gap in the staggered band configuration.

Photoemission by free interlayer excitons is limited by the relative interlayer angle  $\theta$  and the incommensurability of the two TMD lattices  $\delta$ , resulting in a momentum-space mismatch  $\Delta K \approx K\sqrt{\delta^2 + \theta^2}$  between the conduction- and valence-band edges, as shown in Fig. 2(b). Radiative recombination becomes effectively indirect, and thus suppressed by energy and momentum conservation [15]. These constraints are relaxed when interlayer excitons and larger excitonic complexes local-

ize about charged defects, such as donor ions, which are commonly observed as dopants in real samples. Formation of these complexes is favored by the long interlayer exciton lifetimes resulting from the spatial separation of their carriers, which allow for their localization by the deep potential wells provided by the ions. The spread in momentum space of these localized complexes opens the possibility for a finite radiative matrix element  $M \propto \int d^2r e^{i\Delta\mathbf{K}\cdot\mathbf{r}} \Psi(\mathbf{r})$ , where  $\Psi(\mathbf{r})$  is the envelope wave function of the complex.

In this paper, we provide a theory for the radiative recombination of localized interlayer complexes in TMD heterostructures of the form MoX<sub>2</sub>/WX<sub>2</sub>, where the carriers are bound to a donor ion in the MoX<sub>2</sub> layer. Focusing specifically on MoSe<sub>2</sub>/WSe<sub>2</sub>, we use variational and diffusion quantum Monte Carlo (VMC and DMC) simulations [16, 17] to evaluate the binding energies and wave-function overlap integrals of complexes involving a single hole in the WSe<sub>2</sub> layer and up to three electrons in the MoSe<sub>2</sub> layer, accounting for bilayer and encapsulation screening effects.

Motivated by the binding energies obtained from our quantum Monte Carlo (QMC) calculations and PL experiments [18], we study the radiative recombination of the two simplest such complexes consisting of MoX<sub>2</sub> electrons and a single WX<sub>2</sub> hole bound to an impurity center: a donor ion and an exciton ( $D_c^0 h_v$ ), and a donor-bound trion ( $D_c^0 X_{vc}$ ). We predict the PL spectrum from these complexes for well-aligned TMD heterobilayers, and estimate the asymptotic behavior of their PL signals in the regime of strong misalignment based on a perturbative analysis. Our results indicate a rapid decay of the PL signals from the most relevant donor-bound interlayer complexes with the interlayer twist angle ( $\theta$ ), resulting from the asymptotic behavior  $\Gamma \sim \theta^{-8}$  of the radiative rates at strong misalignment. As a consequence, we expect that optical signatures from these complexes can be detected only in closely aligned crystals.

The remainder of this paper is organized as follows. In Sec. II we discuss the model Hamiltonian for the TMD heterobilayer, describe our approach to calculating its op-

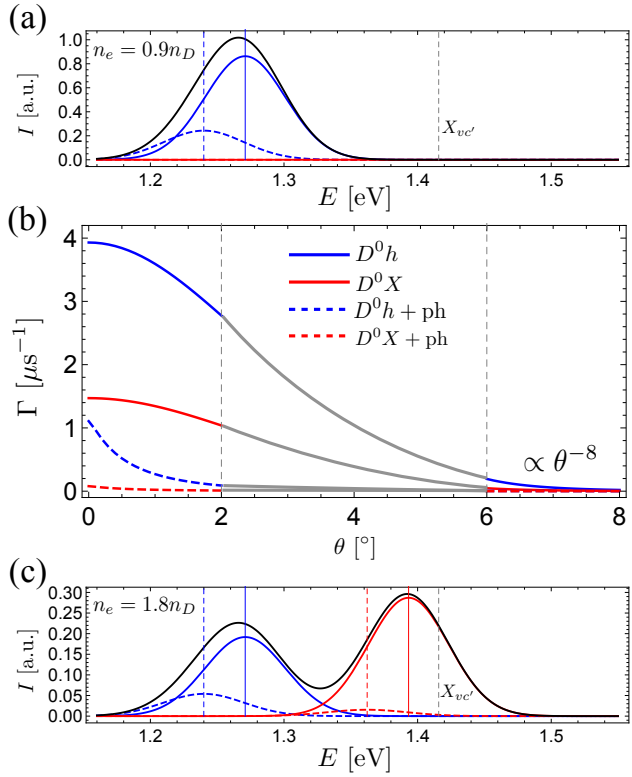


FIG. 1. (a) Simulated PL spectrum of donor-bound interlayer complexes in an aligned ( $\theta = 0$ ) MoSe<sub>2</sub>/WSe<sub>2</sub> bilayer encapsulated in hBN, for an electron density of  $n_e = 0.9n_D$ , with  $n_D$  the donor density. Dashed lines indicate PL from phonon-assisted recombination. The lines are taken to have Gaussian shape with width  $2\sigma = 60$  meV, and the interlayer gap is  $\tilde{E}_g = 1.5$  eV. The vertical gray dashed line in (a) and (c) indicates the position of the free interlayer exciton  $X_{vc'}$ . (b) Radiative rates of the  $D_{c'}^0 h_v$  (per hole) (solid blue) and  $D_{c'}^0 X_{vc'}$  (solid red) complexes, and their phonon-assisted replicas (dashed), in the large and small twist angle ( $\theta$ ) limits. The rates have a strong angular dependence, with asymptotic behaviour  $\sim \theta^{-8}$  for radiative decay driven by short-range interactions, and  $\sim \theta^{-4}$  for phonon-assisted processes. The gray lines for intermediate twist angles  $\theta = 2 - 6^\circ$  have been interpolated by hand. (c) Simulated PL spectrum in the limit of heavy n-doping, showing the appearance of the donor-bound trion ( $D_{c'}^0 X_{vc'}$ ) line when  $n_e > n_D$ . Parameters:  $n_h = 10^{13}$  cm<sup>-2</sup> and  $n_D = 10^{11}$  cm<sup>-2</sup>.

tical properties, and present our DMC results for the binding energies of the main interlayer impurity-bound complexes. In Sec. III we address the PL signatures of these complexes, assuming good alignment between the TMD monolayers in the heterostructure, and estimate the asymptotic behavior of their radiative decay with twist angle in Sec. IV. We consider the effects of electron-phonon interactions in Sec. V, and we find that longitudinal optical phonon modes can introduce red-shifted replicas to the main PL lines. Finally, we estimate the evolution of the PL spectrum of the two main donor-bound interlayer complexes with doping in Sec. VI. Our conclusions are summarized in Fig. 1, and discussed in Sec. VII.

## II. MODEL

### A. Electrostatic interactions in a bilayer system

The reduced dimensionality of a monolayer TMD leads to modified electrostatic interactions between its charge carriers below a characteristic length scale  $r_* = 2\pi\kappa/\epsilon$  (in Gaussian units), determined by the monolayer's in-plane dielectric susceptibility  $\kappa$ , and the (average) dielectric constant  $\epsilon$  of its environment [19, 20]. In a TMD heterobilayer, further screening effects must be considered. The resulting interactions between same-layer carriers  $\mathcal{V}$  in one layer and  $\mathcal{V}'$  in the other, and the interlayer interaction  $\mathcal{W}$ , have Fourier components (Appendix A)

$$\mathcal{V}(\mathbf{q}) = \frac{2\pi(1 + r'_* q - r'_* q e^{-2qd})}{\epsilon q [(1 + r_* q)(1 + r'_* q) - r_* r'_* q^2 e^{-2qd}]}, \quad (1a)$$

$$\mathcal{V}'(\mathbf{q}) = \frac{2\pi(1 + r_* q - r_* q e^{-2qd})}{\epsilon q [(1 + r_* q)(1 + r'_* q) - r_* r'_* q^2 e^{-2qd}]}, \quad (1b)$$

$$\mathcal{W}(\mathbf{q}) = \frac{2\pi e^{-qd}}{\epsilon q [(1 + r_* q)(1 + r'_* q) - r_* r'_* q^2 e^{-2qd}]}, \quad (1c)$$

where  $\mathbf{q}$  is the wave vector,  $d \ll r_*, r'_*$  is the interlayer distance, and  $r_*$  and  $r'_*$  are the corresponding monolayer screening lengths.

Previous works on monolayer TMDs have focused on interactions of the Keldysh form [19] to study their excitonic spectra and optical properties [6, 20–23]. For bilayers, this potential form is obtained from Eqs. (1a)-(1c) in the long-range limit ( $q \ll 1/r_*, 1/r'_*$ ) as

$$\mathcal{V}_<(\mathbf{q}) = \mathcal{V}'_<(\mathbf{q}) = \frac{2\pi}{\epsilon q [1 + (r_* + r'_*)q]}, \quad (2a)$$

$$\mathcal{W}_<(\mathbf{q}) = \frac{2\pi}{\epsilon q [1 + (r_* + r'_* + d)q]}. \quad (2b)$$

By contrast, in the short-range limit ( $q \gg 1/r_*, 1/r'_*$ ) we obtain for the intralayer interactions

$$\mathcal{V}_>(\mathbf{q}) = \frac{2\pi}{\epsilon r_* q^2}, \quad \mathcal{V}'_>(\mathbf{q}) = \frac{2\pi}{\epsilon r'_* q^2}, \quad (3)$$

revealing the absence of screening from the opposite layer in this regime. More strikingly, the short-range interlayer potential vanishes exponentially as  $\mathcal{W}_>(\mathbf{q}) = 2\pi e^{-qd}/(\epsilon r_* r'_* q^3)$ . Neither of these features is captured by extrapolation of Eqs. (2a) and (2b) to large wave numbers.

### B. Photon emission by donor-bound complexes

As in the monolayer case [24–27], optical properties of the heterobilayer are determined by excitonic complexes formed by excess electrons and holes in the sample. Staggered (type-II) band alignment, in which the

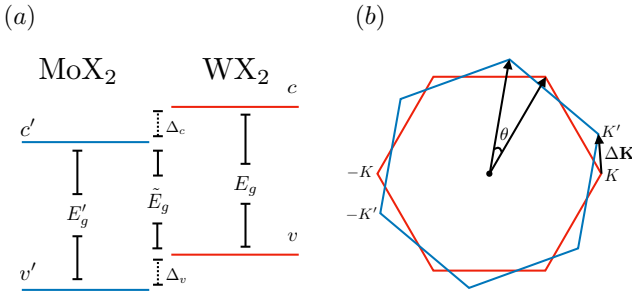


FIG. 2. (a) Schematic of type-II band alignment in a TMD heterobilayer. The CB and VB of the two layers are shifted relative to each other by energies  $\Delta_c$  and  $\Delta_v$ , respectively, giving an interlayer gap of  $\tilde{E}_g$ . (b) The Brillouin zones (BZs) of the misaligned TMD monolayers. Their  $K$  valleys are separated by a momentum vector  $\Delta\mathbf{K}$ , due to the nonzero misalignment angle  $\theta$  and to the difference in lattice constants.

main electron and hole bands belong to opposite layers, is typical of TMD heterostructures [10]. This is shown schematically in Fig. 2(a) for a  $\text{MoX}_2/\text{WX}_2$  structure, where  $\text{X} = \text{S}$  or  $\text{Se}$  represents a chalcogen; the electron and hole bands are labeled  $c'$  and  $v$ , respectively, and the primed (unprimed) band labels correspond to the  $\text{MoX}_2$  ( $\text{WX}_2$ ) layer. Given the reduced band gap  $\tilde{E}_g$  [Fig. 2(a)], the lowest-energy exciton states are spread across the heterostructure, formed by  $c'$ -band electrons and  $v$ -band holes bound by the interaction  $\mathcal{W}(\mathbf{q})$  [12, 13, 28].

The optical activity of interlayer excitons in TMD bilayers is strongly constrained by the interlayer alignment. As shown in Fig. 2(b), the relative twist angle and lattice incommensurability between the two layers produces a mismatch between their Brillouin zones (BZs). Thus, bright interlayer excitons in  $\text{MoX}_2/\text{WX}_2$  structures, consisting of same-valley  $c'$ -band electrons and  $v$ -band holes, have a finite center-of-mass momentum  $\Delta\mathbf{K} = \mathbf{K}' - \mathbf{K}$ . Due to energy and momentum conservation, photon emission by interlayer excitons is only allowed when  $\Delta K \approx 0$  [29].

The above restrictions are relaxed when excitons, and other excitonic complexes are bound to impurity centers in the sample, such as charged defects and donor ions. These complexes are localized within some characteristic length  $a_0^*$ , known as the exciton Bohr radius, such that their momentum-space wave functions are finite up to momenta of order  $1/a_0^*$ . As a result, the recombination rates of impurity-bound interlayer complexes are determined by the large-momentum tail of their wave function, and thus by the short-range interaction (3).

The Hamiltonian for the heterobilayer in the free-

carrier basis is

$$\hat{H} = \hat{H}_0 + \hat{H}_t + \hat{U}_{\text{intra}} + \hat{U}_{\text{inter}}, \quad (4)$$

where the zeroth-order Hamiltonian  $\hat{H}_0$ , describing the CB and VB electrons of the two individual layers, is given in second quantization as

$$\hat{H}_0 = \sum_{\alpha} \sum_{\mathbf{k}, \tau, \sigma} E_{\alpha}(\mathbf{k}) c_{\alpha, \tau, \sigma}^{\dagger}(\mathbf{k}) c_{\alpha, \tau, \sigma}(\mathbf{k}). \quad (5)$$

$c_{\alpha, \tau, \sigma}^{\dagger}(\mathbf{k})$  creates an electron of spin projection  $\sigma = \uparrow, \downarrow$  and momentum  $\mathbf{k}$  relative to the  $\tau\mathbf{K}$  valley ( $\tau = \pm$ ) of band  $\alpha = c', v', c, v$ . The band dispersions are

$$E_{v'}(\mathbf{k}) = -\Delta_v - \frac{\hbar^2 k^2}{2m'_v}, \quad (6a)$$

$$E_v(\mathbf{k}) = -\frac{\hbar^2 k^2}{2m_v}, \quad (6b)$$

$$E_{c'}(\mathbf{k}) = \tilde{E}_g + \frac{\hbar^2 k^2}{2m'_{c'}}, \quad (6c)$$

$$E_c(\mathbf{k}) = \tilde{E}_g + \Delta_c + \frac{\hbar^2 k^2}{2m_c}, \quad (6d)$$

where  $\Delta_c$  ( $\Delta_v$ ) is the spacing between the electron (hole) band edges [Fig. 2(a)].

The tunnelling Hamiltonian describing electron hopping between the layers is given by

$$\begin{aligned} \hat{H}_t &= \sum_{\tau, \sigma} \sum_{\mathbf{G}, \mathbf{G}', \mathbf{k}, \mathbf{k}'} \delta_{\tau\mathbf{K}+\mathbf{k}+\mathbf{G}, \tau'\mathbf{K}'+\mathbf{k}'+\mathbf{G}'} \\ &\times \left\{ [t_{cc}(\mathbf{k} + \mathbf{K} + \mathbf{G}) c_{c\tau\sigma}^{\dagger}(\mathbf{k}) c_{c'\tau'\sigma}(\mathbf{k}') \right. \\ &\left. + t_{vv}(\mathbf{k} + \mathbf{K} + \mathbf{G}) c_{v\tau\sigma}^{\dagger}(\mathbf{k}) c_{v'\tau'\sigma}(\mathbf{k}') ] + \text{H.c.} \right\}, \end{aligned} \quad (7)$$

where  $t_{cc}(\mathbf{k})$  and  $t_{vv}(\mathbf{k})$  are stacking-dependent interlayer hopping strengths between the CBs and VBs;  $\mathbf{G}$  and  $\mathbf{G}'$  correspond to the reciprocal lattice vectors in the hole and electron layers; and the Kronecker delta enforces momentum conservation in the tunnelling process [30, 31]. We focus on configurations close to AA stacking, and use the hopping terms  $t_{\alpha\alpha}(\mathbf{k})$  reported in Ref. [31]. These values are small (few meV) compared to all other scales in the problem, reflecting the vdW and electrical quadrupole nature of the interlayer interactions. As a result,  $\hat{H}_t$  can be treated within perturbation theory. Furthermore, since  $t_{\alpha\alpha}(\mathbf{k})$  decay rapidly with  $k$  [31], we truncate the sums over  $\mathbf{G}$  and  $\mathbf{G}'$  to only the first nonzero vectors, and set  $t_{cc}(\mathbf{k}) \approx t_{cc} = 2.5$  meV and  $t_{vv}(\mathbf{k}) \approx t_{vv} = 16$  meV.

Finally, the direct electrostatic interactions between carriers, and between carriers and a positive donor ion of effective charge  $Z_{\text{donor}}$ , are given by

$$\hat{U}_{\text{intra}} = \frac{e^2}{S} \sum_{\substack{\tau_1, \tau_2 \\ \sigma_1, \sigma_2}} \sum_{\mathbf{k}_1, \mathbf{k}_2, \boldsymbol{\xi}} \left[ \sum_{\alpha, \beta=v, c} \frac{\mathcal{V}(\boldsymbol{\xi})}{(1 + \delta_{\alpha, \beta})} c_{\alpha, \tau_1, \sigma_1}^\dagger(\mathbf{k}_1 + \boldsymbol{\xi}) c_{\beta, \tau_2, \sigma_2}^\dagger(\mathbf{k}_2 - \boldsymbol{\xi}) c_{\beta, \tau_2, \sigma_2}(\mathbf{k}_2) c_{\alpha, \tau_1, \sigma_1}(\mathbf{k}_1) \right. \\ \left. + \sum_{\alpha, \beta=v', c'} \frac{\mathcal{V}(\boldsymbol{\xi})}{(1 + \delta_{\alpha, \beta})} c_{\alpha, \tau_1, \sigma_1}^\dagger(\mathbf{k}_1 + \boldsymbol{\xi}) c_{\beta, \tau_2, \sigma_2}^\dagger(\mathbf{k}_2 - \boldsymbol{\xi}) c_{\beta, \tau_2, \sigma_2}(\mathbf{k}_2) c_{\alpha, \tau_1, \sigma_1}(\mathbf{k}_1) \right] \\ - \frac{Z_{\text{donor}} e^2}{S} \sum_{\tau, \sigma} \sum_{\mathbf{k}, \boldsymbol{\xi}} \sum_{\alpha=v', c'} \mathcal{V}'(\boldsymbol{\xi}) c_{\alpha, \tau, \sigma}^\dagger(\mathbf{k} + \boldsymbol{\xi}) c_{\alpha, \tau, \sigma}(\mathbf{k}), \quad (8a)$$

$$\hat{U}_{\text{inter}} = \frac{e^2}{S} \sum_{\substack{\tau_1, \tau_2 \\ \sigma_1, \sigma_2}} \sum_{\mathbf{k}_1, \mathbf{k}_2, \boldsymbol{\xi}} \sum_{\alpha=v, c} \sum_{\beta=v', c'} \mathcal{W}(\boldsymbol{\xi}) c_{\alpha, \tau_1, \sigma_1}^\dagger(\mathbf{k}_1 + \boldsymbol{\xi}) c_{\beta, \tau_2, \sigma_2}^\dagger(\mathbf{k}_2 - \boldsymbol{\xi}) c_{\beta, \tau_2, \sigma_2}(\mathbf{k}_2) c_{\alpha, \tau_1, \sigma_1}(\mathbf{k}_1) \\ - \frac{Z_{\text{donor}} e^2}{S} \sum_{\tau, \sigma} \sum_{\mathbf{k}, \boldsymbol{\xi}} \sum_{\alpha=v, c} \mathcal{W}(\boldsymbol{\xi}) c_{\alpha, \tau, \sigma}^\dagger(\mathbf{k} + \boldsymbol{\xi}) c_{\alpha, \tau, \sigma}(\mathbf{k}), \quad (8b)$$

where  $\boldsymbol{\xi}$  is the momentum transfer, and  $S$  the sample area. The donor ion is treated as a dispersionless scatterer, and is assumed to be present in the MoX<sub>2</sub> (electron) layer. Henceforth, we assume that a donor yields a single electron to the TMD and set  $Z_{\text{donor}} = 1$ .

The radiative recombination of electrons and holes is driven by the light-matter interaction

$$\hat{H}_{\text{r}} = \frac{e\gamma}{\hbar c} \sum_{\mathbf{q}} \sum_{\mathbf{k}, \tau, \sigma} \sqrt{\frac{4\pi\hbar c}{Vq}} c_{v, \tau, \sigma}^\dagger(\mathbf{k} - \mathbf{q}_{\parallel}) c_{c, \tau, \sigma}(\mathbf{k}) a_\tau^\dagger(\mathbf{q}), \quad (9)$$

in the WX<sub>2</sub> layer and an analogous term  $\hat{H}'_{\text{r}}$  in the MoX<sub>2</sub> layer. Here,  $\gamma^{(\prime)}$  is given by the in-plane momentum matrix element between  $c^{(\prime)}$  and  $v^{(\prime)}$  band states, evaluated at the  $\pm K$  points of the BZ [32].  $a_\tau^\dagger(\mathbf{q})$  creates a photon of momentum  $\mathbf{q}$  and in-plane polarization  $\tau$ , determined by the electron's valley degree of freedom, where  $\tau = +$  ( $\tau = -$ ) represents right-handed (left-handed) circular polarization. The photon momentum  $\mathbf{q} = \mathbf{q}_{\parallel} + \mathbf{q}_{\perp}$  is split into its in-plane and out-of-plane components, respectively, and  $V = SL$ , with  $L$  the height of the optical cavity.

Let  $|\Psi\rangle$  be an interlayer excitonic eigenstate of the Hamiltonian  $\hat{H}_0 + \hat{U}_{\text{intra}} + \hat{U}_{\text{inter}}$  of energy  $E_\Psi$ . Photon emission through the term  $\hat{H}_{\text{r}}$  requires the recombining carriers to be in the same TMD layer. This is allowed by the perturbation  $\hat{H}_{\text{t}}$ , giving the first-order correction to the wave function

$$|\Psi^{(1)}\rangle = \sum_n \frac{\langle n | \hat{H}_{\text{t}} | \Psi \rangle}{E_n - E_\Psi} |n\rangle, \quad (10)$$

where the sum runs over the eigenstates  $|n\rangle$  of  $\hat{H}_0 + \hat{U}_{\text{intra}} + \hat{U}_{\text{inter}}$ , with energies  $E_n$ . The resulting rate of radiative recombination is then given by Fermi's golden rule as

$$\Gamma_\Psi = \frac{2\pi}{\hbar} \sum_f \left| \langle f | [\hat{H}_{\text{r}} + \hat{H}'_{\text{r}}] | \Psi^{(1)} \rangle \right|^2 \delta(E_f - E_\Psi), \quad (11)$$

where  $\{|f\rangle\}$  is the set of possible final states, containing one additional photon. As discussed below, the relevant matrix elements in Eq. (11) can be evaluated numerically in QMC.

### III. RECOMBINATION OF DONOR-BOUND INTERLAYER COMPLEXES

#### A. Model parameters

We now discuss the optical emission signatures of the most relevant donor-bound interlayer excitonic complexes predicted by VMC and DMC simulations. For concreteness, we will focus on MoSe<sub>2</sub>/WSe<sub>2</sub> heterobilayers (X=Se); parameters relevant to this pair of materials are shown in Table I. Furthermore, we assume that the heterobilayer is encapsulated in bulk hBN, and set the dielectric constant to  $\epsilon = 4$ . Our chosen value of 4 corresponds to the high-frequency dielectric constant of hBN, which is reasonable as the exciton binding energy is considerably larger than the highest optical phonon frequency of hBN. The tensor nature of the hBN dielectric constant supplies an effective dielectric constant  $\bar{\epsilon} = \sqrt{\epsilon_{\parallel}\epsilon_{\perp}}$  and renormalizes the interlayer distance  $d$  by a factor  $\sqrt{\epsilon_{\parallel}/\epsilon_{\perp}}$ , where  $\epsilon_{\parallel}$  and  $\epsilon_{\perp}$  are the in-plane and out-of-plane dielectric constants (see Appendix A). However, taking  $\epsilon_{\parallel}(\infty)$  and  $\epsilon_{\perp}(\infty)$  from various sources we find that  $3.1 < \sqrt{\epsilon_{\parallel}\epsilon_{\perp}} < 4.5$  and  $0.71 < \sqrt{\epsilon_{\parallel}/\epsilon_{\perp}} < 0.95$  [33–36]. This justifies, in part, our use of  $\epsilon = 4$  and our use of the physical layer separation, but as a check of the robustness of our results, we have considered a few other dielectric environments for a restricted set of charge complexes.

The Hamiltonian Eq. (4), without  $\hat{H}_{\text{t}}$  (or, with charges being fixed in their layers), was solved using DMC, for various numbers of excess electrons and holes, and in the presence of donor impurities in the MoSe<sub>2</sub> layer. Our DMC total energies are statistically exact: we have considered no complexes containing any pairs of indistin-

guishable fermions, and therefore our trial wave functions are nodeless. The technical details of our DMC calculations are given in Appendix B 1. Binding energies for free and impurity-bound excitons and trions, in different dielectric environments, are reported in Table II.

TABLE I. Model parameters for MoSe<sub>2</sub> and WSe<sub>2</sub>, extracted from Refs. [21, 23, 32, 37, 38], and the heterobilayer MoSe<sub>2</sub>/WSe<sub>2</sub> extracted from Refs. [10, 12, 39]. The interlayer gap  $\tilde{E}_g$  was estimated from the luminescence spectrum reported in Ref. [12], considering the exciton binding energies of Table II. From left to right, the single-layer parameters are: lattice constant  $a$ , VB and CB masses  $m_v$  and  $m_c$ , screening length  $r_*$  in a vacuum environment, and Fermi velocity  $\gamma$ . The heterobilayer parameters are: valence and conduction interlayer spacing  $\Delta_v$  and  $\Delta_c$ , interlayer band gap  $\tilde{E}_g$ , and interlayer distance  $d$ .

	$a$ (Å)	$m_v/m_0$	$m_c/m_0$	$r_*$ (Å)	$\gamma$ (eV Å)
MoSe <sub>2</sub>	3.30	0.44	0.38	39.79	2.53
WSe <sub>2</sub>	3.29	0.34	0.29	45.11	3.17
	$\Delta_v$ (eV)	$\Delta_c$ (eV)	$\tilde{E}_g$ (eV)	$d$ (Å)	
MoSe <sub>2</sub> /WSe <sub>2</sub>	0.36	0.36	1.5	6.48	

The simplest interlayer excitonic complex is a donor-bound exciton  $D_{c'}^0 h_v$ , where  $D_{c'}^0$  represents a positive donor ion that has been neutralized by binding an electron from band  $c'$ , and  $h_v$  a hole from band  $v$ . (When complex labels appear as subscripts in formulas, we will suppress the  $v$  and  $c$  subscripts for clarity.) DMC simulations predict that this complex is unbound due to the screening of the interlayer interaction between holes and the strongly bound neutral donor state  $D_{c'}^0$ , whose binding energy is  $\mathcal{E}_{D^0}^b = -229.03$  meV (Table II). We therefore consider the recombination of a neutral donor  $D_{c'}^0$  with delocalized holes in band  $v$ .

Adding one more electron we obtain a donor-bound trion. Alternatively, this complex can be viewed as an interlayer exciton  $X_{vc'}$  bound by a neutral donor  $D_{c'}^0$ , leading to the notation  $D_{c'}^0 X_{vc'}$ . Remarkably, this larger complex is stable up to  $\sim 256$  K, with binding energy  $\mathcal{E}_{D^0 X}^b \approx 22.53$  meV (Table II) for the most energetically favorable dissociation channel into a neutral donor  $D_{c'}^0$  and an interlayer exciton  $X_{vc'}$ .

In the following sections we calculate the photoemission rates of these two complexes using the formalism described in Sec. II.

### B. $D_{c'}^0 h_v$ : Neutral donor and free hole

The initial state for the recombination process of a neutral donor and a free hole is given in second quantization by

$$|D^0; \mathbf{k}_h\rangle = \frac{1}{\sqrt{S}} \sum_{\mathbf{k}} \tilde{\chi}_{\mathbf{k}} c_{c', \tau', \sigma'}^\dagger(\mathbf{k}) c_{v, \tau, \sigma}(\mathbf{k}_h) |\Omega\rangle, \quad (12)$$

where  $\tilde{\chi}_{\mathbf{k}} = \int \chi(\mathbf{r}) e^{-i\mathbf{k}\cdot\mathbf{r}} d^2r$  is the Fourier transform of the donor-atom wave function centered at the donor site.

TABLE II. Binding energies  $\mathcal{E}^b$  of some charge-carrier complexes in a MoSe<sub>2</sub> monolayer, a WSe<sub>2</sub> monolayer, and a MoSe<sub>2</sub>/WSe<sub>2</sub> heterobilayer in different dielectric environments including: vacuum on both sides, SiO<sub>2</sub> on one side and vacuum on the other, bulk hBN on one side and vacuum on the other, and bulk hBN on both sides. In the heterobilayer it is assumed that the donor ion and electrons occur in the MoSe<sub>2</sub> layer, while the holes are confined to the WSe<sub>2</sub> layer. The material parameters are listed in Table I. The DMC error bars are everywhere smaller than 0.2 meV.

System	$\epsilon$	Binding energy (meV)			
		$X_{vc'}$	$X_{vc'c'}^-$	$D_{c'}^0$	$D_{c'}^0 X_{vc'}$
hBN/MoSe <sub>2</sub> /hBN	4	194	16.2	260	21.0
hBN/WSe <sub>2</sub> /hBN	4	160	13.6	215	18.1
vac./MoSe <sub>2</sub> /WSe <sub>2</sub> /vac.	1	206	6.2	540	40.3
SiO <sub>2</sub> /MoSe <sub>2</sub> /WSe <sub>2</sub> /vac.	2.45	123	5.1	329	30.1
hBN/MoSe <sub>2</sub> /WSe <sub>2</sub> /vac.	2.5	121	5.2	324	29.9
hBN/MoSe <sub>2</sub> /WSe <sub>2</sub> /hBN	4	84.2	4.1	229	22.5

Relative to the neutral vacuum, the state's energy can be written as  $E_{D^0}(\mathbf{k}_h) = E_{c'}(0) - E_v(\mathbf{k}_h) - \mathcal{E}_{D^0}^b$ , with  $\mathcal{E}_{D^0}^b$  the binding energy.

In the close-alignment limit and in the absence of intervalley scattering, the complex described by Eq. (12) can decay through radiative recombination only if  $\tau' = \tau$ . Furthermore, spin-valley locking [37] and the known band ordering of MoSe<sub>2</sub> and WSe<sub>2</sub> monolayers [32] further require that  $\sigma = \sigma'$ . Considering single-photon final states of the form  $|f\rangle = a_\tau^\dagger(\mathbf{q}) |\Omega\rangle$ , with polarization determined by the valley quantum number, and assuming a small twist angle  $\theta \approx 0^\circ$ , Eqs. (10) and (11) give the radiative decay rate

$$\Gamma_{D^0 h}^< = \frac{4\tilde{E}_g}{\hbar} \frac{e^2}{\hbar c} \left[ \frac{3t_{vv}\gamma'}{\hbar c \Delta_v} - \frac{3t_{cc}\gamma}{\hbar c (\Delta_c + \mathcal{E}_{D^0}^b)} \right]^2 \times \left| \int d^2r e^{i\Delta\mathbf{K}\cdot\mathbf{r}} \chi(\mathbf{r}) \right|^2 n_h, \quad (13)$$

where  $n_h$  is the hole density of the sample. To evaluate Eq. (13), we obtain the wave function  $\chi(\mathbf{r})$  of the donor-bound electron by solving the two-body problem with a finite-element method, as detailed in Appendix E. Note that a finite amplitude for radiative recombination depends critically on the electron-hole asymmetry, and on having different tunneling strengths between the CBs and the VBs of the two layers, owing to the symmetry properties of the band states.

### C. $D_{c'}^0 X_{vc'}$ : Donor-bound interlayer trion

As discussed above, a donor-bound trion  $D_{c'}^0 X_{vc'}$  can be viewed as an interlayer exciton bound to a neutral donor ion. Defining the interlayer exciton  $X_{vc'}$  and  $D_{c'}^0$  energies as  $E_X = E_{c'}(0) - E_v(0) - \mathcal{E}_X^b$  and  $E_{D^0} = E_{c'}(0) - \mathcal{E}_{D^0}^b$ , respectively, the energy of a  $D_{c'}^0 X_{vc'}$  complex can be expressed as  $E_{D^0 X} = E_{D^0} + E_X - \mathcal{E}_{D^0 X}^b$ , with  $\mathcal{E}_{D^0 X}^b$  the

binding energy. Its eigenstate is given by

$$|D^0X\rangle = \frac{1}{S^{3/2}} \sum_{\mathbf{k}_h, \mathbf{k}_1, \mathbf{k}_2} \tilde{\Phi}_{\mathbf{k}_h, \mathbf{k}_1, \mathbf{k}_2} \times c_{c', \tau', \sigma}^\dagger(\mathbf{k}_1) c_{c', -\tau', -\sigma'}^\dagger(\mathbf{k}_2) c_{v, \tau, \sigma}(\mathbf{k}_h) |\Omega\rangle, \quad (14)$$

with its two electrons belonging to opposite valleys, thus minimizing their mutual repulsion [see Eqs. (1a) and (1b)]. In this case, we consider decay into states of the form  $|f\rangle = a_\tau^\dagger(\mathbf{q})|D^0\rangle$ , which are energetically favorable given the large binding energies of  $D_c^0$  bound states. The corresponding radiative rate for close interlayer alignment is given by

$$\Gamma_{D^0X}^< \approx \frac{4\tilde{E}_g e^2}{\hbar c} \left| \int d^2r \int d^2r' e^{i\Delta\mathbf{K}\cdot\mathbf{r}} \chi^*(\mathbf{r}') \Phi(\mathbf{r}, \mathbf{r}, \mathbf{r}') \right|^2 \times \left[ \frac{3t_{vv}\gamma'}{\hbar c(\Delta_v + \mathcal{E}_{D^0X}^b + \mathcal{E}_X^b)} - \frac{3t_{cc}\gamma}{\hbar c(\Delta_c + \mathcal{E}_{D^0X}^b + \mathcal{E}_X^b)} \right]^2. \quad (15)$$

The donor atom in the final state can be in its ground state, or in any excited state allowed by angular momentum conservation. This constitutes a series of radiative subchannels, and in principle results in a series of lines with energies determined by the donor atom spectrum. The main subchannel, corresponding to the ground state  $\chi_{1s}(\mathbf{r})$ , produces the main emission line at  $E_* = \tilde{E}_g - (\mathcal{E} + \mathcal{E}_{D^0X}^b + \mathcal{E}_X^b)$ . The first radially symmetric excited state,  $\chi_{2s}(\mathbf{r})$ , will produce an additional line  $\sim 167$  meV above the main line. The overlap integrals between the ground-state donor-bound trion and the 1s and 2s neutral donor states were evaluated using VMC, and the latter was found to be two orders of magnitude smaller. We conclude that excited states can be neglected, and henceforth only the 1s subchannel will be considered. In the case of  $\Delta K = 0$ , the integral in Eq. (15) is given by  $|\int d^2r \int d^2r' \chi^*(\mathbf{r}') \Phi(\mathbf{r}, \mathbf{r}, \mathbf{r}')|^2 = 1.47$  (see Appendix B 3 for details).

To summarize Sec. III, Fig. 1(b) shows the radiative rates of  $D_c^0 h_v$  and  $D_c^0 X_{vc'}$  in an hBN/MoSe<sub>2</sub>/WSe<sub>2</sub>/hBN heterostructure, for small twist angles. The large-angle asymptotic behavior of the radiative rate shown in Fig. 1(b) is discussed next.

#### IV. ASYMPTOTIC BEHAVIOR FOR LARGE INTERLAYER TWIST ANGLES

The asymptotic behavior of the radiative rate for large valley mismatch  $\Delta\mathbf{K} \gtrsim 1/a_0^*$  can be obtained from a perturbative treatment of the short-range interactions Eq. (3). Let  $|\Psi_0\rangle$  be an excitonic state of the Hamiltonian

$$\hat{H}_{LR} = \hat{H}_0 + \hat{U}_{intra}^< + \hat{U}_{inter}^<, \quad (16)$$

of energy  $E_\Psi^0$ , containing the long-range approximation to the carrier-carrier and donor-carrier interaction. The interactions  $\hat{U}_{intra}^<$  and  $\hat{U}_{inter}^<$  are given by the expressions (8a) and (8b), respectively, with the substitutions

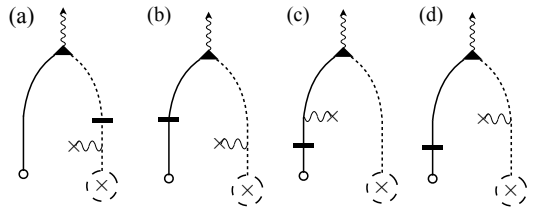


FIG. 3. Diagrams for the radiative recombination of neutral donors  $D_c^0$  with free holes  $h_v$ . The solid (dashed) line represents a free hole (electron); the donor impurity center is represented by a “x” symbol, and the  $D_c^0$  state by “x” in a dashed circle. Horizontal lines correspond to interlayer tunneling, wavy lines to Coulomb scattering, and the triangular vertex represents radiative recombination.

$\mathcal{V}'(\xi) \rightarrow \mathcal{V}'_<(\xi)$  and  $\mathcal{W}(\xi) \rightarrow \mathcal{W}_<(\xi)$  [see Eqs. (2a) and (2b)]. The state  $|\Psi_0\rangle$  is perturbed by the interlayer tunneling term  $\hat{H}_t$ , as well as the short-range interaction  $\hat{U}_{intra}^>$ , obtained by substituting  $\mathcal{V}'(\xi) \rightarrow \mathcal{V}'_>(\xi)$  in Eq. (8a) [see Eq. (3)]. As discussed above, the short-range interlayer term is exponentially suppressed, and can be ignored altogether. As a consequence, short-range impurity scattering can take place exclusively in the electron layer (see diagrams of Fig. 3).

The momentum transfer dependence of Eq. (3) justifies treating  $\hat{U}_{intra}^>$  as a perturbation. The second-order perturbative correction to the wave function relevant for photon emission is given by

$$|\Psi_0^{(2)}\rangle = \sum_{m,n} \frac{\langle n | [\hat{H}_t + \hat{U}_{intra}^>] | m \rangle \langle m | [\hat{H}_t + \hat{U}_{intra}^>] | \Psi_0 \rangle}{(E_m^0 - E_\Psi^0)(E_n^0 - E_\Psi^0)} |n\rangle, \quad (17)$$

where the sums run over the eigenstates  $|n\rangle$  of  $\hat{H}_{LR}$ , with energies  $E_n^0$ . Introducing the light-matter interaction [Eq. (9)], we focus on the diagrams of Fig. 3 for the  $D_c^0 h_v$  complex, and those of Fig. 4 for  $D_c^0 X_{vc'}$ .

In general, all diagrams must be considered when evaluating the radiative decay rate. For simplicity, however, we assume that the CB and VB spacings remain the largest scales in the problem, such that  $\frac{\hbar^2 \Delta K^2}{2m_e} \ll \Delta_c, \Delta_v$ . In this approximation, two out of the four diagrams for  $D_c^0 h_v$  radiative decay cancel out approximately, leaving only the contributions from the diagrams of Figs. 3(a) and (b) (see Appendix C). The resulting radiative decay rate for  $D_c^0 h_v$  in the large twist angle ( $>$ ) limit is given by

$$\Gamma_{D^0h}^> \approx \frac{64\pi^2 e^4 \tilde{E}_g}{\hbar \epsilon^2 r_*'^2 \Delta K^4} \frac{e^2}{\hbar c} \left[ \frac{m_{c'}}{\hbar^2 \Delta K^2} \right]^2 \left[ \frac{3t_{cc}\gamma}{\hbar c \Delta_c} - \frac{3t_{vv}\gamma'}{\hbar c \Delta_v} \right]^2 \times |\chi_0(0)|^2 n_h, \quad (18)$$

where the emitted photon energy is given by  $E_* = \tilde{E}_g - \mathcal{E}_{D^0}^b$ . The factor of three multiplying the tunnelling amplitudes  $t_{cc}$  and  $t_{vv}$  originates from the truncated sum over reciprocal lattice vectors in Eq. (7), as a consequence of the three equivalent  $\mathbf{K}$  points in the Brillouin zone [31]. Finally,  $\chi_0(\mathbf{r})$  is the  $D_c^0$  wave function obtained from the

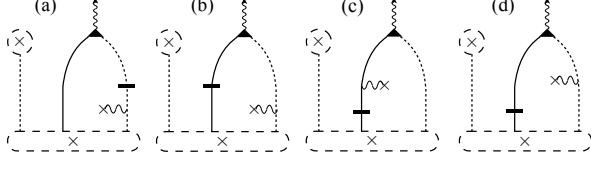


FIG. 4. Diagrams for the first radiative recombination channel of the  $D_{c'}^0 X_{vc'}$  complex. The bound hole recombines with the electron from the nearest valley in the opposite layer, assisted by short-range Coulomb interactions with the donor impurity. The remaining electron stays bound to the impurity center, forming a neutral donor atom.

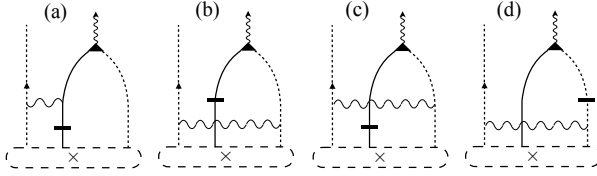


FIG. 5. Diagrams for the second radiative recombination channel of the  $D_{c'}^0 X_{vc'}$  complex. The bound hole recombines with the electron from the nearest valley in the opposite layer, assisted by short-range Coulomb interactions with the second electron, at the far valley. The latter recoils and unbinds from the donor impurity.

Keldysh approximation Hamiltonian  $\hat{H}_{\text{LR}}$ , not to be confused with the full bilayer interaction bound state  $\chi(\mathbf{r})$ . As before, we evaluate the wave function using the finite-element method, and obtain  $|\chi_0(0)|^2 = 2.678 \times 10^{-3} \text{ \AA}^{-2}$  (Appendix E).

With the perturbation  $\hat{U}_{\text{intra}}^>$ , there are two possible channels for radiative recombination of the  $D_{c'}^0 X_{vc'}$  complex, resulting in different final states, and thus two separate lines in the PL spectrum. The first process involves one of the electrons and the hole scattering from the donor impurity and subsequently recombining, emitting a photon and leaving behind a neutral donor as the final state. This is analogous to the decay process considered in Sec. III C, and the corresponding diagrams are shown in Fig. 4. Similarly to the  $D_c^0 h_v$  complex case, the leading approximation to the amplitude is the sum of two diagrams, giving a radiative rate

$$\Gamma_{D_{c'}^0 X}^> \approx \frac{64\pi^2 e^4 \tilde{E}_g}{\hbar \epsilon^2 r_*'^2 \Delta K^4} \frac{e^2}{\hbar c} \left[ \frac{m_{c'}}{\hbar^2 \Delta K^2} \right]^2 \left[ \frac{3t_{cc}\gamma}{\hbar c \Delta_c} - \frac{3t_{vv}\gamma'}{\hbar c \Delta_v} \right]^2 \times \left| \int d^2 r \chi_0^*(\mathbf{r}) \Phi_0(0, 0, \mathbf{r}) \right|^2, \quad (19)$$

where the emitted photon energy is given by  $E_* = \tilde{E}_g - (\mathcal{E}_{D_{c'}^0 X}^b + \mathcal{E}_X^b)$ , and  $\Phi_0(\mathbf{r}_h, \mathbf{r}_e, \mathbf{r}_{e'})$  is the  $D_{c'}^0 X_{vc'}$  wavefunction in the Keldysh approximation.

A second radiative decay process is possible, where the recombining electron and hole scatter with the second electron, at the far valley. The latter electron recoils and is unbound from the impurity, taking some amount of kinetic energy and producing a shift in the emission line.

The corresponding diagrams are shown in Fig. 5, and give a recombination rate

$$\Gamma_{D_{c'}^0 X}^> = \frac{48\pi^2 e^4 \tilde{E}_g}{\hbar \epsilon^2 r_*'^2 \Delta K^4} \frac{e^2}{\hbar c} \left[ \frac{m_{c'}}{\hbar^2 \Delta K^2} \right]^2 \int d^2 r |\Phi_0(\mathbf{r}, \mathbf{r}, \mathbf{r})|^2 \times \left[ \frac{t_{cc}\gamma}{\hbar c \Delta_c} - \frac{t_{vv}\gamma'}{\hbar c \Delta_v} \right]^2. \quad (20)$$

The photon energy in this case is given by  $E_* = \tilde{E}_g - \mathcal{E}_{D_{c'}^0 X}^b - \mathcal{E}_X^b - \frac{\hbar^2 \Delta K^2}{2m_{c'}}$ , and the corresponding line in the PL spectrum is red-shifted with respect to that of the first channel by  $\sim 100$  meV.

The overlap integrals between the initial- and final-state wave functions given in Eqs. (19) and (20) were evaluated in VMC for the Hamiltonian  $\hat{H}_{\text{LR}}$ . We obtain  $\left| \int d^2 r \chi_0^*(\mathbf{r}) \Phi_0(0, 0, \mathbf{r}) \right|^2 = 6.94 \times 10^{-7} \text{ \AA}^{-4}$ , and  $\int d^2 r |\Phi_0(\mathbf{r}, \mathbf{r}, \mathbf{r})|^2 = 3.22 \times 10^{-7} \text{ \AA}^{-4}$ , respectively (see Appendix B 3).

Eqs. (18), (19) and (20) show that the radiative channels considered for the two complexes decay with the interlayer twist angle as  $\theta^{-8}$ , in the limit  $\Delta K \gg 1/r_*, 1/r_*'$ . This is shown in Fig. 1(b) for angles larger than  $6^\circ$ . Our analysis indicates that, even in the case of localized impurity-bound states, the observation of photoluminescence from interlayer excitonic complexes in TMD bilayers requires near perfect alignment between the two layers.

## V. PHONON-ASSISTED RECOMBINATION

Electron-phonon (e-ph) interactions introduce yet another channel for radiative recombination. Similarly to the electron recoil process discussed above, when phonons are emitted during the recombination of a given complex, they absorb part of the energy and produce a red-shifted replica in the PL spectrum. The following analysis is carried out in terms of the VMC wave functions  $|\Psi\rangle$  discussed in Sec. III, evaluated with the exact bilayer interactions  $\mathcal{V}'(\xi)$  and  $\mathcal{W}(\xi)$ .

The e-ph interaction Hamiltonian is given by

$$\begin{aligned} \hat{H}_{\text{e-ph}} = & \sum_{\alpha=v,c} \sum_{\tau,\sigma} \sum_{\mathbf{k},\mathbf{q},\nu} \frac{g_{\nu,\alpha}(\mathbf{q})}{\sqrt{S}} (b_{h,\nu,-\mathbf{q}}^\dagger + b_{h,\nu,\mathbf{q}}) \\ & \times c_{\alpha,\tau,\sigma}^\dagger(\mathbf{k} + \mathbf{q}) c_{\alpha,\tau,\sigma}(\mathbf{k}) \\ & + \sum_{\alpha=v',c'} \sum_{\tau,\sigma} \sum_{\mathbf{k},\mathbf{q},\nu} \frac{g_{\nu,\alpha}(\mathbf{q})}{\sqrt{S}} (b_{e,\nu,-\mathbf{q}}^\dagger + b_{e,\nu,\mathbf{q}}) \\ & \times c_{\alpha,\tau,\sigma}^\dagger(\mathbf{k} + \mathbf{q}) c_{\alpha,\tau,\sigma}(\mathbf{k}), \end{aligned} \quad (21)$$

where  $b_{\Lambda,\nu,\mathbf{q}}^\dagger$  ( $b_{\Lambda,\nu,\mathbf{q}}$ ) is the creation (annihilation) operator for a phonon of momentum  $\mathbf{q}$  and mode  $\nu$  in the electron ( $\Lambda = e$ ) or hole ( $\Lambda = h$ ) layer, which couples to an electron in band  $\alpha = c', v', c, v$  with strength  $g_{\nu,\alpha}(\mathbf{q})$ .

We consider the longitudinal optical ( $\nu = \text{LO}$ ), homopolar ( $\nu = \text{HP}$ ), and longitudinal acoustic ( $\nu = \text{LA}$ )

phonon modes allowed by the lattice symmetry. The e-ph couplings are given by

$$\begin{aligned} g_{\text{LO},\alpha}(\mathbf{q}) &= \frac{1}{A} \sqrt{\frac{\hbar}{2\rho(M_r/M)\omega_{\text{LO}}}} \frac{2\pi Z_\alpha e^2}{1+qr_*}, \\ g_{\text{HP},\alpha}(\mathbf{q}) &= \sqrt{\frac{\hbar}{2\rho\omega_{\text{HP}}}} D_\alpha, \\ g_{\text{LA},\alpha}(\mathbf{q}) &= \sqrt{\frac{\hbar}{2\rho\omega_{\text{LA}}}} \Xi_\alpha q, \end{aligned} \quad (22)$$

where  $\rho$  is the mass density,  $M_r$  is the metal-and-two-chalcogen system reduced mass,  $M$  is the total mass of the unit cell, and  $A$  is the unit-cell area of the corresponding TMD layer.  $\omega_\nu$  is the phonon frequency, which we approximate as a constant for the optical modes, and as  $\omega_{\text{LA}} = c_{\text{LA}} q$  for the LA mode, with  $c_{\text{LA}}$  being the sound velocity.  $Z$  is the Born effective charge,  $r_*$  is the screening length, and  $D_\alpha$  and  $\Xi_\alpha$  are the deformation potentials of the optical and acoustic modes, respectively. The various parameters are taken from Refs. [40–43], and summarized in Table V. We focus on the low-temperature limit, where phonon occupation is low and phonon absorption can be neglected.

Perturbative corrections to the interlayer excitonic state  $|\Psi\rangle$  by the interlayer hopping and e-ph interactions are given by

$$|\Psi^{(2)}\rangle = \sum_{m,n} \frac{\langle n|[\hat{H}_t + \hat{H}_{\text{e-ph}}]|m\rangle\langle m|[\hat{H}_t + \hat{H}_{\text{e-ph}}]|\Psi\rangle}{(E_m - E_\Psi)(E_n - E_\Psi)} |n\rangle. \quad (23)$$

The relevant diagrams for radiative recombination with phonon emission are shown in Figs. 6 and 7 for  $\text{D}_{c'}^0 h_v$  and  $\text{D}_{c'}^0 X_{vc'}$ , respectively. In both figures, panels (a)–(d) correspond to single-phonon emission in the hole layer ( $\text{WSe}_2$ ), whereas panels (e)–(h) correspond to single-phonon emission in the electron layer ( $\text{MoSe}_2$ ). Although in principle the two sets of diagrams give separate lines at energies determined by the phonon energy in each layer, the parameters reported in Table V show that these lines are within only a few meV of each other. For simplicity, we assume that the two layers have the same optical-phonon energies and acoustic-phonon sound velocities, producing a single line in the PL spectrum. The resulting radiative rates are given in the limit of large twist angle ( $>$ ) by (Appendix D)

$$\Gamma_{\text{D}^0 h}^{>,\nu} \approx \frac{48\tilde{E}_g}{\hbar} \frac{e^2}{\hbar c} \left[ \frac{\gamma' t_{vv}}{\hbar c \Delta_v} - \frac{\gamma t_{cc}}{\hbar c \Delta_c} \right]^2 n_h \times \left[ \left( \frac{m_v g_{\nu,v}(\Delta K)}{\hbar^2 \Delta K^2} \right)^2 + \left( \frac{m_{c'} g_{\nu,c'}(\Delta K)}{\hbar^2 \Delta K^2} \right)^2 \right], \quad (24a)$$

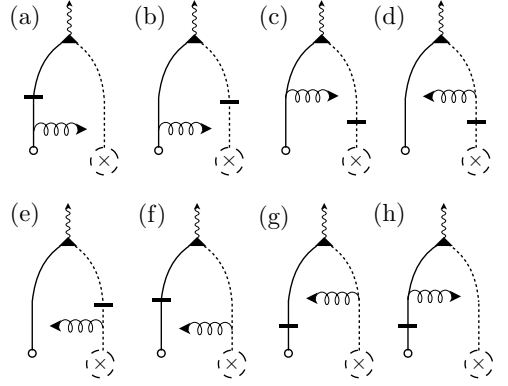


FIG. 6. Diagrams for the radiative recombination of the  $\text{D}_{c'}^0 h_v$  complex with phonon scattering. The top four diagrams correspond to phonon emission in the  $\text{WSe}_2$  layer and the bottom four diagrams correspond to phonon emission in the  $\text{MoSe}_2$  layer.

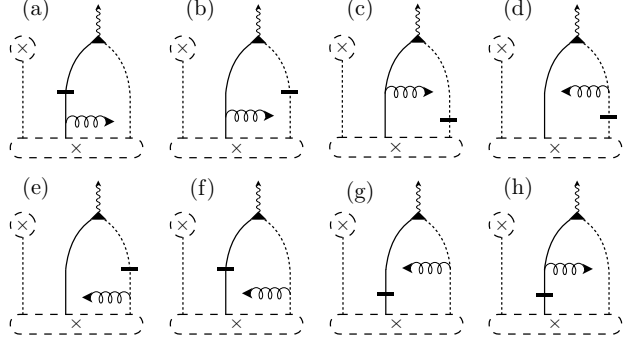


FIG. 7. Diagrams for the radiative recombination of the  $\text{D}_{c'}^0 X_{vc'}$  complex with phonon scattering and  $\text{D}_{c'}^0$  in the final state. The top four diagrams correspond to phonon emission in the  $\text{WSe}_2$  layer and the bottom four diagrams correspond to phonon emission in the  $\text{MoSe}_2$  layer.

$$\begin{aligned} \Gamma_{\text{D}^0 X}^{>,\nu} &\approx \frac{48\tilde{E}_g}{\hbar} \frac{e^2}{\hbar c} \left[ \frac{\gamma' t_{vv}}{\hbar c \Delta_v} - \frac{\gamma t_{cc}}{\hbar c \Delta_c} \right]^2 \\ &\times \left[ \left( \frac{m_v g_{\nu,v}(\Delta K)}{\hbar^2 \Delta K^2} \right)^2 + \left( \frac{m_{c'} g_{\nu,c'}(\Delta K)}{\hbar^2 \Delta K^2} \right)^2 \right] \\ &\times \int d^2 r \left| \int d^2 r' \chi^*(\mathbf{r}') \Phi(\mathbf{r}, \mathbf{r}, \mathbf{r}') \right|^2. \end{aligned} \quad (24b)$$

The VMC estimate of the overlap of  $\chi(\mathbf{r}')$  with  $\Phi(\mathbf{r}, \mathbf{r}, \mathbf{r}')$  can be found in Table VI.

In the small-twist-angle limit ( $<$ ), phonon emission from  $\text{D}_{c'}^0 h_v$  complexes is dominated by the diagram of Fig. 6(a). In that process, the phonon is emitted by a hole in the  $\text{WSe}_2$  layer, which then tunnels to recombine with the electron bound to the donor impurity. By contrast, all other diagrams shown in Fig. 6 involve ionization of the donor atom, which is suppressed by the large binding energy of the  $\text{D}_{c'}^0$  complex. The radiative rates for  $\text{D}_{c'}^0 h_v$  can thus be approximated by (Appendix

TABLE III. Electron-phonon coupling parameters for LO, HP, and LA phonon modes.  $\omega_{\text{LO}}$  and  $\omega_{\text{HP}}$  are the LO- and HP-mode frequencies,  $c_{\text{LA}}$  is the speed of sound for the LA mode,  $\rho$  is the mass density,  $D_\alpha$  and  $\Xi_\alpha$  are the deformation potentials of the optical and acoustic modes, respectively,  $M_r/M$  is the ratio of the metal-and-two-chalcogen system reduced mass to the total mass of the unit cell, and  $Z$  is the Born effective charge.

	$\hbar\omega_{\text{LO}}$ (meV)	$\hbar\omega_{\text{HP}}$ (meV)	$c_{\text{LA}}$ (cm/s)	$\rho$ (g/cm <sup>3</sup> )	$D_c$ (eV/Å)	$D_v$ (eV/Å)	$\Xi_c$ (eV)	$\Xi_v$ (eV)	$M_r/M$	$Z$
MoSe <sub>2</sub>	37	30	$4.8 \times 10^5$	$4.5 \times 10^{-7}$	5.2	4.9	3.4	2.8	0.235	1.8
WSe <sub>2</sub>	31	31	$4.4 \times 10^5$	$6.1 \times 10^{-7}$	2.3	3.1	3.2	2.1	0.249	1.08

D)

$$\Gamma_{D^0 h}^{<, \nu=\text{LO/HP}} \approx \frac{6\tilde{E}_g}{\pi\hbar} \frac{e^2}{\hbar c} \left[ \frac{\gamma' t_{vv}}{\hbar c \Delta_v} \right]^2 \left[ \frac{|g_{\nu, c'}(\Delta K)|^2}{(\hbar\omega_\nu + \mathcal{E}_{D^0}^b)^2} \right] \times \frac{m_v |g_{\nu, v}(\Delta K)|^2}{\hbar^3 \omega_\nu} \left| \int d^2 r e^{i\Delta \mathbf{K} \cdot \mathbf{r}} \chi(\mathbf{r}) \right|^2 n_h, \quad (25a)$$

$$\Gamma_{D^0 h}^{<, \text{LA}} \approx \frac{6\tilde{E}_g}{\pi\hbar} \frac{e^2}{\hbar c} \frac{m_v \Xi_v^2}{\hbar^2 p c_{\text{LA}}^2} \left[ \frac{\gamma' t_{vv}}{\hbar c \Delta_v} \right]^2 \times \left| \int d^2 r e^{i\Delta \mathbf{K} \cdot \mathbf{r}} \chi(\mathbf{r}) \right|^2 n_h. \quad (25b)$$

In the  $D_{c'}^0 X_{vc'}$  case at small twist angles, the phonon emission process is suppressed by the ionization of the complex in the intermediate state and the overlap integral between the initial  $D_{c'}^0 X_{vc'}$  and final  $D_{c'}^0$  states. The rates are given by

$$\Gamma_{D^0 X}^{<, \nu=\text{LO/HP}} = \frac{12\tilde{E}_g}{\hbar} \frac{e^2}{\hbar c} \frac{|g_{\nu, v}(0)|^2 + |g_{\nu, c'}(0)|^2}{(\hbar\omega_\nu + \mathcal{E}_{D^0 X}^b + \mathcal{E}_X^b)^2} \times \left[ \frac{\gamma' t_{vv}}{\hbar c \Delta_v} - \frac{\gamma t_{cc}}{\hbar c \Delta_c} \right]^2 \int d^2 r \left| \int d^2 r' \chi^*(\mathbf{r}') \Phi(\mathbf{r}, \mathbf{r}, \mathbf{r}') \right|^2, \quad (26a)$$

$$\Gamma_{D^0 X}^{<, \text{LA}} = \frac{3\tilde{E}_g}{\sqrt{2}\hbar^3 c_{\text{LA}}} \frac{e^2}{\hbar c} \frac{(m_v + m_{c'})^{3/2}}{\sqrt{\mathcal{E}_{D^0 X}^b + \mathcal{E}_X^b}} \left[ \frac{\gamma' t_{vv}}{\hbar c \Delta_v} - \frac{\gamma t_{cc}}{\hbar c \Delta_c} \right]^2 \times \left[ \frac{\Xi_v^2}{\rho} \left| \int d^2 r \int d^2 r' e^{-i\Delta \mathbf{K} \cdot \mathbf{r}} \chi^*(\mathbf{r}') \Phi(\mathbf{r}, \mathbf{r}, \mathbf{r}') \right|^2 \right. \\ \left. + \frac{\Xi_{c'}^2}{\rho'} \left| \int d^2 r \int d^2 r' e^{i\Delta \mathbf{K} \cdot \mathbf{r}} \chi^*(\mathbf{r}') \Phi(\mathbf{r}, \mathbf{r}, \mathbf{r}') \right|^2 \right], \quad (26b)$$

where  $\rho$  and  $\rho'$  are the mass densities of WSe<sub>2</sub> and MoSe<sub>2</sub>, respectively (Table V).

Eqs. (24a)–(26b) contain a factor of three originating from the tunnelling process, which gives three distinct intermediate states with different emitted phonon wave vectors, related by  $C_3$  symmetry. As a result, the interference leading to the factor of nine in the interaction-driven processes of Secs. III and IV is absent in this case.

Additional contributions to the LO phonon emission come from e-ph interaction of a carrier in one layer with an LO phonon in the other. This is made possible by the long range of the LO phonon-induced potential. The

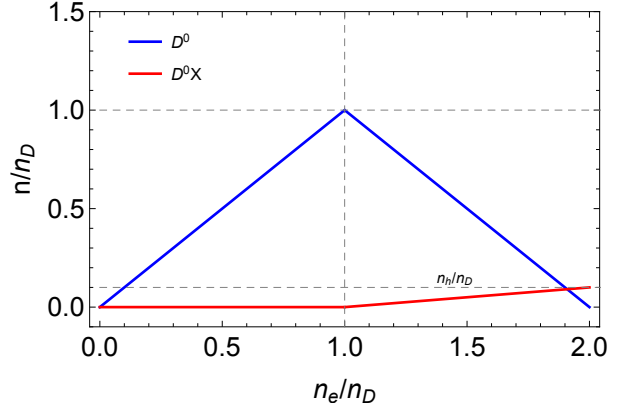


FIG. 8. Model for the density of complexes  $D_{c'}^0$  and  $D_{c'}^0 X_{vc'}$  as a function of the electron density  $n_e$ .

interlayer separation results in an exponential suppression of the potential in the interlayer distance and momentum transfer as  $e^{-\Delta K d}$ , which nonetheless is approximately unity in the limit of close alignment. Thus, we add this contribution to the LO-phonon-assisted recombination rates for  $D_{c'}^0 h_v$  and  $D_{c'}^0 X_{vc'}$  complexes in the small-twist-angle limit.

The total phonon emission rates for the two complexes, combining the three phonon modes, are shown in Fig. 1(b) as functions of the twist angle. As mentioned above, the phonon contribution to the recombination rate is most significant for the  $D_{c'}^0 h_v$  complex, being an order of magnitude larger than for  $D_{c'}^0 X_{vc'}$ . The LO phonon mode in the hole layer (WSe<sub>2</sub>) is the dominant phonon-assisted process overall, and gives a significant decay rate in the small-twist-angle limit. As a result, we predict additional phonon-replica lines in the PL spectrum, red-shifted by the phonon energy  $\hbar\omega_{\text{LO}} = 31$  meV with respect to the main  $D_{c'}^0 h_v$  and  $D_{c'}^0 X_{vc'}$  lines. The  $D_{c'}^0 h_v$  phonon-replica line gives the most dominant feature, with decay rates comparable to the main  $D_{c'}^0 h_v$  line.

## VI. INTENSITY DEPENDENCE ON DOPING

In addition to the decay rates, the relative line intensities also depend on the distribution of  $D_{c'}^0 h$  and  $D_{c'}^0 X_{vc'}$  complexes in the system. At charge neutrality, neutral excitonic complexes such as  $D_{c'}^0 h_v$  are energetically favorable, whereas additional electrons introduced into the sample will bind to existing neutral donors to form  $D_{c'}^0 X_{vc'}$  complexes. Thus the relative population of

complexes can be controlled through doping.

In this section we model the evolution of the PL spectrum with the carrier density. We assume a constant density  $n_h$  of laser-pumped holes and a large density of donor impurities in the sample, and consider the tuning of the electron density  $n_e$  by electrostatic gating [18]. Under these assumptions, and given that the net population of donor-bound complexes is limited by the donor density  $n_D$ , we limit our discussion to the regime where  $n_h \ll n_e \sim n_D$ .

We use a simplified zero-temperature model for the occupations of the two complexes, shown in Fig. 8. There are two main regimes determined by the sample-dependent donor density  $n_D$ . In the p-doped regime, defined by  $0 < n_e < n_D$ , added electrons neutralize the excess positive donors, forming  $D_{c'}^0$  complexes that can recombine with the optically pumped holes. In this regime, the formation of  $D_{c'}^0 X_{vc'}$  complexes is energetically unfavorable, and thus thermally suppressed until all donors have been neutralized.

By contrast, in the n-doped regime, defined by  $n_D < n_e < 2n_D$ , it is energetically favorable for additional electrons to bind with an existing neutral donor to form either a charged donor state  $D_{c'c'}^-$  (Table IV), or a donor-bound trion  $D_{c'}^0 X_{vc'}$ . For the latter case we must consider that laser-pumped holes are scarce ( $n_h \ll n_D$ ), and thus the probability of forming a  $D_{c'}^0 X_{vc'}$  complex will be proportional to  $n_h/n_D$ . The increase in electron density is accompanied by a decrease in  $D_{c'}^0 h_v$  numbers, and a much slower increase in the  $D_{c'}^0 X_{vc'}$  population, until the number of donor-bound trions in the system equals the number of available holes. This is shown in Fig. 8.

The line intensities within this model are given by

$$I_{D^0h} \approx \Gamma_{D^0h} \begin{cases} n_e, & n_e < n_D \\ n_D \left[ 1 - \frac{n_e - n_D}{n_D} \right], & n_D < n_e < 2n_D \end{cases}, \quad (27)$$

and

$$I_{D^0X} \approx \Gamma_{D^0X} \begin{cases} 0, & n_e < n_D \\ n_h \frac{n_e - n_D}{n_D}, & n_D < n_e < 2n_D \end{cases}. \quad (28)$$

The resulting simulated PL spectrum is shown in Fig. 9 for different doping densities, given in terms of the donor density in the MoSe<sub>2</sub> layer. A Gaussian lineshape was used for the lines with an experimentally motivated broadening [18] of  $2\sigma = 60$  meV. The spectrum shows the three dominant lines,  $D_{c'}^0 h_v$ ,  $D_{c'}^0 X_{vc'}$ , and the red-shifted phonon replica of  $D_{c'}^0 h_v$ , with the lines' peak energies determined by the DMC-obtained binding energies. The three complexes evolve with doping as prescribed by the occupation model [Eqs. (27) and (28)]. The  $D_{c'}^0 h_v$  complex and its phonon replica dominate at low doping, but the  $D_{c'}^0 X_{vc'}$  complex grows slowly in intensity with increasing doping, leading to a simultaneous reduction in the intensity of the  $D_{c'}^0 h_v$  complex. For the broadening used in the simulated PL spectrum, the proximity of the three lines results in an intricate line form, providing a signature in PL experiments for the intrinsic structure of the interlayer emission line.

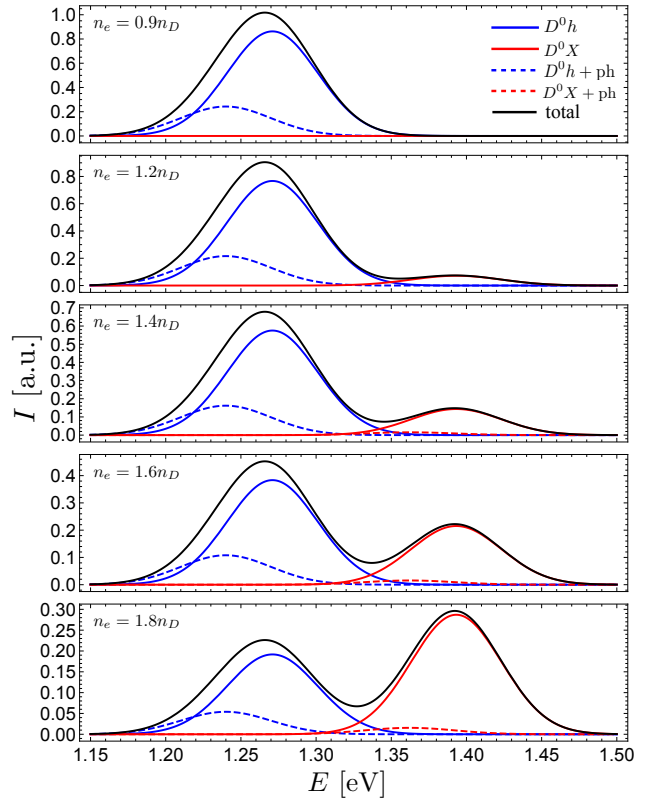


FIG. 9. Simulated normalized PL spectra for a closely aligned ( $\theta \approx 0^\circ$ ) MoSe<sub>2</sub>/WSe<sub>2</sub> heterobilayer, originating from the  $D_{c'}^0 h_v$  and  $D_{c'}^0 X_{vc'}$  complexes at different electron densities  $n_e$ , given in terms of the fixed donor density  $n_D$ . Dashed curves correspond to the phonon replicas. The lines are assumed to have Gaussian shapes of width  $2\sigma = 60$  meV, and we use  $n_h = 10^{11} \text{ cm}^{-2}$  and  $n_D = 10^{13} \text{ cm}^{-2}$ .

## VII. CONCLUSIONS

The momentum mismatch between twisted and incommensurate heterobilayer TMDs prevents efficient radiative recombination of interlayer complexes composed of electrons and holes localized on opposite layers. In this paper we have provided a mechanism to bridge the momentum gap involving donor impurities present in the heterobilayer system, both at small and large twist angles. The donor impurities were found to provide deep potential wells ( $\sim 200$  meV), resulting in strongly bound interlayer complexes, as revealed by DMC calculations. Focusing on the simplest multiparticle complexes, we obtain radiative rates of up to a few  $\mu\text{s}^{-1}$  for the neutral donor with a free hole  $D_{c'}^0 h_v$  and the donor-bound trion  $D_{c'}^0 X_{vc'}$  complexes for closely aligned layers, and a strong twist-angle suppression for large misalignment with the asymptotic form  $\propto \theta^{-8}$ . A comparable contribution was found for the  $D_{c'}^0 h_v$  complex from emission of optical phonons, resulting in a total of three dominant and doping-tunable lines in the PL spectrum. The  $D_{c'}^0 h_v$  and its phonon replica are expected to dominate the emission spectrum for electron densities below the sample-dependent donor concentration; conversely, PL

from the  $D_{c'}^0 X_{vc'}$  complex is expected to dominate the interlayer sector of the spectrum when the electron density exceeds the density of donors.

## ACKNOWLEDGMENTS

M.D., D.A.R-T., and V.I.F. wish to thank F. Vialla and F. Koppens for fruitful discussions. M.D., D.A.R-T., and V.I.F. acknowledge support from ERC Syn-

ergy Grant Hetero2D, EPSRC EP/N010345, EPSRC EP/P026850/1, Lloyd Register Foundation Nanotechnology grant, and support from the European Graphene Flagship Project. R.J.H. is fully funded by the Graphene NOWNANO centre for doctoral training (EPSRC grant no. EP/L01548X/1). M.S. was funded by the EPSRC standard grant “Non-perturbative and stochastic approaches to many-body localization” (Grant No. EP/P010180/1). Computer time was provided by Lancaster University’s High-End Computing facility, and we have also made use of the N8 HPC – funded by the N8 consortium and the EPSRC (Grant No. EP/K000225/1).

- 
- [1] A. K. Geim and I. V. Grigorieva, *Nature* **499**, 419 (2013).
  - [2] K. S. Novoselov, A. Mishchenko, A. Carvalho, and A. H. Castro Neto, *Science* **353**, aac9439 (2016).
  - [3] W. Zhang, Q. Wang, Y. Chen, Z. Wang, and A. T. S. Wee, *2D Mater.* **3**, 022001 (2016).
  - [4] M. M. Furchi, A. Pospischil, F. Libisch, J. Burgdörfer, and T. Mueller, *Nano Letters* **14**, 4785 (2014).
  - [5] C.-H. Lee, G.-H. Lee, A. M. van der Zande, W. Chen, Y. Li, M. Han, X. Cui, G. Arefe, C. Nuckolls, T. F. Heinz, J. Guo, J. Hone, and P. Kim, *Nature Nanotechnology* **9**, 676 EP (2014).
  - [6] M. Szyniszewski, E. Mostaani, N. D. Drummond, and V. I. Fal’ko, *Phys. Rev. B* **95**, 081301 (2017).
  - [7] A. T. Hanbicki, M. Currie, G. Kioseoglou, A. L. Friedman, and B. T. Jonker, *Solid State Commun.* **203**, 16 (2015).
  - [8] T. Cao, G. Wang, W. Han, H. Ye, C. Zhu, J. Shi, Q. Niu, P. Tan, E. Wang, B. Liu, and J. Feng, *Nat. Commun.* **3**, 887 (2012).
  - [9] X. Xu, W. Yao, D. Xiao, and T. F. Heinz, *Nat. Phys.* **10**, 343 (2014).
  - [10] C. Gong, H. Zhang, W. Wang, L. Colombo, R. M. Wallace, and K. Cho, *Appl. Phys. Lett.* **103**, 053513 (2013).
  - [11] J. Kang, S. Tongay, J. Zhou, J. Li, and J. Wu, *Appl. Phys. Lett.* **102**, 012111 (2013).
  - [12] P. Rivera, J. R. Schaibley, A. M. Jones, J. S. Ross, S. Wu, G. Aivazian, P. Klement, K. Seyler, G. Clark, N. J. Ghimire, J. Yan, D. G. Mandrus, W. Yao, and X. Xu, *Nat. Commun.* **6**, 6242 (2015).
  - [13] P. Nagler, G. Plechinger, M. V. Ballottin, A. Mitioglu, S. Meier, N. Paradiso, C. Strunk, A. Chernikov, P. C. M. Christianen, C. Schüller, and T. Korn, *2D Mater.* **4**, 025112 (2017).
  - [14] E. M. Alexeev, A. Catanzaro, O. V. Skrypka, P. K. Nayak, S. Ahn, S. Pak, J. Lee, J. I. Sohn, K. S. Novoselov, H. S. Shin, and A. I. Tartakovskii, *Nano Letters* **17**, 5342 (2017), <https://doi.org/10.1021/acs.nanolett.7b01763>.
  - [15] H. Yu, Y. Wang, Q. Tong, X. Xu, and W. Yao, *Phys. Rev. Lett.* **115**, 187002 (2015).
  - [16] D. M. Ceperley and B. J. Alder, *Phys. Rev. Lett.* **45**, 566 (1980).
  - [17] W. M. C. Foulkes, L. Mitas, R. J. Needs, and G. Rajagopal, *Rev. Mod. Phys.* **73**, 33 (2001).
  - [18] F. Vialla and F. Koppens, (2017), (private communication).
  - [19] L. V. Keldysh, *J. Exp. Theor. Phys.* **29**, 658 (1979).
  - [20] B. Ganchev, N. Drummond, I. Aleiner, and V. Fal’ko, *Phys. Rev. Lett.* **114**, 107401 (2015).
  - [21] T. C. Berkelbach, M. S. Hybertsen, and D. R. Reichman, *Phys. Rev. B* **88**, 045318 (2013).
  - [22] M. Van der Donck, M. Zarenia, and F. M. Peeters, *Phys. Rev. B* **96**, 035131 (2017).
  - [23] E. Mostaani, M. Szyniszewski, C. H. Price, R. Maezono, M. Danovich, R. J. Hunt, N. D. Drummond, and V. I. Fal’ko, *Phys. Rev. B* **96**, 075431 (2017).
  - [24] A. Ramasubramaniam, *Phys. Rev. B* **86**, 115409 (2012).
  - [25] K. F. Mak, K. He, C. Lee, G. H. Lee, J. Hone, T. F. Heinz, and J. Shan, *Nature Materials* **12**, 207 EP (2012).
  - [26] J. S. Ross, S. Wu, H. Yu, N. J. Ghimire, A. M. Jones, G. Aivazian, J. Yan, D. G. Mandrus, D. Xiao, W. Yao, and X. Xu, *Nat. Commun.* **4**, 1474 EP (2013).
  - [27] Y. Lin, X. Ling, L. Yu, S. Huang, A. L. Hsu, Y.-H. Lee, J. Kong, M. S. Dresselhaus, and T. Palacios, *Nano Letters* **14**, 5569 (2014), <http://dx.doi.org/10.1021/nl501988y>.
  - [28] Y. Yu, S. Hu, L. Su, L. Huang, Y. Liu, Z. Jin, A. A. Purezky, D. B. Geohegan, K. W. Kim, Y. Zhang, and L. Cao, *Nano Letters* **15**, 486 (2015), <http://dx.doi.org/10.1021/nl5038177>.
  - [29] H. Wang, C. Zhang, W. Chan, C. Manolatou, S. Tiwari, and F. Rana, *Phys. Rev. B* **93**, 045407 (2016).
  - [30] M. Koshino and P. Moon, *J. Phys. Soc. Jpn.* **84**, 121001 (2015).
  - [31] Y. Wang, Z. Wang, W. Yao, G.-B. Liu, and H. Yu, *Phys. Rev. B* **95**, 115429 (2017).
  - [32] A. Kormányos, G. Burkard, M. Gmitra, J. Fabian, V. Zólyomi, N. D. Drummond, and V. Fal’ko, *2D Mater.* **2**, 022001 (2015).
  - [33] R. Geick, C. H. Perry, and G. Rupprecht, *Phys. Rev.* **146**, 543 (1966).
  - [34] M. F. Plass, W. Fukarek, A. Kolitsch, N. Schell, and W. Möller, *Thin Solid Films* **305**, 172 (1997).
  - [35] K.-L. Barth, W. Fukarek, H.-P. Maucher, M. F. Plass, and A. Lunk, *Thin Solid Films* **313**, 697 (1998).
  - [36] S. L. Rumyantsev, M. E. Levinstein, A. D. Jackson, S. N. Mohammad, G. L. Harris, M. G. Spencer, and M. Shur, in *Properties of Advanced Semiconductor Materials GaN, AlN, InN, BN, SiC, SiGe*, edited by M. E. Levinstein, S. L. Rumyantsev, and M. S. Shur (John Wiley & Sons New York, NY, USA, 2001) Chap. 4, pp. 67–92.
  - [37] D. Xiao, G.-B. Liu, W. Feng, X. Xu, and W. Yao, *Phys. Rev. Lett.* **108**, 196802 (2012).
  - [38] A. Kumar and P. Ahluwalia, *Physica B: Condens. Matter* **407**, 4627 (2012).
  - [39] B. Amin, N. Singh, and U. Schwingenschlögl, *Phys. Rev. B* **92**, 075439 (2015).

- [40] M. Danovich, I. L. Aleiner, N. D. Drummond, and V. I. Fal'ko, IEEE J. Sel. Top. Quantum Electron. **23**, 168 (2017).
- [41] Z. Jin, X. Li, J. T. Mullen, and K. W. Kim, Phys. Rev. B **90**, 045422 (2014).
- [42] X. Gu and R. Yang, Appl. Phys. Lett. **105**, 131903 (2014).
- [43] K. Kaasbjerg, K. S. Thygesen, and A.-P. Jauho, Phys. Rev. B **87**, 235312 (2013).
- [44] H. Ogata, Publ. Res. Inst. Math. Sci. **41**, 949 (2005).
- [45] N. D. Drummond, M. D. Towler, and R. J. Needs, Phys. Rev. B **70**, 235119 (2004).
- [46] P. López Ríos, P. Seth, N. D. Drummond, and R. J. Needs, Phys. Rev. E **86**, 036703 (2012).
- [47] T. Kato, Comm. Pure Appl. Math. **10**, 151 (1957).
- [48] C. J. Umrigar, K. G. Wilson, and J. W. Wilkins, Phys. Rev. Lett. **60**, 1719 (1988).
- [49] N. D. Drummond and R. J. Needs, Phys. Rev. B **72**, 085124 (2005).
- [50] C. J. Umrigar, J. Toulouse, C. Filippi, S. Sorella, and R. G. Hennig, Phys. Rev. Lett. **98**, 110201 (2007).
- [51] R. J. Needs, M. D. Towler, N. D. Drummond, and P. López Ríos, J. Phys. Condens. Matter **22**, 023201 (2010).
- [52] *Mathematica, Version 11.0.1* (Wolfram Research, Inc., Champaign, Illinois, U.S.A., 2016).

## Appendix A: Long-range interaction between charge carriers

### 1. Multilayer Keldysh interaction

Consider a vdW heterostructure of 2D semiconductors comprised of  $N$  parallel layers (labelled  $i = \{1, 2, \dots, N\}$ ), each having in-plane susceptibility  $\kappa_i$  and  $z$ -coordinate  $d_i$ . Suppose this heterostructure is immersed in an isotropic medium of dielectric constant  $\epsilon$ . In practice the dielectric constant is taken to be the average of the dielectric constants of the media above and below the heterobilayer.

Suppose that a test charge density

$$\rho_{\text{tot}}^j(\mathbf{r}, z) = \rho^j(\mathbf{r})\delta(z - d_j), \quad (\text{A1})$$

is present in layer  $j$ . The resulting electric displacement field is

$$\mathbf{D} = -\frac{\epsilon}{4\pi}\nabla\phi(\mathbf{r}, z) - \sum_i \kappa_i[\nabla_{\parallel}\phi(\mathbf{r}, d_i)]\delta(z - d_i), \quad (\text{A2})$$

where  $\nabla_{\parallel}$  is the 2D gradient operator (excluding the  $z$ -component). Gauss's law yields

$$\begin{aligned} \rho^j(\mathbf{r}, z)\delta(z - d_j) &= -\frac{\epsilon}{4\pi}\nabla^2\phi(\mathbf{r}, z) \\ &\quad - \sum_i \kappa_i[\nabla_{\parallel}^2\phi(\mathbf{r}, d_i)]\delta(z - d_i). \end{aligned} \quad (\text{A3})$$

Taking the Fourier transform gives

$$\rho^j(\mathbf{q})e^{-ikd_j} = \frac{\epsilon}{4\pi}(q^2 + k^2)\phi(\mathbf{q}, k) + q^2 \sum_i \kappa_i\phi(\mathbf{q}, d_i)e^{-ikd_i}, \quad (\text{A4})$$

which, after Fourier inversion in the  $k$  variable only, gives

$$\rho^j(\mathbf{q})e^{-q|z-d_j|} = \frac{\epsilon}{2\pi}q\phi(\mathbf{q}, z) + q^2 \sum_i \kappa_i\phi(\mathbf{q}, d_i)e^{-q|z-d_i|}. \quad (\text{A5})$$

Evaluating Eq. (A5) at each layer ( $z = d_l$ ,  $l = \{1, 2, \dots, N\}$ ), we find

$$\begin{aligned} \rho^j e^{-q|d_l - d_j|} &= q[\epsilon/(2\pi) - \kappa_l q]\phi(\mathbf{q}, d_l) \\ &\quad + q^2 \sum_{i \neq l} \kappa_i\phi(\mathbf{q}, d_i)e^{-q|d_l - d_i|}, \end{aligned} \quad (\text{A6})$$

which is a matrix equation

$$\rho_l^j(\mathbf{q}) = \sum_i M_{li}(\mathbf{q})\phi_i(\mathbf{q}), \quad (\text{A7})$$

where

$$\begin{aligned} \rho_l^j(\mathbf{q}) &= \rho^j(\mathbf{q})e^{-q|d_l - d_j|}, \\ \phi_l(\mathbf{q}) &= \phi(\mathbf{q}, d_l), \\ M_{li} &= \begin{cases} q[\epsilon/(2\pi) + \kappa_l q] & \text{if } i = l \\ q^2\kappa_i e^{-q|d_l - d_i|} & \text{otherwise} \end{cases}. \end{aligned} \quad (\text{A8})$$

The solution to Eq. (A7) is a set of  $\phi_i(\mathbf{q}) \equiv \rho^j(\mathbf{q}) \times v_{ji}(\mathbf{q})$ , with  $v_{ji}(\mathbf{q})$  being the Fourier components of the interaction potential between layer  $j$  and layer  $i$ . If  $j = i$  then this is the intralayer interaction in layer  $j$ . This procedure should, in general, be repeated for  $j = 1, 2, \dots, N$ ; however, if there is sufficient symmetry (e.g., a mirror symmetry about a plane through the center of the heterostructure) then only a subset of  $j$  values will require explicit solution of Eq. (A7).

The same analysis applies in the case that the surrounding dielectric medium is anisotropic, having dielectric tensor

$$\tilde{\epsilon} = \begin{pmatrix} \epsilon_{\parallel} & 0 & 0 \\ 0 & \epsilon_{\parallel} & 0 \\ 0 & 0 & \epsilon_{\perp} \end{pmatrix}, \quad (\text{A9})$$

provided the substitutions

$$d \rightarrow D = \sqrt{\epsilon_{\parallel}/\epsilon_{\perp}}d, \quad (\text{A10})$$

$$\epsilon \rightarrow \bar{\epsilon} = \sqrt{\epsilon_{\parallel}\epsilon_{\perp}}, \quad (\text{A11})$$

are also made.

### 2. Numerical evaluation of the bilayer Keldysh interaction

In the bilayer case ( $N = 2$ ), it is straightforward to solve Eq. (A7) to obtain the intra- ( $\mathcal{V}$  and  $\mathcal{V}'$ ) and interlayer ( $\mathcal{W}$ ) potentials of Eqs. (1a)–(1c).

Continuum QMC calculations require the potential energy to be evaluated in real space. We therefore require the inverse Fourier transforms of Eqs. (1a)–(1c), which reduce to Hankel transforms due to the circular symmetry of the interaction potentials.

At long range (small  $q$ ), the intralayer interaction  $\mathcal{V}(\mathbf{q}) = 2\pi/\{\epsilon q[1 + (r_* + r'_*)q]\} + O(q)$  reduces to the monolayer Keldysh form [19], with an effective screening length  $r_*^{\text{eff}} = r_* + r'_*$ . The inverse Fourier transform can be performed analytically in this limit, giving

$$\begin{aligned}\mathcal{V}(r) \approx & \frac{\pi}{2\epsilon(r_* + r'_*)} \\ & \times [H_0(r/(r_* + r'_*)) - Y_0(r/(r_* + r'_*))] \\ & + O(r^{-3}),\end{aligned}\quad (\text{A12})$$

where  $H_0$  and  $Y_0$  are a Struve function and a Bessel function of the second kind, respectively. Equation (A12) is a good approximation at long range.

At short range (large  $q$ ), the intralayer interaction of Eq. (1a) again reduces to the monolayer Keldysh form, but this time with  $r_*^{\text{eff}} = r_*$ , i.e., the second layer becomes irrelevant. On the other hand, at very long range, the monolayer Keldysh interaction is also valid, since  $\mathcal{V}(\mathbf{q}) = 2\pi/(\epsilon q) + O(1)$  at small  $q$  so that the interaction is of Coulomb form. Thus the monolayer Keldysh interaction

$$\mathcal{V}(r) \approx \frac{\pi}{2\epsilon r_*^{\text{eff}}} [H_0(r/r_*^{\text{eff}}) - Y_0(r/r_*^{\text{eff}})] + O(r^{-2}), \quad (\text{A13})$$

is a reasonable approximation to the intralayer interaction at *both* short and very long range.

To evaluate the “full” intralayer interaction numerically, we used the quadrature method of Ogata [44] to perform the Hankel transform of  $\mathcal{V}(\mathbf{q}) - 2\pi/\{\epsilon q[1 + r_*q]\}$ , then added the result to the monolayer Keldysh interaction of Eq. (A13). Partitioning the interaction into a long-range part and a numerically evaluated short-range part ensures that the quadrature is relatively straightforward, and that we can introduce a cutoff at large  $r$ , beyond which the numerical corrective term is negligible.

At small  $q$ , the interlayer interaction of Eq. (1c) reduces to the displaced Coulomb form  $\mathcal{W}(q) = 2\pi e^{-(r_* + r'_* + d)q}/(\epsilon q) + O(q)$ ; hence the long-range interlayer potential in real space is given by

$$\mathcal{W}(r) \approx \frac{1}{4\pi\sqrt{r^2 + (r_* + r'_* + d)^2}} + O(r^{-3}). \quad (\text{A14})$$

At short range in real space the interlayer interaction should be nondivergent. Equation (A14) satisfies this qualitative requirement.

To evaluate the “full” interlayer interaction numerically, we performed the numerical Hankel transform of  $\mathcal{W}(\mathbf{q}) - 2\pi e^{-(r_* + r'_* + d)q}/(\epsilon q)$ , then added the result to Eq. (A14).

There is an alternative long-range approximation to the interlayer potential, which is more like the intralayer potential. Noting that  $\mathcal{W}(\mathbf{q}) = 2\pi/\{\epsilon q[1 + (r_* + r'_* + d)q]\} + O(q)$ , the long-range interlayer potential reduces to a Keldysh potential with  $r_*^{\text{eff}} = r_* + r'_* + d$ , giving

$$\begin{aligned}\mathcal{W}(r) \approx & \frac{\pi}{2\epsilon(r_* + r'_* + d)} \\ & \times \left[ H_0\left(\frac{r}{r_* + r'_* + d}\right) - Y_0\left(\frac{r}{r_* + r'_* + d}\right) \right] \\ & + O(r^{-3}).\end{aligned}\quad (\text{A15})$$

This introduces unphysical singular behavior into the interlayer interaction at short range.

## Appendix B: QMC calculations

### 1. Technical details

We performed VMC and DMC calculations [16, 17] for complexes of distinguishable charge carriers and fixed ions interacting via the “full” bilayer potential [Eqs. (1a)–(1c)] and the approximate small- $q$  Keldysh form of the potential [Eqs. (A12) and (A15)], as described in Appendix A 2. We used trial wave functions of Jastrow form, where the Jastrow exponents contained smoothly truncated polynomial particle-particle terms, ion-particle terms, ion-particle-particle, and particle-particle-particle terms [45, 46]. Additional terms satisfying the analogs of the Kato cusp conditions [6, 20, 47] were applied to the trial wave function between pairs of particles wherever there was a logarithmic divergence in the interaction between them, including the unphysical divergences in the approximate Keldysh interaction. Free parameters were optimized using VMC with variance [48, 49] and energy minimization [50] as implemented in the CASINO code [51].

In our DMC calculations we used two DMC time steps in the ratio 1:4 and corresponding target populations in the ratio 4:1, allowing a simultaneous extrapolation to zero time step and infinite population. Since the charge carriers are distinguishable, there is no fixed-node error and hence DMC provides exact ground-state solutions to the effective-mass model of interacting charge carriers with the chosen model interaction.

### 2. Energies of complexes in the hBN/MoSe<sub>2</sub>/WSe<sub>2</sub>/hBN heterostructure

Table IV shows the resulting total energies of complexes in the hBN/MoSe<sub>2</sub>/WSe<sub>2</sub>/hBN heterostructure. For completeness we include results in which the electrons are found in either layer; however, the results of immediate relevance to this paper are those for which the electrons are all found in the MoSe<sub>2</sub> layer. DMC results for two-particle complexes were found to agree with calculations performed using Mathematica’s finite-element method [52] (see Appendix E). Using total energies, one can assess the most energetically favorable dissociations (see Table V) and therefore calculate binding energies of various complexes.

It is clear from Table V that the approximate Keldysh interaction performs well at calculating binding energies provided the dissociation does not involve significant changes to short-range pair distributions. As an extreme case, the binding energy of an exciton, which is simply equal to its total energy and hence does not benefit from any cancellation of errors, is overestimated by 23% when the approximate Keldysh interaction is used.

TABLE IV. Total DMC energies of various charge-carrier complexes in the hBN/MoSe<sub>2</sub>/WSe<sub>2</sub>/hBN heterostructure calculated using the Keldysh approximation to the bilayer potential [Eqs. (A12) and (A15)] and the full bilayer interaction [Eqs. (1a)–(1c)]. Primes (') indicate that a charge carrier is in the MoSe<sub>2</sub> layer; otherwise the charge carrier is in the WSe<sub>2</sub> layer. Donor charges are always assumed to be in the MoSe<sub>2</sub> layer. The subscripts *c* and *v* indicate whether charge carriers are electrons (*c*) or holes (*v*).

Complex	DMC total energy (meV)		
	Approx.	Keldysh	Bilayer potential
X <sub>vc'</sub>	-103.958669(5)	-84.232(1)	
D <sub>c'</sub> <sup>0</sup>	-163.2478711(5)	-229.03306(1)	
X <sub>vc'c'</sub> <sup>-</sup>	-108.1967(4)	-88.32(3)	
D <sub>c'c'</sub> <sup>-</sup>	-176.9426(3)	-249.60(2)	
D <sub>c'c'</sub> <sup>0</sup> h <sub>v</sub>	-163.4819(8)	-	
D <sub>c'c'</sub> <sup>0</sup> X <sub>vc'</sub>	-278.73(2)	-335.781(4)	
D <sub>c'c'</sub> <sup>-</sup> X <sub>vc'</sub>	-292.83(1)	-	
X <sub>vc</sub>	-114.601814(1)	-140.4303329(4)	
D <sub>c</sub> <sup>0</sup>	-124.890219(9)	-102.5996(7)	
X <sub>vc'c'</sub> <sup>-</sup>	-120.6018(5)	-	
X <sub>vc'c'c'</sub> <sup>-</sup>	-123.7189(5)	-152.25(1)	
D <sub>cc'</sub> <sup>-</sup>	-165.8499(5)	-	
D <sub>cc</sub>	-129.3199(9)	-	
D <sup>+</sup> X <sub>vc</sub>	-133.758(2)	-141.716(8)	
D <sub>c'c'</sub> <sup>0</sup> X <sub>vc</sub>	-279.776(5)	-	
D <sub>c'c'</sub> <sup>-</sup> X <sub>vc</sub>	-301.81(1)	-	
D <sub>c'c'</sub> <sup>0</sup> X <sub>vc'c'</sub> <sup>-</sup>	-295.00(1)	-	

TABLE V. Dissociations of complexes and the associated binding energies in hBN/MoSe<sub>2</sub>/WSe<sub>2</sub>/hBN. The naming convention for the carrier complexes is explained in the caption of Table IV.

Dissociation process	Binding energy (meV)		
	Approx.	Keldysh	Bilayer pot.
X <sub>vc'c'</sub> <sup>-</sup> → X <sub>vc'</sub> + e <sub>c'</sub>	4.2380(4)	4.09(3)	
D <sub>c'c'</sub> <sup>0</sup> X <sub>vc'</sub> → X <sub>vc'</sub> + D <sub>c'</sub> <sup>0</sup>	11.52(2)	22.516(4)	
D <sub>c'c'c'</sub> X <sub>vc'</sub> → X <sub>vc'</sub> + D <sub>c'c'</sub> <sup>0</sup>	11.93(1)	-	
D <sub>c'c'</sub> <sup>-</sup> → D <sub>c'</sub> <sup>0</sup> + e <sub>c'</sub>	13.6948(3)	20.57(1)	
D <sub>c'c'c'</sub> <sup>0</sup> h <sub>v</sub> → D <sub>c'</sub> <sup>0</sup> + h <sub>v</sub>	0.2340(8)	-	
X <sub>vc'c'</sub> <sup>-</sup> → X <sub>vc</sub> + e <sub>c'</sub>	6.0000(5)	< 0	
X <sub>vc'c'</sub> <sup>-</sup> → X <sub>v</sub> + e <sub>c'</sub>	9.1170(5)	11.83(1)	
D <sub>c'c'c'</sub> X <sub>vc</sub> → X <sub>vc</sub> + D <sub>c'</sub> <sup>0</sup>	1.926(5)	-	
D <sub>c'c'c'</sub> X <sub>vc</sub> → X <sub>vc</sub> + D <sub>c'c'</sub> <sup>0</sup>	10.26(1)	-	
D <sub>c'c'</sub> <sup>-</sup> → D <sub>c'</sub> <sup>0</sup> + e <sub>c'</sub>	2.6020(5)	-	
D <sub>c'c'c'</sub> <sup>0</sup> X <sub>vc'c'</sub> <sup>-</sup> → D <sub>c'</sub> <sup>0</sup> + X <sub>vc'c'</sub> <sup>-</sup>	8.03(1)	-	
D <sub>cc'</sub> <sup>-</sup> → D <sub>c'</sub> <sup>0</sup> + e <sub>c'</sub>	4.4297(9)	< 0	
D <sup>+</sup> X <sub>vc</sub> → D <sup>+</sup> + X <sub>vc</sub>	19.156(2)	1.286(8)	

### 3. Calculation of the overlap integrals

#### a. VMC evaluation of the normalization integral of a many-body wave function

Consider a complex of  $N$  quantum particles with unnormalized wave function  $\Phi(\mathbf{R})$ , where  $\mathbf{R} = (\mathbf{r}_1, \dots, \mathbf{r}_N)$  is the  $2N$ -dimensional vector of all particle coordinates. Let  $\Psi(\mathbf{R})$  be a normalized, bound-state sampling wave function, which ideally has a large overlap with  $\Phi$  and

the same asymptotic behavior. Then

$$\int |\Phi(\mathbf{R})|^2 d^{2N}\mathbf{R} = \int |\Psi(\mathbf{R})|^2 \left| \frac{\Phi(\mathbf{R})}{\Psi(\mathbf{R})} \right|^2 d^{2N}\mathbf{R} \\ = \left\langle \left| \frac{\Phi(\mathbf{R})}{\Psi(\mathbf{R})} \right|^2 \right\rangle_{|\Psi|^2}. \quad (\text{B1})$$

Hence we can evaluate the normalization of  $\Phi$  by VMC sampling of  $|\Psi(\mathbf{R})|^2$ . We used the simple Jastrow form

$$\Psi(\mathbf{R}) = \prod_{i=1}^N \left( \sqrt{\frac{2}{\pi}} ce^{-cr_i} \right), \quad (\text{B2})$$

for the sampling wave function, where the exponent  $c$  is a positive, adjustable parameter that was chosen to maximize the efficiency of the calculation.

#### b. Evaluation of overlap integrals

Numerical estimates of the various overlap integrals in the expressions for the radiative recombination rates of donor-bound triions in a hBN/MoSe<sub>2</sub>/WSe<sub>2</sub>/hBN system are reported in Table VI. The ground state  $\chi_{1s}(\mathbf{r}_e)$  and the first excited state  $\chi_{2s}(\mathbf{r}_e)$  of the neutral donor atom ( $D_c^0$ ) were calculated using a finite-element method (see Appendix E). Using a VMC-optimized trial wave function  $\Phi(\mathbf{r}_h, \mathbf{r}_{e_1}, \mathbf{r}_{e_2})$  for the ground state of the donor-bound negative trion ( $D_{c'}^0 X_{vc'}$ ), we employed a grid-based method to evaluate those overlap integrals in Table VI that can be reduced to one-dimensional radial integrals. The remaining integrals were evaluated by a VMC method, as described below.

Let  $\Psi$  be a sampling wave function, as defined in Appendix B 3a. The overlap of the trion wave function with the donor-atom wave function when an electron and a hole are pinned vertically above one another is

$$\iint \chi^*(\mathbf{r}_1) \Phi(\mathbf{r}_2, \mathbf{r}_2, \mathbf{r}_1) d^2\mathbf{r}_1 d^2\mathbf{r}_2 \\ = \int |\Psi(\mathbf{R})|^2 \frac{\chi^*(\mathbf{r}_2) \Phi(\mathbf{r}_1, \mathbf{r}_2, \mathbf{r}_1)}{|\Psi(\mathbf{R})|^2} d^4\mathbf{R} \\ = \left\langle \frac{\chi^*(\mathbf{r}_2) \Phi(\mathbf{r}_1, \mathbf{r}_2, \mathbf{r}_1)}{|\Psi(\mathbf{R})|^2} \right\rangle_{|\Psi|^2}. \quad (\text{B3})$$

The last expression can readily be evaluated by VMC sampling of  $|\Psi|^2$ , using accurate numerical representations of the donor-atom wave function  $\chi(\mathbf{r}_e)$  obtained in the finite-element calculations.

The overlap integrals are accurate to at least three significant figures; however there is an unknown error arising from the fact that the trial wave function  $\Phi(\mathbf{r}_h, \mathbf{r}_{e_1}, \mathbf{r}_{e_2})$  only approximates the exact ground state.

### Appendix C: Radiative recombination assisted by short-range Coulomb interactions

Consider the wave function  $\chi(\mathbf{r})$  for  $D_c^0$  complexes in the long-range (Keldysh) approximation described in Sec.

TABLE VI. Overlap integrals required for calculations of radiative recombination rates. Calculations are performed for a hBN/MoSe<sub>2</sub>/WSe<sub>2</sub>/hBN system.  $\Phi(\mathbf{r}_h, \mathbf{r}_{e1}, \mathbf{r}_{e2})$  is the ground-state wave function of the donor-bound negative trion, with both donor and electrons in the MoSe<sub>2</sub> layer and the hole in the WSe<sub>2</sub> layer ( $D_{c'}^0 X_{vc'}$ ).  $\chi_{1s}(\mathbf{r}_e)$  and  $\chi_{2s}(\mathbf{r}_e)$  are the ground-state and first-excited-state (rotationally invariant) wave functions of the neutral donor atom in the MoSe<sub>2</sub> layer ( $D_{c'}^0$ ).

Overlap	Approx.	Keldysh	Bilayer pot.
$\frac{ \Phi(\mathbf{0}, \mathbf{0}, \mathbf{0}) ^2}{\int  \Phi ^2 d^6 \mathbf{R}}$	$1.29 \times 10^{-9}$	$\text{\AA}^{-6}$	$2.75 \times 10^{-9} \text{\AA}^{-6}$
$\frac{ \int \Phi(\mathbf{r}, \mathbf{r}, 0) d^2 \mathbf{r} ^2}{\int  \Phi ^2 d^6 \mathbf{R}}$	$8.09 \times 10^{-3}$	$\text{\AA}^{-2}$	$6.08 \times 10^{-3} \text{\AA}^{-2}$
$\frac{\int  \Phi(\mathbf{r}, \mathbf{r}, \mathbf{r}) ^2 d^2 \mathbf{r}}{\int  \Phi ^2 d^6 \mathbf{R}}$	$1.28 \times 10^{-6}$	$\text{\AA}^{-4}$	$1.38 \times 10^{-6} \text{\AA}^{-4}$
$\frac{\int  \Phi(\mathbf{r}, \mathbf{r}, \mathbf{r}) ^2 d^2 \mathbf{r}}{\int  \Phi ^2 d^6 \mathbf{R}}$	$3.22 \times 10^{-7}$	$\text{\AA}^{-4}$	$2.37 \times 10^{-7} \text{\AA}^{-4}$
$\frac{ \int \chi_{1s}(\mathbf{r}) \Phi(\mathbf{0}, \mathbf{0}, \mathbf{r}) d^2 \mathbf{r} ^2}{\int  \Phi ^2 d^6 \mathbf{R} \times \int  \chi_{1s} ^2 d^2 \mathbf{r}}$	$6.94 \times 10^{-7}$	$\text{\AA}^{-4}$	$1.21 \times 10^{-6} \text{\AA}^{-4}$
$\frac{ \int \chi_{1s}(\mathbf{r}') \Phi(\mathbf{r}, \mathbf{r}, \mathbf{r}') d^2 \mathbf{r} d^2 \mathbf{r}' ^2}{\int  \Phi ^2 d^6 \mathbf{R} \times \int  \chi_{1s} ^2 d^2 \mathbf{r}}$	3.54		1.47
$\frac{ \int \chi_{1s}(\mathbf{r}') \Phi(\mathbf{r}, \mathbf{r}, \mathbf{r}') d^2 \mathbf{r}' ^2 d^2 \mathbf{r}}{\int  \Phi ^2 d^6 \mathbf{R} \times \int  \chi_{1s} ^2 d^2 \mathbf{r}}$	$5.90 \times 10^{-4}$	$\text{\AA}^{-2}$	$3.85 \times 10^{-4} \text{\AA}^{-2}$
$\frac{ \int \chi_{2s}(\mathbf{r}) \Phi(\mathbf{0}, \mathbf{0}, \mathbf{r}) d^2 \mathbf{r} ^2}{\int  \Phi ^2 d^6 \mathbf{R} \times \int  \chi_{2s} ^2 d^2 \mathbf{r}}$	$2.01 \times 10^{-8}$	$\text{\AA}^{-4}$	$1.13 \times 10^{-7} \text{\AA}^{-4}$
$\frac{ \int \chi_{2s}(\mathbf{r}') \Phi(\mathbf{r}, \mathbf{r}, \mathbf{r}') d^2 \mathbf{r} d^2 \mathbf{r}' ^2}{\int  \Phi ^2 d^6 \mathbf{R} \times \int  \chi_{2s} ^2 d^2 \mathbf{r}}$	0.0379		0.0254
$\frac{ \int \chi_{2s}(\mathbf{r}') \Phi(\mathbf{r}, \mathbf{r}, \mathbf{r}') d^2 \mathbf{r}' ^2 d^2 \mathbf{r}}{\int  \Phi ^2 d^6 \mathbf{R} \times \int  \chi_{2s} ^2 d^2 \mathbf{r}}$	$1.04 \times 10^{-5}$	$\text{\AA}^{-2}$	$1.89 \times 10^{-5} \text{\AA}^{-2}$

IV. The complex state can be written in the form of Eq. (12), with the substitution  $\tilde{\chi}_{\mathbf{k}} \rightarrow \tilde{\chi}_{\mathbf{k}}^0$ , and short-range electrostatic interactions and interlayer tunneling can be treated as perturbations to this initial state. Setting  $\tau' = \tau$  and  $\sigma' = \sigma$  in Eq. (12), radiative decay is determined by the matrix element  $\langle \tau, \mathbf{q} | \hat{H}_r | D^0; \mathbf{k}_h \rangle^{(2)}$ , where  $|\tau, \mathbf{q}\rangle = a_{\tau}^{\dagger}(\mathbf{q}) |\Omega\rangle$  is the final state in which a photon of momentum  $\mathbf{q}$  and the appropriate polarization  $\tau$  has been emitted after recombination of the bound electron with the delocalized hole. The notation  $|A\rangle^{(2)}$  indicates that the state includes corrections up to second order in perturbation theory, in this case from the interlayer tunneling ( $\hat{H}_t$ ) and short-range interaction ( $\hat{U}_{\text{intra}}^>$ ) terms.

The diagrams of Fig. 3 correspond to those corrections to the wave function that are relevant for radiative recombination in the large-twist-angle regime, where  $\mathcal{E}_{D^0}^b \ll \frac{\hbar^2 \Delta K^2}{2m_{\alpha}}$ . Following the order of the diagrams in the figure, and assuming that  $k_h, q \ll \Delta K$ , the optical matrix element for  $D_{c'}^0 h_v$  recombination is given in terms of the real-space impurity wave function by

$$\begin{aligned} \langle \tau, \mathbf{q} | \hat{H}_r | D^0; \mathbf{k}_h \rangle^{(2)} = & \left[ -\frac{\gamma t_{cc}/\hbar c}{(\mathcal{E}_{D^0}^b + \Delta_c) \left( \mathcal{E}_{D^0}^b + \frac{\hbar^2 \Delta K^2}{2m_{c'}} \right)} + \frac{\gamma' t_{vv}/\hbar c}{\left( \mathcal{E}_{D^0}^b + \Delta_v + \frac{\hbar^2 \Delta K^2}{2m_{c'}} + \frac{\hbar^2 \Delta K^2}{2m_{v'}} \right) \left( \mathcal{E}_{D^0}^b + \frac{\hbar^2 \Delta K^2}{2m_{c'}} \right)} \right. \\ & \left. - \frac{\gamma' t_{vv}/\hbar c}{\Delta_v \left( \Delta_v + \frac{\hbar^2 \Delta K^2}{2m_{v'}} \right)} + \frac{\gamma' t_{vv}/\hbar c}{\left( \mathcal{E}_{D^0}^b + \Delta_v + \frac{\hbar^2 \Delta K^2}{2m_{c'}} + \frac{\hbar^2 \Delta K^2}{2m_{v'}} \right) \left( \Delta_v + \frac{\hbar^2 \Delta K^2}{2m_{v'}} \right)} \right] \frac{6\pi e^3 \chi(0)}{\epsilon r_*^* S \Delta K^2} \sqrt{\frac{4\pi \hbar c}{L \sqrt{q_{\perp}^2 + q_{\parallel}^2}}}, \end{aligned} \quad (\text{C1})$$

We additionally assume that the CB and VB spacings remain a large scale in the problem, such that  $\frac{\hbar^2 \Delta K^2}{2m_{\alpha}} \ll \Delta_c, \Delta_v$ . In this approximation, the third and fourth terms in Eq. (C1) cancel out, corresponding to diagrams Fig. 3(c) and (d). Substituting the resulting expression into Eq. (11) gives Eq. (18), where the probability that the hole state is occupied is introduced through the hole density  $N(\mathbf{k}_h)$ . This analysis can be carried out for  $D_{c'}^0 X_{vc'}$  complexes, yielding Eqs. (19) and (20).

The large momentum components introduced by the short-range interaction terms are irrelevant in the small-twist-angle regime, which is dominated by the small momentum sector of the wave function. In this case, the optical matrix element is obtained from the perturbed state  $|D^0; \mathbf{k}_h\rangle^{(1)}$ , including first-order tunneling correc-

tions [Eq. (10)]. The optical matrix element is

$$\begin{aligned} \langle \tau, \mathbf{q} | \hat{H}_r | D^0; \mathbf{k}_h \rangle = & \frac{1}{\sqrt{S}} \int d^2 r e^{i(\Delta \mathbf{K} + \mathbf{k}_h + \mathbf{q}) \cdot \mathbf{r}} \chi(\mathbf{r}) \\ & \times \sqrt{\frac{4\pi \hbar c e^2}{SLq}} \left[ \frac{3t_{vv}\gamma'}{\hbar c \Delta_v} - \frac{3t_{cc}\gamma}{\hbar c (\Delta_c + \mathcal{E}_{D^0}^b)} \right]. \end{aligned} \quad (\text{C2})$$

Substituting into Eq. (11) leads to Eq. (13), and similar procedures are used to obtain Eq. (15) for  $D_{c'}^0 X_{vc'}$  complexes. Notice that the second radiative channel for  $D_{c'}^0 X_{vc'}$  discussed in the main text does not apply to this regime. The small-twist-angle analogue to the recoil process due to electron-electron interactions involves a small momentum transfer, and is thus already contained in the unperturbed state  $|D^0 X\rangle$ .

## Appendix D: Phonon effects on radiative recombination

The discussion of Appendix C can easily be adapted to e-ph interactions,  $\hat{H}_{\text{e-ph}}$  [Eq. (21)]. In the following we adopt the assumptions introduced in Appendix C; namely,  $\frac{\hbar^2 \Delta K^2}{2m_\alpha}$ ,  $\mathcal{E}_{D^0}^b \ll \Delta_c, \Delta_v$ . In addition, we use  $\hbar\omega_{\Lambda,\nu}(\xi) \ll \Delta_c, \Delta_v$ , which is always valid in our cases of interest.

In the large-twist-angle regime, consider the process whereby the electron in a  $D_{c'}^0$  bridges the valley mismatch by emitting a phonon in mode  $\nu$  and momentum  $\xi$ , with  $\xi \sim \Delta\mathbf{K}$ , in either the electron ( $\Lambda = \text{e}$ ) or hole ( $\Lambda = \text{h}$ ) layer. The electron recombines with a delocalized hole of momentum  $\mathbf{k}_h$ , emitting a photon of momentum  $\mathbf{q}$  and polarization  $\mu$ , leading to the final state

$$_h\langle \tau, \mathbf{q}; \nu, \xi | \hat{H}_r | D^0; \mathbf{k}_h \rangle = a_\tau^\dagger(\mathbf{q}) b_{\Lambda, \nu, -\xi}^\dagger | \Omega \rangle. \quad (\text{D1})$$

Considering the phonon energies presented in Table V, in this regime we have  $\frac{\hbar^2 \Delta K^2}{2m_\alpha} \gg \hbar\omega_{\Lambda,\nu}$ , and the radiative matrix elements with phonon emission can be approximated by

$$\begin{aligned} _h\langle \tau, \mathbf{q}; \nu, \xi | \hat{H}_r | D^0; \mathbf{k}_h \rangle &\approx \frac{\tilde{\chi}(\mathbf{k}_h + \xi - \Delta\mathbf{K})}{S} g_{v,\nu}(\Delta K) \\ &\times \sqrt{\frac{4\pi\hbar c}{SLq}} \frac{\gamma't_{vv}}{\hbar c \Delta_v} \left[ \frac{6m_v}{\hbar^2 \Delta K^2} - \frac{6m_{c'}}{\hbar^2 \Delta K^2} \right], \end{aligned} \quad (\text{D2a})$$

$$\begin{aligned} _e\langle \tau, \mathbf{q}; \nu, \xi | \hat{H}_r | D^0; \mathbf{k}_h \rangle &\approx \frac{\tilde{\chi}(\mathbf{k}_h + \xi - \Delta\mathbf{K})}{S} g_{c',\nu}(\Delta K) \\ &\times \sqrt{\frac{4\pi\hbar c}{SLq}} \frac{\gamma t_{cc}}{\hbar c \Delta_c} \left[ \frac{6m_{c'}}{\hbar^2 \Delta K^2} - \frac{6m_v}{\hbar^2 \Delta K^2} \right]. \end{aligned} \quad (\text{D2b})$$

The distinct final states lead to two independent (noninterfering) contributions to the radiative decay rate, obtained by substituting Eqs. (D2a) and (D2b) into Eq. (11). The result is Eq. (24a), and a similar procedure leads to Eq. (24b) for the phonon-assisted decay of  $D_{c'}^0 X_{vc'}$  complexes.

The situation is more subtle in the small-twist-angle regime, where  $\hbar\omega_{\Lambda,\nu} \lesssim \hbar^2 \Delta K^2 / (2m_\alpha)$ , and the phonon dispersion becomes important. The optical matrix elements are

$$\begin{aligned} _h\langle \tau, \mathbf{q}; \xi, \nu | \hat{H}_r | D^0; \mathbf{k}_h \rangle &\approx \frac{\tilde{\chi}(\mathbf{k} + \xi - \Delta\mathbf{K})}{S} g_{v,\nu}(\xi) \\ &\times \sqrt{\frac{4\pi\hbar c}{SLq}} \left[ \frac{3\gamma't_{vv}}{\hbar c \Delta_v \left( \frac{\hbar^2 \xi^2}{2m_v} + \hbar\omega_\nu(\xi) \right)} \right. \\ &\left. - \frac{3\gamma t_{cc}}{\hbar c \Delta_c \left( \frac{\hbar^2 \xi^2}{2m_v} + \hbar\omega_\nu(\xi) + \mathcal{E}_{D^0}^b \right)} \right], \end{aligned} \quad (\text{D3})$$

$$\begin{aligned} _e\langle \tau, \mathbf{q}; \xi, \nu | \hat{H}_r | D^0; \mathbf{k}_h \rangle &= \sqrt{\frac{4\pi\hbar c}{SLq}} \frac{\tilde{\chi}(\mathbf{k} + \xi - \Delta\mathbf{K})}{S} \\ &\times \left[ \frac{3\gamma t_{cc} g_{\nu,c'}(\xi)}{\hbar c \Delta_c (\hbar\omega_\nu(\xi) + \mathcal{E}_{D^0}^b)} - \frac{3\gamma't_{vv} g_{\nu,c'}(\xi)}{\hbar c \Delta_v (\hbar\omega_\nu(\xi) + \mathcal{E}_{D^0}^b)} \right]. \end{aligned} \quad (\text{D4})$$

Following Ref. [31], we use  $t_{cc} \ll t_{vv}$  to simplify these expressions. Using Fermi's golden rule and integrating over the photon momentum we obtain the decay rates

$$\begin{aligned} \Gamma_{D^0 h}^{<, \nu} &\approx \sum_{\xi} \left[ \frac{|g_{v,\nu}(0)|^2}{\left( \frac{\hbar^2 \xi^2}{2m_v} + \hbar\omega_\nu \right)^2} + \frac{|g_{c',\nu}(0)|^2}{(\hbar\omega_\nu + \mathcal{E}_{D^0}^b)^2} \right] \\ &\times \int d^2 r \int d^2 r' e^{i(\xi - \Delta\mathbf{K}) \cdot (r' - r)} \chi(\mathbf{r}) \chi^*(\mathbf{r}') \\ &\times \frac{e^2}{\hbar c} \frac{12 \tilde{E}_g n_h}{\hbar S} \left[ \frac{\gamma't_{vv}}{\hbar c \Delta_v} \right]^2; \quad \nu = \text{LO, HP}, \end{aligned} \quad (\text{D5a})$$

$$\begin{aligned} \Gamma_{D^0 h}^{<, \text{LA}} &\approx \sum_{\xi} \left[ \frac{|g_{v,\text{LA}}(\xi)|^2}{\left( \frac{\hbar^2 \xi^2}{2m_v} + \hbar c_{\text{LA}} \xi \right)^2} + \frac{|g_{c',\text{LA}}(\xi)|^2}{\mathcal{E}_{D^0}^b{}^2} \right] \\ &\times \int d^2 r \int d^2 r' e^{i\xi \cdot (r' - r)} \chi(\mathbf{r}) \chi^*(\mathbf{r}') \\ &\times \frac{e^2}{\hbar c} \frac{12 \tilde{E}_g n_h}{\hbar S} \left[ \frac{\gamma't_{vv}}{\hbar c \Delta_v} \right]^2, \end{aligned} \quad (\text{D5b})$$

for optical and acoustic phonon modes, respectively.

The divergence at  $\xi = 0$  in Eq. (D5b) makes the first term dominant in the sum over  $\xi$ , and we can neglect the second. The sum can be evaluated exactly in the continuous limit. Defining  $\mathcal{F}(x) = -x[Y_1(x) + H_{-1}(x)]$ , where  $H_n(x)$  and  $Y_n(x)$  are the  $n$ th Struve function and Bessel function of the second kind, respectively, we obtain

$$\begin{aligned} \Gamma_{D^0 h}^{<, \text{LA}} &\approx \frac{e^2}{\hbar c} \frac{3\Xi_v^2 \tilde{E}_g m_v n_h}{\hbar^3 \rho c_{\text{LA}}^2} \left[ \frac{\gamma't_{vv}}{\hbar c \Delta_v} \right]^2 \\ &\times \int d^2 r \int d^2 r' e^{i\xi \cdot (r' - r)} \chi(\mathbf{r}) \chi^*(\mathbf{r}') \mathcal{F}\left(\frac{2m_v \hbar c_{\text{LA}} |\mathbf{r}' - \mathbf{r}|}{\hbar^2}\right). \end{aligned} \quad (\text{D6})$$

From the values reported in Table V we find that the function  $\mathcal{F}$  in the integrand decays over a characteristic length scale of 100 nm, much greater than the spread of the localized wave function  $\chi(\mathbf{r})$ . Therefore, to a good approximation, we can substitute  $\mathcal{F}(0) = 2/\pi$  to evaluate the integral. The final results for all phonon modes considered in Eqs. (25a) and (25b), and Eqs. (26a) and (26b) are obtained by a similar procedure.

## Appendix E: Finite-element calculation of two body states in heterobilayer system

The Schrödinger equation for two particles interacting through a radially symmetric potential  $\mathcal{U}(r)$  is given by

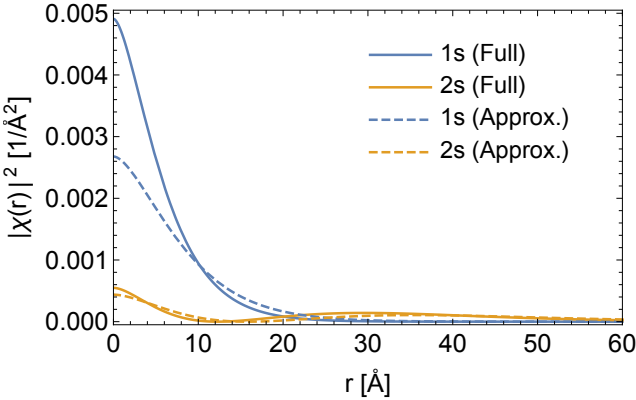


FIG. 10. Probability distributions ( $|\chi(r)|^2$ ) of the first two radially symmetric donor atom states in hBN/MoSe<sub>2</sub>/WSe<sub>2</sub>/hBN. The solid lines were obtained using the full bilayer potential Eq. (1a), and correspond to states with binding energies  $\mathcal{E}_{1s}^b = -229.03$  meV and  $\mathcal{E}_{2s}^b = -61.73$  meV. The dashed lines were obtained using the approximate intralayer Keldysh form Eq. (A12).

[6],

$$\left[ -\frac{\hbar^2}{2m_1} \nabla_e^2 - \frac{\hbar^2}{2m_2} \nabla_h^2 - e^2 \mathcal{U}(r_{12}) \right] \Psi = E\Psi, \quad (\text{E1})$$

where the form of the interaction  $\mathcal{U}$  between charge carriers is explained in Appendix A 2, depending on the layer in which each particle is found.

Transforming the coordinates to the relative motion  $\mathbf{r} = \mathbf{r}_1 - \mathbf{r}_2$  and the center-of-mass motion  $\mathbf{R} = \frac{m_1 \mathbf{r}_1 + m_2 \mathbf{r}_2}{m_1 + m_2}$  allows separation of the Schrödinger equation to the center-of-mass part whose solution is given by the plane wave  $\phi(R) = \frac{1}{\sqrt{S}} e^{i\mathbf{K}\cdot\mathbf{R}}$  and the energy  $E = \frac{\hbar^2 K^2}{2(m_1 + m_2)}$ , and the relative-motion part given by

$$\left[ -\frac{\hbar^2}{2\mu} \nabla^2 - e^2 \mathcal{U}(r) \right] \Psi = E\Psi, \quad (\text{E2})$$

where  $\mu = m_1 m_2 / (m_1 + m_2)$  is the reduced mass.

Transforming the equation into dimensionless quantities [6, 23] using the excitonic Bohr radius  $a_0^* = \frac{e\hbar^2}{\mu e^2}$  and the excitonic Rydberg energy  $R_y^* = \frac{\mu e^4}{2\epsilon^2 \hbar^2}$  gives

$$\left[ -\tilde{\nabla}^2 - \frac{1}{R_y^*} \mathcal{U}(a_0^* \tilde{r}) \right] \Psi = \tilde{E} \Psi. \quad (\text{E3})$$

where  $\tilde{r} = r/a_0^*$  and  $\tilde{E} = E/R_y^*$ . Using separation of variables the general solution is given by

$$\Psi(\mathbf{r}) = R(r)\Phi(\phi), \quad (\text{E4})$$

where the angular part solution is

$$\Phi(\phi) = \frac{1}{\sqrt{2\pi}} e^{il\phi}. \quad (\text{E5})$$

$l = 0, \pm 1, \pm 2, \dots$  is the azimuthal quantum number with  $\Phi(\phi)$  being an eigenfunction of the angular momentum operator  $L_z = -i\hbar \frac{\partial}{\partial \phi}$  with eigenvalue  $\hbar l$ . The equation for the radial part is

$$-R''(\tilde{r}) - \frac{1}{\tilde{r}} R'(\tilde{r}) + \frac{l^2}{\tilde{r}^2} R(\tilde{r}) - \tilde{v}(\tilde{r}) R(\tilde{r}) = \tilde{E} R(\tilde{r}), \quad (\text{E6})$$

where  $\tilde{v}(\tilde{r}) = \mathcal{U}(a_0^* \tilde{r})/R_y^*$ . To solve Eq. (E6) numerically we use the substitution  $u(\tilde{r}) = R(\tilde{r})\tilde{r}$ , allowing us to impose Dirichlet boundary conditions:  $u(\tilde{r}) = 0$  at  $\tilde{r} = 0$  and  $\tilde{r} = \infty$ . The equation can be solved using the finite-element method implemented in Mathematica [52]. For the charged donor interacting with an electron in the MoSe<sub>2</sub> layer, we have  $\mu = m'_c$ , and we solve Eq. (E6) using both the approximate Keldysh interaction and the full bilayer potential for the intralayer interaction between the donor and electron. The normalized probability distributions for the first two radially symmetric states (1s, 2s) obtained using both potentials are plotted in Fig. 10.

# Chapter 6

## Multilayer films of TMDCs

### 6.1 Introduction

Quantum wells formed from growing heterostructures of conventional III-V semiconductors have been extensively studied and applied for various optoelectronic devices such as infrared photo detectors and infrared quantum cascade lasers, utilising the intersubband transitions [70, 71]. Two dimensional materials and TMDCs in particular, provide an alternative and superior approach in terms of versatility, fabrication and functionality, in the form of van der Waals quantum wells, where the coupled layers result in splitting of the conduction and valence bands into multiple subbands. Stacking few-layers of TMDCs results in shifting of the valence band edge from the  $K$  point to the  $\Gamma$  point, and the conduction band edge to near the  $Q$  valleys. In order to describe the subbands and the intersubband transitions in few-layer TMDCs for both p-doped and n-doped samples, we construct a hybrid  $\mathbf{k} \cdot \mathbf{p}$ -tight binding model for the conduction and valence subbands in multilayer 2H-stacked TMDCs, which we parametrise using DFT calculations of the four main TMDCs. Using the developed model we find the intersubband spacings and their dependence on the number of layers, we describe the symmetry related selection rules for intersubband transitions, we address issues of broadening for the absorption line shapes due to the subbands dispersions and due to phonon relaxation, and obtain the absorption spectrum for few-layer films.

We find that the four studied TMDCs cover densely the spectrum range  $2 \mu\text{m} < \lambda < 30 \mu\text{m}$  for the first intersubband transition in few-layer films consisting of  $N = 2 - 7$  layers, therefore allowing to extend the applicability of TMDCs from the visible range

direct band gap, to the infrared range in the few-layer subbands. Additionally, we find a dispersion broadening effect, which is the dominant broadening source at room temperature ( $\sim k_B T$ ), with the phonons providing a weaker contribution of  $\sim$  few meV, making few-layer TMDCs promising for optoelectronic device applications in the infrared and far-infrared spectral range.

## 6.2 Intersubband optics in few-layer films of TMDCs

The results presented in this chapter are to be submitted in: “Hybrid  $k \cdot p$ -tight binding model for subbands and infrared intersubband optics in few-layer films of transition metal dichalcogenides:  $\text{MoS}_2$ ,  $\text{MoSe}_2$ ,  $\text{WS}_2$ , and  $\text{WSe}_2$ ”, (2018), submitted.

My contribution to this work: Performed the parametrization and fitting of the model to the DFT calculations, prepared all the figures, analysed the results and written the manuscript.

Full author list: M. Danovich, D. Ruiz-Tijerina, C. Yelgel, V. Zólyomi, V. I. Fal’ko

Author contributions: C.Y. and V. Z. provided the DFT band structure calculations. D.T. contributed to the writing of the manuscript, written appendix B and C, and to overall discussion of the calculations.

# Hybrid $k \cdot p$ -tight binding model for subbands and infrared intersubband optics in few-layer films of transition metal dichalcogenides: MoS<sub>2</sub>, MoSe<sub>2</sub>, WS<sub>2</sub>, and WSe<sub>2</sub>

Mark Danovich,<sup>1</sup> David A. Ruiz-Tijerina,<sup>1</sup> Celal Yelgel,<sup>1</sup> Viktor Zólyomi,<sup>1</sup> and Vladimir I. Fal'ko<sup>1</sup>

<sup>1</sup>National Graphene Institute, University of Manchester, Booth St E, Manchester M13 9PL, UK

(Dated: March 23, 2018)

We present a DFT-parametrized hybrid  $k \cdot p$ -tight binding model (HkpTB) for electronic properties of atomically thin films of transition-metal dichalcogenides, 2H-MX<sub>2</sub> (M=Mo, W; X=S, Se). We use this model to analyze intersubband transitions in p- and n-doped 2H – MX<sub>2</sub> films and predict the lineshapes of the intersubband excitations, determined by the subband-dependent two-dimensional electron and hole masses, as well as excitation lifetimes due to emission and absorption of optical phonons. We find that the intersubband spectra of atomically thin films of the 2H-MX<sub>2</sub> family with thicknesses of  $N = 2 – 7$  layers densely cover the infrared spectral range of wavelengths between 2  $\mu\text{m}$  and 30  $\mu\text{m}$ .

## I. INTRODUCTION

The 2H-MX<sub>2</sub> transition metal dichalcogenide compounds (M=Mo, W; X=S, Se) are layered materials, where chalcogens and metal atoms form covalent bonds within 2D layers with hexagonal lattice structure, and neighbouring layers couple weakly through electrical quadrupole and van der Waals interactions. This feature of chemical bonding makes atomically thin films of MX<sub>2</sub> sufficiently stable for extensive experimental studies aimed at their implementation in various optoelectronic devices<sup>1–3</sup>. In those recent studies, the closest attention has been paid to the inter-band optical properties of the monolayer transition metal dichalcogenide (TMD) crystals<sup>4–7</sup>, due to their direct band gap<sup>8</sup>, valley-spin coupling<sup>9–11</sup> and long spin and valley memory of photo-excited carriers<sup>12</sup>, spiced up by the Berry curvature effects for electrons and excitons in these two-dimensional semiconductors<sup>13</sup>. This is because in monolayer MoS<sub>2</sub>, MoSe<sub>2</sub>, WS<sub>2</sub>, and WSe<sub>2</sub> the valence and conduction band edges both appear at the Brillouin zone (BZ) corners  $K$  and  $K'$ , where the electronic Bloch states carry intrinsic angular momentum.

Thicker crystals of 2H-MX<sub>2</sub> quickly lose the direct band gap property upon increasing the film thickness to two or three layers.<sup>14–21</sup> Density functional theory of few-layer transition metal dichalcogenides predicts<sup>17,19</sup> that for holes the band edge relocates to the  $\Gamma$ -point, whereas for electrons it appears at six points situated somewhere near the  $Q$ -points at the middle of each  $\overline{\Gamma K}$  segment (see inset in Fig. 1). This has been demonstrated by studies of Shubnikov-de Haas oscillations in n-doped MoS<sub>2</sub>.<sup>22</sup> While the indirect character of few-layer TMD band structures suppresses their inter-band photo response, the multiplicity of subbands  $n|N$  ( $1 \leq n \leq N$ ) at the conduction and valence band edges of the  $N$ -layer crystal, open a new avenue for optical studies of atomically-thin TMD films.

Here, we analyse theoretically intersubband transitions in few-layer MoS<sub>2</sub>, MoSe<sub>2</sub>, WS<sub>2</sub> and WSe<sub>2</sub>, and show that the absorption/emission spectra of the primary transitions in p- and n-doped crystals (Fig. 1) densely cover

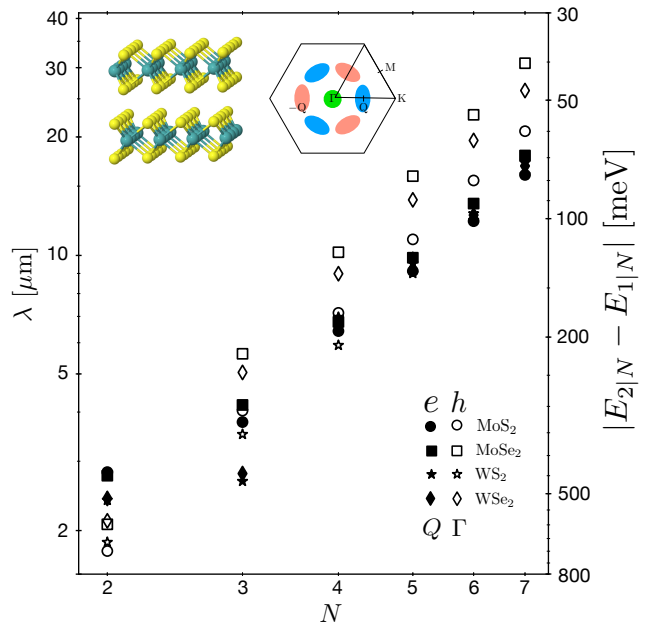


FIG. 1. Energy spacings between the first two conduction (filled symbols, solid lines) and valence (empty symbols, dashed lines) subbands  $1|N$  and  $2|N$  as a function of number of layers  $N$  of the four TMDs, corresponding to n and p-doping, respectively, for  $2 \leq N \leq 7$ . Both axes are in log scale, showing the approximate quadratic dependence of the spacings on the number of layers. The left vertical axis shows the wavelength  $\lambda$  in  $\mu\text{m}$ , corresponding to the energy spacings, and the right vertical axis shows the energy spacings in meV. The inset shows the building block of 2H-MX<sub>2</sub> bulk crystals, composed of two monolayers with metal atoms in the middle and chalcogens in the outer sublayers of each monolayer, and the Brillouin zone with the  $\Gamma$ -point and  $Q$ -valleys highlighted, corresponding to the conduction and valence band edges.

the infrared (IR) spectrum down to the far-infrared range (FIR) of photon energies. The analysis of subband properties of few-layer 2H-MX<sub>2</sub> presented in this paper is based on the hybrid  $k \cdot p$  theory-tight-binding

model (HkpTB) approach, recently applied to the description of multilayer films of post-transitional metal chalcogenides (such as InSe and GaSe).<sup>23,24</sup> This approach consists of minimal  $\mathbf{k} \cdot \mathbf{p}$  theory Hamiltonians for 2H-MX<sub>2</sub> monolayers,<sup>25,26</sup> supplemented by a  $\mathbf{k} \cdot \mathbf{p}$  expansion of the interlayer hopping near the relevant point (here,  $\Gamma$  or Q) in the BZ, with all parameters fitted to DFT-calculated few-layer dispersions, and  $k_z$  dispersions in bulk crystals.

First, in Section II we describe the lattice structure and discuss symmetries of few-layer 2D crystals of 2H-MX<sub>2</sub>, especially the difference between films with odd and even numbers of layers and the corresponding degeneracies in their band structures. The DFT-parametrised HkpTB models for few-layer TMDs are formulated in Sections III and IV for the valence band edge (holes) near the  $\Gamma$ -point and for conduction band (electrons) near the Q-points, respectively.

We use these models to calculate subband energies, dispersions and wave functions of electron/hole subbands in N-layer crystals of all four 2H-MX<sub>2</sub> compounds, and optical oscillator strengths for radiative intersubband transitions. Furthermore, we analyse the inelastic broadening due to optical phonon emission, and the resulting spectral line shapes of IR/FIR absorption by p- and n-doped 2H-MX<sub>2</sub> films. We find that the intersubband relaxation rates, determined by electron-phonon interactions, are much slower (one to two orders of magnitude) than the intra-subband relaxation in the same materials,<sup>27,28</sup> and also these are an order of magnitude slower than intersubband relaxation of electrons and holes in III-V semiconductor quantum wells.<sup>29</sup> Also, in Section III B we show that the difference between the two-dimensional masses  $m_{1|N}$  and  $m_{2|N}$  of electrons and holes in consecutive subbands leads to an additional temperature-dependent broadening of the intersubband transitions,  $\sigma \sim \left|1 - \frac{m_{1|N}}{m_{2|N}}\right| \max\{k_B T, \epsilon_F\}$ , which appears to be the dominant intrinsic broadening effect for the IR/FIR absorption by 2H-MX<sub>2</sub> films at room temperature.

## II. MULTILAYERS OF HEXAGONAL TRANSITION METAL DICHALCOGENIDES: OVERVIEW

The lattice structure of monolayer TMDs MX<sub>2</sub> (M = Mo, W; X = S, Se) contains two hexagonal sublattices of metal and chalcogen atoms in its unit cell, as shown in Fig. 2b. The chalcogens form two sublayers, one above and one below the metal sublayer, forming a trigonal prismatic structure with the metal atom connected to three chalcogens above and below. The monolayer point group symmetry is  $D_{3h}$ , consisting of  $C_3$  rotations,  $\sigma_v$  in-plane mirror reflections, and  $\sigma_h$  out-of-plane mirror reflections. The most common bulk allotrope for these transition metal dichalcogenides has 2H-stacking,<sup>30</sup> built by adding subsequent layers rotated by 180° with respect to the centre of the hexagon,

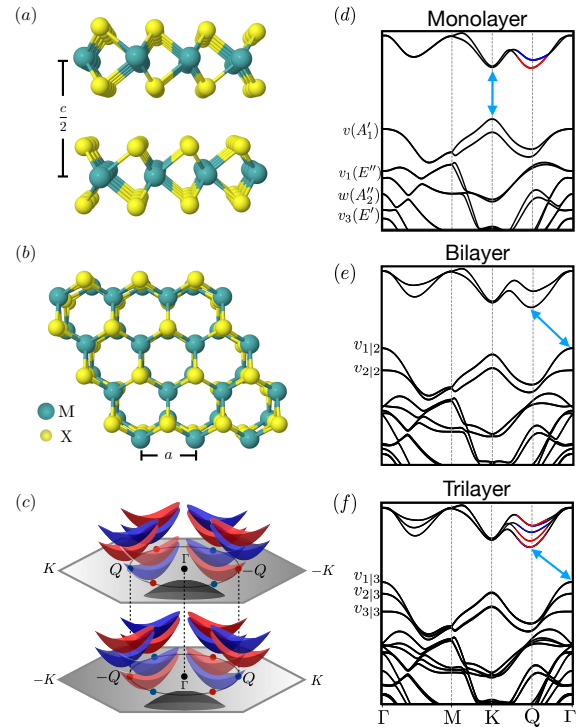


FIG. 2. (a) Crystal structure of a bilayer 2H-stacked TMD (MX<sub>2</sub>), the building block of multilayer TMDs, viewed from the side and (b) top. M and X represent the metal and chalcogen atoms, respectively. (c) Brillouin zones of the two monolayers in the 2H-stacked bilayer rotated by 180° relative to each other, and schematics of the band dispersions at the valence band  $\Gamma$ -point and conduction band Q-point, including the six symmetry-related Q-valleys and spin-orbit splitting. (d)-(f) DFT band structures of monolayer, bilayer and trilayer WS<sub>2</sub>, showing the transition from direct-gap ( $K - K$ ) monolayer, to indirect-gap ( $\Gamma - Q$ ) multilayer semiconductor. At the  $\Gamma$ -point, we label the different valence bands in the monolayer and the irreducible representations of the  $D_{3h}$  point group.<sup>25</sup> The bilayer and trilayer valence subbands are further labelled according to the subscript notation  $n|N$ , where  $n$  is the subband number and  $N$  the number of layers. For odd number of layers ( $N = 1, 3$ ), where spin-orbit splitting is present, the conduction subbands near the Q-point are coloured according to the spin projection quantum number  $s_z$ , with red (blue) corresponding to  $s = \uparrow$  ( $s = \downarrow$ ), giving a total of  $2N$  spin-polarized states. Kramer's doublets are given by  $E_s(\mathbf{k}) = E_{-s}(-\mathbf{k})$ . For  $N = 2$  all bands are spin degenerate, resulting in  $N$  doubly-degenerate states,  $E_s(\mathbf{k}) = E_{-s}(\mathbf{k})$ .

resulting in a structure where the chalcogen atoms from one layer are directly above or below metal atoms in the other layer (See Fig. 2a,b). The interlayer distance  $\frac{c}{2}$ , with  $c$  the out-of-plane lattice constant, is shown in Fig. 2a, and Fig. 2b shows the in-plane lattice constant  $a$ . The resulting 3D layered crystal has a bipartite structure with two monolayers in the unit cell, belonging to the space group P63/mmc.

Multilayer TMDs with an even number of layers be-

long to the point group  $D_{3d}$ , which contains spatial inversion ( $\mathbf{r} \rightarrow -\mathbf{r}$ ) but lacks out-of-plane mirror symmetry. The combination of spatial inversion and time reversal symmetry prescribed at zero magnetic field results in a constrain on the spin splitting of the electronic states for even number of layers,  $E_s(\mathbf{k}) = E_{-s}(\mathbf{k})$ , where  $s$  is the spin projection quantum number, such that all states throughout the BZ must be spin degenerate. Similarly to the monolayer case, multilayer films with an odd number of layers belong to the point group  $D_{3h}$ , which contains the  $z \rightarrow -z$  mirror symmetry  $\sigma_h$  but lacks spatial inversion symmetry. Therefore,  $s_z$  is a good quantum number for which spin degeneracy (present in films with even number of layers) can be lifted by spin-orbit (SO) coupling. While the SO splitting is absent for bands based on  $p_z$  and  $d_{z^2}$  orbitals at the  $\Gamma$ -point, it is substantial near the  $Q$ -points, leading to the alternation of subband properties. That is, the subbands are spin degenerate for even numbers of layers, resulting in a six-fold degeneracy of dispersion along the  $\Gamma - K$  line. For odd number of layers, subband spectra are three-fold degenerate, but with  $E_s(\mathbf{k}) = E_{-s}(-\mathbf{k})$ .

In Figs. 2(d)–(f) we show how the DFT-calculated band structure of WS<sub>2</sub>, representative of all four TMDs, evolves from monolayer to trilayer (DFT band structures of all four transition metal dichalcogenides are shown in Appendix F). The DFT calculations were performed using a plane-wave basis within the local density approximation (LDA), with the Quantum Espresso<sup>31</sup> PWSCF *ab initio* package. We considered the Perdew-Zunger exchange correlation scheme,<sup>32</sup> with fully-relativistic norm-conserving pseudo-potentials, including non-collinear corrections. Pseudopotentials for Mo, W, S, and Se atoms were generated using atomic code ld1.x of the PWSCF package.<sup>33</sup> The cutoff energy in the plane-wave expansion was set to 60 Ry, and the BZ sampling of electronic states was approximated using a Monkhorst-Pack uniform  $\mathbf{k}$ -grid of  $24 \times 24 \times 1$  for all structures.<sup>34</sup> We adopted a Methfessel-Paxton smearing<sup>35</sup> of 0.005 Ry and set the total energy convergence to less than  $10^{-6}$  eV in all calculations. Spin-orbit coupling was included in all electronic band structure calculations. To eliminate spurious interactions between adjacent supercells, a 20 Å vacuum buffer space was inserted in the out-of-plane direction. The interlayer separations in the four TMDs were taken to be the experimental values, 6.149 Å,<sup>36</sup> 6.463 Å,<sup>37</sup> 6.173 Å,<sup>38</sup> and 6.477 Å,<sup>39</sup> with LDA-optimised in-plane lattice constants of 3.157 Å, 3.288 Å, 3.161 Å, and 3.291 Å for MoS<sub>2</sub>, MoSe<sub>2</sub>, WS<sub>2</sub>, and WSe<sub>2</sub>, respectively.

Using WS<sub>2</sub> as an example, Fig. 2 illustrates that a monolayer MX<sub>2</sub> has a direct band gap at the K point of the BZ. The  $z \rightarrow -z$  mirror symmetry and lack of inversion symmetry result in SO-split conduction and valence bands, classified by their  $s_z$  quantum number (Fig. 2d). The large SO splitting at the valence band (VB)  $K$ -point and conduction band (CB)  $Q$ -point result from their metal  $d_{xy}$  and  $d_{x^2-y^2}$  orbital compositions. This is

in contrast to the CB  $K$ -point, which is primarily made of metal  $d_{z^2}$  orbitals, resulting in weaker SO splitting.<sup>5,26</sup> In a 2H-MX<sub>2</sub> bilayer, the combination of spatial inversion and time reversal symmetry forbids SO splitting, resulting in two spin-degenerate subbands (four bands in total) in the CB and VB, split by the interlayer coupling (Fig. 2e). Additionally, the interlayer coupling shifts the band edges to the  $\Gamma$ -point (VB) and in the vicinity of the  $Q$ -point (CB), making indirect gap semiconductors.

In the trilayer 2H-MX<sub>2</sub>, the valence and conduction band edges remain at the  $\Gamma$  and near  $Q$  points. As shown in Fig. 2f, the CB subbands are split by SO coupling at the  $Q$ -point due to the lack of spatial inversion symmetry in the case of odd numbers of layers. The resulting spectrum consists of two SO-split subbands in the middle, and two pairs of nearly spin-degenerate subbands above and below (see Appendix C for details). For the valence subbands, however, SO splitting is forbidden exactly at the  $\Gamma$ -point, due to it being its own time reversal counterpart, resulting in three nearly spin degenerate subbands (exact degeneracy for even  $N$ , and spin-splitting  $E_{s_z}(\mathbf{k}) - E_{-s_z}(\mathbf{k}) \propto k^3$  for odd  $N$ ). This trend, which consists of the alternation of SO-split (for odd  $N$ ) and spin-degenerate (for even  $N$ ) subbands persists for TMD films with a larger number of layers, and all the same features are present in the spectra of all four 2H-MX<sub>2</sub> shown in Appendix F. Finally, we note that the in-plane (2D) carrier dispersions in different subbands  $n|N$  (both on the VB and CB side) are different, which affects the intersubband absorption line shapes, as we discuss in Sections III and IV.

### III. HOLE SUBBANDS IN P-DOPED FEW-LAYER TMDS

Fig. 2d shows the monolayer valence bands relevant for the multilayer description, based on symmetry and energy considerations. The  $v$  and  $w$  valence bands are non-degenerate at the  $\Gamma$ -point, with the  $v$ -band composed of the metal  $d_{z^2}$  orbital and chalcogen  $p_z$  orbitals, whereas the  $w$ -band is composed of metal and chalcogen  $p_z$  orbitals. Bands  $v_1$  and  $v_3$  belong to two-dimensional irreducible representations (Irreps), with the  $v_1$  band composed of chalcogen  $p_x, p_y$  and metal  $d_{xz}, d_{yz}$  orbitals, and the  $v_3$ -band formed by chalcogen  $p_x, p_y$  and metal  $d_{xy}, d_{x^2-y^2}$  orbitals.<sup>5,25,26</sup> In the multilayer case, the  $w$  and  $v$ -bands strongly repel as the  $w$  band gets closer in energy to the  $v$ -band. The  $v_1$  and  $v_3$  bands, on the other hand, are weakly split with a narrow spread due to their orbital characters, and are pushed downwards relative to the  $v$  band edge. The two-dimensional Irreps of  $v_1$  and  $v_3$  allow their coupling with the VB being only through SO interactions (see Appendix B). These features involving the symmetry, orbital composition and proximity of the valence bands, supported by our numerical calculations, indicate that the VB is most strongly hybridized with the  $w$ -band, while the other valence bands  $v_1, v_3$ , pro-

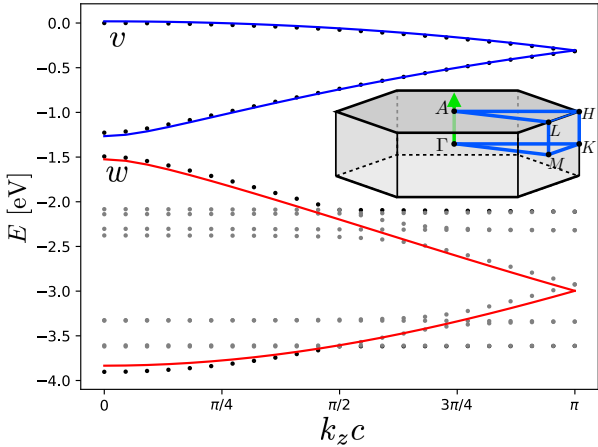


FIG. 3. Bulk dispersion of 2H–stacked WS<sub>2</sub> along the  $\overline{GA}$  line. The DFT data (points) are well fitted by the two–band model Eq. (4) (solid lines). The grey points correspond to the  $v_1$  and  $v_3$  valence bands. Inset: The first Brillouin zone of bulk TMDs.

vide corrections in second–order perturbation theory to the model parameters through the action of SO coupling (see Appendix B). Additionally, as pointed out in Section II, in two–dimensional 2H–MX<sub>2</sub> crystals the CB and VB are almost spin-degenerate at the  $\Gamma$ –point, despite the fact that atomic SO coupling in TMD compounds is strong. Therefore, to describe the valence subbands at

the  $\Gamma$  point, we construct a spinless two–band model including the  $v$  and  $w$  bands, fitting the band parameters and interlayer hopping terms to the DFT calculated band structure, where SO coupling is included implicitly. As indicated in Fig. 2d, these bands belong to the  $A'_1$  and  $A''_2$  Irreps of the  $D_{3h}$  group of the  $\Gamma$ –point,<sup>25,26</sup> respectively. Therefore, bands  $v$  and  $w$  are respectively even and odd under  $\sigma_h$  transformations, and do not mix in the monolayer case. However, in multilayers, band mixing across consecutive layers is allowed by symmetry.

### A. HkpTB for the $\Gamma$ –point valence band edge

The monolayer dispersions of the valence bands  $\sigma = v$  and  $w$ , are described by isotropic parabolic dispersions with band-dependent effective masses

$$E_\sigma(\mathbf{k}) = E_\sigma^0 - \frac{\hbar^2 k^2}{2m_\sigma}. \quad (1)$$

To construct the multilayer Hamiltonian we include symmetry-constrained interlayer couplings, given to lowest orders in  $\mathbf{k}$  by

$$t_\sigma(\mathbf{k}) = t_\sigma^{(0)} + t_\sigma^{(2)}k^2; \quad t_{vw}(\mathbf{k}) = t_{vw}^{(0)} + t_{vw}^{(2)}k^2, \quad (2)$$

where  $t_v$  and  $t_w$  are interlayer intra–band hopping terms, and  $t_{vw}$  couples different bands in two consecutive layers.

The multilayer Hamiltonian is given by

$$\begin{aligned} \hat{H}_{N\Gamma}(\mathbf{k}) = & \sum_{s=\uparrow,\downarrow} \sum_{\sigma=v,w} \sum_{n=1}^{\lceil N/2 \rceil} \left[ E_\sigma(\mathbf{k}) + 2\delta_\sigma + 2\mu_\sigma(\mathbf{k}) \right] \left[ a_{ns\sigma}^\dagger(\mathbf{k}) a_{ns\sigma}(\mathbf{k}) + \Theta\left(\frac{N}{2} - n\right) b_{ns\sigma}^\dagger(\mathbf{k}) b_{ns\sigma}(\mathbf{k}) \right] \\ & - \sum_{s=\uparrow,\downarrow} \sum_{\sigma=v,w} \left[ \delta_\sigma + \mu_\sigma(\mathbf{k}) \right] \left[ a_{1s\sigma}^\dagger(\mathbf{k}) a_{1s\sigma}(\mathbf{k}) + \left(1 - \frac{\vartheta(N)}{2}\right) b_{N/2,s,\sigma}^\dagger(\mathbf{k}) b_{N/2,s,\sigma}(\mathbf{k}) + \frac{\vartheta(N)}{2} a_{(N+1)/2,s,\sigma}^\dagger(\mathbf{k}) a_{(N+1)/2,s,\sigma}(\mathbf{k}) \right] \\ & + \sum_{s=\uparrow,\downarrow} \sum_{\sigma=v,w} \left( \sum_{n=1}^{\lceil N/2 \rceil} t_\sigma(\mathbf{k}) \Theta\left(\frac{N}{2} - n\right) \left[ a_{ns\sigma}^\dagger(\mathbf{k}) b_{ns\sigma}(\mathbf{k}) + \text{H.c.} \right] + \sum_{n=1}^{\lceil N/2 \rceil - 1} t_\sigma(\mathbf{k}) \left[ a_{n+1,s,\sigma}^\dagger(\mathbf{k}) b_{ns\sigma}(\mathbf{k}) + \text{H.c.} \right] \right) \\ & + \sum_{s=\uparrow,\downarrow} \sum_{\sigma=v,w} \sum_{n=1}^{\lceil N/2 \rceil} t_{vw}(\mathbf{k}) \Theta\left(\frac{N}{2} - n\right) \left[ a_{nsv}^\dagger(\mathbf{k}) b_{nsw}(\mathbf{k}) - a_{nsw}^\dagger(\mathbf{k}) b_{nv}(\mathbf{k}) + \text{H.c.} \right] \\ & + \sum_{s=\uparrow,\downarrow} \sum_{\sigma=v,w} \sum_{n=1}^{\lceil N/2 \rceil - 1} t_{vw}(\mathbf{k}) \left[ a_{n+1,s,w}^\dagger(\mathbf{k}) b_{nsv}(\mathbf{k}) - a_{n+1,s,v}^\dagger(\mathbf{k}) b_{nsw}(\mathbf{k}) + \text{H.c.} \right], \end{aligned} \quad (3)$$

where we have defined  $\vartheta(N) = 1 - (-1)^N$ .  $a_{ns\sigma}^{(\dagger)}(\mathbf{k})$  and  $b_{ns\sigma}^{(\dagger)}(\mathbf{k})$  annihilate(create) a band– $\sigma$  electron with spin projection  $s$  and in–plane wave vector  $\mathbf{k}$  in the odd and even layers of the  $n^{\text{th}}$  unit cell, respectively. Additional model parameters include the on–site energy

corrections  $\delta_v$  and  $\delta_w$ , and  $k$ –dependent corrections of the form  $\mu_\sigma(\mathbf{k}) = \mu_\sigma k^2$ , for the  $v$  and  $w$  bands, respectively, which take into account both the pseudo–interlayer potentials, as well as the spin–flip induced interband–interlayer hopping (Appendix B). For odd  $N$  the system has  $\lfloor N/2 \rfloor$  complete unit cells and a trun-

cated last unit cell  $n = \lceil N/2 \rceil$ , where  $\lfloor A \rfloor$  and  $\lceil A \rceil$  are the floor and ceiling functions, respectively. This case is considered in Eq. (3) through the Heaviside function  $\Theta(\frac{N}{2} - n)$ , which removes the operators  $b_{N/2,\sigma}^{(\dagger)}(\mathbf{k})$  when  $N$  is odd. The minus sign in the last row of Eq. (3) for the interband interlayer hoppings ( $t_{vw}$ ) is due to the opposite parity under  $z \rightarrow -z$  of the  $v$  and  $w$  bands, described in Sec. III.

$$H_\Gamma(\mathbf{k}, k_z) = \begin{pmatrix} E_v(\mathbf{k}) + 2\delta_v + 2\mu_v(\mathbf{k}) & 0 & 2t_v(\mathbf{k}) \cos(\frac{k_z c}{2}) & 2it_{vw}(\mathbf{k}) \sin(\frac{k_z c}{2}) \\ 0 & E_w(\mathbf{k}) + 2\delta_w + 2\mu_w(\mathbf{k}) & -2it_{vw}(\mathbf{k}) \sin(\frac{k_z c}{2}) & 2t_w(\mathbf{k}) \cos(\frac{k_z c}{2}) \\ 2t_v(\mathbf{k}) \cos(\frac{k_z c}{2}) & 2it_{vw}(\mathbf{k}) \sin(\frac{k_z c}{2}) & E_v(\mathbf{k}) + 2\delta_v + 2\mu_v(\mathbf{k}) & 0 \\ -2it_{vw}(\mathbf{k}) \sin(\frac{k_z c}{2}) & 2t_w(\mathbf{k}) \cos(\frac{k_z c}{2}) & 0 & E_w(\mathbf{k}) + 2\delta_w + 2\mu_w(\mathbf{k}) \end{pmatrix}, \quad (4)$$

obtained from the model Eq. (3). Eq. (4) is written in the basis of the  $v$  and  $w$  bands of layers one and two of the bulk 2H crystal unit cell. The fitted parameters for the four TMDs are given in Tables I and II, and detailed comparisons of the HkpTB model to DFT results for all four few-layer TMDs are shown in Fig. 4.

Noting that the bulk VB edge is located at the  $\Gamma$ -point (Fig. 3), the dispersion near the band edge can be obtained from Eq. (4) as

$$E_\Gamma(k_z, \mathbf{k}) \approx -\frac{\hbar^2 k_z^2}{2m_{v,z}} - \frac{\hbar^2 k_z^2}{2m_{v,xy}} (1 + \zeta k_z^2), \quad (5)$$

where the bulk parameters are given in terms of the HkpTB model parameters,

$$m_{v,z}^{-1} = \frac{\hbar^2}{2d^2} \left( \frac{4t_{vw}^{(0)^2}}{\Delta E} + t_v^{(0)} \right) \quad (6a)$$

is the out-of-plane bulk effective mass, with  $d = c/2$  the interlayer distance and  $\Delta E = E_v - E_w - 2t_v^{(0)} + 2t_w^{(0)} + 2\delta_v - 2\delta_w$  the bulk gap between the top most  $v$  and lowest  $w$  bands at the  $\Gamma$ -point.

$$m_{v,xy}^{-1} = \left[ 1 + \frac{4m_v}{\hbar^2} (t_v^{(2)} - \mu_v) \right] m_v^{-1}, \quad (6b)$$

is the in-plane bulk effective mass, and

$$\zeta = -\frac{\hbar^{-2} m_v d^2}{[1 + \frac{4m_v}{\hbar^2} (t_v^{(2)} - \mu_v)]} \left\{ 2t_v^{(2)} + \frac{4\hbar^2 t_{vw}^2}{\Delta E^2} \frac{m_w - m_v}{m_v m_w} + 16t_{vw} \left( \frac{t_{vw}^{(2)}}{\Delta E} + \frac{t_{vw}}{\Delta E^2} (t_v^{(2)} - t_w^{(2)} + \mu_w - \mu_v) \right) \right\}, \quad (6c)$$

is an anisotropic non-linearity factor. (The fitted values of these parameters directly to the DFT calculations are given in Table I).

We obtain the model parameters in Eq. (3) by fitting the results of numerical diagonalization of Eq. (3) to DFT calculations of the bulk and few-layer dispersions for each 2H-MX<sub>2</sub>. For example, the DFT bulk  $k_z$ -dispersion of WS<sub>2</sub> is shown in Fig. 3 for the  $\overline{\Gamma}\overline{A}$  cut through the 3D BZ. The solid lines in Fig. 3 correspond to the bands of the bipartite Bloch Hamiltonian

TABLE I. Model parameters fitted to DFT data for the monolayer valence bands  $E_v(\mathbf{k})$  and  $E_w(\mathbf{k})$ , and bulk valence band dispersion for the four TMDs. The monolayer parameters include the band edges energy difference  $E_v^0 - E_w^0$ , and the effective masses  $m_v, m_w$  given in terms of the free electron mass  $m_0$ . The 3D bulk parameters include the out-of-plane and in-plane effective masses  $m_{v,z}, m_{v,xy}$ , respectively, and the in-plane dispersion non-linearity parameter  $\zeta$ .

	$E_v^0 - E_w^0$ [eV]	$m_v$ [ $m_0$ ]	$m_w$ [ $m_0$ ]
	$m_{v,z}$ [ $m_0$ ]	$m_{v,xy}$ [ $m_0$ ]	$\zeta$ [ $\text{\AA}^2$ ]
MoS <sub>2</sub>	1.75	3.726	0.304
	1.04	0.693	-5.24
MoSe <sub>2</sub>	1.56	5.575	0.505
	1.42	0.786	-5.99
WS <sub>2</sub>	2.08	2.885	0.353
	0.840	0.615	-5.86
WSe <sub>2</sub>	1.81	3.420	0.760
	1.08	0.700	-5.45

TABLE II. Model parameters fitted to DFT data for the valence band interlayer hopping terms  $t_v(\mathbf{k})$ ,  $t_w(\mathbf{k})$  and  $t_{vw}(\mathbf{k})$ .  $\delta_v$ ,  $\delta_w$ ,  $\mu_v$ , and  $\mu_w$  are the on-site energy offsets due to the pseudo-interlayer potential and spin-flip coupling terms.

	$t_v^{(0)}$ [eV]	$t_w^{(0)}$ [eV]	$t_v^{(2)}$ [eV $\text{\AA}^2$ ]	$t_w^{(2)}$ [eV $\text{\AA}^2$ ]
	$t_{vw}^{(0)}$ [eV]	$t_{vw}^{(2)}$ [eV $\text{\AA}^2$ ]	$\delta_v$ [meV]	$\delta_w$ [meV]
	$\mu_v$ [eV $\text{\AA}^2$ ]	$\mu_w$ [eV $\text{\AA}^2$ ]		
MoS <sub>2</sub>	-0.333	0.592	1.744	2.684
	0.432	-1.206	-62.18	-41.43
			-0.351	6.770
MoSe <sub>2</sub>	-0.307	0.657	1.830	2.626
	0.453	-1.140	-29.13	-10.85
			-0.261	2.736
WS <sub>2</sub>	-0.322	0.574	1.718	3.205
	0.404	-1.226	-36.98	-48.89
			-0.614	5.834
WSe <sub>2</sub>	-0.291	0.649	1.814	-1.382
	0.4309	-0.049	-25.27	-69.93
			-0.519	0.192

Then, the subband energies and dispersions in TMD films with  $N \gg 1$  can be analysed by quantizing hole states with dispersions described by Eq. (5) in a slab of thickness  $L = Nd$ . When doing so, one has to complement Eq. (5) with the general Dirichlet-Neumann boundary condition for the standing waves of holes at both film surfaces

$$[\pm \nu d \partial_z \psi(z) + \psi(z)]_{z=\pm \frac{L}{2}} = 0, \quad (7)$$

where the  $\pm$  correspond to the top and bottom layers, respectively, and  $\nu$  is a dimensionless parameter. Assuming a solution of the form  $\psi(z) = ue^{ik_z z} + ve^{-ik_z z}$ , one finds from Eq. (7) that  $k_z$  in Eq. (5) obeys

$$Lk_z + 2 \arctan(\nu k_z d) = \pi n, \quad (8)$$

where the integer  $n$  is the subband index. For large number of layers and low-energy subbands (near the band edge),  $k_z \sim \frac{1}{L} \ll \frac{1}{d}$ , and  $\arctan(\nu k_z d) \approx \nu k_z d$ , so that we can approximate

$$k_z \approx \frac{\pi n}{d(N + 2\nu)}, \quad (9)$$

leading to the subband energies and dispersions

$$E_{n \ll N|N}(\mathbf{k}) = -\frac{\hbar^2}{2m_{v,z}} \frac{\pi^2 n^2}{d^2(N + 2\nu)^2} - \frac{\hbar^2 k^2}{2m_{v,xy}} \left[ 1 + \frac{\zeta \pi^2 n^2}{d^2(N + 2\nu)^2} \right]. \quad (10)$$

The large- $N$  asymptotics of the separation between the lowest two subbands,  $|E_{1|N} - E_{2|N}|$ , was used to determine the value of the boundary parameter  $\nu$  for holes in each TMD, resulting in  $\nu \approx 0$  for MoS<sub>2</sub> and MoSe<sub>2</sub>,  $\nu = 0.11$  for WS<sub>2</sub>, and  $\nu = 0.007$  for WSe<sub>2</sub>, using the dispersions and lowest intersubband splittings shown in Figs. 4 and 5. The good agreement between the full HkpTB model and the asymptotic analysis shown in Fig. 5 enables us to describe the main intersubband transition  $1|N \rightarrow 2|N$  in p-doped N-layer 2H-MX<sub>2</sub> as

$$|E_{1|N} - E_{2|N}| = \frac{3\pi^2 \hbar^2}{2m_{v,z} d^2(N + 2\nu)^2}. \quad (11)$$

Furthermore, the hole subband effective masses

$$m_{n|N}^{-1} = m_{v,xy}^{-1} \left[ 1 + \frac{\zeta \pi^2 n^2}{d^2(N + 2\nu)^2} \right], \quad (12)$$

obtained from Eq. (10), describe well the subband dependence of the in-plane masses, as seen in Fig. 4.

## B. Selection rules for intersubband transitions, and dispersion-induced line broadening

Next, we use the model developed above for the description of hole subbands to study intersubband optical

transitions, electron-phonon relaxation, and absorption line shapes of IR/FIR light.

The optical transition amplitude between two given subbands  $n$  and  $n'$  is determined by the out-of-plane dipole moment

$$\begin{aligned} d_z^{n,n'}(\mathbf{k}) &= e \langle n, \mathbf{k} | z | n', \mathbf{k} \rangle \\ &= e \sum_{j=1}^N \sum_{\sigma=v,w} z_j C_{n,j,\sigma}^*(\mathbf{k}) C_{n',j,\sigma}(\mathbf{k}), \end{aligned} \quad (13)$$

where  $N$  is the total number of layers,  $z_j$  denotes the  $z$  coordinate of layer  $j$ , and  $C_{n,j,\sigma}(\mathbf{k})$  are the components of the  $n^{\text{th}}$  subband eigenstate. The calculated dipole moment matrix element for the first two intersubband transitions is plotted in Fig. 6 as a function of the number of layers. The selection rules for intersubband transitions driven by out-of-plane polarized light are determined by the odd parity of  $z$  under both spatial inversion and mirror reflection ( $\sigma_h$ ). The subband states for even and odd number of layers also have a definite parity under spatial inversion and mirror reflection, respectively, due to the crystal's symmetry. Therefore, intersubband transitions between same parity subbands are forbidden, as shown in Fig. 6 for the first two intersubband transitions. All this makes the  $1|N \rightarrow 2|N$  transition the dominant feature in the IR/FIR absorption by thin TMD films.

The intersubband absorption line shape is affected by the difference between the effective masses of subbands  $1|N$  and  $2|N$ . The lighter in-plane hole mass in the initial state ( $1|N$  subband) as compared to the final state ( $2|N$  subband) spreads the absorption spectrum toward lower energies. Heavy p-doping of the TMD film or Boltzmann distribution of the holes in the case of light p-doping, sets the lower limit for the line width of the  $1|N \rightarrow 2|N$  absorption line, which we call the density of states (DoS) broadening

$$\sigma = \left( 1 - \frac{m_{1|N}}{m_{2|N}} \right) \max\{\epsilon_F, k_B T\} \log 2. \quad (14)$$

Here,  $k_B$  is the Boltzmann constant,  $T$  is the temperature, and  $m_1, m_2$  are the effective masses of the first and second subbands. This limit for the line width is illustrated in Fig. 7a for N-layer 2H-MX<sub>2</sub> at room temperature. We note here that this “density of states” broadening is similar to the inhomogeneous broadening, in the sense that it can be overcome by placing the TMD film inside an optical resonator that would select intersubband modes with particular values of in-plane momentum  $\mathbf{k}$ .

## C. Broadening due to electron-phonon intra- and intersubband relaxation

In contrast to the elastic DoS broadening, phonon-induced intra- and intersubband relaxation broaden the absorption line in a way that cannot be avoided by a clever choice of the electromagnetic environment. Below

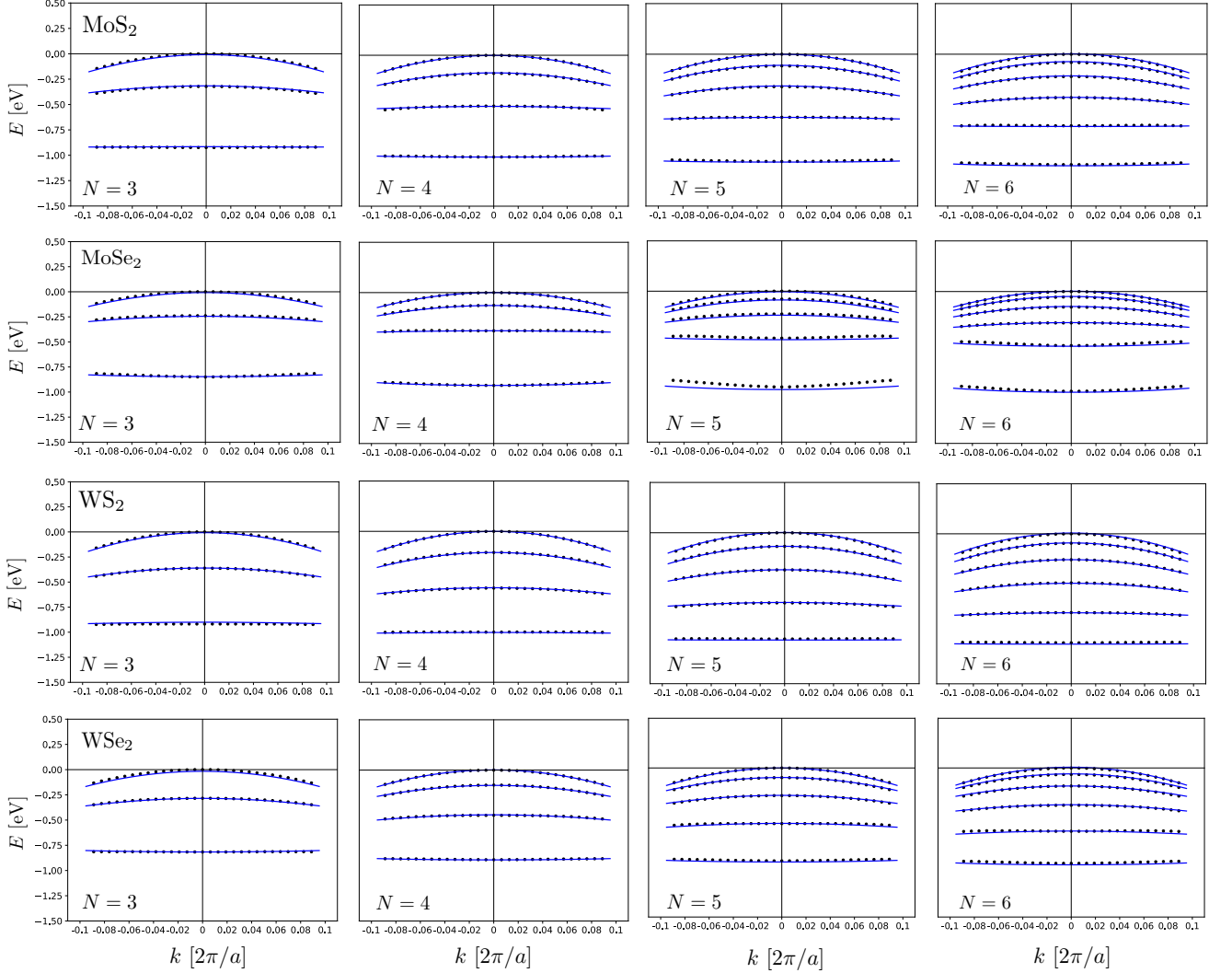


FIG. 4. Model dispersions (solid lines) near the  $\Gamma$ -point fitted to the DFT calculated (points) for the four TMDs (rows) for three to six layers (columns).

we consider emission/absorption of homopolar (HP), longitudinal (LO) and out-of-plane (ZO) optical phonons, which we assume to be dispersionless. This choice is motivated by the fact that these are the strongest coupled modes in TMDs, as established by earlier studies.<sup>27,40</sup> Also, we take phonon modes of few-layer films as independent and degenerate. This approximation is justified by the fact that splittings due to hybridization between layers are much smaller than the monolayer phonon frequency.<sup>41</sup>

The hole-phonon couplings for a phonon in mode  $\mu = \text{HP, LO, or ZO}$  in layer  $j$ , interacting with a hole in layer  $i$ , are given by (see Appendices D and E)

$$g_{\text{HP}}^{j,i}(\mathbf{q}) = \delta_{ij} \sqrt{\frac{\hbar}{2\rho\omega_{\text{HP}}}} D_v, \quad (15a)$$

$$g_{\text{LO}}^{j,i}(\mathbf{q}) = \sqrt{\frac{\hbar}{2\rho \frac{M_r}{M} \omega_{\text{LO}}}} \frac{2\pi ie^2 Z(-1)^j}{A(1+r_*q)} e^{-qd|i-j|}, \quad (15b)$$

$$g_{\text{ZO}}^{j,i}(\mathbf{q}) = \sqrt{\frac{\hbar}{2\rho \frac{M_r}{M} \omega_{\text{ZO}}}} \frac{2\pi e^2 Z_z}{A} e^{-qd|i-j|} \frac{i-j}{|i-j|}, \quad (15c)$$

where  $\omega_\mu$  denotes the corresponding phonon frequency;  $\rho$  is the mass density of the material;  $D_v$  is the deformation potential in the valence band;  $A$  is the unit cell area;  $M$  and  $M_r$  are the total unit-cell mass and reduced mass of the metal and two chalcogens, respectively;  $Z$  and  $Z_z$  are the in-plane and out-of-plane Born effective charges, respectively; and  $r_*$  is the screening length in the material.

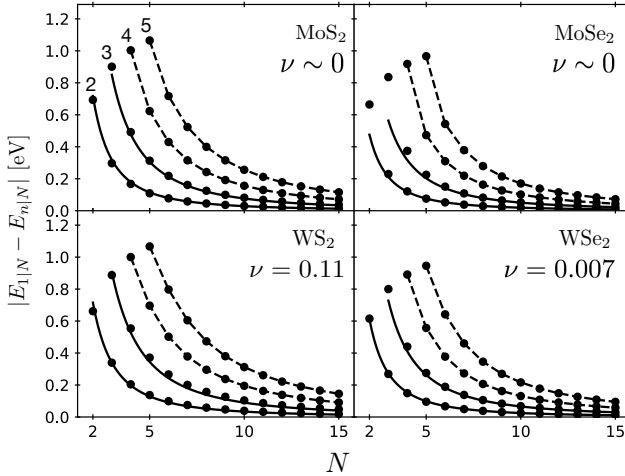


FIG. 5. Energy spacings between the first and next few valence subbands for the four TMDs, as a function of the number of layers  $N$ . The  $\nu$  parameter corresponding to each TMD is given in each panel. The solid lines for the first two transitions are obtained using Eq. (10), showing a good fit between the model and DFT.

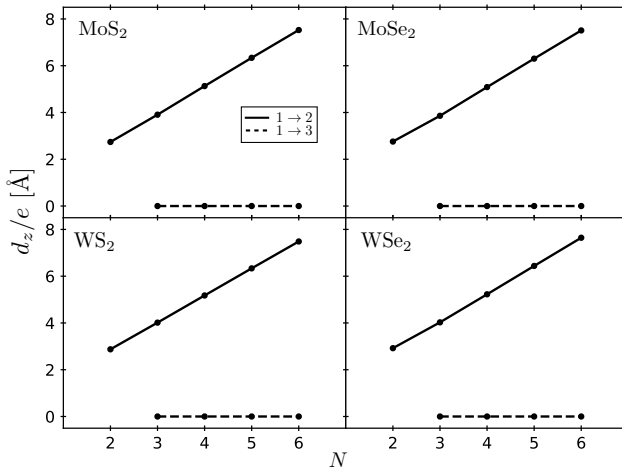


FIG. 6. Out-of-plane dipole moment matrix elements for the VB subbands, for the first two intersubband transitions  $1 \rightarrow 2$  (solid) and  $1 \rightarrow 3$  (dashed).

The various parameters taken from Refs. 27, 40, 42, and 43 are given in Table III.

The phonon induced broadening is determined by the lifetime of the hole in the excited subband state, which includes contributions from intersubband relaxation due to emission (low- $T$  and high- $T$ ) and intrasubband absorption (high- $T$ ) (Fig. 7b). We note that intrasubband emission contributions are thermally activated, since they require carriers to be thermally excited to energies higher than the corresponding phonon energy. The typical energy of thermally distributed carriers at room temper-

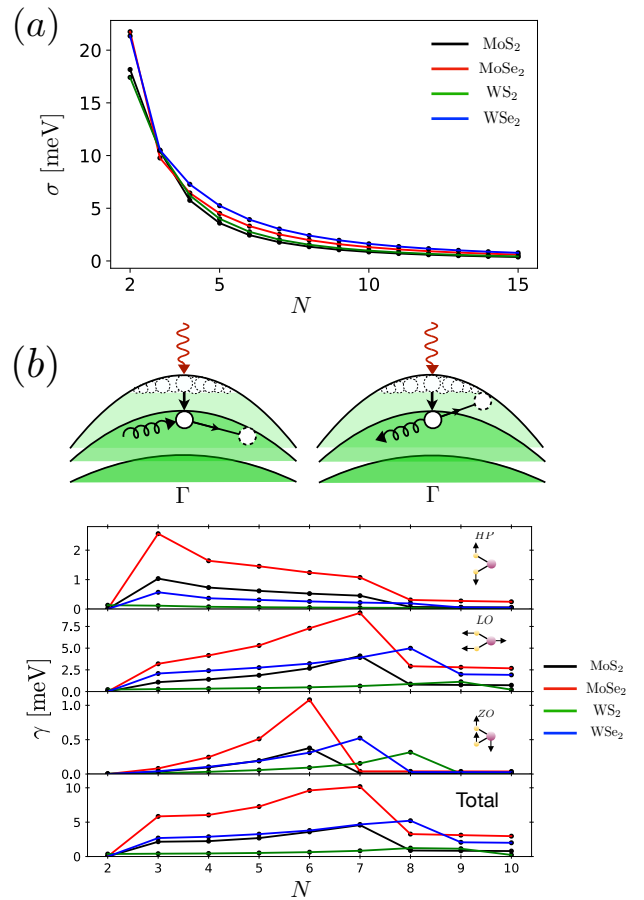


FIG. 7. (a) Absorption line widths for VB subbands at room temperature (300 K) as a function of number of layers for the four TMDs, considering only DoS broadening. (b) Phonon induced broadening at room temperature ( $T = 300$  K) due to intersubband emission and intrasubband absorption of optical phonons modes (top to bottom) HP, LO and ZO, for the four TMDs as a function of number of layers  $N$ , with the combined broadening shown in bottom panel.

ture is  $\frac{1}{2}k_B T \sim 13$  meV, whereas the phonon energies are of order 30–50 meV (Table III), making this process irrelevant. Similarly, the process involving intersubband absorption from the second subband to the third is suppressed by the larger intersubband spacings, as compared to the phonon energies and the first intersubband spacings for  $N \lesssim 10$ , and therefore will not be considered.

The phonon-induced broadening is accounted for by

$$\gamma = 2\pi \sum_{\mu, \mathbf{q}, j} \left| \sum_i \sum_{\sigma=v,w} g_{\mu}^{j,i}(\mathbf{q}) C_{n,i,\sigma}^*(\mathbf{q}) C_{m,i,\sigma}(0) \right|^2 \times \{ [1 + n_T(\hbar\omega_{\mu})] \delta [E_m(0) - E_n(\mathbf{q}) - \hbar\omega_{\mu}] + \delta_{nm} n_T(\hbar\omega_{\mu}) \delta [E_m(0) - E_n(\mathbf{q}) + \hbar\omega_{\mu}] \}, \quad (16)$$

where the sums are over the phonon modes  $\mu = \text{HP, LO, ZO}$ , the phonon wave vector  $\mathbf{q}$  and the layer

TABLE III. Electron-phonon coupling parameters for LO, HP, and ZO phonon modes.  $\omega_{\text{HP}}$ ,  $\omega_{\text{LO}}$  and  $\omega_{\text{ZO}}$  are the HP, LO and ZO mode energies;  $\rho$  is the mass density;  $D_v$ ,  $D_c$  are the valence and conduction deformation potentials;  $Z$ ,  $Z_z$  are the in-plane and out of plane Born effective charges;  $r_*$  is the screening length;  $M_r/M$  is the ratio of the reduced mass of the metal and chalcogens to the total unit cell mass; and  $A$  is the unit cell area.

	$\hbar\omega_{\text{HP}}$ [meV]	$\hbar\omega_{\text{LO}}$ [meV]	$\hbar\omega_{\text{ZO}}$ [meV]	$\rho$ [g/cm <sup>2</sup> ]	$D_v$ [eV/Å]	$D_c$ [eV/Å]	$Z$	$Z_z$	$r_*$ [Å]	$M_r/M$	$A$ [Å <sup>2</sup> ]
MoS <sub>2</sub>	51	49	59	$3.1 \times 10^{-7}$	3.5	7.1	1.08	0.1	41	0.24	8.65
MoSe <sub>2</sub>	30	37	44	$4.5 \times 10^{-7}$	3.8	7.8	1.8	0.15	52	0.249	9.37
WS <sub>2</sub>	52	44	55	$4.8 \times 10^{-7}$	1.5	3.4	0.47	0.07	38	0.29	8.65
WSe <sub>2</sub>	31	31	39	$6.1 \times 10^{-7}$	2.2	2.7	1.08	0.12	45	0.25	9.37

number  $1 \leq j \leq N$ .  $C_{n,i,\sigma}$  are the components of the  $n^{\text{th}}$  subband eigenstate on layer  $i$  in band  $\sigma$ , and  $n_T(\hbar\omega_\mu)$  is the Bose-Einstein distribution for a phonon in mode  $\mu$  at temperature  $T$ . The first term in the curly brackets describes intersubband phonon emission, whereas the second term describes intrasubband phonon absorption.

The resulting phonon-induced broadenings at room temperature are shown in Fig. 7b. The main contribution comes from intersubband relaxation, with intrasubband absorption suppressed by the phonon occupation number. The intersubband LO phonon contribution dominates the broadening due to the strong coupling attributed to the large in-plane Born effective charge, and the long range nature of the coupling. The reduced broadening for  $N = 2$  is due to the large intersubband spacing, which suppresses intersubband relaxation, and the fact that the second subband is almost flat, which suppresses intrasubband absorption. The peaks in the broadenings for certain numbers of layers correspond to near resonances between the phonon energies and the intersubband spacings. Phonon broadening is seen to be most detrimental for MoSe<sub>2</sub> in particular, and in general for all TMDs at 7 or 8 layers. Beyond this number of layers, the phonon energies become larger than the intersubband spacings, thus preventing intersubband relaxation, however, intrasubband absorption is still present and dominates for  $N > 7$ . Finally, we note that the broadening values are found to be smaller than those observed in III-V quantum wells,<sup>29</sup> implying a weaker detrimental effect on the absorption/emission line shape in these materials.

#### D. Room-temperature absorption spectrum in p-doped TMD films

The cumulative effect of inelastic (e-ph) and elastic (DoS) broadening of the intersubband  $1|N \rightarrow 2|N$  absorption spectra of lightly p-doped TMD films is described by

$$I(\hbar\omega) = \frac{4\pi}{\hbar} |E_z(\hbar\omega)|^2 \sum_{\mathbf{k}} |d_z^{1,2}(\mathbf{k})|^2 f_T(\mathbf{k}) \times \frac{\gamma/\pi}{(E_1(\mathbf{k}) - E_2(\mathbf{k}) - \hbar\omega)^2 + \gamma^2}, \quad (17)$$

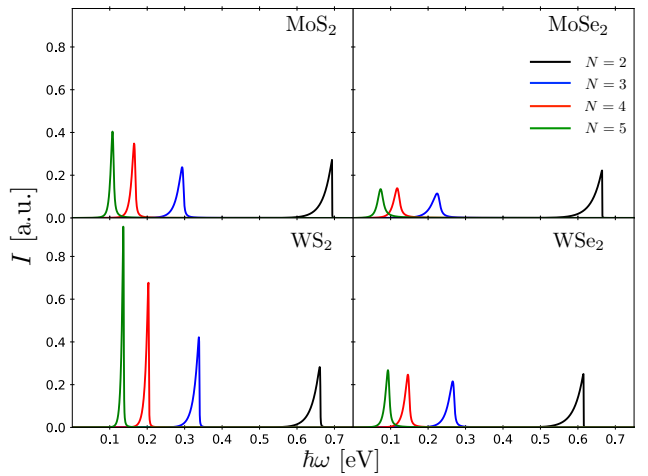


FIG. 8. Optical absorption lines for  $N = 2 - 5$  layers of lightly p-doped MoS<sub>2</sub>, MoSe<sub>2</sub>, WS<sub>2</sub>, and WSe<sub>2</sub> at room temperature ( $T = 300$  K).

where  $f_T(\mathbf{k})$  is the Fermi function for hole occupation in the lowest subband corresponding to hole density  $n_h$ , and temperature  $T$  (we assume that all higher-energy hole subbands are empty). The resulting absorption spectra at room temperature for the four TMDs with different number of layers are shown in Fig. 8. The spectra show the combination of DoS broadening, which produces a tail towards lower photon energies, with the phonon-induced broadening, most relevant for  $N > 2$ , which gives a small tail towards higher energies, making the lines more symmetric and reducing their amplitudes. The smaller phonon couplings in WS<sub>2</sub> result in tall, narrow and asymmetric line shapes, with intensity increasing with the number of layers, reflecting the growing dipole matrix element. This is in contrast to MoSe<sub>2</sub>, where the larger phonon induced broadening results in smaller and more symmetric peaks for  $N > 2$ .

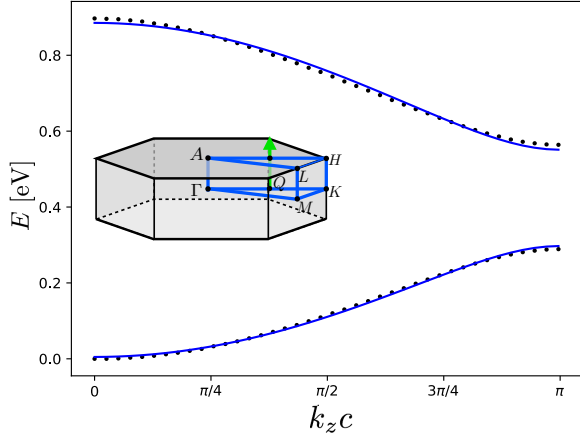


FIG. 9. Bulk dispersion of 2H-stacked WS<sub>2</sub> along the Brillouin zone path  $\overline{Q\Gamma}$ , defined by  $k_x = k_y = 0$  and  $k_z \in [0; \pi/c]$ , where  $k_x$  and  $k_y$  are measured relative to the  $Q$ -point, as shown in the inset. DFT data (points) are well fitted by the model Eq. (21) (solid line). Inset: The first Brillouin zone of bulk TMDs.

#### IV. ELECTRON SUBBANDS IN N-DOPED FEW-LAYER TMDS

##### A. HkpTB for the conduction band near the $Q$ -point

The conduction band edges in monolayer MoS<sub>2</sub>, MoSe<sub>2</sub>, WS<sub>2</sub>, and WSe<sub>2</sub> are located at the  $K$ -points,

but accompanied by local dispersion minima that appear near the six inequivalent points  $\tau\mathbf{Q}$ ,  $\tau C_3\mathbf{Q}$  and  $\tau C_3^2\mathbf{Q}$ , where  $\tau = \pm 1$ , and  $\mathbf{Q} = \frac{2\pi}{3a}\hat{x}$  is the mid-point between  $\Gamma$  and  $\mathbf{K}$  ( $a$  is the lattice constant). For a given value of  $\tau$ , there are three valleys connected by  $C_3$  rotations about the BZ centre (Fig. 2c), such that we need only describe the dispersion near the two points  $\tau\mathbf{Q}$ , which are related by time reversal.

For spin projection  $s$ , the monolayer dispersion near the  $\tau\mathbf{Q}$  valley is given by<sup>26</sup>

$$E_s^\tau(\mathbf{k}) = \frac{\hbar^2(k_x - q_s^\tau)^2}{2m_{x,s}^\tau} + \frac{\hbar^2k_y^2}{2m_{y,s}^\tau} + E_0 + \tau s \Delta_0, \quad (18)$$

where  $m_{x,s}^\tau$  and  $m_{y,s}^\tau$  are effective masses;  $E_0$  is a constant energy shift;  $2\Delta_0$  is the spin-orbit splitting between the spin-up and spin-down band edges; and  $q_s^\tau$  is the band-edge momentum relative to the valley along the  $\hat{x}$  axis. From time reversal symmetry we obtain the dispersion for the opposite valley as  $E_s^\tau(\mathbf{k}) = E_{-s}^{-\tau}(-\mathbf{k})$ , which requires ( $\alpha = x, y$ )  $m_{\alpha,s}^\tau = m_{\alpha,-s}^{-\tau}$  and  $q_s^\tau = -q_{-s}^{-\tau}$ .

As described in Sec. II, the 2H-stacked bilayer consists of subsequent layers rotated by 180° with respect to each other. In reciprocal space, this means that a conduction-band state of spin projection  $s$  and momentum  $\tau\mathbf{Q} + \mathbf{k}$  of the first layer will hybridize with its in-plane inversion partner of spin  $s$  and momentum  $-\tau\mathbf{Q} - \mathbf{k}$  in the second one (Fig. 2c). The multilayer Hamiltonian for the conduction subbands about  $\tau\mathbf{Q}$  is given by

$$\begin{aligned} H_{NQ}^\tau(\mathbf{k}) = & \sum_{n=1}^{\lceil N/2 \rceil} \sum_{s=\uparrow,\downarrow} [E_s^\tau(\mathbf{k}) + (\delta_{n,1} + \delta_{n,\lceil N/2 \rceil}) \delta E] [a_{n,\tau,s}^\dagger(\mathbf{k}) a_{n,\tau,s}(\mathbf{k}) + \Theta(\frac{N}{2} - n) b_{n,-\tau,-s}^\dagger(-\mathbf{k}) b_{n,-\tau,-s}(-\mathbf{k})] \\ & + \sum_{n=1}^{\lceil N/2 \rceil} \sum_{s=\uparrow,\downarrow} t_\tau(\mathbf{k}) \Theta(\frac{N}{2} - n) [b_{n,-\tau,s}^\dagger(-\mathbf{k}) a_{n,\tau,s}(\mathbf{k}) + \text{H.c.}] + \sum_{n=1}^{\lceil N/2 \rceil - 1} \sum_{s=\uparrow,\downarrow} t_\tau^*(\mathbf{k}) [b_{n,-\tau,s}^\dagger(-\mathbf{k}) a_{n+1,\tau,s}(\mathbf{k}) + \text{H.c.}] \\ & + \sum_{n=1}^{\lceil N/2 \rceil - 1} \sum_{s=\uparrow,\downarrow} t' [a_{n+1,\tau,s}^\dagger(\mathbf{k}) a_{n,\tau,s}(\mathbf{k}) + b_{n+1,-\tau,s}^\dagger(-\mathbf{k}) b_{n,-\tau,s}(-\mathbf{k})], \end{aligned} \quad (19)$$

where  $a_{n,\tau,s}^{(\dagger)}(\mathbf{k})$  and  $b_{n,\tau,s}^{(\dagger)}(\mathbf{k})$  annihilate(create) electrons of spin projection  $s$ , in-plane wave vector  $\mathbf{k}$  and valley quantum number  $\tau$ , on the odd and even layers of the  $n^{\text{th}}$  bulk unit cell. The alternation of spin indices and hopping terms are a result of the 2H-stacking. The model is parameterized by the terms in  $t_\tau(\mathbf{k})$  given in Eq. (20), the interlayer pseudo-potential  $\delta E$ , implemented as an on-site energy shift at the boundary layers, and the next-nearest neighbor hopping  $t'$  included to improve the fitting to DFT bands. The interlayer hopping has the form

(see Appendix A)

$$t_\tau(\mathbf{k}) = t_0 + \tau t_1 k_x + i u_1 k_y + t_2 k_x^2 + u_2 k_y^2, \quad (20)$$

up to second order in the in-plane crystal momentum. Given the lack of  $\sigma_h$  symmetry for even  $N$ , the spin projection  $s_z$  is, strictly speaking, not a good quantum number, and spin mixing is allowed. This is discussed in Appendix A. However, using an expansion about the  $Q$ -point in our DFT results shows that spin mixing is much weaker<sup>44</sup> than  $t_\tau(\mathbf{k})$ , and can be neglected. We

TABLE IV. Monolayer and bulk conduction band parameters fitted to DFT calculations of the four TMDs. The effective masses are given in terms of the free electron mass  $m_0$ . The band edge energy  $E_0$  is given relative to the valence band edge at the  $\Gamma$ -point, and  $2\Delta_0$  is the spin-orbit splitting at the  $Q$ -point. The monolayer parameters include the effective masses in the  $x$  and  $y$  directions for the spin split bands, and the band minima offsets  $q_\downarrow$  and  $q_\uparrow$ . The conduction band bulk dispersion parameters include the in-plane effective masses  $m_{c,x}, m_{c,y}$ , and out-of-plane mass  $m_{c,z}$ ; band minima offsets  $\kappa_0$  and  $\beta$ , and in-plane dispersion non-linearity parameters  $\zeta_x$  and  $\zeta_y$ .

	$m_{x,\uparrow} [m_0]$	$m_{y,\uparrow} [m_0]$	$q_\uparrow [10^{-3} \text{Å}^{-1}]$	$m_{x,\downarrow} [m_0]$	$m_{y,\downarrow} [m_0]$	$q_\downarrow [10^{-3} \text{Å}^{-1}]$	$E_0 [\text{eV}]$	$2\Delta_0 [\text{meV}]$
	$m_{c,z} [m_0]$	$m_{c,x} [m_0]$	$m_{c,y} [m_0]$	$\zeta_x [\text{Å}^2]$	$\zeta_y [\text{Å}^2]$	$\kappa_0 [\text{Å}^{-1}]$	$\beta [10^{-4} \text{Å}]$	
MoS <sub>2</sub>	0.595	1.035	20.49	0.666	1.105	7.16	1.994	67.0
	0.525	0.550	0.735	-3.90	-7.94	0.0456	-1.3	
MoSe <sub>2</sub>	0.583	1.060	54.21	0.518	1.106	26.93	1.891	21.0
	0.500	0.510	0.760	-4.65	-4.26	0.0663	0.32	
WS <sub>2</sub>	0.529	0.722	13.74	0.763	0.892	-20.65	2.059	254
	0.510	0.528	0.596	-4.30	-4.12	0.0344	0.53	
WSe <sub>2</sub>	0.468	0.753	49.63	0.676	0.908	1.88	1.94	214
	0.466	0.479	0.608	-4.19	-5.80	0.0599	-0.9	

TABLE V. Model parameters fitted to DFT data for the conduction band interlayer hopping terms.  $\delta E$  is an energy offset for the first and last layers of the structure that accounts for surface effects.

	$t_0 [\text{eV}]$	$t_1 [\text{eV}\text{\AA}^2]$	$t_2 [\text{eV}\text{\AA}^2]$
	$t' [\text{meV}]$	$u_2 [\text{eV}\text{\AA}^2]$	$\delta E [\text{meV}]$
MoS <sub>2</sub>	0.203	0.213	0.0419
	12.7	-0.662	8.90
MoSe <sub>2</sub>	0.215	0.180	-0.145
	20.5	-0.447	-4.29
WS <sub>2</sub>	0.210	0.233	-0.123
	5.24	-0.864	-3.95
WSe <sub>2</sub>	0.211	0.209	0.231
	9.54	-0.797	4.21

also found  $u_1$  to be several orders of magnitude smaller than  $t_1$ ; as a result, we consider  $t_\tau(\mathbf{k})$  to be real.

In the bulk limit we have the bipartite Hamiltonian

$$\begin{aligned}
 H_Q^\tau(\mathbf{k}, k_z) = & \varepsilon_0(\mathbf{k}, k_z) s_0 \pi_0 + \tau \Delta(\mathbf{k}) s_3 \pi_3 \\
 & + 2t_\tau(\mathbf{k}) \cos\left(\frac{k_z c}{2}\right) s_0 \pi_1, \\
 \varepsilon_0(\mathbf{k}, k_z) = & \frac{E_\uparrow^+(\mathbf{k}) + E_\downarrow^+(\mathbf{k})}{2} + 2t' \cos(k_z c), \\
 \Delta(\mathbf{k}) = & \frac{E_\uparrow^+(\mathbf{k}) - E_\downarrow^+(\mathbf{k})}{2},
 \end{aligned} \tag{21}$$

where  $\Delta(\mathbf{k})$  is the  $\mathbf{k}$ -dependent monolayer spin-orbit splitting for wave vector  $\mathbf{k}$  measured relative to the  $Q$ -point;  $s_i$  and  $\pi_i$  ( $i = 0$  to 3) are Pauli matrices acting on the spin and layer degrees of freedom, respectively, and  $s_0$  and  $\pi_0$  are the identity in their corresponding subspaces. The model parameters for the four TMDs were fitted to the DFT-calculated monolayer and 3D bulk dispersions, and are presented in Tables IV and V. A sample bulk fitting is shown in Fig. 9 for WS<sub>2</sub>, along the path defined by  $k_x = k_y = 0$  ( $Q$ -point) and  $k_z \in [0, \pi/c]$ , with the solid line corresponding to the model Eq. (21). Detailed

comparisons of the model to DFT results for few-layer structures of the four main TMDs are shown in Fig. 10.

As discussed in Sec. II, the global symmetry alternation between  $\sigma_h$  for odd  $N$ , and spatial inversion symmetry for even  $N$ , results in the striking qualitative differences between the cases with even and odd number of layers in Fig. 10. The two-fold spin degeneracy observed for even  $N$  is a consequence of spatial inversion and time reversal symmetry, resulting in  $E_s^\tau(\mathbf{k}) = E_{-s}^\tau(\mathbf{k})$ . By contrast,  $\sigma_h$  mirror symmetry for  $N$  odd makes  $s_z$  a good quantum number, while the lack of inversion symmetry allows for spin-orbit splitting. Notice also that the two middle spin-split subbands remain fixed for all odd values of  $N$ , while the rest of the bands are nearly spin-degenerate. As discussed in Appendix C, these features can be traced back to the SO splitting in the monolayer case, and the particular form of Hamiltonians  $H_{NQ}^\tau(\mathbf{k})$  for odd  $N$ .

Expanding the lowest eigenvalue of Eq. (21) for valley  $\tau$  about  $k_z = 0$ , corresponding to the bulk conduction band edge (Fig. 9), the dispersion can be written as

$$\begin{aligned}
 E_Q^\tau(\mathbf{k}, k_z) \approx & \frac{\hbar^2}{2m_{c,x}} (k_x - \tau[\kappa_0 - \beta k_z^2])^2 (1 + \zeta_x k_z^2) \\
 & + \frac{\hbar^2 k_y^2}{2m_{c,y}} (1 + \zeta_y k_z^2) + \frac{\hbar^2 k_z^2}{2m_{c,z}} + E_Q^0,
 \end{aligned} \tag{22}$$

where  $m_{c,z}$  is the out-of-plane bulk effective mass;  $m_{c,x}, m_{c,y}$  are the in-plane effective masses in the  $x$  and  $y$  directions, respectively;  $\zeta_x, \zeta_y$  are anisotropic, non-linearity factors;  $\kappa_0$  and  $\beta$  account for the band minima offset in the  $\hat{x}$  direction from the  $Q$ -point; and  $E_Q^0$  is a constant energy shift. These constants are related to our HkpTB model parameters through the expressions [see Eq. (18)]

$$m_{c,x} = \frac{2m_{x,\uparrow}^\tau m_{x,\downarrow}^\tau}{m_{x,\uparrow}^\tau + m_{x,\downarrow}^\tau}, \tag{23a}$$

$$m_{c,y} = \frac{2m_{y,\uparrow}^\tau m_{y,\downarrow}^\tau}{m_{y,\uparrow}^\tau + m_{y,\downarrow}^\tau}, \tag{23b}$$

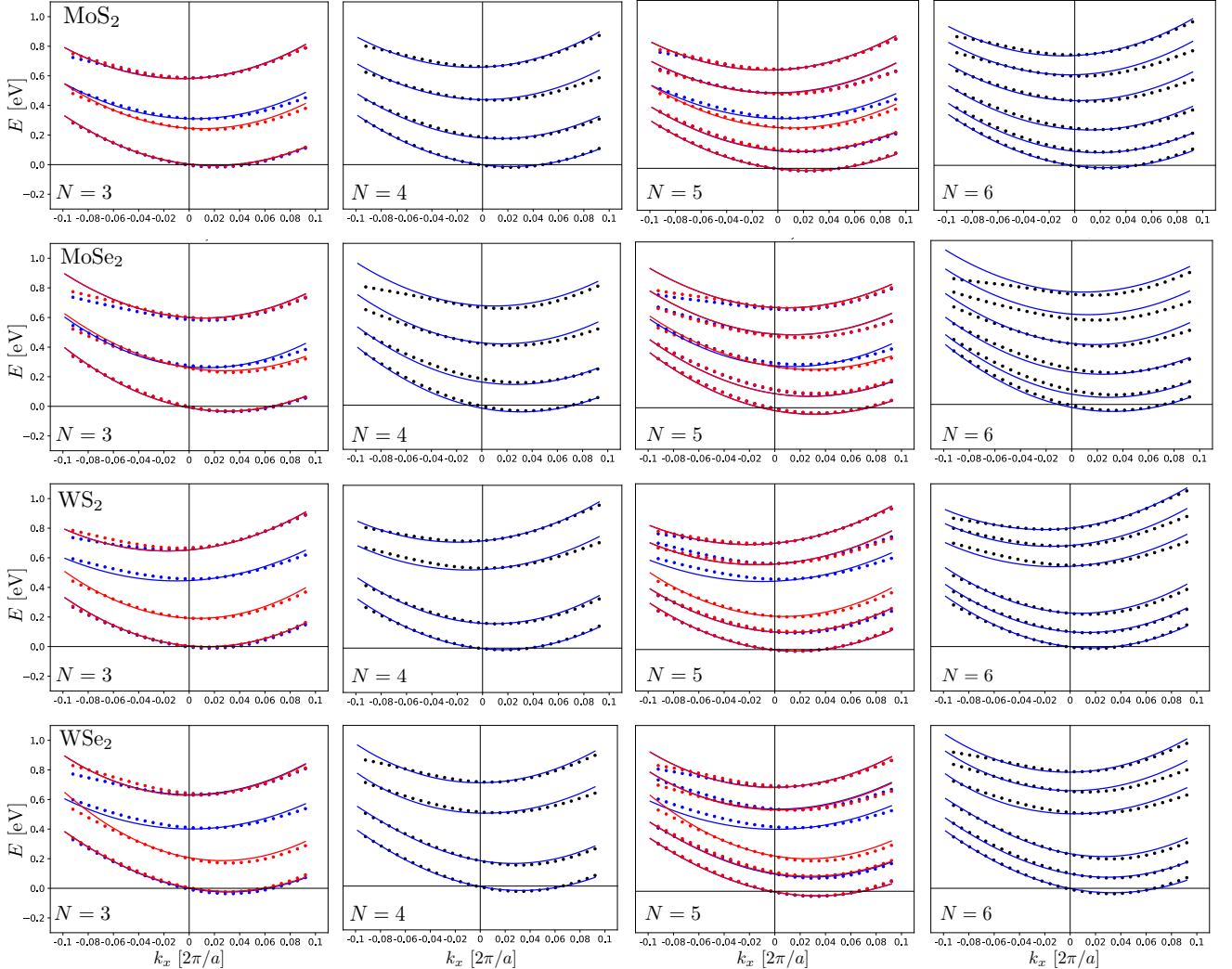


FIG. 10. Model dispersions (solid lines) near the  $Q$ -point ( $k = 0$ ) in the  $k_x$  direction fitted to the DFT calculated (points) for the four TMDs (rows) for three to six layers (columns). For odd number of layers, the colours indicate to the spin projection with blue (red) corresponding to spin down (up), whereas for even number of layers both spin projections are degenerate.

$$m_{c,z} = \frac{\hbar^2}{8d^2} \left[ \frac{t_0^2}{4\Delta_0} \left( 1 - \frac{t_1^2}{t_1^2 + 2t_0 t_1} \right) - t' + \frac{t_1^2 + 2t_0 t_2}{4\Delta_0} \left( \kappa_0 + \frac{t_0 t_1}{t_1^2 + 2t_0 t_2} \right)^2 \right]^{-1}, \quad (23c)$$

$$\kappa_0 = \frac{m_{x,\uparrow}^+ q_\downarrow^+ + m_{x,\downarrow}^+ q_\uparrow^+}{m_{x,\uparrow}^+ + m_{x,\downarrow}^+}, \quad (23d)$$

$$\beta = \frac{2m_{c,x} d^2}{\hbar^2} \frac{t_1^2 + 2t_0 t_2}{\Delta_0} \left( \kappa_0 + \frac{t_0 t_1}{t_1^2 + 2t_0 t_2} \right), \quad (23e)$$

$$\zeta_x = \frac{2m_{c,x} d^2}{\hbar^2} \frac{t_1^2 + 2t_0 t_2}{\Delta_0}, \quad (23f)$$

$$\zeta_y = \frac{4m_{c,y} d^2}{\hbar^2} \frac{t_0 u_2}{\Delta_0}, \quad (23g)$$

$$E_Q^0 = E_0 - 2\Delta_0 + \frac{\hbar^2}{4} \frac{(q_\uparrow^\tau + q_\downarrow^\tau)^2}{m_{x,\uparrow}^\tau + m_{x,\downarrow}^\tau} + 2t'. \quad (23h)$$

Similarly to the subbands on the valence-band side (Sec. III), the conduction subbands in TMD films with  $N \gg 1$  can be analysed by quantizing the electron states in a slab of finite thickness  $L = Nd$ , with dispersions described by Eq. (22). However, note that the coefficients of Eqs. (23a) through (23h) are independent of spin projection and valley, and thus not representative of the odd  $N$  case. This is a consequence of the explicit inversion symmetry of the bulk model Eq. (21). Nonetheless, the

SO splitting resulting from the lack of inversion symmetry and the presence of  $\sigma_h$  symmetry in a system with odd  $N$ , can be introduced through the TMD quantum well boundary conditions.

The unit cell for 2H crystals contains two layers, which below we label A and B [see Eq. (19)]. For odd  $N$ , inversion symmetry is broken in opposite ways for the two layers in the unit cell, given that, as discussed in Sec. I, they are rotated by  $180^\circ$  with respect to each other. This results in different boundary conditions for electrons at a given termination of the TMD film, depending on whether the final layer is of type A or B. This generalises the boundary conditions used for the valence band at  $\Gamma$ -point [Eq. (7)] to

$$[\pm(\nu_0 + s\tau\nu_1) d\partial_z \psi_s^\tau(z) + \psi_s^\tau(z)]_{z=\pm\frac{L}{2}} = 0, \quad (24a)$$

for the boundary at  $z = \pm L/2$  when the film terminates on an A layer, and

$$[\pm(\nu_0 - s\tau\nu_1) d\partial_z \psi_s^\tau(z) + \psi_s^\tau(z)]_{z=\pm\frac{L}{2}} = 0, \quad (24b)$$

when the final layer at position  $z = \pm L/2$  is of type B. Here,  $\nu_0, \nu_1 \ll N$  are dimensionless parameters. This results in spin- and valley-dependent quantization conditions

$$k_{z,n|N}^{s,\tau} \approx \frac{\pi n}{d[N + 2\nu_0 + s\tau\nu_1\vartheta(N)]}, \quad (25)$$

where  $\vartheta(N) = 1 - (-1)^N$  gives 0 for even  $N$  and 2 for odd  $N$ . Overall, the low-energy spectrum of a thin film has the form

$$\begin{aligned} E_{n \ll N|N}^{s,\tau}(\mathbf{k}) &= \frac{\hbar^2}{2m_{c,z}} \frac{\pi^2 n^2}{d^2[N + 2\nu_0 + s\tau\nu_1\vartheta(N)]^2} \\ &+ \frac{\hbar^2}{2m_{c,x;n|N}^{s,\tau}}(k_x - \kappa_{n|N}^{s,\tau})^2 + \frac{\hbar^2 k_y^2}{2m_{c,y;n|N}^{s,\tau}}, \end{aligned} \quad (26)$$

where the subband in-plane effective masses in the  $\alpha = x, y$  directions are

$$\left[m_{\alpha,n|N}^{s,\tau}\right]^{-1} \approx m_{c,\alpha}^{-1} \left[1 + \frac{\zeta_\alpha \pi^2 n^2}{d^2[N + 2\nu_0 + s\tau\nu_1\vartheta(N)]^2}\right], \quad (27a)$$

and the momentum offset from the  $Q$ -point is given by

$$\kappa_{n|N}^{s,\tau} \approx \tau\kappa_0 + \frac{\tau n^2 \pi^2 \beta}{d^2[N + 2\nu_0 + s\tau\nu_1\vartheta(N)]^2}. \quad (27b)$$

As in the monolayer case, the low-energy subband dispersions described by Eq. (26) near the six valleys at BZ points  $\tau\mathbf{Q}$ ,  $\tau C_3\mathbf{Q}$  and  $\tau C_3^2\mathbf{Q}$ , can be divided into two triads related by time reversal symmetry, with quantum numbers  $\tau = \pm 1$ . The three valleys for a given  $\tau$  are connected by  $C_3$  rotations, as sketched in the inset of Fig. 2. As a consequence, for odd number of layers, where inversion symmetry is broken and SO splitting is parameterized by  $\nu_1$ , the spin and valley degrees

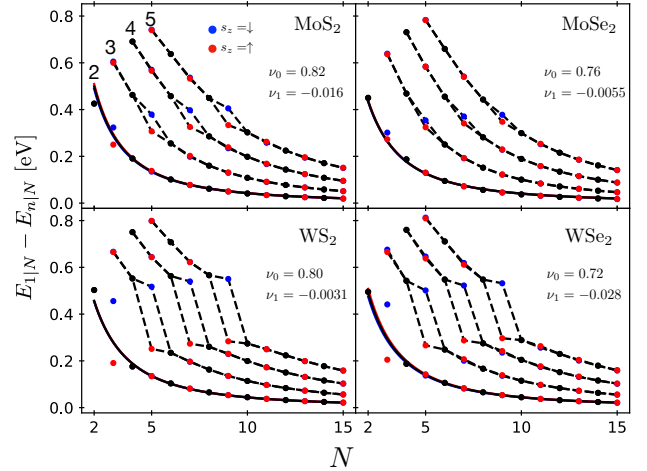


FIG. 11. Energy spacings between the first and next few conduction subbands for the four TMDs, as functions of the number of layers  $N$ . The solid lines in each panel corresponds to Eq. (28) for the main transition between the first and second subbands using the DFT bulk parameters, showing good agreement between the HkpTB model and DFT. Parameters  $\nu_0$  and  $\nu_1$ , fitted for  $N \geq 4$ , are given for the four TMDs in their corresponding panels. Blue (red) points and solid lines in each panel represent spin down (up) polarized subband spacings and fittings. Black points and solid line correspond to subband spacings for even  $N$  layers, where subbands are spin degenerate.

of freedom of the bottom subband are locked, and the low-energy states have valley degeneracy of  $g_{\text{odd}} = 6$ . Conversely, for even number of layers the bottom subbands are spin-degenerate, giving a total degeneracy of  $g_{\text{even}} = 12$ . These large subband degeneracies and multi-valley structures, together with the anisotropic dispersions found within each valley, may have important implications for the transport and quantum Hall properties of  $n$ -doped multilayer TMDs.<sup>45</sup>

## B. Intersubband transitions and dispersion-induced line broadening in $n$ -doped $N$ -layer TMDs

Numerically diagonalizing the HkpTB Hamiltonian in Eq. (19) with the parameters of Tables IV and V, we obtain the energy spacings between the first and next few subbands of TMD films shown in Fig. 11. Using Eq. (26), we estimate the separation between the lowest two subbands of a given spin projection  $s$  as

$$\begin{aligned} E_{2|N}^{s,\tau} - E_{1|N}^{s,\tau} &\approx \frac{15\pi^4 \hbar^2 \beta^2}{2m_{c,x} d^4 (N + 2\nu_0)^4} + \frac{3\pi^2 \hbar^2}{2m_{c,z} d^2 (N + 2\nu_0)^2} \\ &- \vartheta(N) s\tau\nu_1 \frac{6\pi^2 \hbar^2}{2m_{c,z} d^2 (N + 2\nu_0)^3}. \end{aligned} \quad (28)$$

Similarly, we estimate the splitting between the lowest subbands of opposite spin as

$$E_{1|N}^{-s,\tau} - E_{1|N}^{s,\tau} \approx s\tau\nu_1\vartheta(N) \frac{2\pi^2\hbar^2}{2m_{c,z}d^2(N+2\nu_0)^3}. \quad (29)$$

We used Eqs. (28) and (29) to determine the boundary parameters  $\nu_0$  and  $\nu_1$  for each of the considered TMDs (MoS<sub>2</sub>:  $\nu_0 = 0.82, \nu_1 = -0.016$ , MoSe<sub>2</sub>:  $\nu_0 = 0.76, \nu_1 = -0.0055$ , WS<sub>2</sub>:  $\nu_0 = 0.80, \nu_1 = -0.0031$ , WSe<sub>2</sub>:  $\nu_0 = 0.72, \nu_1 = -0.028$ ). The results are shown with the solid lines in Fig. 11. The spin-orbit splitting between the lowest two spin polarized subbands is of order few-meV for the four TMDs.

Next, we use the model developed above for electron subbands to study intersubband optical transitions, intersubband electron-phonon relaxation, and the intersubband absorption line shapes for IR/FIR light. As discussed in Sec. III B, the optical transition amplitude between two given subbands  $n, n'$  is determined by the out-of-plane dipole moment

$$\begin{aligned} d_{\tau,s;z}^{n,n'}(\mathbf{k}) &= e\langle n, s; \tau, \mathbf{k} | z | n', s; \tau, \mathbf{k} \rangle \\ &= e \sum_{j=1}^N z_j C_{n,j}^{\tau,s*}(\mathbf{k}) C_{n',j}^{\tau,s}(\mathbf{k}), \end{aligned} \quad (30)$$

where  $N$  is the total number of layers,  $z_j$  denotes the  $z$  coordinate of layer  $j$ , and  $C_{n,j}^{\tau,s}(\mathbf{k})$  are the components of the  $n^{\text{th}}$  subband eigenstate of spin projection  $s$  and valley quantum number  $\tau$ . The calculated dipole moment matrix element as a function of number of layers for the first two intersubband transitions is plotted in Fig. 12.

Similarly to the valence subbands case, optical transitions in films with odd number of layers  $N$  are allowed only between states with opposite-parity subband indices, corresponding to opposite parity under  $\sigma_h$  transformation. The spin-orbit splitting present for odd  $N$  results in a spin selection rule, allowing transitions only between subbands with the same out-of-plane spin projection  $s_z$ . For even  $N$ , where  $\sigma_h$  symmetry is absent, transitions between subbands with same-parity indices are allowed. This is in contrast to the VB at the  $\Gamma$ -point, and is a consequence of the multiple-valley structure of the CB, which makes it possible to form degenerate even and odd (under inversion) combinations of states, giving a finite dipole moment, as shown in Fig. 12 for the first two intersubband transitions, considering both spin-down and spin-up polarized subbands. This makes  $1|N \rightarrow 2|N$  transition the dominant feature in the IR/FIR absorption by thin n-doped TMD films.

Similarly to the holes in p-doped TMDs, the line shape of the electron intersubband absorption in n-doped films is also affected by the difference between the subband effective masses of subbands  $1|N$  and  $2|N$ . However, in contrast to the case of holes, for electrons the line shapes depend also on the relative in-plane wave vectors of the conduction subband minima, as well as the anisotropic

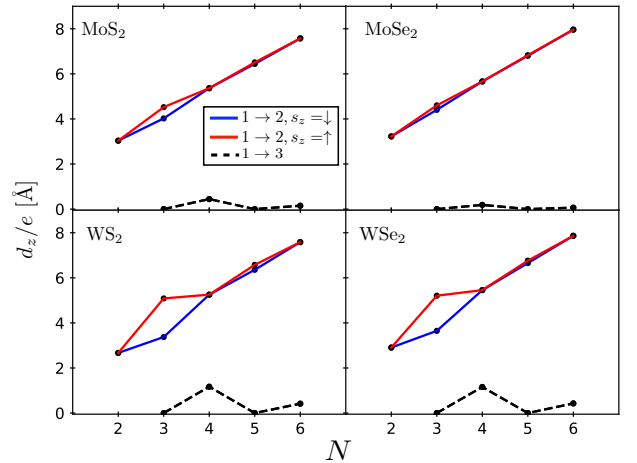


FIG. 12. Out-of-plane dipole moment matrix elements for the first two conduction intersubband transitions,  $1 \rightarrow 2$  (solid) and  $1 \rightarrow 3$  (dashed). Transitions between spin down (up) subbands are shown in blue (red).

subband dispersions. The resulting broadening for  $N$ -layer 2H-MX<sub>2</sub> films at room temperature, obtained numerically from the calculated line shapes, is shown in Fig. 13a. Our calculations show that the aforementioned DoS broadening factors result in a typically larger broadening, which spreads the absorption spectrum towards both lower and higher energies from the main transition.

### C. Electron-phonon relaxation and room-temperature absorption spectra in n-doped TMD films

The phonon-induced broadening for conduction subbands  $m$  and  $n$ , generated by intra- and intersubband relaxation, is accounted for by

$$\begin{aligned} \gamma_{n,m}^{\tau,s} &= 2\pi \sum_{\mu, \mathbf{q}, i} \left| \sum_i g_{\mu}^{j,i}(\mathbf{q}) C_{n,i}^{\tau,s*}(\kappa_m^{\tau,s} \hat{x} + \mathbf{q}) C_{m,i}^{\tau,s}(\kappa_m^{\tau,s} \hat{x}) \right|^2 \\ &\times \{ [1 + n_T(\hbar\omega_{\mu})] \delta [E_m(\kappa_m^{\tau,s} \hat{x}) - E_n(\kappa_m^{\tau,s} \hat{x} + \mathbf{q}) - \hbar\omega_{\mu}] \\ &+ \delta_{nm} n_T(\hbar\omega_{\mu}) \delta [E_m(\kappa_m^{\tau,s} \hat{x}) - E_m(\kappa_m^{\tau,s} \hat{x} + \mathbf{q}) + \hbar\omega_{\mu}] \}, \end{aligned} \quad (31)$$

where  $\kappa_m^{\tau,s}$  is the subband edge offset from the  $Q$ -point of subband  $m$  with spin projection  $s$ , and  $g_{\mu}^{j,i}$  are the electron-phonon couplings for the three phonon modes  $\mu = \text{HP, LO and ZO}$  given in Eq. (15), with  $D_v$  replaced by  $D_c$  for the HP phonon. The first term in Eq. (31) describes intersubband relaxation due to phonon emission, whereas the second describes intrasubband phonon absorption in the excited subband. The phonon induced broadening for the four TMDs obtained using the electron-phonon coupling parameters in Table III are shown in Fig. 13b. The dominant contri-

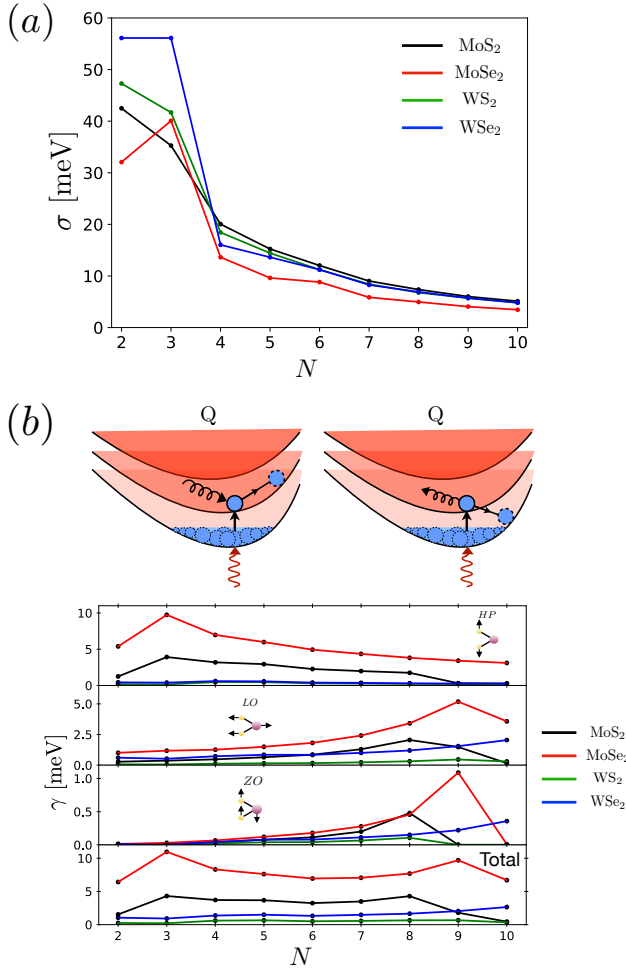


FIG. 13. (a) Absorption line widths for CB subbands at room temperature ( $T = 300$  K) as a function of number of layers for the four TMDs, considering only DoS broadening. (b) Phonon-induced broadening at room temperature ( $T = 300$  K) due to intersubband emission and intrasubband absorption of optical phonons modes (top to bottom) HP, LO and ZO, for the four TMDs as a function of number of layers  $N$ , with the total broadening shown in the bottom panel.

bution comes from intersubband relaxation due to HP and LO phonon modes, with a smaller contribution from the thermally-suppressed intrasubband absorption. The large HP phonon deformation potential at the  $Q$ -point, as compared to its value at the  $\Gamma$ -point,<sup>42</sup> in particular for MoS<sub>2</sub> and MoSe<sub>2</sub> (see Table III), results in a large contribution to the broadening. Additional differences between the phonon-induced broadenings for the conduction and valence subbands originate from the different intersubband spacings as a function of number of layers (Figs. 5, 11), and different dispersions (Figs. 4, 10). As in the valence subbands case, the phonon broadening is most significant for MoSe<sub>2</sub> due to stronger electron-phonon coupling.

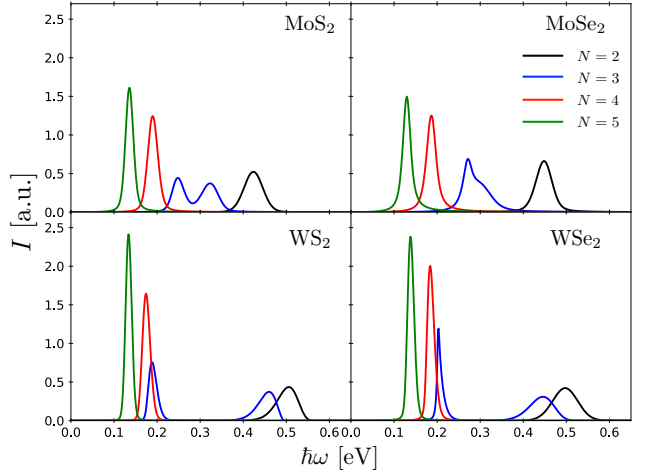


FIG. 14. Optical absorption lines for  $N = 2 - 5$  layers of lightly n-doped MoS<sub>2</sub>, MoSe<sub>2</sub>, WS<sub>2</sub>, and WSe<sub>2</sub>, taking into account intrinsic broadening at room temperature ( $T = 300$  K). In the case of odd  $N$ , lines corresponding to different subband spin projections are summed.

The absorption spectra of n-doped TMD films calculated using Fermi's golden rule, as in Eq. (17), and taking the discussions of IV A, IV B and IV C into account, are shown in Fig. 14 for  $N = 2$  to 5 layers. The predicted absorption spectra for the four TMDs are seen to be more symmetric than those for the holes, primarily due to the effect of different dispersions in consecutive subbands, here aggravated by the shifts  $\kappa_{n|N}^{\tau,s}$  and the BZ position of the subbands minima, in addition to the difference between the in-plane subband effective masses. The large SO splitting between the middle two subbands for  $N = 3$  results in two distinct lines, whereas for  $N = 5$  the spin-polarized subbands are nearly degenerate, resulting in the overlap of the two lines and giving a combined line with twice the amplitude.

## V. CONCLUSIONS

We have presented hybrid  $k \cdot p$ -tight binding models for the conduction and valence band edges of multilayer TMDs, capable of reproducing the rich low-energy subband dispersions, and allowing us to describe the inter-subband optical transitions when coupled to out-of-plane polarized light. In particular, we find that:

- The subbands at the CB edge are found near the  $Q$ -valleys of the Brillouin zone, whereas the valence band edge is found at the  $\Gamma$ -point. The main differences between the two sets of subbands is due to the significant spin-orbit splitting, multi-valley structure, and anisotropic dispersions of the conduction subbands, by contrast to the valence subbands. These differences manifest themselves in

the absorption line shapes and additional selection rules, particularly for odd number of layers, where spin-orbit splitting is present.

- The four studied TMDs were found to have main intersubband transition energies for the conduction and valence subbands, which densely cover the spectrum range of wavelengths from  $\lambda = 2 \mu\text{m}$  to  $30 \mu\text{m}$  ( $\hbar\omega = 40 \text{ meV}$  to  $700 \text{ meV}$ ), for  $N = 2$  to 7 layers. This allows tailoring structures of a specific material, appropriate type of doping, and number of layers for a particular device application, from IR to the THz range.
- Two contributions to the absorption line shape broadening are identified. The first, broadening due to intersubband phonon relaxation is found to produce a meV limit to the intersubband linewidth. This is in contrast to III-V quantum wells, where phonon broadening is found to be more damaging to the intersubband transition line quality factor.<sup>29</sup> A second, elastic contribution to the line broadening caused by the different 2D masses of carriers in consecutive subbands yields a thermal broadening of the order of  $k_B T$ . Similarly to inhomogeneous broadening, this effect can be reduced by coupling the transition in the film to a standing wave of light in a high-Q resonator.

Finally, we propose a specific design of van der Waals multilayer structure utilizing the intersubband transitions in atomically-thin films of TMDs. The sketch in Fig. 15 depicts the band configuration of a few-layer transition metal dichalcogenide film, encapsulated by hexagonal boron nitride (hBN) and placed between two graphene electrodes. Applying a bias (and possibly also gate) voltage between the two electrodes results in a shift of the Dirac points relative to each other, and allows for the alignment of the Dirac point of the “top” graphene electrode with the lower energy subband in the TMD, while keeping the Fermi level in graphene above the higher-energy subband. The carriers can then tunnel from the graphene electrode into the higher-energy subband. Once in the excited subband state, the carrier can undergo an intersubband transition, emitting light polarized in the out-of-plane direction, followed by tunneling to the second graphene electrode from the bottom subband state.

A potentially more favourable realization of the above process which avoids carrier loss directly from the second subband, or carrier tunnelling into the bottom subband, involves using ABC-stacked few-layer graphene. The band structure of ABC few-layer graphene has a Van Hove singularity in its density of states at the edge between conduction and valence bands. Aligning the Van Hove singularities of two such electrodes with the second and first subbands, respectively, would enable one to achieve preferential injection and extraction of carriers into/from the TMD film, thus offering a new way to produce functional optical fibre cables.

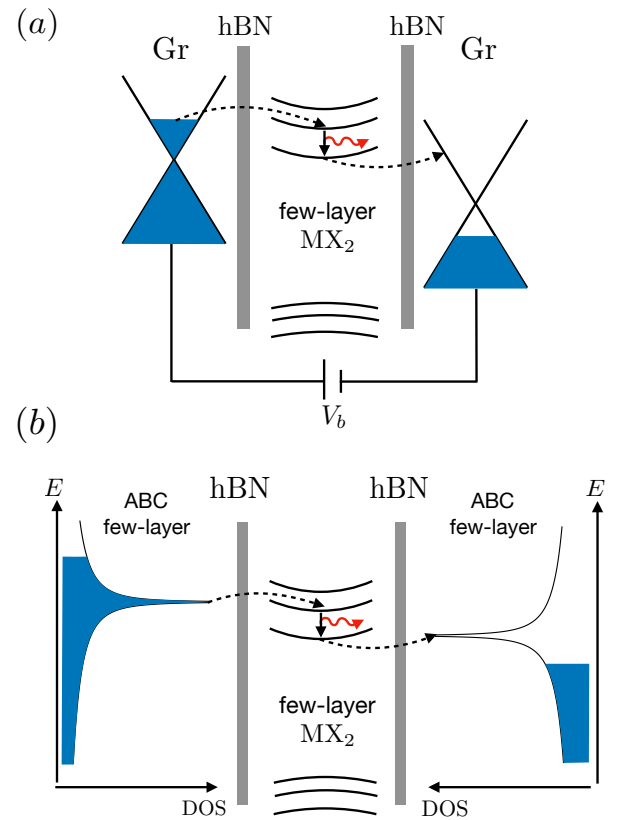


FIG. 15. proposed device application for intersubband transitions in few layer TMDs. (a) Few layer TMDs encapsulated between two hexagonal Boron Nitride (hBN) crystals and two graphene (G) electrodes with an applied bias voltage between them. The applied bias voltage allows to realize light emission through intersubband transitions in the few layer TMD system, by carriers tunnelling between the two graphene electrodes. (b) An alternative realization using few-layer ABC stacked graphene instead of monolayer, utilizing the Van Hove singularity in the density of states. The bias voltage aligns the Van Hove singularities near the second and first subbands, making the desired emission process more favourable,

The proposed “LEGO”-type design of IR/THz emitting materials has potential for implementation as part of a composite optical fibre, where the coupling to the out-of-plane polarized photon would be supported by the wave-guide mode.

## ACKNOWLEDGMENTS

The authors acknowledge funding by the European Union’s Graphene Flagship Project, ERC Synergy and EPSRC Grand Challenges grants, and the Lloyd Register Foundation. V.Z. and V.I.F. acknowledge support from the N8 Polaris service, and the use of the ARCHER supercomputer (RAP Project e547). The authors would

like to thank F. Koppens, K. Novoselov, R. Gorbachev, M. Potemski, R. Curry, C. Kocabas and S. Magorrian for fruitful discussions.

### Appendix A: Symmetry constraints for the bilayer Hamiltonians

For  $N = 2$  (bilayer), the Hamiltonian must be invariant under spatial inversion  $\mathcal{P}$ ,  $x \rightarrow -x$  mirror symmetry  $\mathcal{D}(\sigma_v)$ , and time reversal  $\mathcal{T}$ . For the conduction-band model about the  $Q$  point, this gives the conditions<sup>46</sup>

$$\mathcal{P}H_2^\tau(\mathbf{k})\mathcal{P}^{-1} = H_2^{-\tau}(-\mathbf{k}) \quad (\text{A1a})$$

$$\mathcal{D}(\sigma_v)H_2^\tau(k_x, k_y)\mathcal{D}^{-1}(\sigma_v) = H_2^{-\tau}(-k_x, k_y) \quad (\text{A1b})$$

$$\mathcal{T}H_2^\tau(\mathbf{k})\mathcal{T}^{-1} = H_2^{-\tau}(-\mathbf{k}). \quad (\text{A1c})$$

We have  $\mathcal{P} = \pi_1 s_0$ ,  $\mathcal{D}(\sigma_v) = \pi_0 s_1$  and  $\mathcal{T}_2 = -i\pi_0 s_2 \mathcal{C}$ , where  $\pi_j$  ( $s_j$ ) are Pauli matrices acting on the layer (spin) subspace, and  $\mathcal{C}$  represents complex conjugation. As a result, the most general valley-spin structure for the bilayer Hamiltonian at the  $\tau\mathbf{Q}$  valley is

$$\delta^\tau(\mathbf{k}) = \sum_{i,j=0}^3 A_{ij}^\tau(\mathbf{k})\pi_i s_j, \quad (\text{A2})$$

where the symmetry constraints (A1a)-(A1c) require that

$$A_{i0}^\tau(k_x, k_y) = A_{i0}^{-\tau}(-k_x, k_y) = A_{j0}^\tau(k_x, -k_y), \quad i = 0, 1, \quad (\text{A3a})$$

$$A_{20}^\tau(k_x, k_y) = A_{20}^{-\tau}(-k_x, k_y) = -A_{20}^\tau(k_x, -k_y), \quad (\text{A3b})$$

$$A_{31}^\tau(k_x, k_y) = A_{31}^{-\tau}(-k_x, k_y) = -A_{31}^\tau(k_x, -k_y), \quad (\text{A3c})$$

$$A_{32}^\tau(k_x, k_y) = -A_{32}^{-\tau}(-k_x, k_y) = A_{32}^\tau(k_x, -k_y), \quad (\text{A3d})$$

$$A_{33}^\tau(k_x, k_y) = -A_{33}^{-\tau}(-k_x, k_y) = A_{33}^\tau(k_x, -k_y). \quad (\text{A3e})$$

One can check that for  $N = 2$ , Eq. (19) corresponds to  $A_{00}^\tau(\mathbf{k}) = \frac{E_\uparrow^+(\mathbf{k}) + E_\downarrow^+(\mathbf{k})}{2}$ ,  $A_{33}^\tau(\mathbf{k}) = \tau \frac{E_\uparrow^+(\mathbf{k}) - E_\downarrow^+(\mathbf{k})}{2}$ ,  $A_{10}^\tau(\mathbf{k}) = t_0 + \tau t_1 k_x + t_2 k_x^2 + u_2 k_y^2$  and  $A_{20}^\tau(\mathbf{k}) = -u_1 k_y$ , and that these terms meet the symmetry requirements. Furthermore, we carried out fittings to DFT data using the additional spin-orbit terms  $A_{32}^\tau(\mathbf{k}) = \alpha k_x$  and  $A_{31}^\tau(\mathbf{k}) = \beta k_y$ . The fittings give  $|\alpha|, |\beta|, |u_1| \ll |t_1|$ ; hence, we conclude that these terms can be neglected.

For the interlayer hopping used in the HkpTB model for the valence band near  $\Gamma$ , setting  $N = 2$  in Eq. (3) and using a basis ordering similar to that of Eq. (4), we have  $\mathcal{T} = \pi_0 \sigma_0 \mathcal{C}$ ,  $\mathcal{P} = \pi_1 \sigma_3$  and  $\mathcal{D}(\sigma_v) = \pi_0 \sigma_0$ , where  $\sigma_i$  act on the band ( $v$  and  $w$ ) subspace. The symmetry conditions require

$$\text{Re } t_\sigma(\mathbf{k}) = \text{Re } t_\sigma(-\mathbf{k}) = \text{Re } t_\sigma(-k_x, k_y), \quad (\text{A4a})$$

$$\text{Im } t_\sigma(\mathbf{k}) = -\text{Im } t_\sigma(-\mathbf{k}) = \text{Im } t_\sigma(-k_x, k_y), \quad (\text{A4b})$$

$$t_{vw}(\mathbf{k}) = t_{vw}(-\mathbf{k}) = t_{vw}(-k_x, k_y), \quad t_{vw} \in \mathbb{R}. \quad (\text{A4c})$$

### Appendix B: Spin-orbit-coupling induced interband coupling at the $\Gamma$ -point valence bands

Here, we analyse the role of spin-orbit coupling and coupling to distant bands in determining parameters for the valence-band HkpTB model.

The spin-orbit coupling is given by  $\hat{H}_{SO} = \lambda \hat{\mathbf{L}} \cdot \hat{\mathbf{S}}$ , where  $\hat{\mathbf{L}}$  and  $\hat{\mathbf{S}}$  are the orbital and spin angular momentum operators. This can also be written in terms of the ladder operators  $L_\pm = L_x \pm iL_y$  and  $S_\pm = (S_x \pm iS_y)/2$  as

$$\hat{H}_{SO} = \lambda(L_z S_z + L_+ S_- + L_- S_+), \quad (\text{B1})$$

where  $L_\pm S_\mp$  describe a spin flip with corresponding change in orbital angular momentum projection. These terms couple the  $v$  and  $w$  bands with the bands  $v_1$  and  $v_3$  (Fig. 2d), which in the absence of SO coupling are doubly degenerate. Band  $v_1$  ( $E''$  Irrep of  $C_{3d}$ ) has basis functions which are odd under  $z \rightarrow -z$  (metal  $d_{\pm 1}$  orbitals being the dominant component<sup>26</sup>, as well as chalcogen  $p_{\pm 1}$ ). Band  $v_3$  ( $E'$  Irrep of  $C_{3d}$ ) has basis functions even under  $z \rightarrow -z$  (metal  $d_{\pm 2}$  orbitals and chalcogen  $p_{\pm 1}$ ). Including SO coupling results in the splitting of these bands into new bands denoted by the orbital and spin angular momentum projections along  $\hat{z}$ ,  $v_1(\pm 3/2), v_3(\pm 3/2)$ , and  $v_1(\pm 1/2), v_3(\pm 1/2)$ , corresponding to total angular momentum projections of  $J_z = \pm 3/2$  and  $J_z = \pm 1/2$ , respectively.

The  $v$ -band belongs to the one-dimensional  $A'_1$  Irrep (even under  $z \rightarrow -z$ , with metal  $d_0$  dominant and chalcogen  $p_0$ ), and has  $L_z = 0$  and  $s_z = \pm 1/2$ . Similarly, the  $w$ -band belongs to the one-dimensional  $A''_2$  Irrep, and is dominated by the odd (under  $z \rightarrow -z$ ) chalcogen  $p_0$  orbitals, giving two states with  $L_z = 0$  and  $s_z = \pm 1/2$ .

Therefore, in the bilayer, where  $z \rightarrow -z$  symmetry is broken, the  $v$  and  $w$ -bands can couple to  $v_1$  and  $v_3$  bands, with the appropriate spin-flip terms. In the second-order perturbation theory, this coupling produces corrections to the on-site energy

$$\delta_\sigma = \sum_{\substack{L_z, s_z \\ i=1,3 \\ \sigma=v,w}} \frac{|\langle v_i(L_z, s_z) | \lambda L_\pm S_\mp | \sigma(L_z = 0, s_z = \pm 1/2) \rangle|^2}{E_\sigma - E_{v_i(L_z, s_z)}}. \quad (\text{B2})$$

Note that these corrections are the same for both spin components of the  $v$  or  $w$  bands, with only one of the terms  $L_\pm S_\mp$  contributing for a given spin state.

An additional SO induced interband coupling with a spin-flip may be present in the multilayer case, affecting the interlayer coupling

$$\hat{H}'_{SO} = \mu \hat{z} \cdot (\mathbf{k} \times \mathbf{S}) = i\mu(S_- k_+ - S_+ k_-), \quad (\text{B3})$$

where the pre-factor  $\mu$  is related to the gradient of the interlayer pseudo-potential  $\mu \propto \partial_z V$ , and we defined  $k_\pm = k_x \pm ik_y$ . In contrast to the previous coupling, this coupling has a  $k$ -dependence, which affects the dispersions. The coupling in Eq. (B3) is odd under spatial

inversion. Due to the 2H–stacked bilayer having spatial inversion symmetry, the coupling is non–zero only between different bands in the two layers. In second order perturbation theory, we get a nominal redefinition of the 2D mass used in the HkpTB model, by adding the term

$$\mu_\sigma(\mathbf{k}) = \sum_{\substack{v_i \\ \sigma=v,w}} \frac{|\langle v_i | \mu S_\mp k_\pm | \sigma \rangle|^2}{E_\sigma - E_{v_i}} = \mu_\sigma k^2, \quad (\text{B4})$$

with  $\mu_\sigma$  a fitting parameter.

### Appendix C: Spin–split bands at the Brillouin zone edge for odd number of layers

The effective  $Q$ –point Hamiltonians  $H_{NQ}^\tau(\mathbf{k})$  for  $N$  odd can be split into two decoupled blocks of different spin projection as  $H_{NQ}^\tau(\mathbf{k}) = \text{diag}\{h_N^{\tau,\uparrow}(\mathbf{k}), h_N^{\tau,\downarrow}(\mathbf{k})\}$ , where the blocks have the alternating  $N \times N$  matrix form

$$h_N^{\tau,s}(\mathbf{k}) = \begin{pmatrix} \varepsilon_0(\mathbf{k}) + s\tau\Delta(\mathbf{k}) & t_\tau(\mathbf{k}) & 0 & 0 & \cdots & 0 \\ t_\tau^*(\mathbf{k}) & \varepsilon_0(\mathbf{k}) - s\tau\Delta(\mathbf{k}) & t_\tau^*(\mathbf{k}) & 0 & \cdots & 0 \\ 0 & t_\tau(\mathbf{k}) & \varepsilon_0(\mathbf{k}) + s\tau\Delta(\mathbf{k}) & t_\tau(\mathbf{k}) & \cdots & 0 \\ 0 & 0 & t_\tau^*(\mathbf{k}) & \varepsilon_0(\mathbf{k}) - s\tau\Delta(\mathbf{k}) & \cdots & 0 \\ \vdots & \vdots & \vdots & \vdots & \ddots & t_\tau(\mathbf{k}) \\ 0 & 0 & 0 & \cdots & t_\tau^*(\mathbf{k}) & \varepsilon_0(\mathbf{k}) + s\tau\Delta(\mathbf{k}) \end{pmatrix}, \quad (\text{C1})$$

and we have defined

$$\varepsilon_0(\mathbf{k}) = \frac{E_\uparrow^+(\mathbf{k}) + E_\downarrow^+(\mathbf{k})}{2}, \quad (\text{C2a})$$

$$\Delta(\mathbf{k}) = \frac{E_\uparrow^+(\mathbf{k}) - E_\downarrow^+(\mathbf{k})}{2}. \quad (\text{C2b})$$

Defining the even-dimensional  $(N-1) \times (N-1)$  matrix

$$\tilde{h}_{N-1}^{\tau,s}(\mathbf{k}) = \begin{pmatrix} \varepsilon_0(\mathbf{k}) - s\tau\Delta(\mathbf{k}) & t_\tau^*(\mathbf{k}) & 0 & \cdots & 0 \\ t_\tau(\mathbf{k}) & \varepsilon_0(\mathbf{k}) + s\tau\Delta(\mathbf{k}) & t_\tau(\mathbf{k}) & \cdots & 0 \\ 0 & t_\tau^*(\mathbf{k}) & \varepsilon_0(\mathbf{k}) - s\tau\Delta(\mathbf{k}) & \cdots & 0 \\ \vdots & \vdots & \vdots & \ddots & t_\tau(\mathbf{k}) \\ 0 & 0 & \cdots & t_\tau^*(\mathbf{k}) & \varepsilon_0(\mathbf{k}) + s\tau\Delta(\mathbf{k}) \end{pmatrix}, \quad (\text{C3})$$

the eigenvalues  $\varepsilon$  of (C1) are given by a secular equation

$$\begin{aligned} \det\{\varepsilon - h_N^{\tau,s}\} &= [\varepsilon - \varepsilon_0(\mathbf{k}) - s\tau\Delta(\mathbf{k})] \det\{\varepsilon - \tilde{h}_{N-1}^{\tau,s}\} \\ &\quad - |t_\tau(\mathbf{k})|^2 \det\{\varepsilon - h_{N-2}^{\tau,s}\} \\ &= [\varepsilon - \varepsilon_0(\mathbf{k}) - s\tau\Delta(\mathbf{k})] \det\{\varepsilon - \tilde{h}_{N-1}^{\tau,s}\} \\ &\quad - |t_\tau(\mathbf{k})|^2 \left( [\varepsilon - \varepsilon_0(\mathbf{k}) - s\tau\Delta(\mathbf{k})] \det\{\varepsilon - \tilde{h}_{N-3}^{\tau,s}\} \right. \\ &\quad \left. - |t_\tau(\mathbf{k})|^2 \det\{\varepsilon - h_{N-4}^{\tau,s}\} \right) = \dots \end{aligned} \quad (\text{C4})$$

Using the fact that  $\det\{\varepsilon - h_1^{\tau,s}\} = \varepsilon - \varepsilon_0(\mathbf{k}) - s\tau\Delta(\mathbf{k})$ , we can continue expanding Eq. (C4) to obtain

$$\begin{aligned} \det\{\varepsilon - h_N^{\tau,s}\} &= [\varepsilon - \varepsilon_0(\mathbf{k}) - s\tau\Delta(\mathbf{k})] \\ &\times \left( \sum_{m=0}^{\frac{N-3}{2}} (-1)^m |t_\tau(\mathbf{k})|^{2m} \det\{\varepsilon - \tilde{h}_{N-(2m+1)}\} \right. \\ &\quad \left. + (-1)^{\frac{N-1}{2}} |t_\tau(\mathbf{k})|^{N-1} \right), \end{aligned} \quad (\text{C5})$$

which explicitly shows that  $[\varepsilon - \varepsilon_0(\mathbf{k}) - s\tau\Delta(\mathbf{k})]$  is an overall factor, and thus  $\varepsilon = \varepsilon_0(\mathbf{k}) + s\tau\Delta(\mathbf{k}) \equiv \varepsilon_s^\tau(\mathbf{k})$  is always an eigenvalue, regardless of the (odd) value of  $N$ . For a given  $\tau$ , the different  $s$  quantum numbers give two spin–split monolayer dispersions  $\varepsilon_s^\tau(\mathbf{k})$  about the  $\tau C_3^m \mathbf{Q}$  ( $m = 0, 1, 2$ ) points, corresponding to the features observed in Fig. 10. The fact that this prediction is verified in the DFT band structures clearly confirms the validity of our hybrid model.

For large odd  $N$ , nearly spin-degenerate bands grow denser on either side of the spin–split bands  $\varepsilon_s^\tau(\mathbf{k})$  without crossing them, as shown in Fig. 16a. The reason for this becomes clear when we take the bulk limit, and find that the spin–split states form the band edges around a central gap in the subband structure. This is shown in Fig. 16b. Indeed, in the limit of large  $N$  the Hamiltonian (C1) corresponds to the bulk Hamiltonian at  $k_z = \pi/c$ , since  $\varepsilon_0(\mathbf{k}) = \varepsilon_0(\mathbf{k}, k_z = \frac{\pi}{c})$  [see Eq. (21)].

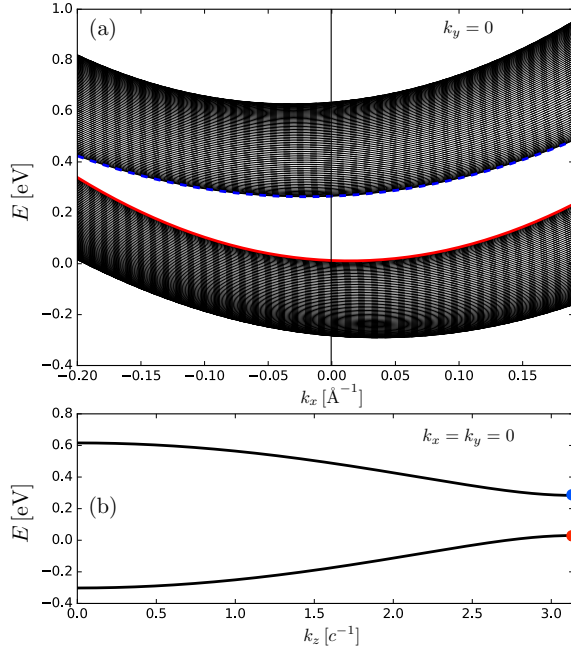


FIG. 16. (a) Subband structure of 101-layer WS<sub>2</sub> near  $\tau\mathbf{Q}$  ( $k_x = 0$ ), along the  $\Gamma\bar{K}$  line. Spin up (down) bands are shown with solid (dashed) curves. The spin–split bands  $\varepsilon_s^\tau(\mathbf{k})$ , pinned in the middle of the odd  $N$  subband structure, are shown in blue and red. (b) Bulk band structure for WS<sub>2</sub> along the  $QA$  line. Blue and red dots mark the position of the spin–split bands in the Brillouin zone.

#### Appendix D: Electron-phonon coupling for LO phonon in multilayer system

In this appendix we derive the expression used for the electron-phonon coupling with LO phonon in a multilayer system. As described in the text, we treat the LO phonon in each layer as independent and degenerate. However, in the LO phonon case, the generated electrostatic potential due LO phonon in one layer interacts with the electrons in all the other layers in the system. Following similar steps as in ref. [47].

Within a monolayer, the LO phonon induced in-plane polarization is given by its in-plane Fourier component,

$$\mathbf{P}_\mathbf{q}(z) = \frac{eZ}{\epsilon(q)A} \mathbf{u}_\mathbf{q} \delta(z), \quad (\text{D1})$$

where  $Z$  is the Born effective charge on the metal and chalcogens,  $A$  is the unit cell area,  $\mathbf{u}_\mathbf{q} = \sqrt{\frac{\hbar}{2M_r N_{\text{cell}} \omega_{\text{LO}}}} \hat{\mathbf{e}}$  is the phonon-induced atomic displacement in the direction connecting the metal and chalcogens in the unit cell, with  $M_r$  the reduced mass of the metal and chalcogens,  $N$  the number of unit cells in the sample, and  $\omega_{\text{LO}}$  the LO phonon frequency.  $\epsilon(q)$  is the dielectric function characterizing the response of the material to the phonon induced electric field.

The induced charge density in the layer is given by  $\rho = -\nabla \cdot \mathbf{P}$ , with the Fourier component

$$\rho_\mathbf{q} = -i\mathbf{q} \cdot \mathbf{P}_\mathbf{q}. \quad (\text{D2})$$

The potential resulting from the charge distribution is given by Poisson's equation  $\nabla^2 \phi = -4\pi\rho$ . Fourier-transforming in three dimensions gives,

$$\phi_\mathbf{q}(k) = \frac{-4\pi ieZ}{\epsilon(q)A} \frac{\mathbf{q} \cdot \mathbf{u}_\mathbf{q}}{q^2 + k^2}, \quad (\text{D3})$$

where  $k$  is the Fourier parameter in the  $z$  direction. Inverse Fourier transforming in  $k$  gives the  $z$  dependence of the potential with in-plane Fourier component  $\mathbf{q}$

$$\phi_\mathbf{q}(z) = -i \frac{2\pi e Z u_\mathbf{q}}{\epsilon(q)A} e^{-q|z|}. \quad (\text{D4})$$

The electron-phonon coupling for an electron localized in an isolated monolayer is given by  $g(q) = e\phi_q(0) = -i \frac{2\pi e^2 Z u_q}{\epsilon A}$ . This form of the coupling is similar to the form derived in Refs. [40 and 48], where the polarizability of a two-dimensional dielectric was taken into account by the replacement  $\epsilon(q) \rightarrow 1 + r_* q$ , with  $r_*$  the screening length in the material. For multilayer 2H-stacked TMDs, as the polarization in subsequent layers alternates in its sign, the resulting electrostatic potential also alternates in its sign.

#### Appendix E: Electron-phonon coupling for ZO phonon in multilayer system

The atomic vibrations for the ZO optical phonon mode result in a polarization in the out of plane direction due to the opposite motions of the metal and two chalcogens, and the finite Born effective charges in the  $z$ -direction. The interaction energy in the multilayer system between charges and phonon-induced out of plane polarizations in all layers is given by<sup>49</sup>

$$E_{\text{int}} = \sum_{n,m} \int d^2r d^2r' \frac{\rho_n(\mathbf{r}) P_{z,m}(\mathbf{r}') d(n-m)}{\Delta r^3}, \quad (\text{E1})$$

$$\Delta r = [(\mathbf{r} - \mathbf{r}')^2 + d^2(n-m)^2]^{1/2},$$

where  $\rho_n(\mathbf{r})$  is the charge density on layer  $n$ ,  $P_{z,m}(\mathbf{r}')$  is the out of plane polarization in layer  $m$  caused by the ZO optical phonon,  $d$  the interlayer separation, and we sum over all layer pairs. Fourier-transforming the charge density and polarization in the in-plane momentum components gives

$$\rho_n(\mathbf{r}) = \int \frac{d^2q}{(2\pi)^2} e^{i\mathbf{q} \cdot \mathbf{r}} \rho_m(\mathbf{q}), \quad (\text{E2})$$

and similarly for the polarization. The interaction energy then takes the form,

$$E_{\text{int}} = \sum_{n,m} \int d^2r d^2r' \frac{d(n-m)}{\Delta r^3} \times \int \frac{d^2q d^2q'}{(2\pi)^4} e^{i\mathbf{q}\cdot\mathbf{r}} e^{i\mathbf{q}'\cdot\mathbf{r}'} \rho_n(\mathbf{q}) P_{z,m}(\mathbf{q}'). \quad (\text{E3})$$

Defining the new variables  $\tilde{\mathbf{r}} = \mathbf{r} - \mathbf{r}'$ ,  $\mathbf{R} = \mathbf{r} + \mathbf{r}'$  and integrating over  $\mathbf{R}$  gives  $\delta_{q,-q'}$ ,

$$E_{\text{e-ph}} = \sum_{n,m} \int d^2\tilde{r} \int \frac{d^2q}{(2\pi)^2} \frac{d(n-m)}{\Delta \tilde{r}^3} e^{i\mathbf{q}\cdot\tilde{\mathbf{r}}} \times \rho_n^*(\mathbf{q}) P_{z,m}(\mathbf{q}), \quad (\text{E4})$$

where in the last row we used  $\rho_n^*(\mathbf{q}) = \rho_n(-\mathbf{q})$ , since the density is real. Carrying out the integration over  $\tilde{\mathbf{r}}$  gives

$$E_{\text{e-ph}} = \sum'_{n,m} \frac{2\pi(n-m)}{|n-m|} \int \frac{d^2q}{(2\pi)^2} e^{-qd|n-m|} |\rho_n^*(\mathbf{q}) P_{z,m}(\mathbf{q})|, \quad (\text{E5})$$

where the ' over the sum means that the summation excludes the term with  $n = m$ . Quantizing the phonon polarization and the carrier density gives

$$\rho_n^*(\mathbf{q}) = e \sum_{\mathbf{k}} c_{\mathbf{k},n}^\dagger c_{\mathbf{k}+\mathbf{q},n}, \quad (\text{E6})$$

$$P_{z,m}(\mathbf{q}) = \frac{eZ_z}{A} \sqrt{\frac{\hbar}{2N_{\text{cell}} M_r \omega}} (a_{-\mathbf{q},m} + a_{\mathbf{q},m}^\dagger),$$

where  $c_{\mathbf{k},n}(c_{\mathbf{k},n}^\dagger)$  is the annihilation (creation) operator for an electron in state  $\mathbf{k}$  in layer  $n$ , and  $a_{\mathbf{q},m}(a_{\mathbf{q},m}^\dagger)$  is the annihilation (creation) operator for a phonon with in-plane wave vector  $\mathbf{q}$ . The phonon-induced polarization is given, similarly to the LO phonon case, by the Born effective charge and the phonon displacement.

The electron-phonon interaction Hamiltonian is then

given by

$$H_{\text{e-ph}} = \frac{2\pi e^2 Z_z}{A} \sqrt{\frac{\hbar}{2N_{\text{cell}} M_r \omega_{ZO}}} \sum'_{n,m} \sum_{\mathbf{k},\mathbf{q}} \frac{n-m}{|n-m|} e^{-qd|n-m|} \times c_{\mathbf{k},n}^\dagger c_{\mathbf{k}+\mathbf{q},n} (a_{-\mathbf{q},m} + a_{\mathbf{q},m}^\dagger). \quad (\text{E7})$$

## Appendix F: DFT-calculated band structures for few-layer TMDs

In Figs. 17-20 we show the DFT band structures for the four TMDs, which were used for the model parametrization. The DFT calculations were performed using a plane-wave basis within the local density approximation (LDA), with the Quantum Espresso<sup>31</sup> PWSCF *ab initio* package. We considered the Perdew-Zunger exchange correlation scheme<sup>32</sup>, with fully-relativistic norm-conserving pseudo-potentials, including non-collinear corrections. Pseudopotentials for Mo, W, S, and Se atoms were generated using atomic code ld1.x of the PWSCF package<sup>33</sup>. The cutoff energy in the plane-wave expansion was set to 60 Ry, and the BZ sampling of electronic states was approximated using a Monkhorst-Pack uniform k-grid of  $24 \times 24 \times 1$  for all structures.<sup>34</sup> We adopted a Methfessel-Paxton smearing<sup>35</sup> of 0.005 Ry and set the total energy convergence to less than  $10^{-6}$  eV in all calculations. Spin-orbit coupling was included in all electronic band structure calculations. To eliminate spurious interactions between adjacent supercells, a 20 Å vacuum buffer space was inserted in the out-of-plane direction. The interlayer separations in the four TMDs were taken to be the experimental values, 6.149 Å<sup>36</sup>, 6.463 Å<sup>37</sup>, 6.173 Å<sup>38</sup>, and 6.477 Å<sup>39</sup>, with LDA-optimised in-plane lattice constants of 3.157 Å, 3.288 Å, 3.161 Å, and 3.291 Å for MoS<sub>2</sub>, MoSe<sub>2</sub>, WS<sub>2</sub>, and WSe<sub>2</sub>, respectively.

- 
- <sup>1</sup> D. Jariwala, V. K. Sangwan, L. J. Lauhon, T. J. Marks, and M. C. Hersam, ACS Nano **8**, 1102 (2014).  
<sup>2</sup> W. Choi, N. Choudhary, G. H. Han, J. Park, D. Akinwande, and Y. H. Lee, Materials Today **20**, 116 (2017).  
<sup>3</sup> Y. Zhao, W. Yu, and G. Ouyang, Journal of Physics D: Applied Physics **51**, 015111 (2018).  
<sup>4</sup> Q. H. Wang, K. Kalantar-Zadeh, A. Kis, J. N. Coleman, and M. S. Strano, Nature Nanotechnology **7**, 699 EP (2012).  
<sup>5</sup> G.-B. Liu, D. Xiao, Y. Yao, X. Xu, and W. Yao, Chem. Soc. Rev. **44**, 2643 (2015).  
<sup>6</sup> K. F. Mak and J. Shan, Nature Photonics **10**, 216 EP (2016).  
<sup>7</sup> U. Wurstbauer, B. Miller, E. Parzinger, and A. W. Holleitner, Journal of Physics D: Applied Physics **50**, 173001 (2017).

- <sup>8</sup> K. F. Mak, C. Lee, J. Hone, J. Shan, and T. F. Heinz, Phys. Rev. Lett. **105**, 136805 (2010).  
<sup>9</sup> G. Aivazian, Z. Gong, A. M. Jones, R.-L. Chu, J. Yan, D. G. Mandrus, C. Zhang, D. Cobden, W. Yao, and X. Xu, Nature Physics **11**, 148 EP (2015).  
<sup>10</sup> D. MacNeill, C. Heikes, K. F. Mak, Z. Anderson, A. Kormányos, V. Zólyomi, J. Park, and D. C. Ralph, Phys. Rev. Lett. **114**, 037401 (2015).  
<sup>11</sup> B. Zhu, H. Zeng, J. Dai, and X. Cui, Advanced Materials **26**, 5504 (2014).  
<sup>12</sup> L. Yang, N. A. Sinitsyn, W. Chen, J. Yuan, J. Zhang, J. Lou, and S. A. Crooker, Nature Physics **11**, 830 EP (2015).  
<sup>13</sup> H. Yu, G.-B. Liu, P. Gong, X. Xu, and W. Yao, Nature Communications **5**, 3876 EP (2014).

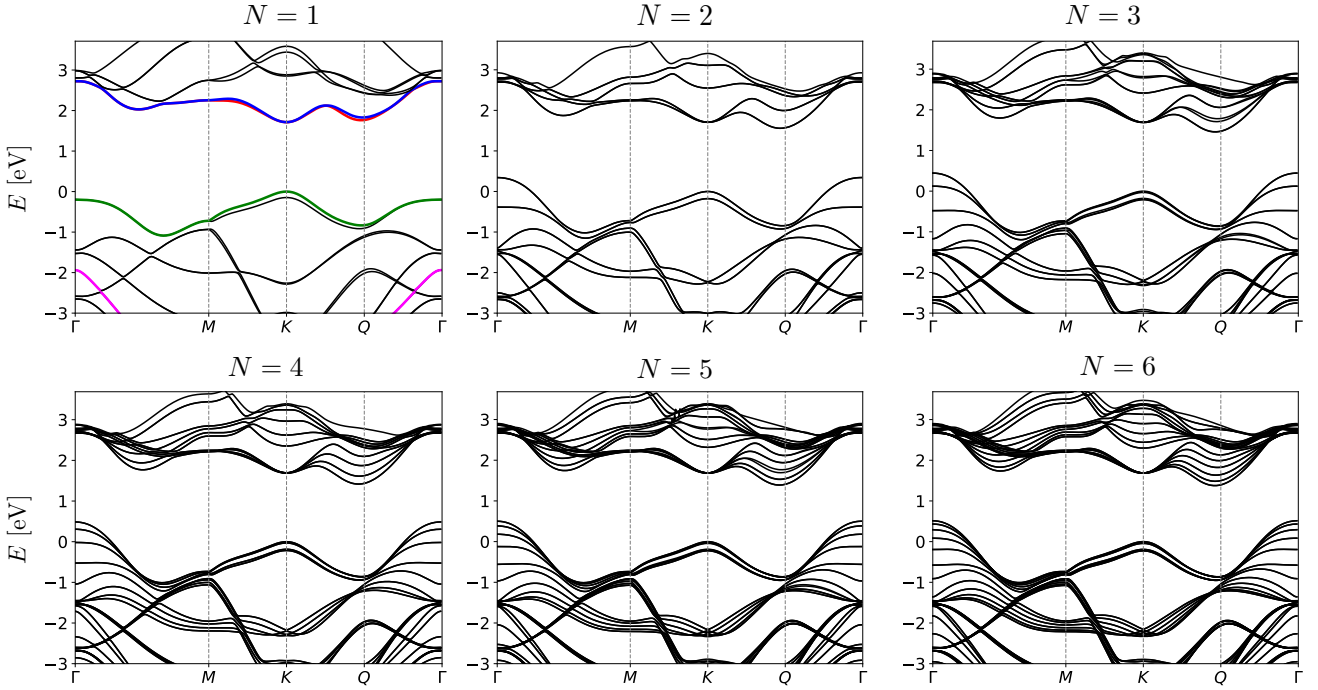


FIG. 17. DFT calculated band structure of  $N$ -layer 2H-MoS<sub>2</sub>, for  $N = 1$  to 6. In the monolayer case we highlight the CB (blue for spin down, red for spin up), VB (green) and lower valence band  $w$  (magenta). Few-layer MoS<sub>2</sub> band structures have been presented in Refs. 14, 16–19.

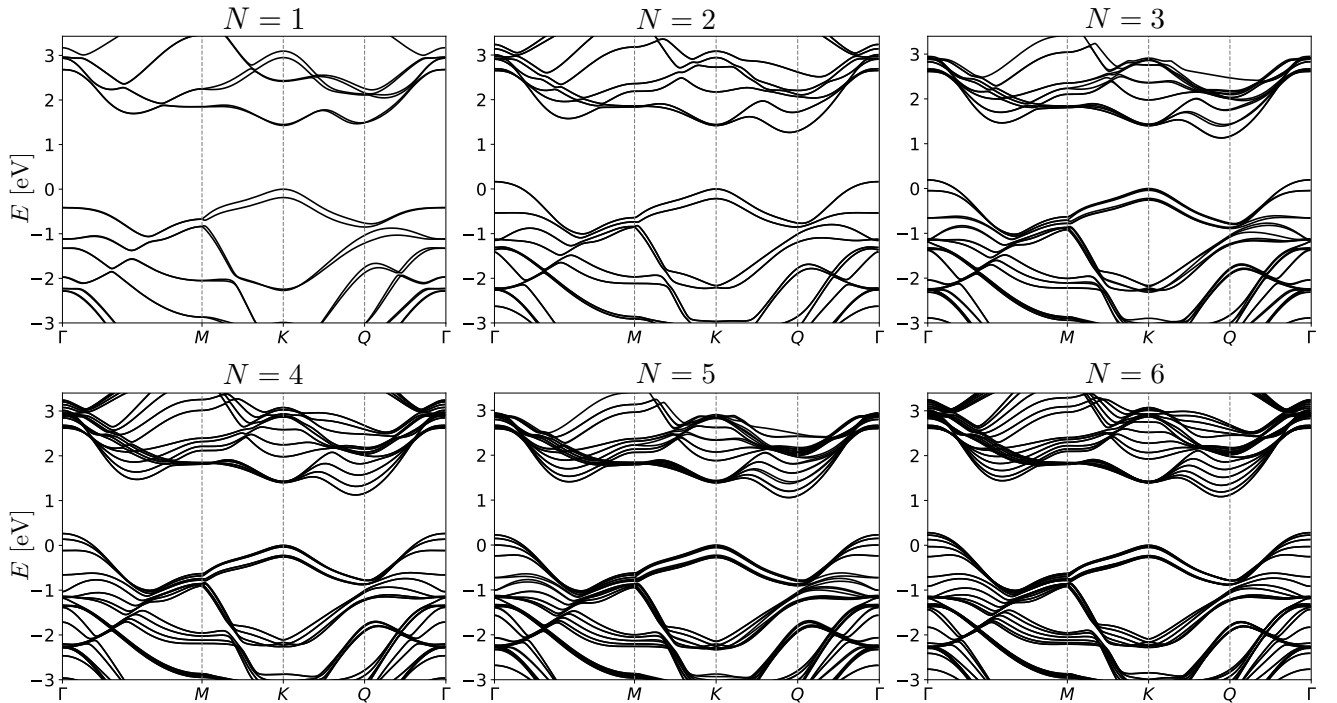


FIG. 18. DFT calculated band structure of  $N$ -layer 2H-MoSe<sub>2</sub>, for  $N = 1$  to 6. Few-layer MoSe<sub>2</sub> band structures have been presented in Refs. 16, 18, 20, and 21.

<sup>14</sup> T. Cheiwchanchamnangij and W. R. L. Lambrecht, Phys. Rev. B **85**, 205302 (2012).

<sup>15</sup> E. Cappelluti, R. Roldán, J. A. Silva-Guillén, P. Ordejón, and F. Guinea, Phys. Rev. B **88**, 075409 (2013).

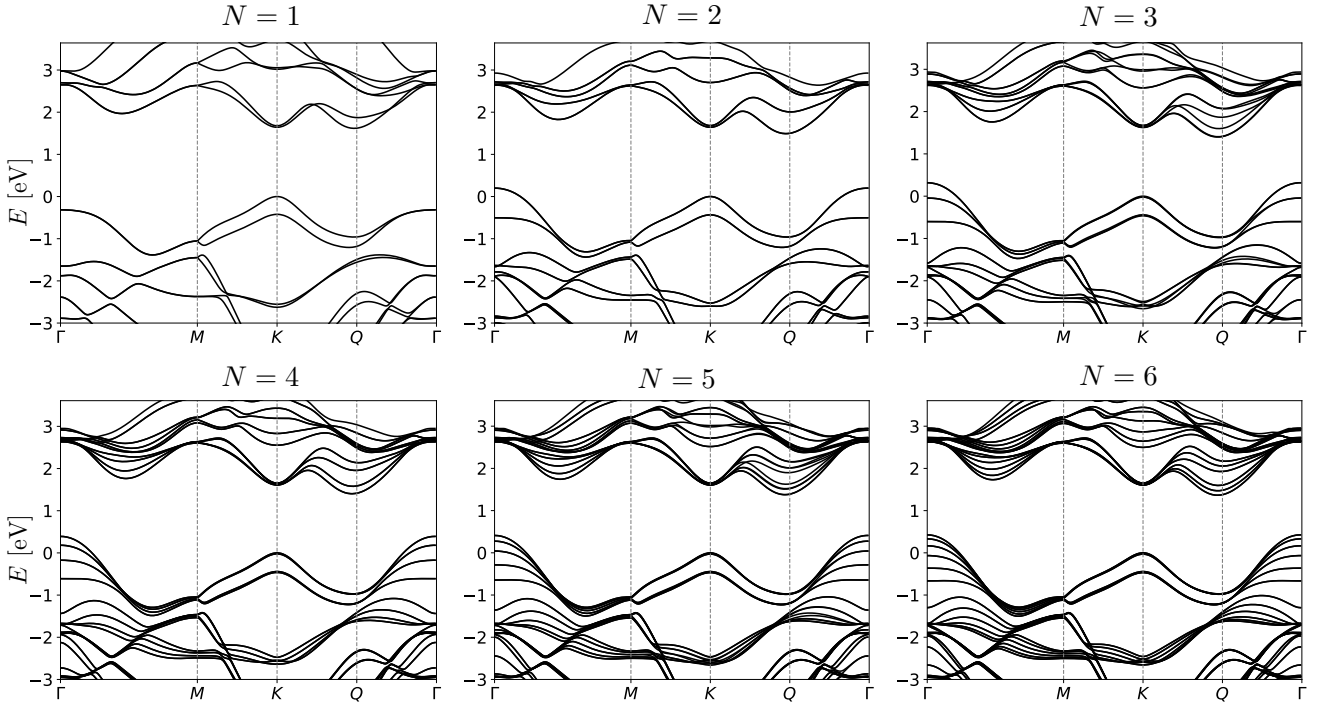


FIG. 19. DFT calculated band structure of  $N$ -layer 2H-WS<sub>2</sub>, for  $N = 1$  to 6. Few-layer WS<sub>2</sub> band structures have been presented in Refs. 16 and 18.

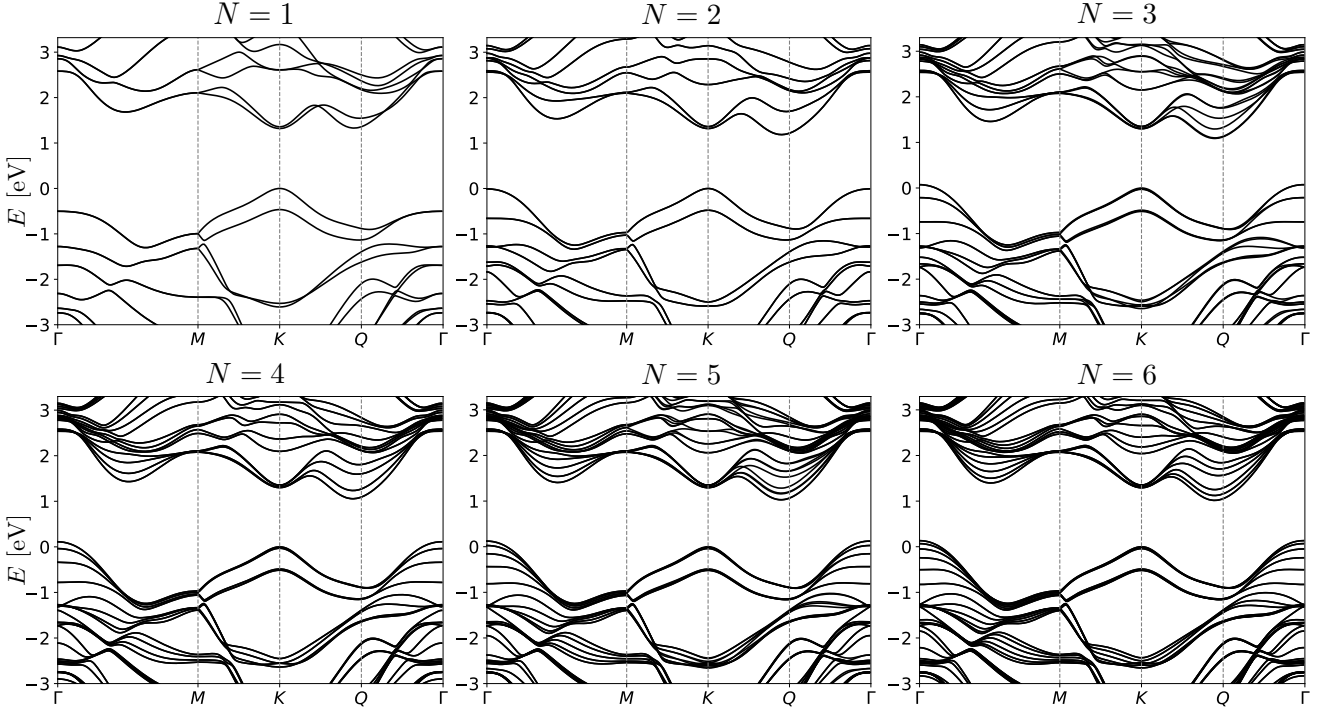


FIG. 20. DFT calculated band structure of  $N$ -layer 2H-WSe<sub>2</sub>, for  $N = 1$  to 6. Few-layer WSe<sub>2</sub> band structures have been presented in Refs. 16, 18, and 21.

<sup>16</sup> L. Debbichi, O. Eriksson, and S. Lebègue, Phys. Rev. B **89**, 205311 (2014).

<sup>17</sup> J. E. Padilha, H. Peelaers, A. Janotti, and C. G. Van de Walle, Phys. Rev. B **90**, 205420 (2014).

- <sup>18</sup> T.-R. Chang, H. Lin, H.-T. Jeng, and A. Bansil, *Scientific Reports* **4**, 6270 EP (2014).
- <sup>19</sup> S. Fang, R. Kuade Defo, S. N. Shirodkar, S. Lieu, G. A. Tritsaris, and E. Kaxiras, *Phys. Rev. B* **92**, 205108 (2015).
- <sup>20</sup> A. J. Bradley, M. M. Ugeda, F. H. da Jornada, D. Y. Qiu, W. Ruan, Y. Zhang, S. Wickenburg, A. Riss, J. Lu, S.-K. Mo, Z. Hussain, Z.-X. Shen, S. G. Louie, and M. F. Crommie, *Nano Letters* **15**, 2594 (2015), pMID: 25775022, <http://dx.doi.org/10.1021/acs.nanolett.5b00160>.
- <sup>21</sup> Y. Sun, D. Wang, and Z. Shuai, *The Journal of Physical Chemistry C* **120**, 21866 (2016), <http://dx.doi.org/10.1021/acs.jpcc.6b08748>.
- <sup>22</sup> R. Pisoni, Y. Lee, H. Overweg, M. Eich, P. Simonet, K. Watanabe, T. Taniguchi, R. Gorbatchev, T. Ihn, and K. Ensslin, *Nano Letters*, *Nano Letters* **17**, 5008 (2017).
- <sup>23</sup> S. J. Magorrian, V. Zólyomi, and V. I. Fal'ko, *Phys. Rev. B* **94**, 245431 (2016).
- <sup>24</sup> D. A. Bandurin, A. V. Tyurnina, G. L. Yu, A. Mishchenko, V. Zólyomi, S. V. Morozov, R. K. Kumar, R. V. Gorbatchev, Z. R. Kudrynskyi, S. Pezzini, Z. D. Kovalyuk, U. Zeitler, K. S. Novoselov, A. Patanè, L. Eaves, I. V. Grigorieva, V. I. Fal'ko, A. K. Geim, and Y. Cao, *Nature Nanotechnology* **12**, 223 EP (2016).
- <sup>25</sup> A. Kormányos, V. Zólyomi, N. D. Drummond, P. Rakyta, G. Burkard, and V. I. Fal'ko, *Phys. Rev. B* **88**, 045416 (2013).
- <sup>26</sup> A. Kormányos, G. Burkard, M. Gmitra, J. Fabian, V. Zólyomi, N. D. Drummond, and V. Fal'ko, *2D Materials* **2**, 022001 (2015).
- <sup>27</sup> M. Danovich, I. L. Aleiner, N. D. Drummond, and V. I. Fal'ko, *IEEE Journal of Selected Topics in Quantum Electronics* **23**, 168 (2017).
- <sup>28</sup> D. Kozawa, R. Kumar, A. Carvalho, K. Kumar Amara, W. Zhao, S. Wang, M. Toh, R. M. Ribeiro, A. H. Castro Neto, K. Matsuda, and G. Eda, *Nature Communications* **5**, 4543 EP (2014).
- <sup>29</sup> T. Unuma, M. Yoshita, T. Noda, H. Sakaki, and H. Akiyama, *Journal of Applied Physics*, *Journal of Applied Physics* **93**, 1586 (2003).
- <sup>30</sup> L. F. Mattheiss, *Phys. Rev. B* **8**, 3719 (1973).
- <sup>31</sup> P. Giannozzi, S. Baroni, N. Bonini, M. Calandra, R. Car, C. Cavazzoni, D. Ceresoli, G. L. Chiarotti, M. Cococcioni, I. Dabo, A. D. Corso, S. de Gironcoli, S. Fabris, G. Fratesi, R. Gebauer, U. Gerstmann, C. Gougaussis, A. Kokalj, M. Lazzeri, L. Martin-Samos, N. Marzari, F. Mauri, R. Mazzarello, S. Paolini, A. Pasquarello, L. Paulatto, C. Sbraccia, S. Scandolo, G. Sclauzero, A. P. Seitsonen, A. Smogunov, P. Umari, and R. M. Wentzcovitch, *Journal of Physics: Condensed Matter* **21**, 395502 (2009).
- <sup>32</sup> J. P. Perdew and A. Zunger, *Phys. Rev. B* **23**, 5048 (1981).
- <sup>33</sup> A. Dal Corso, *Computational Materials Science* **95**, 337 (2014).
- <sup>34</sup> H. J. Monkhorst and J. D. Pack, *Phys. Rev. B* **13**, 5188 (1976).
- <sup>35</sup> M. Methfessel and A. T. Paxton, *Phys. Rev. B* **40**, 3616 (1989).
- <sup>36</sup> T. Böker, R. Severin, A. Müller, C. Janowitz, R. Manzke, D. Voß, P. Krüger, A. Mazur, and J. Pollmann, *Phys. Rev. B* **64**, 235305 (2001).
- <sup>37</sup> A. A. Al-Hilli and B. L. Evans, *Journal of Crystal Growth* **15**, 93 (1972).
- <sup>38</sup> T. J. Wieting, *Journal of Physics and Chemistry of Solids* **31**, 2148 (1970).
- <sup>39</sup> W. T. Hicks, *Journal of The Electrochemical Society* **111**, 1058 (1964), <http://jes.ecsdl.org/content/111/9/1058.full.pdf+html>.
- <sup>40</sup> T. Sohier, M. Calandra, and F. Mauri, *Phys. Rev. B* **94**, 085415 (2016).
- <sup>41</sup> G. Froehlicher, E. Lorchat, F. Fernique, C. Joshi, A. Molina-Sánchez, L. Wirtz, and S. Berciaud, *Nano Letters* **15**, 6481 (2015), pMID: 26371970, <http://dx.doi.org/10.1021/acs.nanolett.5b02683>.
- <sup>42</sup> Z. Jin, X. Li, J. T. Mullen, and K. W. Kim, *Phys. Rev. B* **90**, 045422 (2014).
- <sup>43</sup> X. Gu and R. Yang, *Applied Physics Letters* **105**, 131903 (2014).
- <sup>44</sup> M. Gibertini, F. M. D. Pellegrino, N. Marzari, and M. Polini, *Phys. Rev. B* **90**, 245411 (2014).
- <sup>45</sup> Z. Wu, S. Xu, H. Lu, A. Khamoshi, G.-B. Liu, T. Han, Y. Wu, J. Lin, G. Long, Y. He, Y. Cai, Y. Yao, F. Zhang, and N. Wang, *Nature Communications* **7**, 12955 EP (2016).
- <sup>46</sup> A. B. Bernevig and T. L. Hugues, *Topological insulators and topological superconductors* (Princeton University Press, Princeton, NJ, 2013).
- <sup>47</sup> K. Kaasbjerg, K. S. Thygesen, and K. W. Jacobsen, *Phys. Rev. B* **85**, 115317 (2012).
- <sup>48</sup> M. Danovich, I. L. Aleiner, N. D. Drummond, and V. I. Falko, *IEEE Journal of Selected Topics in Quantum Electronics* **23**, 168 (2017).
- <sup>49</sup> B. Ganchev, N. Drummond, I. Aleiner, and V. Fal'ko, *Phys. Rev. Lett.* **114**, 107401 (2015).

# Chapter 7

## Conclusions

The work presented in this thesis aimed at furthering the understanding of processes affecting and determining the optical properties of two dimensional transition metal dichalcogenides. In the published works presented we have covered monolayer, heterobilayer and multilayer structures, demonstrating the versatility, limitations and applicability of these materials for future optoelectronic devices and applications.

Below we provide a summary of the main results obtained and an outlook on possible future work.

In Chapter 3 we studied the kinetics of processes involving electrons and holes determining the efficiency of light emission in monolayer TMDCs. We have shown that the electron-phonon coupling with the homopolar and longitudinal optical phonons in these two dimensional materials results in sub-ps relaxation times of the photo-excited carriers, which facilitate the fast formation of excitons capable of emitting light, making these materials favourable for light emitting devices. Additionally, we have demonstrated how the intrinsically dark excitons forming the ground state bound complexes in  $\text{WS}_2$  and  $\text{WSe}_2$ , can recombine radiatively through a phonon assisted process, which is  $\sim 10^4$  times weaker as compared to the bright exciton's rate. Comparing the radiative process to a non-radiative Auger process revealed that it can dominate over the radiative process for relatively low carrier densities  $< 10^{11} \text{ cm}^{-2}$ , providing a possible explanation to the experimentally observed low quantum efficiencies in these materials, despite their favourable properties for light emission.

The observed low quantum efficiencies for light emission in  $\text{MoS}_2$ ,  $\text{MoSe}_2$  are still

not clear due to the ground states excitons being bright, and therefore cannot be explained using the same Auger process proposed for WS<sub>2</sub>, WSe<sub>2</sub>, and require an alternative microscopic process involving the bright ground state excitons.

The effect of different dielectric environments encapsulating the monolayer TMDCs need be further investigated. The presence of the dielectric environment will result in modification to the electron-phonon coupling due to additional dielectric screening, however will also allow for electron-phonon coupling with the substrate phonons.

In Chapter 4, we studied the various bound complexes in monolayer TMDCs. We predicted the appearance of semidark trions and biexcitons in the photoluminescence spectra of WS<sub>2</sub> and WSe<sub>2</sub>. These complexes were shown to become bright through a proposed virtual electron-electron intervalley scattering, providing a finite optical matrix element for these complexes, leading to radiative lifetimes an order of magnitude larger than those of the bright complexes. The semidark trions and biexcitons are predicted to have associated photon energies, which are shifted with respect to the bright counterparts by twice the spin-orbit splitting in the conduction band, and should be most dominant at very low temperatures as compared to the spin-orbit splitting, due to the bright excitonic complexes in these materials requiring an activation energy.

The behaviour of the various bound complexes under a magnetic field revealed large deviations in the measured g-factor (measuring difference in emitted photon energies in the two valleys as a function of magnetic field), which lack a proper explanation. Therefore, further studies may involve the incorporation of a magnetic field and studying its influence on the bound complexes and the emitted light.

In Chapter 5, we have shown that in twisted and incommensurate MoSe<sub>2</sub>/WSe<sub>2</sub> heterobilayer systems, where the momentum mismatch between the electrons and holes in the opposite valleys prevents the direct radiative recombination of interlayer complexes, donor bound interlayer complexes ( $D^0h$  and  $D^0X$ ) have radiative rates of few  $\sim \mu s^{-1}$  for closely aligned layers with a donor density of  $n_D \sim 10^{13} \text{ cm}^{-2}$ , where the finite optical matrix element is provided by the momentum spread of the localized complexes wave functions. For large misalignment, the screened bilayer potential for the short range interaction between the carriers and donor results in a strong asymptotic angular dependence of  $\propto \theta^{-8}$ , making these lines observable mainly for closely aligned

layers. Additional emission lines were found due to LO phonon assisted recombination, with significant rates in particular for the  $D^0h$  complex. The predicted photoluminescence spectrum, therefore contains three main distinct lines with the intensity of the lines depending on the carrier density, which affects the number of relevant donor bound complexes present in the sample, with the neutral donor and hole complex  $D^0h$  and its phonon replica dominating at low carrier density, whereas the donor bound trion  $D^0X$  dominating at high carrier density (as compared with the donor density). This work extends the understanding and interpretation of the spectra of heterobilayers of TMDCs for lattice mismatched and weakly misaligned layers, demonstrating the importance of impurities for the radiative recombination of interlayer complexes.

Future work which generalizes the presented work may include the similar investigation of acceptor bound complexes, with the acceptors localized on the typically p-doped Tungsten based layer. Additionally, future work may involve exploring other combinations of materials, with different band alignments, and different stacking, which in particular modify the tunnelling amplitudes.

For closely aligned layers, an additional perturbation arises due to the moiré potential, which can have a periodicity larger than the complex's extent in real space. The moiré potential will further localize the interlayer complex and modify the observed photoluminescence spectra.

The electrons and holes, separated by the interlayer distance, result in the formation of an electric dipole in the out-of-plane direction. Multiple complexes therefore will have a dipole-dipole interaction, which may affect the observed spectra. The dipole additionally interacts with the applied electric field from the gates used to electrostatically dope the system, resulting in a Stark shift to the photon energies, which was not accounted for.

In Chapter 6, we have shown that few-layer transition metal dichalcogenids contain a rich subband structure both in the valence band for p-doped and in the conduction band for n-doped few-layer films, with the four studied transition metal dichalcogenides covering densely the infrared to far-infrared spectral range, thus demonstrating a yet to be explored potential of these materials in the form of few-layers quantum wells, opening new research directions in the field of two dimensional transition metal dichalcogenides. The subband structure in the conduction band shows an alternating

behaviour in terms of spin-orbit splitting between the subbands, for even and odd number of layers, reflecting the symmetry properties of the 2H-stacked few-layer films. The parity (mirror or inversion) symmetry of the few-layer films results in selection rules for the intersubband transitions due to absorption of out-of-plane polarized light, with transition between same parity subbands being forbidden. The obtained absorption lineshapes show a dispersion broadening ( $\sim k_B T$ ) due to the subband dependent effective masses. Additional broadening mechanism due to intersubband phonon relaxation was found to give a contribution of few meV, which is weaker as compared to conventional semiconductors quantum wells. Few-layer transition metal dichalcogenides therefore provide a promising platform for optoelectronic devices operating in the infrared to far-infrared spectral range.

Future work for the utilisation of intersubband transitions requires the modelling of the effects of electrostatic gating and screening in the few-layer films on the subbands and their optical properties.

Finally, the multi-degenerate, spin-orbit split, and anisotropic Q-valleys in the conduction band of few-layer films of TMDCs make them a promising platform for quantum Hall ferromagnetism studies.

# Appendix A

## Electron-phonon coupling of homopolar and longitudinal optical phonons in 2D TMDCs

In this appendix we provide a more detailed derivation for the electron-phonon coupling with the longitudinal optical phonon in 2D TMDCs, used in Chapters 3 (Ref. [21]) and 6.

The HP phonon mode transforms according to the identity irrep  $A'_1$  of the  $D_{3h}$  point group, such that the coupling can be described by the zeroth order deformation potential  $D$  as

$$\delta V_{HP} = Du_{HP}. \quad (\text{A.1})$$

Quantizing the lattice displacement as

$$u_{HP,\mathbf{q}} = \sqrt{\frac{\hbar}{2NM\omega_{HP}}} (a_{-\mathbf{q}}^\dagger + a_{\mathbf{q}}), \quad (\text{A.2})$$

where  $N$  is the number of unit cells,  $M$  is the unit cell mass,  $\omega_{HP}$  is the phonon frequency, and  $a_{\mathbf{q}}^{(\dagger)}$  is the annihilation(creation) of a phonon with wave vector  $\mathbf{q}$ , we get for the electron-phonon coupling

$$g_{HP} = \sqrt{\frac{\hbar}{2NM\omega_{HP}}} D. \quad (\text{A.3})$$

In the LO phonon case, the lattice induced displacements of the ions in the unit cell results in a polarization, which results in an electrostatic potential which the electrons interact with [42]. To obtain the coupling of electrons with the polar LO phonons

at long wavelengths, we consider the electrostatic energy of a monolayer given in the continuum limit by [48],

$$E_{int} = \frac{1}{2} \int \frac{d^2 \mathbf{r} d^2 \mathbf{r}'}{|\mathbf{r} - \mathbf{r}'|} \sigma(\mathbf{r}) \sigma(\mathbf{r}') + \frac{1}{2\kappa} \int d^2 \mathbf{r} P_\perp^2; \\ \sigma(\mathbf{r}) = e\rho(\mathbf{r}) - \nabla \cdot \mathbf{P}_{op} - \nabla \cdot \mathbf{P}_\perp, \quad (\text{A.4})$$

where  $\rho(\mathbf{r})$  is the 2D electron density,  $\mathbf{P}_{op}$  is the polarization induced by the optical phonon,  $\mathbf{P}_\perp$  is the remaining in-plane polarization component, and  $\kappa$  is the in-plane polarizability or rigidity. Fourier transforming Eq. A.4, and integrating out the in-plane polarization  $\mathbf{P}_\perp$  by minimizing the energy with respect to it, thus using an adiabatic approximation for the in-plane polarization, giving

$$E_{int} = \frac{1}{2} \int \frac{d^2 \mathbf{q}}{(2\pi)^2} \frac{2\pi(\mathbf{q} \cdot \mathbf{P}_{op,\mathbf{q}} - ie\rho_\mathbf{q})(\mathbf{q} \cdot \mathbf{P}_{op,\mathbf{q}}^* + ie\rho_\mathbf{q}^*)}{q(1 + qr_*)}, \quad (\text{A.5})$$

where we defined the screening length  $r_* \equiv 2\pi\kappa$  in terms of the in-plane polarizability. The denominator term  $\epsilon(\mathbf{q}) = 1 + qr_*$ , plays the role of a momentum dependent dielectric function, which is characteristic of Coulomb interaction in 2D materials [19]. From Eq. (A.5) we can read out the contribution to the electrostatic energy coming from the electron-phonon interaction from the terms containing the phonon induced polarization  $\mathbf{P}_{op,\mathbf{q}}$  and the electron density  $\rho_\mathbf{q}$ ,

$$H_{e-ph} = \int \frac{d^2 \mathbf{q}}{(2\pi)^2} \frac{2\pi ie\mathbf{q} \cdot \mathbf{P}_{op,\mathbf{q}} \rho_\mathbf{q}^*}{q(1 + qr_*)}, \quad (\text{A.6})$$

where  $\rho_q, P_{op,q}$  are the Fourier components of the carrier density and polarization. The LO phonon induced polarization is given by the dipole moment per unit area,

$$\mathbf{P}_{op} = \frac{Ze}{A} \mathbf{u}(\mathbf{r}), \quad (\text{A.7})$$

where  $A$  is the unit cell area,  $\mathbf{u}(\mathbf{r})$  is the relative displacement of the ions, and  $Z$  is the Born effective charge of the displaced ions (opposite charge on the metal and two chalcogens). Quantizing the lattice vibrations, the phonon induced displacement Fourier component is given by

$$\mathbf{u}_\mathbf{q} = \sqrt{\frac{\hbar}{2NM_r\omega_{LO}}} \hat{\mathbf{e}}_\mathbf{q} (a_{-\mathbf{q}}^\dagger + a_\mathbf{q}), \quad (\text{A.8})$$

where  $N$  is a normalization factor equal to the number of unit cells in the sample,  $\omega_{LO}$  is the LO phonon frequency,  $M_r$  is the reduced mass of the metal and two chalcogen

atoms, and  $\hat{\mathbf{e}}$  is a unit vector in the direction of relative displacement of the ions. The charge density is given in second quantized form by

$$\rho_{\mathbf{q}}^* = \sum_{\mathbf{k}} c_{\mathbf{k}+\mathbf{q}}^\dagger c_{\mathbf{k}}. \quad (\text{A.9})$$

Finally, combining Eqs. (A.7, A.8, A.9) into Eq. (A.6), and converting the integration into summation we get,

$$H_{e-ph} = \sum_{\mathbf{k}, \mathbf{q}} \frac{2\pi i e^2 Z}{A(1 + qr_*)} \sqrt{\frac{\hbar}{2NM_r\omega_{LO}}} c_{\mathbf{k}+\mathbf{q}}^\dagger c_{\mathbf{k}} (a_{-\mathbf{q}}^\dagger + a_{\mathbf{q}}). \quad (\text{A.10})$$

The LO phonon coupling is then given as

$$g_{LO, \mathbf{q}} = \frac{2\pi i e^2 Z}{A(1 + qr_*)} \sqrt{\frac{\hbar}{2NM_r\omega_{LO}}}. \quad (\text{A.11})$$

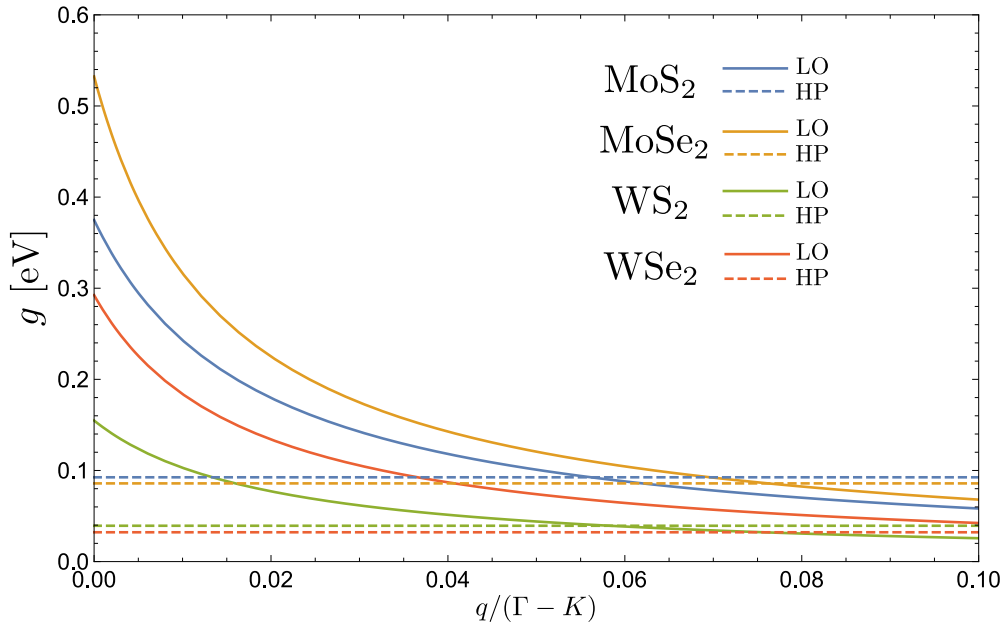


Figure A.1: Phonon coupling for the LO (solid) and HP (dashed) phonon modes as a function of the phonon wave vector  $q$  for the four TMDCs materials studied.

# Bibliography

- [1] A. K. Geim and I. V. Grigorieva. “Van der Waals heterostructures”. In: *Nature* 499 (July 2013), p. 419.
- [2] Kin Fai Mak, Changgu Lee, James Hone, Jie Shan, and Tony F. Heinz. “Atomically Thin MoS<sub>2</sub>: A New Direct-Gap Semiconductor”. In: *Phys. Rev. Lett.* 105 (13 2010), p. 136805.
- [3] Ting Cao et al. “Valley-selective circular dichroism of monolayer molybdenum disulphide”. In: *Nature Communications* 3 (June 2012).
- [4] Kin Fai Mak, Keliang He, Jie Shan, and Tony F. Heinz. “Control of valley polarization in monolayer MoS<sub>2</sub> by optical helicity”. In: *Nat Nano* 7.8 (Aug. 2012), pp. 494–498.
- [5] Di Xiao, Gui-Bin Liu, Wanxiang Feng, Xiaodong Xu, and Wang Yao. “Coupled Spin and Valley Physics in Monolayers of MoS<sub>2</sub> and Other Group-VI Dichalcogenides”. In: *Phys. Rev. Lett.* 108 (19 2012), p. 196802.
- [6] K. F. Mak, K. L. McGill, J. Park, and P. L. McEuen. “The valley Hall effect in MoS<sub>2</sub> transistors”. In: *Science* 344.6191 (2014), pp. 1489–1492. ISSN: 0036-8075.
- [7] Hongyi Yu and Wang Yao. “Magnetization without polarization”. In: *Nature Materials* 16 (Aug. 2017), p. 876.
- [8] Z. Y. Zhu, Y. C. Cheng, and U. Schwingenschlögl. “Giant spin-orbit-induced spin splitting in two-dimensional transition-metal dichalcogenide semiconductors”. In: *Phys. Rev. B* 84 (15 2011), p. 153402.
- [9] Xiaoze Liu et al. “Strong light–matter coupling in two-dimensional atomic crystals”. In: *Nature Photonics* 9 (Dec. 2014), p. 30.

- [10] Keliang He et al. “Tightly Bound Excitons in Monolayer WSe<sub>2</sub>”. In: *Phys. Rev. Lett.* 113 (2 2014), p. 026803.
- [11] Kin Fai Mak et al. “Tightly bound trions in monolayer MoS<sub>2</sub>”. In: *Nature Materials* 12 (Dec. 2012), p. 207.
- [12] Oriol Lopez-Sanchez, Dominik Lembke, Metin Kayci, Aleksandra Radenovic, and Andras Kis. “Ultrasensitive photodetectors based on monolayer MoS<sub>2</sub>”. In: *Nature Nanotechnology* 8 (June 2013), p. 497.
- [13] Andreas Pospischil, Marco M. Furchi, and Thomas Mueller. “Solar-energy conversion and light emission in an atomic monolayer p–n diode”. In: *Nature Nanotechnology* 9 (Mar. 2014), p. 257.
- [14] Britton W. H. Baugher, Hugh O. H. Churchill, Yafang Yang, and Pablo Jarillo-Herrero. “Optoelectronic devices based on electrically tunable p–n diodes in a monolayer dichalcogenide”. In: *Nature Nanotechnology* 9 (Mar. 2014), p. 262.
- [15] F. Withers et al. “Light-emitting diodes by band-structure engineering in van der Waals heterostructures”. In: *Nature Materials* 14 (Feb. 2015), p. 301.
- [16] Jason S. Ross et al. “Electrically tunable excitonic light-emitting diodes based on monolayer WSe<sub>2</sub> p–n junctions”. In: *Nature Nanotechnology* 9 (Mar. 2014), p. 268.
- [17] Marco M. Furchi, Andreas Pospischil, Florian Libisch, Joachim Burgdörfer, and Thomas Mueller. “Photovoltaic Effect in an Electrically Tunable van der Waals Heterojunction”. In: *Nano Letters* 14.8 (Aug. 2014), pp. 4785–4791.
- [18] Yu-Ming He et al. “Single quantum emitters in monolayer semiconductors”. In: *Nature Nanotechnology* 10 (May 2015), p. 497.
- [19] Pierluigi Cudazzo, Ilya V. Tokatly, and Angel Rubio. “Dielectric screening in two-dimensional insulators: Implications for excitonic and impurity states in graphane”. In: *Phys. Rev. B* 84 (8 2011), p. 085406.
- [20] Alexey Chernikov et al. “Exciton Binding Energy and Nonhydrogenic Rydberg Series in Monolayer WS<sub>2</sub>”. In: *Phys. Rev. Lett.* 113 (7 2014), p. 076802.

- [21] M. Danovich, I. L. Aleiner, N. D. Drummond, and V. I. Falko. “Fast Relaxation of Photo-Excited Carriers in 2-D Transition Metal Dichalcogenides”. In: *IEEE Journal of Selected Topics in Quantum Electronics* 23.1 (2017), pp. 168–172. DOI: 10.1109/JSTQE.2016.2583059.
- [22] Mark Danovich, Viktor Zólyomi, and Vladimir I. Fal’ko. “Dark trions and biexcitons in WS<sub>2</sub> and WSe<sub>2</sub> made bright by e-e scattering”. In: *Scientific Reports* 7 (Apr. 2017), p. 45998. DOI: 10.1038/srep45998.
- [23] E. Mostaani et al. “Diffusion quantum Monte Carlo study of excitonic complexes in two-dimensional transition-metal dichalcogenides”. In: *Phys. Rev. B* 96 (7 2017), p. 075431. DOI: 10.1103/PhysRevB.96.075431.
- [24] Mark Danovich, David A. Ruiz-Tijerina, Ryan J. Hunt, Marcin Szyniszewski, Neil D. Drummond, and Vladimir I. Fal’ko. *Localized interlayer complexes in heterobilayer transition metal dichalcogenides*. 2018. eprint: arXiv:1802.06005.
- [25] P Giannozzi et al. “Advanced capabilities for materials modelling with Q uantum ESPRESSO”. In: *Journal of Physics: Condensed Matter* 29.46 (2017), p. 465901. URL: <http://stacks.iop.org/0953-8984/29/i=46/a=465901>.
- [26] Andor Kormányos, Viktor Zólyomi, Neil D. Drummond, Péter Rakyta, Guido Burkard, and Vladimir I. Fal’ko. “Monolayer MoS<sub>2</sub>: Trigonal warping, the  $\Gamma$  valley, and spin-orbit coupling effects”. In: *Phys. Rev. B* 88 (4 2013), p. 045416.
- [27] Andor Kormányos et al. “k p theory for two-dimensional transition metal dichalcogenide semiconductors”. In: *2D Materials* 2.2 (2015), p. 022001. DOI: 10.1088/2053-1583/2/2/022001.
- [28] Gui-Bin Liu, Wen-Yu Shan, Yugui Yao, Wang Yao, and Di Xiao. “Three-band tight-binding model for monolayers of group-VIB transition metal dichalcogenides”. In: *Phys. Rev. B* 88 (8 2013), p. 085433.
- [29] Shiang Fang, Rodrick Kuate Defo, Sharmila N. Shirodkar, Simon Lieu, Georgios A. Tritsaris, and Efthimios Kaxiras. “Ab initio Tight-Binding Hamiltonian for Transition Metal Dichalcogenides”. In: *Phys. Rev. B* 92 (20 2015), p. 205108.

- [30] Gui-Bin Liu, Di Xiao, Yugui Yao, Xiaodong Xu, and Wang Yao. “Electronic structures and theoretical modelling of two-dimensional group-VIB transition metal dichalcogenides”. In: *Chem. Soc. Rev.* 44 (9 2015), pp. 2643–2663.
- [31] Marco Gibertini, Francesco M. D. Pellegrino, Nicola Marzari, and Marco Polini. “Spin-resolved optical conductivity of two-dimensional group-VIB transition-metal dichalcogenides”. In: *Phys. Rev. B* 90 (24 2014), p. 245411.
- [32] K. K. Kośmider, J. W. González, and J. Fernández-Rossier. “Large spin splitting in the conduction band of transition metal dichalcogenide monolayers”. In: *Phys. Rev. B* 88 (24 2013), p. 245436.
- [33] Di Xiao, Gui-Bin Liu, Wanxiang Feng, Xiaodong Xu, and Wang Yao. “Coupled Spin and Valley Physics in Monolayers of MoS<sub>2</sub> and Other Group-VI Dichalcogenides”. In: *Phys. Rev. Lett.* 108 (19 2012), p. 196802.
- [34] Pu Gong, Hongyi Yu, Yong Wang, and Wang Yao. “Optical selection rules for excitonic Rydberg series in the massive Dirac cones of hexagonal two-dimensional materials”. In: *Phys. Rev. B* 95 (12 2017), p. 125420.
- [35] A O Slobodeniuk and D M Basko. “Spin–flip processes and radiative decay of dark intravalley excitons in transition metal dichalcogenide monolayers”. In: *2D Materials* 3.3 (2016), p. 035009.
- [36] Timothy C. Berkelbach, Mark S. Hybertsen, and David R. Reichman. “Bright and dark singlet excitons via linear and two-photon spectroscopy in monolayer transition-metal dichalcogenides”. In: *Phys. Rev. B* 92 (8 2015), p. 085413.
- [37] Hualing Zeng, Junfeng Dai, Wang Yao, Di Xiao, and Xiaodong Cui. “Valley polarization in MoS<sub>2</sub> monolayers by optical pumping”. In: *Nature Nanotechnology* 7 (June 2012), p. 490.
- [38] Mark Danovich, Viktor Zólyomi, Vladimir I Fal’ko, and Igor L Aleiner. “Auger recombination of dark excitons in WS<sub>2</sub> and WSe<sub>2</sub> monolayers”. In: *2D Materials* 3.3 (2016), p. 035011.

- [39] Kristen Kaasbjerg, Kristian S. Thygesen, and Antti-Pekka Jauho. “Acoustic phonon limited mobility in two-dimensional semiconductors: Deformation potential and piezoelectric scattering in monolayer MoS<sub>2</sub> from first principles”. In: *Phys. Rev. B* 87 (23 2013), p. 235312.
- [40] J. Ribeiro-Soares et al. “Group theory analysis of phonons in two-dimensional transition metal dichalcogenides”. In: *Phys. Rev. B* 90 (11 2014), p. 115438.
- [41] Kristen Kaasbjerg, Kristian S. Thygesen, and Karsten W. Jacobsen. “Phonon-limited mobility in *n*-type single-layer MoS<sub>2</sub> from first principles”. In: *Phys. Rev. B* 85 (11 2012), p. 115317.
- [42] Thibault Sohier, Matteo Calandra, and Francesco Mauri. “Two-dimensional Fröhlich interaction in transition-metal dichalcogenide monolayers: Theoretical modeling and first-principles calculations”. In: *Phys. Rev. B* 94 (8 2016), p. 085415.
- [43] M. Szyniszewski, E. Mostaani, N. D. Drummond, and V. I. Fal’ko. “Binding energies of trions and biexcitons in two-dimensional semiconductors from diffusion quantum Monte Carlo calculations”. In: *Phys. Rev. B* 95 (8 2017), p. 081301.
- [44] Timothy C. Berkelbach, Mark S. Hybertsen, and David R. Reichman. “Theory of neutral and charged excitons in monolayer transition metal dichalcogenides”. In: *Phys. Rev. B* 88 (4 2013), p. 045318.
- [45] Jason S. Ross et al. “Electrical control of neutral and charged excitons in a monolayer semiconductor”. In: *Nature Communications* 4 (Feb. 2013), p. 1474.
- [46] Kin Fai Mak et al. “Tightly bound trions in monolayer MoS<sub>2</sub>”. In: *Nature Materials* 12 (Dec. 2012), p. 207.
- [47] Alexey Chernikov et al. “Exciton Binding Energy and Nonhydrogenic Rydberg Series in Monolayer WS<sub>2</sub>”. In: *Phys. Rev. Lett.* 113 (7 2014), p. 076802.
- [48] Bogdan Ganchev, Neil Drummond, Igor Aleiner, and Vladimir Fal’ko. “Three-Particle Complexes in Two-Dimensional Semiconductors”. In: *Phys. Rev. Lett.* 114 (10 2015), p. 107401.

- [49] Pierluigi Cudazzo, Ilya V. Tokatly, and Angel Rubio. “Dielectric screening in two-dimensional insulators: Implications for excitonic and impurity states in graphane”. In: *Phys. Rev. B* 84 (8 2011), p. 085406.
- [50] Hongyi Yu, Xiaodong Cui, Xiaodong Xu, and Wang Yao. “Valley excitons in two-dimensional semiconductors”. In: *National Science Review* 2.1 (Mar. 2015), pp. 57–70.
- [51] Xiaoze Liu et al. “Strong light–matter coupling in two-dimensional atomic crystals”. In: *Nature Photonics* 9 (Dec. 2014), p. 30.
- [52] Haining Wang, Changjian Zhang, Weimin Chan, Christina Manolatou, Sandip Tiwari, and Farhan Rana. “Radiative lifetimes of excitons and trions in monolayers of the metal dichalcogenide MoS<sub>2</sub>”. In: *Phys. Rev. B* 93 (4 2016), p. 045407.
- [53] Maurizia Palummo, Marco Bernardi, and Jeffrey C. Grossman. “Exciton Radiative Lifetimes in Two-Dimensional Transition Metal Dichalcogenides”. In: *Nano Letters* 15.5 (May 2015), pp. 2794–2800.
- [54] C. Robert et al. “Exciton radiative lifetime in transition metal dichalcogenide monolayers”. In: *Phys. Rev. B* 93 (20 2016), p. 205423.
- [55] Hongyi Yu, Xiaodong Cui, Xiaodong Xu, and Wang Yao. “Valley excitons in two-dimensional semiconductors”. In: *National Science Review* 2.1 (Mar. 2015), pp. 57–70.
- [56] Xiao-Xiao Zhang, Yumeng You, Shu Yang Frank Zhao, and Tony F. Heinz. “Experimental Evidence for Dark Excitons in Monolayer WSe<sub>2</sub>”. In: *Phys. Rev. Lett.* 115 (25 2015), p. 257403.
- [57] F. Withers et al. “WSe2 Light-Emitting Tunneling Transistors with Enhanced Brightness at Room Temperature”. In: *Nano Letters* 15.12 (Dec. 2015), pp. 8223–8228.
- [58] Roman Ya Kezerashvili and Shalva M. Tsiklauri. “Trion and Biexciton in Monolayer Transition Metal Dichalcogenides”. In: *Few-Body Systems* 58.1 (2016), p. 18. DOI: 10.1007/s00601-016-1186-x.
- [59] E. Courtade et al. *Charged excitons in monolayer WSe<sub>2</sub>: experiment and theory*. 2017. eprint: arXiv:1705.02110.

- [60] Jason W. Christopher, Bennett B. Goldberg, and Anna K. Swan. “Long tailed trions in monolayer MoS<sub>2</sub>: Temperature dependent asymmetry and resulting red-shift of trion photoluminescence spectra”. In: *Scientific Reports* 7.1 (2017), p. 14062.
- [61] Axel Esser, Erich Runge, Roland Zimmermann, and Wolfgang Langbein. “Photoluminescence and radiative lifetime of trions in GaAs quantum wells”. In: *Phys. Rev. B* 62 (12 2000), pp. 8232–8239.
- [62] V. Ongun, Javad G. Azadani, Ce Yang, Steven J. Koester, and Tony Low. “Band alignment of two-dimensional semiconductors for designing heterostructures with momentum space matching”. In: *Phys. Rev. B* 94 (3 2016), p. 035125.
- [63] Cheng Gong, Hengji Zhang, Weihua Wang, Luigi Colombo, Robert M. Wallace, and Kyeongjae Cho. “Band alignment of two-dimensional transition metal dichalcogenides: Application in tunnel field effect transistors”. In: *Applied Physics Letters* 103.5 (2013), p. 053513.
- [64] Jun Kang, Sefaattin Tongay, Jian Zhou, Jingbo Li, and Junqiao Wu. “Band offsets and heterostructures of two-dimensional semiconductors”. In: *Applied Physics Letters* 102.1 (2013), p. 012111.
- [65] Pasqual Rivera et al. “Observation of long-lived interlayer excitons in monolayer MoSe<sub>2</sub>–WSe<sub>2</sub> heterostructures”. In: *Nature Communications* 6 (Feb. 2015), p. 6242.
- [66] Yong Wang, Zhan Wang, Wang Yao, Gui-Bin Liu, and Hongyi Yu. “Interlayer coupling in commensurate and incommensurate bilayer structures of transition-metal dichalcogenides”. In: *Phys. Rev. B* 95 (11 2017), p. 115429.
- [67] Hongyi Yu, Yong Wang, Qingjun Tong, Xiaodong Xu, and Wang Yao. “Anomalous Light Cones and Valley Optical Selection Rules of Interlayer Excitons in Twisted Heterobilayers”. In: *Phys. Rev. Lett.* 115 (18 2015), p. 187002.
- [68] Chendong Zhang et al. “Interlayer couplings, Moiré patterns, and 2D electronic superlattices in MoS<sub>2</sub>/WSe<sub>2</sub> hetero-bilayers”. In: *Science Advances* 3.1 (Jan. 2017).

- [69] Qingjun Tong, Hongyi Yu, Qizhong Zhu, Yong Wang, Xiaodong Xu, and Wang Yao. “Topological mosaics in moir  superlattices of van der Waals heterobilayers”. In: *Nature Physics* 13 (Nov. 2016), p. 356.
- [70] B. F. Levine. “Quantum well infrared photodetectors”. In: *Journal of Applied Physics* 74.8 (1993), R1–R81.
- [71] Rui Q. Yang. “Infrared laser based on intersubband transitions in quantum wells”. In: *Superlattices and Microstructures* 17.1 (1995), pp. 77–83.